Neumann Problem for Helmholtz Equation in Two-Dimensional Open Domains with Applications

By

Turker Topal

A thesis submitted to Macquarie University

for the degree of Doctor of Philosophy

Department of Mathematics and Statistics

December 2021

MACQUARIE
University
SYDNEY·AUSTRALIA

Summary

The research described in the thesis is devoted to a rigorous solution of the Neumann boundary value problem for the Helmholtz equation in two-dimensional open arbitrary domains, and its application to the diverse problems of practical acoustics and electro-engineering. The Method of Analytical Regularisation is used to transform the initial surface integral equation in the form of a double layer potential to well-conditioned coupled infinite systems of linear algebraic equations, thus addressing the hyper-singular kernel arising from the normal derivative of the double layer potential. The compactness of the matrix operators provides the fast convergence of the truncated versions of the infinite systems, numerical solution of which may be obtained with any predetermined accuracy.

Furthermore, complex eigenvalues of natural complex oscillations for various structures have been analysed extensively, using the spectral parameter (frequency) for which the matrix operator has zero valued determinant. A root finding algorithm is developed to improve the accuracy of the calculations as well as the computation time and performance. The developed method uses the spectral map of truncated system condition number for initial approximations. There are no restrictions imposed on boundaries of domains (except requirements on smoothness of the bounding contours), frequency range and size of entries (slits). To take advantage of all these merits of the solution, an object-oriented software for its numerical implementation has been developed: bounding contours of slotted arbitrary cylinders are generated by interpolation functions and Sobolev's approximation, providing a smooth parametrisation.

The numerical results cover spectral studies and resonance excitation of the slotted cylinders. Spectral studies of classical (closed) waveguides, ridged waveguides, and magnetron-type resonator cavities reveal an excellent agreement with the results available in literature. Complex eigenvalues associated with slotted arbitrary cylinders are obtained for the first time. Classical cylinders (circular, elliptic and rectangular) as well as their corrugated and modified shapes (single and paired acoustic resonators with attached necks, polygonal and sinusoidally corrugated cylinders) are investigated.

Finally, wave scattering from slotted circular, elliptic, rectangular cavities, duct and bent duct cavities, parabolic reflector antennas (with and without flanges), corner reflectors, finite sinusoidally profiled gratings, and complex shapes such as an airplane and a submarine are studied. The MAR approach allows calculation of radar cross sections, scattering patterns and

field distributions for a frequency range from a few to a half-thousand wavelengths, covering the low-frequency region (Rayleigh scattering), the resonance regime (diffraction), and the high-frequency regions.

Statement of Originality

I certify that the work in this thesis has not previously been submitted for a degree nor has it been submitted as part of the requirements for a degree to any other university or institution other than Macquarie University.

I also certify that this thesis is an original piece of research and has been written by me. Any help and assistance that I have received in my research work and the preparation of the thesis itself has been appropriately acknowledged.

In addition, I certify that all information sources and literature used are indicated in the thesis.

_____

Turker Topal

Acknowledgements

Contents

List of Figures

List of Tables

List of Code Snippets

1

Introduction

1.1 Preliminary Remarks

This thesis concerns some investigations of the Neumann boundary value problems for the Helmholtz Equation arising in two-dimensional (2D) open structures. A few remarks and observations that are common to each chapter should be made. First, there is a direct correspondence between acoustic and electromagnetic scattering from 2D objects which are open or closed infinitely long cylinders, and in general of arbitrary cross section. In the following chapters we mostly analyse closed or slotted 2D cavities with infinitesimally thin walls, without investigating solid acoustically penetrable or dielectric cylinders. We study acoustic wave scattering from sound-hard (SH) or rigid cylinders, and in parallel, we study electromagnetic scattering of $H-$polarised waves from perfect electric conductor (PEC) cylinders. Although acoustic waves are longitudinal waves while electromagnetic waves are transverse, they share similar wave equations and boundary conditions. In our case, both acoustic and electromagnetic scattering is described by the 2D Helmholtz equation $(\Delta + k^2)U = 0$ with wavenumber $k = 2\pi/\lambda$ satisfying the Neumann boundary condition at the surface S of the cylinder. In acoustics, the function U represents the *velocity potential* while in electromagnetics it describes the *longitudinal component of magnetic field H_z*. Therefore, by proper reformulation of the physical terms and correct treatment of the numerical result, the same method can be used to obtain the solution to either

an acoustic or an electromagnetic problem.

Beyond this theoretical aspect, the similarity of electromagnetic and acoustic scattering has practical applications. For example, based on these similarities a method of measuring electromagnetic radar cross section (RCS) using underwater acoustic technology is proposed in [1]. The non-trivial analogy between propagation of the TEM mode and propagation of viscoelastic S waves (shear waves with the displacement in the horizontal plane) in the plane of symmetry of a monoclinic medium is shown in [2]. The similarities are further highlighted in [3]; it is shown that the two-dimensional Maxwell equations are mathematically equivalent to the S-wave equation based on a Maxwell stress–strain relation. The corresponding terms are listed as follows: magnetic field/particle velocity, electric field/stress, dielectric permittivity/elastic compliance, resistivity/viscosity, and magnetic permeability/density. Acoustic-electromagnetic analogies in diffraction phenomena are discussed in [4] where similarities between acoustic and electromagnetic wave fields occurring in bounded areas, such as waveguides, when electromagnetic waves are not purely transversal are presented. The acoustic-electromagnetic analogies exist in structures such as plane, rectangular, or cylindrical infinite waveguides, if the fields are analysed by means of potentials - the velocity potential for sound waves and the Hertz potentials for electromagnetic waves.

A list of publications on the correspondence between acoustic and electromagnetic problems might be substantially extended, but in context of the present thesis this would be excessive. In this thesis we do not use any non-trivial acoustic-electromagnetic analogies (discussed for example in [2] and [3]). When the Dirichlet boundary condition for the 2D Helmholtz equation is imposed, the solution of the corresponding problem describes wave scattering of acoustic radiation from a sound-soft (SS) cylinder and electromagnetic $E-$polarised radiation from a PEC cylinder. In case of the Neumann boundary condition, it describes acoustic radiation from an SH cylinder or $H-$polarised radiation from PEC cylinder. When restricted for closed domains only, the solution for Dirichlet Boundary Value Problem (BVP) and Neuman BVP can be obtained in form of *Magnetic Field Integral Equation (MFIE)* which is numerically well conditioned. However, the solution for open domains is obtained in form of *Electric Field Integral Equation (EFIE)* which contains a weak singularity for Dirichlet BVP and a hyper-singularity for Neumann BVP.

The second remark is related to the well-known observation that any open cavity with rigid walls may be regarded as a Helmholtz resonator. This fact is of great importance in many

practical areas of acoustics; it is often considered as a basic acoustic application but sometimes it can be used for special acoustic applications. For example, the paper [5] presents a method that uses acoustic Frequency Response Functions (FRF) to predict modifications in a novel acoustic system: a cavity of a rocket engine combustion chamber. Insertion of Helmholtz Resonators (HR) is applied as a cavity modification: the use of HR in such chambers attenuates the effect of combustion instability, which can seriously damage an engine. The acoustical-electromagnetic analogy has resulted in a number of theoretical studies ([6–8]) and practical applications ([9, 10]).

Another remark should be made on the spectral investigation of 2D closed or slotted cylinders that may be regarded as 2D cavities supporting a regime of standing waves, or providing regime of wave propagation in waveguides. In both cases, the values of "cavity resonances" and "cut-off frequencies" for 2D arbitrary cylinders are numerically identical. It simply means that the spectrum of acoustic (or electromagnetic) oscillations in 2D cavities is at the same time the spectrum of cut-off frequencies for propagating modes in acoustic (or electromagnetic) waveguides of the same cross sections.

A final remark concerns applications of slotted and closed cavities in acoustics and electromagnetics. In acoustics, sound-soft cavities are mostly utilised for simulation of underwater scattering problems while sound-hard cavities are used for modelling wave scattering problems arising in aero-acoustics. In electromagnetics, the problems of wave scattering and wave propagation of both $E-$polarised and $H-$polarised waves for closed cavities are equally significant and valuable. For slotted cavities, the case of $H-$polarisation brings an additional physical effect when the spectrum of the complex oscillations is supplemented by the Helmholtz mode with an eigenvalue which precedes that of the fundamental mode. In our opinion, the solution of the Neumann problem for the Helmholtz equation uncovers more possibilities for the design of practical devices in acoustical and electro-engineering. This thesis is devoted to the comprehensive theoretical examination of this problem, which in turn significantly extends the areas of application in practical acoustics and electro-engineering.

1.2 Brief Survey of Regularisation Techniques for the Solution of Surface Integral Equations

The Neumann problem for the Helmholtz equation in two-dimensional space, incorporating closed or slotted cavities of arbitrary cross section, obeys the principle of superposition. This

equation is usually analysed by methods of potential theory, and they explicitly or implicitly rely on the linearity of the underlying partial differential equation. An example of the solution of the Helmholtz equation with the Neumann boundary condition at the surface of a closed (or open) cavity, sought in the form of the double-layer potential, is presented in [11]. Using the boundary condition, the problem is reduced to solving a hyper-singular integral equation. Such equations appear in many areas of mathematical physics and motivate thorough studies. It should be noted that the solution of this equation with various level of mathematical rigour or correctness has been investigated by many authors. The extensive literature and number of publications on the subject indicate the continuing present-day interest in this problem. A detailed review of various solution methods can be found in [11–18]. Let us briefly outline the main approaches to numerical solutions of hyper-singular integral equations in wave scattering.

It is widely postulated in the literature that the time-harmonic acoustic and electromagnetic scattering problems are among the engineering problems for which boundary element methods (BEM) have already shown to yield powerful numerical techniques. This general assertion should be more critically examined. BEMs proceed by representing the unknown quantity defined on the boundary as an unknown linear combination of known basis elements, and a finite linear system of linear equations is obtained by either Galerkin's method, or the least squares method or more general Petrov-Galerkin techniques; point-matching or collocation approaches can also be used ([19]). In all cases, the aim is to refine the basis (increasing its order) until the obtained numerical solution is deemed sufficiently accurate. This procedure can be expected to converge to the exact solution as the order is increased if the underlying integral equation is of second kind, but such an expectation of a first kind integral equation is unreasonable. Typically, the error (or difference from the exact solution) in the numerical solution at first decreases as the basis order is increased, reaching a non-zero minimum, but then increases and usually diverges to infinity. It can thus be difficult, if not impossible, to identify a numerical solution that is "reasonably" accurate. The situation is most acute when the scattering structure is nearly resonant, i.e., the cavity sustains high-Q oscillations, in which case either very high order systems are required for any accuracy (with excessive computational resource requirements), or it is impossible to obtain any reasonable numerical solution ([20]).

The popularity of integral equation methods among the engineering community is explained by the possibility of obtaining the numerical solution of integral equations by their discretisation. In the realisation of numerical schemes, there is a well-known drawback in that the standard

integral equation formulations obtained from the Green's representation formula fail to have a unique solution at frequencies corresponding to the eigenfrequencies of the adjoint associated interior problem for time-harmonic acoustics. This is not a physical drawback, nor does it appear when the problem is represented by partial differential equations, but it arises entirely as a result of a deficiency of the integral equation representation ([12]).

To avoid this drawback, two conventional techniques have been developed for acoustically hard body scattering. The first one is called CHIEF, the combined Helmholtz integral equation formulation ([21]), which is perhaps the most extensively used in engineering applications. The second technique is derived by Burton and Miller ([22]) which linearly combines the Helmholtz integral equation with its normal derivative equation. The details of both approaches are discussed in [13], and the comparison of these two methods reveals their complications ([23–26]). The CHIEF method imposes an additional constraint on the solution of the boundary integral equation by requiring it to vanish at selected positions inside the boundary to suppress the resonant solution that has no physical significance in the external problem. The alternative approach proposed by Burton and Miller (BM) involves solving a hyper-singular integral equation in which the original boundary integral equation is the real part and the boundary integral equation for the normal derivative is the imaginary part. In both cases, the equations that need to be solved contain mathematical singularities associated with the conventional formulation of the boundary integral equation and much effort since then has been made in the expeditious and efficient treatment of these singularities.

Sometimes, implementation of purely numerical approaches in solving the hyper-singular integral equations requires state of the art techniques to cope with concrete shapes of scatterers. For example, as reported in [26], the BM method uses a coupling parameter which, in theory, is a complex number with a non-vanishing imaginary part. In practice, it is usually chosen proportional or even equal to i/k. A literature review of papers about the BM method and its implementations reveals that in some cases it is better to use $-i/k$ as the coupling parameter. Surprisingly, an unexpectedly large number of studies are based on the wrong choice of the sign in the coupling parameter. Herein, it is described which sign of the coupling parameter should be used for different configurations. Furthermore, it is shown that the wrong sign does not just make the solution process inefficient but in some cases can lead to completely wrong results. To reduce the condition number of the resulting BM formulation at low frequencies, a regularised version $\alpha = ik/(k^2 + \lambda)$ of the classical BM coupling factor $\alpha = i/k$ is proposed in [27]. It

becomes evident that the enforcement of the BM method does not guarantee the uniform relative error of calculations across a wide frequency band.

The peculiarities of the different methods of discretisation, usually applied to both the electric field integral equation (EFIE) and the magnetic field integral equation (MFIE), are discussed in many publications (see, for example, [28]). In particular, it is stressed that direct methods involving the inversion of dense matrix systems are not realistic alternatives for many scattering problems of practical interest, and iterative algorithms are often required. In such cases, the numerical consequences of poor conditioning of the EFIE are more significant. The unbounded increase of the condition number of the discretised EFIE as the discretisation interval tends to zero generally leads to an unbounded increase in the iteration count of complex Krylov subspace algorithms ([29]). Naturally, the surface integral equations are the Fredholm equations of the first kind with their main prominent feature being "ill-posedness". In fact, the straightforward application of usual numerical methods to the matrices obtained by discretisation of these types of equations gives rise to implausible and incorrect numerical answers. As a matter of fact, a paradoxical behaviour appears: the finer the discretisation, the worse the divergence of the solution from the actual solution can become.

A detailed overview of numerical methods for first kind Fredholm integral equations and its critical analysis is presented in [30]. From the point of view of current methods for solving the first kind Fredholm integral equation, the main approach is to use a *regularisation algorithm* and adopt various regularisation operators to solve different integral equations. Another approach uses the wavelet method which gives a set of wavelet bases as the basis functions to approximate the integral equation, and solves the integral equation by improving the basis function or improving the iterative algorithm. In addition, multi-scale iteration methods, the Lagrange polynomial interpolation methods, algebraic solution methods, statistical methods, orthogonal inversion methods, and others can be applied to specific equations. These methods employ approximation of differing types. It is not only challenging to select correct approximation functions, but also finding a numerical solution based on such approximation functions is a complex task.

The algorithms for *numerical regularisation* can be constructed in many ways. We will not go into a detailed discussion of the merits and shortcomings of various numerical regularisation techniques, since none of them nor their modifications are used in this thesis. Nevertheless, this problem is considered in, for example, the publications [30, 31]. In general, most of the numerical

regularisation techniques presented so far in the literature for evaluating the hyper-singular integrals in the boundary integral equations (BIE) arise from certain identities associated with the fundamental solution to the Laplace equation. This is due to the fact that the Laplace operator in the Helmholtz equation is responsible for the singular behaviour of the kernels of the BIE.

From this overview of the problem, let us summarise the key observations which will contribute to our treatment of its effective solution. First, the exterior Neumann problem (formulated in terms of double layer potentials [11]), breaks down for closed objects when the wavenumber k equals the eigenvalue of the interior Dirichlet problem: the same is true for the exterior Dirichlet problem (formulated in terms of single layer potentials [11]) and the corresponding interior Neumann problem. When the wavenumber k takes certain discrete values, the interior problem with homogeneous boundary conditions has non-trivial solutions. These values of k are the eigenvalues of the interior problem and the corresponding non-trivial solutions are its eigenfunctions. It can be shown that these eigenvalues must be real ([32]). At these values the corresponding integral equation governing the exterior problem breaks down, i.e., it may either fail to yield a unique solution or be insoluble for the given inhomogeneous term. The investigation [33] gives a detailed treatment of this. It is shown that the exterior Neumann (Dirichlet) problem breaks down whenever the wavenumber k equals the eigenvalue of the interior Dirichlet (Neumann) problem.

Secondly, surface integral equations when used for the solution of the problems both in open and closed domains by their nature are first kind Fredholm integral equations which are ill-posed. The enforcement of direct numerical methods for their solution is not a simple procedure; there are issues concerning the computational accuracy, uniform validity in different parts of frequency range, behaviour at resonance frequencies, etc. Even the most advanced numerical techniques are not capable of overcoming the generic ill-conditioning of the original equations. For this reason, robust numerical solvers are obtained by subjecting these equations to numerical (or analytical) transforms (regularisation, preconditioning, etc.). In other words, it is highly desirable to convert the originally ill-conditioned equations to well-conditioned second kind Fredholm equations, whether it is done numerically or analytically.

In this thesis we mainly consider open 2D cylinders of arbitrary cross section. Equally for acoustic and electromagnetic scattering, the mathematically rigorous and correct problem statement involves mixed boundary conditions: the Neumann boundary condition at the surface

of the slotted cylinder and the Dirichlet boundary condition across a slit. The term "mixed" indicates the absence of such distinctions between the internal or external problem as the "internal" or "external" regions of space are in fact coupled with each other through the openings (slits). The presence of a slit leads to the leakage of acoustic (or electromagnetic) energy through the slit to external space, i.e. leads to dissipation of energy from the interior of a cylinder, and hence to the radiation losses. In this case, the spectrum of real eigenvalues, which is characteristic for a closed cylinder, is replaced by a spectrum of complex eigenvalues and the non-uniqueness of the external Neumann or Dirichlet problem for closed cylinders disappears: the mixed boundary value problem describing a slotted cylinder now has a unique solution. The solution uniqueness of the acoustic (or electromagnetic) scattering problems in open domains is proved in many publications (see, for example [34]).

We revisit the regularisation of the surface integral equation to discuss a few relatively new methods, in addition to the publications mentioned above. In [35–37], a similar idea to those in [12] is used, where a procedure of regularisation is described for both weakly singular and hyper-singular kernels. The weakly singular integrals are de-singularised by subtracting a term from the integrand and adding it back with its exact value. The hyper-singular kernel is further de-singularised using some properties of the interior Laplace problem. As asserted by authors, the new formulations are advantageous in a sense that they can be computed directly by using standard quadrature formulas. In [35] a boundary integral formulation for the solution of the Helmholtz equation is developed in which all traditional singular behaviour in the boundary integrals is removed analytically. In a reformulated boundary integral solution of the Laplace equation and the Stokes equation of fluid mechanics all singular terms in the integrals are removed analytically ([36]). The regularisation of all the singular behaviour on the boundary means that the surface integrals can be evaluated using any convenient quadrature method. Except for some minor peculiarities, a similar approach to de-singularisation is demonstrated in [37]. A different way of de-singularisation can be found in [38], where the singularity of the MFIE and its extraction is considered. Another interesting variant of regularisation is demonstrated in [18], where it is achieved via the analytical inversion of the hyper-singular part of the combined field integral equation, without negative repercussions on computational complexity.

Despite the development of rather advanced and theoretically solid methods for the solution

of the surface integral equations and wide-spread use of them by the acoustic and electro-engineering communities, there is still a need for more efficient methods which would be capable of comprehensive and accurate analysis of wave scattering problems, including finding the eigenvalues in closed and open arbitrary cylinders. Furthermore, it is highly desirable to use one unique method to cover the different parts of the frequency range: the low-frequency region (Rayleigh scattering), where wavelength λ greatly exceeds the characteristic size a of a scatterer ($\lambda \gg a$); the resonance (diffraction) region ($\lambda \sim a$); and the high-frequency region ($\lambda \ll a$).

The Method of Analytical regularisation (MAR), developed in this thesis for the solution of the Neumann boundary value problem for 2D Helmholtz equation addresses all the issues above. The basic principles of the method are discussed in the next section.

1.3 Distinctive Features of the Method of Analytical Regularisation

In this thesis we implement a rigorous approach, the Method of Analytical Regularisation (MAR), which is applied to acoustic and electromagnetic wave scattering by slotted sound-hard (rigid) and PEC cavities bounded by arbitrary smooth contours. It is an analytical-numerical method, which is based on the analytical inversion of the singular part of the original operator occurring in the integral equation formulation of the scattering problem, and is derived from the double-layer potential representation of the scattered field. For this reason, in many publications, the historically employed title "method of regularisation" is replaced by the more specific "method of analytical regularisation" or "method of semi-inversion". Although these two terms are often used interchangeably, the semi-inversion method does not allow for a free choice of space mapping, which is very important from the numerical point of view [39]. Returning to the process, it converts the double-layer (or single-layer potential for case of the Dirichlet problem) formulation to a second kind Fredholm matrix equation (of infinite dimension), which is solved by truncation to a finite dimension system. Simplistically, this method may be explained as follows.

Let us represent the surface integral equation in operator form ([11])

$$Ax = b \qquad (1.1)$$

where A is the problem operator (involving the free-space Green's functions), x is the solution vector to be found and b is the known right-hand side of the equation, given by an incident acoustic (or electromagnetic) radiation. The first step in the MAR is the splitting of operator A into singular (A_0) and regular (A_1) parts:

$$A = A_0 + A_1 \tag{1.2}$$

where A_0 is extracted from A in analytical form so that the operator $A_1 = A - A_0$ formed as the difference between the initial operator A and its singular part A_0 is regular ("smooth"). As a result, we arrive at the equation

$$(A_0 + A_1)\, x = b. \tag{1.3}$$

The second step is the analytical construction of the inverse operator A_0^{-1}. Then operator A_0^{-1} is applied to both parts of equation (1.3)

$$A_0^{-1}\,(A_0 + A_1)\, x = A_0^{-1} b, \tag{1.4}$$

which leads to a second kind Fredholm equation

$$(I + H)\, x = B, \tag{1.5}$$

where $I = A_0^{-1} A_0$ ($\|I\| = 1$) is the identity operator, $H = A_0^{-1} A_1$ is a *completely continuous (compact)* operator in the corresponding functional class, and the right-hand side of the equation $B = A_0^{-1} b$ belongs to the same class. The splitting of operator A into A_0 and A_1, and analytical construction of A_0^{-1} is not an arbitrary process and explained in detail in Chapter 2. The solution class is entirely defined by the smoothness of the bounding contours of closed cavities, and the presence of the sharp edges in case of cavities with openings. In all cases equation (1.5) is presented in discretised form as well-conditioned infinite systems of linear algebraic equations. When solving 2D wave scattering problems for closed (or open) cavities, discretisation is attained by the expansion of all terms contributing to the integral equation functions in exponential series $\left\{e^{in\vartheta}\right\}_{n=-\infty}^{\infty}$, which are complete and orthogonal in the interval $\vartheta \in [-\pi, \pi]$ (i.e. Fourier series).

One of the Fredholm theorems, known as the Fredholm alternative in its version for linear algebra, allows us to use the truncation method to solve the infinite-dimensional matrix equations of type (1.5), in which the solution of the infinite-dimensional matrix equations is approximated

by the solution of a truncated finite-dimensional linear system of equations, characterised by the truncation number N. The MAR provides extremely fast convergence of the solution $\{\tilde{x}_n\}_{n=0}^N$ of the truncated systems to the exact solution $\{x_n\}_{n=0}^\infty$ as $N \to \infty$. The convergence rate of truncated systems is examined in the thesis.

The MAR is not a new method. It has had almost sixty years of development [40]; the first forty years of its use has been described in the review [41]. A significant number of publications where the MAR is used are devoted to wave scattering from canonically shaped objects, i.e., scatterers the bounding surfaces of which are described by complete or partial coordinate surfaces. Solution of the boundary problems for the Helmholtz (or Maxwell) equations for such structures may be obtained by the method of separation of variables. The effectiveness of the MAR is demonstrated in the two-volume monograph [42, 43] where potential and wave scattering problems for canonically shaped open cavities have been investigated. In addition, the short surveys [44] and [45] highlight new aspects of the MAR application. The existence of a powerful mathematical tool in solving wave scattering problems for canonical structures was an incentive for generalisations of the MAR for analysis of wave scattering problems for a wide class of open arbitrarily shaped cavities.

The first generalisation of the MAR was realised in two-dimensional wave-scattering problems for slotted arbitrary cylinders. The first steps were made as far back as 1985 for the Dirichlet boundary conditions ([46]) and in 1987 for the Neumann boundary conditions ([47]). In these short publications, the mathematical formal scheme was reported. An exhaustive mathematical treatment of the generalised MAR with the proof of solution existence and uniqueness, expansion of the hyper-singular kernels in the neighbourhood of their singular points and many other useful aspects for the realisation of numerical algorithms is presented in [48]. Moreover, further substantial manipulations and developments are required and necessary for the practical implementation of a numerical algorithm, especially where the Neumann problem for the Helmholtz equation is investigated. (These are also absent in the publications [46, 47]). Possibly this is the main reason why this rigorous and highly effective approach to the Neumann problem for the Helmholtz equation has found little usage, focusing on closed problems ([49, 50]). By contrast, it should be noted, that the employment of the MAR for the Dirichlet problem has found its full realisation and implementation, passing all the way from the pioneering paper [46] to comprehensive practical investigations ([51–55]). The full implementation of the numerical solution to the Neumann problem for the Helmholtz equation for a range of two-dimensional

open domains is a major and novel outcome of this thesis. The developments necessary for the practical implementation of MAR solution are detailed in Chapter 2. Both the method of solution and the applications to Helmholtz resonators, to spectral studies of slotted cavities, their complex eigenvalues and resonant wave scattering, and other applications detailed in subsequent chapters are new contributions to the field of study.

After this brief review of publications relevant to the research topic of this thesis, let us write down the truncated form of equation (1.5) (here $L \equiv I + H$) :

$$L_N x_N = B_N. \tag{1.6}$$

The focus for the spectral problem is on the underlying matrix operator and the complex eigenvalues at which non-trivial solutions of the homogenous equation ($B_N \equiv 0$) occur. The dispersion equation then emerges as the requirement

$$\det L_N(k) = 0. \tag{1.7}$$

as a parameter of wavenumber k. The compact nature of operator H ensures that any individual root of the dispersion equation converges to its exact value as truncation number N increases. This feature makes the MAR approach both accurate and efficient and allows us to use the well-known routines for finding the complex roots of the complex-valued function representing the determinant of the truncated system. It thus represents a new approach to obtaining highly accurate spectral information for slotted cavities with modest computational resource requirements. The fruitfulness of this approach was demonstrated, in particular, in [54], in the context of finding the spectrum of the complex eigenvalues in a slotted sound-soft cavity.

1.4   Research Objectives

In this thesis, we apply the Method of Analytical Regularization, for the first time, to the Neumann boundary value problem for arbitrarily shaped open/closed domains, using piecewise cubic Hermite interpolation and Sobolev space approximation by Friedrich's mollifier. We aim to achieve the same effectiveness of results as obtained for Dirichlet boundary value problem noting that the problem is more complex because the corresponding integral equation has a hyper-singular kernel.

Once the solution is obtained, it is the subject of further applied and computational mathematical studies where the theoretically effective solutions are converted into computational routines of high effectiveness. We aim to develop computer codes that are efficient and fast while providing flexibility to apply a wide class of objects and practical applications.

Various aspects of thesis include obtaining well-conditioned algebraic systems employing a compact perturbation of the identity operator in l_2, examining the fast convergence of the truncation method, and demonstrating how accuracy of the computations can be predetermined.

From the theoretical point of view, this program provides a highly satisfactory completion of the studies related to the rigorous solution of acoustic (or electromagnetic) wave scattering by two-dimensional arbitrary shaped open or closed cavities (or waveguides), encompassing both sound soft ($E-$polarisation) and sound-hard ($H-$polarisation) cases.

From a practical viewpoint, contour smoothing by means of Sobolev approximation, to construct a smooth parametrization that has continuous higher order derivatives, is combined with the Method of Analytical Regularization for the first time. This enables us to carry out detailed investigation and calculation of the complex eigenvalues of various structures for which Method of Regularization has not been applied before.

1.5   Outline of the Thesis

In Chapter 2, the mathematically challenging Neumann boundary value problem for the Helmholtz equation in open 2D domains is rigorously solved. By enforcement of the Method of Analytical Regularisation, the originally ill-posed integral equation with hyper-singular kernel is reduced to coupled well-conditioned infinite systems of linear algebraic equations. The compactness of the matrix operators ensures an effective solution of these equations is obtained by the truncation method. The fast convergence of the solution of the truncated equation to the exact solution is provided by calculation of the truncation error function $e(N)$, which tends to zero as $N \to \infty$. The ease of the matrix filling, when matrix elements are mostly computed by the Fast Fourier Transform and recursive procedures, and absence of the limitation on modelling the slotted arbitrary cylinders make the developed approach a reliable and highly accurate instrument for the diverse practical problems arising in acoustics and electromagnetics. By taking advantage of shape preserving interpolation functions together with Sobolev's approximation using the Frederich's mollifier (also known as standard mollifier function), the capability of

the MAR for investigation of polygonal and arbitrary cross sections (i.e. rectangular, triangular, and double-ridge waveguides) is demonstrated.

Chapter 3 is devoted to the investigation of the Helmholtz resonators described for acoustic resonators of cylindrical and rectangular shapes widely used in practice. The application of the MAR to this important area of engineering acoustics shows the universality and accuracy of the method. The preliminary investigation of the performance of multiple Helmholtz Resonators considers a pair of resonators for circular and rectangular types and may be useful in making estimates of their coupling for design of practical devices. The effects of parameters defining the structures are presented in terms of unloaded Q−factors of the respective resonators.

In Chapter 4, we demonstrate the applicability of the developed method to the highly delicate problem of spectral studies for 2D open arbitrary cylinders. In our opinion, the successful treatment of complex open cavities conducted in this chapter is due, not only to the rigorous method itself, but also to the procedure of parametrisation of the arbitrary bounding contours described in detail in Chapter 2. Practically all of the presented results on the complex values of natural complex oscillations are obtained for the first time. It is shown that the accuracy of the approach used allows us to investigate without limitations the fine structure of the spectra, resolve problems of mode competition and separate higher modes, the complex eigenvalues of which may differ only in the fifth or sixth significant decimal place. Considering the-state-of-the-art in spectral studies for open structures, we would assert that the presented method possesses some unique merits and may be successfully applied in practice when solving non-trivial practical problems arising in acoustics and electromagnetics.

In Chapter 5, we investigate the resonance scattering of slotted cylinders of various shapes. In all cases the qualitative predictions of the resonance response is substantiated by the spectral studies of the slotted arbitrary cylinders. The discovery of delicate details in resonance scattering are obtained by these reliable high-accuracy computational algorithms. The phenomenon of the resonance duplet which is characteristic for open systems possessing natural complex oscillations with sufficiently high Q−factors is described. The total distribution of the scattered acoustic field at all observation angles is observed by employing the normalised scattering pattern, or in other words, the bistatic cross section. Examples of wave scattering for bent ducts demonstrates one more aspect of the universality of the MAR.

Further advanced applications of the MAR to the analysis of high-frequency scattering is demonstrated in Chapter 6. We apply the MAR to the classical parabolic cylindrical reflectors,

focusing on finding the fine details in the distribution of the reflected electromagnetic field in the neighbourhood of the geometrical optics (GO) focal line. Parabolic reflectors with attached flanges are also considered, where the effect of flange size on total field distribution is analysed. Although the performed calculations including corner reflectors are of illustrative character, they clearly demonstrate the potential for further accurate analysis. Finite sinusoidal gratings are also investigated in this chapter. Studies of the diffraction space harmonics (Floquet modes) for large gratings exceeding a half-thousand wavelengths show the high efficiency of the MAR. The capability of the MAR for comprehensive analysis of backscattering from complex 2D targets is shortly discussed at the end of this chapter.

Finally, the Conclusions chapter summarises the outcomes of this thesis and discusses further fruitful directions for future development and applications of the MAR.

<div style="text-align: right;">

2

</div>

The Neumann Boundary Value Problem for the Helmholtz Equation and the MAR

In this chapter, the MAR is applied to solving the problem of plane wave scattering from slotted sound-hard 2D arbitrary cavities. As noted in section 1.1, this problem is equivalent to the problem of scattering of $H-$polarised plane waves from slotted infinitely long PEC cylinders of arbitrary cross section. The approach is mainly based on ideas contained in [47, 48]. The expansion suggested in [47] of the hyper-singular kernel in the neighbourhood of the singular points is used for further numerical analysis.

2.1 Problem Statement

Geometry of the problem of an arbitrary slotted PEC cylinder excited by $H-$polarised radiation is shown in Figure 2.1. The arbitrarily shaped cavity with a longitudinal slit is bounded by the contour L which is part of a closed contour S, i.e. $L \subseteq S$.

Formulation of the scattering problem is as follows. A rigid slotted cavity of arbitrary shape is illuminated by an obliquely incident plane wave; the incidence angle α is measured from the positive part of the x-axis in counter-clockwise direction, as shown in Figure 2.1. We want to find the scattered velocity potential U^{sc} which along with incident potential $U^0 = e^{ik(x\cos\alpha + y\sin\alpha)}$
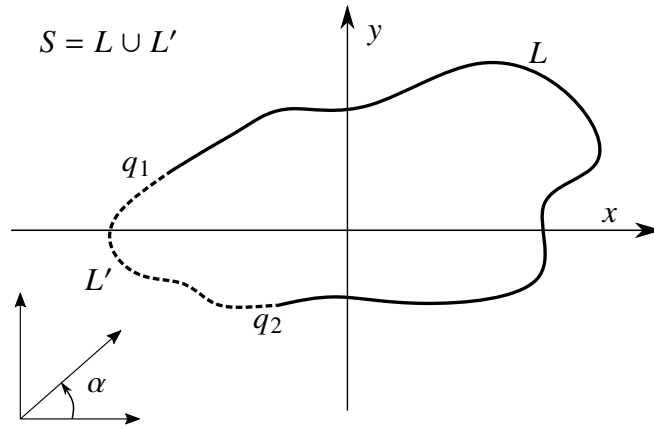
Figure 2.1: 2D arbitrary slotted rigid cavity illuminated by an incident plane wave at angle α.

defines the total field $U^{tot} = U^0 + U^{sc}$. The time harmonic dependence $e^{-i\omega t}$ is suppressed throughout the text. The function $U^{sc}(q)$ must satisfy the following conditions:

a) the homogeneous Helmholtz equation for all $q \in \mathbb{R}^2$:

$$\left(\Delta + k^2\right) U^s(q) = 0; \tag{2.1}$$

b) the mixed boundary conditions at each point $q \in S$:

$$\lim_{h \to 0} \frac{\partial U^{sc}\left(q \pm h\, n_q\right)}{\partial n_q} + \frac{\partial U_0\left(q\right)}{\partial n_q} = 0, \quad q \in L, \tag{2.2}$$

$$\lim_{h \to 0} U^{sc}\left(q + h n_q\right) = \lim_{h \to 0} U^{sc}\left(q - h n_q\right), \quad q \in S \setminus L, \tag{2.3}$$

where n_q is a unit vector denoting the outward normal to the contour S at the point q;

c) the radiation condition:

$$\frac{\partial U^{sc}(q)}{\partial q} - ik U^{sc}\left(q\right) = o\left(|q|^{-1/2}\right), \quad |q| \to \infty, \tag{2.4}$$

which means that the scattered field must behave as an outgoing cylindrical wave at infinity;

d) the edge condition concerning the endpoints q_1, q_2 of the slotted cavity, requiring that

grad $U^{sc}(q)$ is of the form

$$\text{grad } U^{sc}(q) = \frac{h(q)}{\sqrt{|q - q_1||q - q_2|}}, \tag{2.5}$$

where $h(q)$ is a smooth vector-function bounded across the entire plane.

The mathematically correct problem statement should involve all conditions of the uniqueness theorem. If it exists, the solution of the problem defined by the conditions (a)-(d) above admits an integral representation in the form of a double-layer potential ([11]),

$$U^{sc}(q) = \int_L \frac{\partial G_2(k|q - p|)}{\partial n_p} Z(p) \, dl_p, \quad q \in R^2 \setminus L, \tag{2.6}$$

where the Green's function $G_2(k|q - p|)$ is defined by

$$G_2(k|q - p|) = -\frac{i}{4} H_0^{(1)}(k|q - p|). \tag{2.7}$$

Here $Z(p)$ is an unknown function to be found and represents the jump of the scattered velocity potential at contour L, i.e.

$$Z(p) = U^{sc}(p - 0) - U^{sc}(p + 0), \quad p \in L, \tag{2.8}$$

and dl_p is the differential of arc length. In electromagnetics, the function $Z(p)$ corresponds to the jump of the surface current density at the infinitesimally thin walls of a cavity. As proved in [48], the fulfilment of the conditions (2.1) - (2.5) leads to the relationship

$$\lim_{h \to \pm 0} \frac{\partial}{\partial n_q} \int_L Z(p) \frac{\partial G_2(k|q + hn_q - p|)}{\partial n_p} dl_p = -\frac{\partial U^0(q)}{\partial n_q}, \quad q \in L. \tag{2.9}$$

Further transformations of equation (2.9) are studied extensively in [47, 48], and in [49]. We suppose that the contour is parametrised in the Cartesian coordinate system by a smooth vector-function

$$\eta(\vartheta) = \{x(\vartheta), y(\vartheta)\}, \vartheta \in [-\pi, \pi]$$

such that, after its 2π periodic continuation, it is smooth on $\vartheta \in (-\infty, \infty)$ and $\eta(-\pi) = \eta(\pi)$. Screen L is parametrised by a sub-interval $[-\vartheta_0, \vartheta_0]$: $L = \{(x(\vartheta), y(\vartheta)), \vartheta \in [-\vartheta_0, \vartheta_0]\}$ whilst the slot $L' = \{(x(\vartheta), y(\vartheta)), \vartheta \in [-\pi, -\vartheta_0) \cup (\vartheta_0, \pi]\}$ is created by the removal of

the segment from S, where $S = L \cup L'$; the choice of L' is not unique and may be chosen as convenient for the problem at hand. In establishing all mathematical arguments in analytical regularisation, we assume that the vector-valued function $\eta\,(\theta)$ is infinitely differentiable, i.e., $\eta\,(\theta) \in C^\infty\,(-\infty, \infty)$. However, in a numerical implementation of the solution algorithm, it is sufficient to require continuity of the first and second derivatives and existence of the third derivative. We also require satisfaction of the condition

$$l\,(\vartheta) = \sqrt{[x'\,(\vartheta)]^2 + [y'\,(\vartheta)]^2} > 0, \tag{2.10}$$

which guarantees that $\eta = \eta\,(\vartheta)$ is a one-to-one mapping. In addition, we assume that point $\eta(\vartheta)$ moves in the anticlockwise direction along the contour S as ϑ increases. Hence, the differential of arc length at point $p = p\,(\tau)$ is

$$dl_p = dl\,(\tau) = l\,(\tau)\,d\tau = \sqrt{[x'\,(\tau)]^2 + [y'\,(\tau)]^2}\,d\tau, \tag{2.11}$$

and the distance between two points $p = p(\tau)$ and $q = q(\theta)$ is

$$R = |p - q| = \sqrt{[x\,(\tau) - x\,(\theta)]^2 + [y\,(\tau) - y\,(\theta)]^2}. \tag{2.12}$$

Using this parametrisation we can introduce a new discontinuous function $z\,(\tau)$ defined on the complete interval of variation $\tau \in [-\pi, \pi]$ as

$$z\,(\tau) = \begin{cases} Z\,(\tau) & , \quad \tau \in [-\vartheta_0, \vartheta_0] \\ 0 & , \quad \tau \in [-\pi, -\vartheta_0) \cup (\vartheta_0, \pi]\,. \end{cases} \tag{2.13}$$

Following [48], we interchange the order of integration and differentiation, to transform (2.9) to

$$\lim_{h \to \pm 0} \int_{-\pi}^{\pi} \frac{\partial^2 G_2\,(k\,|q + hn_q - p|)}{\partial n_q \partial n_p} z\,(\tau)\,l\,(\tau)\,d\tau = -\frac{\partial U^0\,(q\,(\vartheta))}{\partial n_{q(\vartheta)}} \tag{2.14}$$

where $p\,(\tau) \in S$, $q\,(\vartheta) \in L$, $\vartheta \in [-\vartheta_0, \vartheta_0]$.

2.2   Solution of the Surface Integral Equation by the MAR

Although the process of analytical extraction of the singular part of the kernel in equation (2.14) is briefly described in [49] for the complete interval of parameter ϑ, (when $\vartheta \in [-\pi, \pi]$), it can also be applied in the case of the incomplete interval $\vartheta \in [-\vartheta_0, \vartheta_0]$ due to its independence on the limits of parameter ϑ. Taking into account this observation and considering that this extraction is the key to further transformation of (2.14) into a well-conditioned equation, we demonstrate the principal points of the extraction process below.

After evaluating the limit in (2.14), we arrive at the equation

$$\int_{-\pi}^{\pi} D_0(\vartheta, \tau) z(\tau) l(\tau) d\tau = -\frac{\partial u^0(q(\vartheta))}{\partial n_q(\vartheta)}, \quad \vartheta \in [-\vartheta_0, \vartheta_0], \tag{2.15}$$

where

$$D_0(\vartheta, \tau) \equiv \frac{\partial^2 G_2(k|q-p|)}{\partial n_q \partial n_p}. \tag{2.16}$$

As mentioned in Section 1.2, a variety of approaches have been used to treat this hypersingular kernel. Our method of regularising this equation employs the approach of [46–48] with the goal of achieving a second kind system of equations which are readily amenable to numerical solution techniques that are reliable and stable.

Interchanging of the limit and integration to obtain equation (2.15) is justified as the unknown function is a function of p, while the normal derivative ∂n_q of the Green's function is calculated in the vicinity of the boundary for a small positive value of h, thus $|q + hn_q - p| > 0$. The kernel $D_0(\vartheta, \tau)$ contains the non-integrable algebraic singularity in the form $(\vartheta - \tau)^{-2}$, and the logarithmic singularity (when $\vartheta - \tau \to 0$). It was proved in [48] that the function $D_0(\vartheta, \tau)$ allows the decomposition

$$D_0(\vartheta, \tau) = \frac{1}{2\pi l(\vartheta) l(\tau)} \left[K(\vartheta, \tau) - \frac{1}{4\left(\sin\frac{\vartheta-\tau}{2}\right)^2} \right], \tag{2.17}$$

where the function $K(\vartheta, \tau)$ has only a logarithmic singularity. When $\vartheta \to \tau$, $K(\vartheta, \tau)$ takes the form:

$$K(\vartheta, \tau) \sim C + \frac{1}{2} k^2 l(\vartheta) l(\tau) \log \left| 2 \sin \frac{\vartheta - \tau}{2} \right|. \tag{2.18}$$

After substitution of the decomposed kernel into equation (2.15) and making use of the well-known differentiation formula

$$
\frac{\partial^2}{\partial \vartheta^2} \log \left| 2 \sin \frac{\vartheta - \tau}{2} \right| = -\frac{1}{4 \left(\sin \frac{\vartheta - \tau}{2} \right)^2}, \tag{2.19}
$$

we obtain the equivalent integral-differential equation

$$
\frac{d^2}{d\vartheta^2} \int_{-\pi}^{\pi} z(\tau) \log \left| 2 \sin \frac{\vartheta - \tau}{2} \right| d\tau + \int_{-\pi}^{\pi} z(\tau) K(\vartheta, \tau) \, d\tau = F(\theta), \vartheta \in [-\vartheta_0, \vartheta_0], \tag{2.20}
$$

where the kernel $K(\vartheta, \tau)$ and right-hand side function $F(\tau)$ are defined by

$$
K(\vartheta, \tau) = 2\pi \, l(\vartheta) \, l(\tau) \, D_0(\vartheta, \tau) + \left[4 \left(\sin \frac{\vartheta - \tau}{2} \right)^2 \right]^{-1},
$$
$$
F(\vartheta) = -2\pi \, l(\vartheta) \left[\frac{\partial U^0(q)}{\partial n_q} \right]_{q=\eta(\vartheta)}. \tag{2.21}
$$

The next stage of regularisation is decomposition of the kernel $K(\vartheta, \tau)$ into a purely singular part and a "smooth" (regular) part $K_s(\vartheta, \tau)$:

$$
K_s(\vartheta, \tau) = K(\vartheta, \tau) - \frac{1}{2} k l(\vartheta) \, k l(\tau) \log \left| 2 \sin \frac{\vartheta - \tau}{2} \right|. \tag{2.22}
$$

The function $K_s(\vartheta, \tau)$ is smooth in a sense that all of its first derivatives are continuous and its second derivatives have only logarithmic singularities in the plane $(-\infty, \infty) \times (-\infty, \infty)$ after the 2π-periodic continuation of the function $K_s(\vartheta, \tau)$ with respect to both variables. This allows for its expansion in a double Fourier series, where the Fourier coefficients can be found numerically. Before the expansion, it is necessary to organise the correct calculation of the function $K_s(\vartheta, \tau)$. When $\vartheta \neq \tau$, $K_s(\vartheta, \tau)$ may be calculated directly using equations (2.16), (2.21), and (2.22):

$$
K_s(\vartheta, \tau) = 2\pi \, l(\vartheta) \, l(\tau) \, D_0(\vartheta, \tau) + \left[4 \left(\sin \frac{\vartheta - \tau}{2} \right)^2 \right]^{-1}
$$
$$
- \frac{1}{2} k l(\vartheta) \, k l(\tau) \log \left| 2 \sin \frac{\vartheta - \tau}{2} \right|, \vartheta \neq \tau. \tag{2.23}
$$

Since the function $D_0(\vartheta, \tau)$ possesses both algebraic and logarithmic singularities as $\vartheta \to \tau$,

equation (2.23) can not be used for computation of $K_s(\vartheta, \tau)$ at $\vartheta = \tau$. The expression for the function $K_s(\vartheta, \vartheta)$ with an arbitrary parametrisation $\eta(\vartheta)$ was derived analytically in [48], which we use in numerical computations:

$$
\begin{aligned}
K_s(\vartheta, \vartheta) = \frac{1}{2}(kl)^2 \log\frac{kl}{2} - \frac{1}{(kl)^2}\left[\frac{1}{6}k^2 P^{1,3} - \frac{1}{4}k^2 P^{2,2}\right] \\
- \frac{1}{2(kl)^4}\left[k^2 M^{1,2}\right]^2 - (kl)^2\left[-i\frac{\pi}{4} - \frac{\gamma}{2} + \frac{1}{4}\right] + \frac{1}{12}...,
\end{aligned}
\tag{2.24}
$$

where $\gamma = 0.57721566\ldots$ is the Euler's constant, and

$$
P^{i,j} \equiv P^{i,j}(\vartheta) = x^{(i)}(\vartheta)\,x^{(j)}(\vartheta) + y^{(i)}(\vartheta)\,y^{(j)}(\vartheta)
$$

$$
M^{i,j} \equiv M^{i,j}(\vartheta) = x^{(i)}(\vartheta)\,y^{(j)}(\vartheta) - y^{(i)}(\vartheta)\,x^{(j)}(\vartheta), \quad i,j = 1,2.
$$

Here $x^{(s)}(\vartheta)$ and $y^{(s)}(\vartheta)$ are the derivatives of order s of the functions $x(\vartheta)$ and $y(\vartheta)$, respectively. Thus, employment of the expression in equation (2.24) requires computation of only the first three derivatives of the arc length function $\eta(\vartheta)$.

The dual series equations are now formed by the Fourier expansion of the terms in equations (2.13) and (2.20), which are defined on two disjoint intervals of the variable ϑ : $[-\vartheta_0, \vartheta_0]$ and $[-\pi, -\vartheta_0) \cup (\vartheta_0, \pi]$, respectively. Thus after expansion of the unknown function $z(\tau)$ in the Fourier series

$$
z(\tau) = \sum_{n=-\infty}^{\infty} \xi_n e^{in\tau},
\tag{2.25}
$$

we immediately obtain one of the equations using (2.13)

$$
\sum_{n=-\infty}^{\infty} \xi_n e^{in\tau} = 0, \quad \tau \in [-\pi, -\vartheta_0) \cup (\vartheta_0, \pi].
\tag{2.26}
$$

Obtaining the companion series equation defined on the complementary interval of the variable $\vartheta \in [-\vartheta_0, \vartheta_0]$ is not as straightforward. It requires transformation of the integral-differential equation (2.20). The singular behaviour of the function $K_s(\vartheta, \tau)$ is the same as for the corresponding kernel function arising in the Dirichlet problem ([52]) since its singularity is of logarithmic type. It means that the Fourier coefficients of the function $K_s(\vartheta, \tau)$ can be found

numerically with the use of the Fast Fourier Transform (FFT), as was done in [52]:

$$K_s(\vartheta, \tau) = \sum_{m=-\infty}^{\infty} \sum_{n=-\infty}^{\infty} \kappa_{mn}^{(s)} e^{i(m\vartheta + n\tau)}, \quad \vartheta, \tau \in [-\pi, \pi]. \tag{2.27}$$

Once the coefficients $\kappa_{mn}^{(s)}$ are found, one can compute the Fourier coefficients κ_{mn} of the kernel $K(\vartheta, \tau)$:

$$K(\vartheta, \tau) = \sum_{m=-\infty}^{\infty} \sum_{n=-\infty}^{\infty} \kappa_{mn} e^{i(m\vartheta + n\tau)}, \quad \vartheta, \tau \in [-\pi, \pi]. \tag{2.28}$$

Since the functions $K(\vartheta, \tau)$ and $K_s(\vartheta, \tau)$ are related by equation (2.18) and the function $L(\vartheta, \tau)$ has the expansion in Fourier series

$$L(\vartheta, \tau) = \frac{1}{2} [kl(\vartheta)] \cdot [kl(\tau)] \log \left| 2 \sin \frac{\vartheta - \tau}{2} \right| = \sum_{m=-\infty}^{\infty} \sum_{n=-\infty}^{\infty} L_{mn} e^{i(m\vartheta + n\tau)}, \ \vartheta, \tau \in [-\pi, \pi], \tag{2.29}$$

then $\kappa_{mn} = \kappa_{mn}^{(s)} - L_{mn}$. To find L_{mn}, we use the well-known expansion

$$\log \left| 2 \sin \frac{\vartheta - \tau}{2} \right| = \sum_{\substack{n=-\infty \\ n \neq 0}}^{\infty} \frac{1}{|n|} e^{in(\vartheta - \tau)}. \tag{2.30}$$

The right-hand side $F(\vartheta)$ of equation (2.20) is expanded into the Fourier series numerically:

$$\frac{1}{\pi} F(\vartheta) = -2l(\vartheta) \frac{\partial U^0(q(\vartheta))}{\partial n_{q(\vartheta)}} = \sum_{n=-\infty}^{\infty} f_n e^{in\vartheta}. \tag{2.31}$$

Using the Fourier series expansions above and the orthogonal property of the set of the functions $\{e^{in\vartheta}\}_{n=-\infty}^{\infty}$ on the complete interval $\vartheta \in [-\pi, \pi]$, equation (2.20) is transformed into the series equation:

$$\sum_{n=-\infty}^{\infty} \left\{ |n| \xi_n + 2 \sum_{m=-\infty}^{\infty} \kappa_{n,-m} \xi_m \right\} e^{in\vartheta} = \sum_{n=-\infty}^{\infty} f_n e^{in\vartheta}, \quad \vartheta \in [-\vartheta_0, \vartheta_0]. \tag{2.32}$$

Thus, the dual series equations take the form

$$\sum_{n=-\infty}^{\infty} \left\{ |n| \xi_n + 2 \sum_{m=-\infty}^{\infty} \kappa_{n,-m} \xi_m \right\} e^{in\vartheta} = \sum_{n=-\infty}^{\infty} f_n e^{in\vartheta}, \qquad \vartheta \in [-\vartheta_0, \vartheta_0],$$

$$\sum_{n=-\infty}^{\infty} \xi_n e^{in\vartheta} = 0, \qquad \vartheta \in [-\pi, -\vartheta_0) \cup (\vartheta_0, \pi]. \tag{2.33}$$

The customary way of solving equations (2.33) is to utilise the mathematical apparatus of the theory of analytical functions so that equations (2.33) are treated as a Riemann-Hilbert boundary value problem. This approach has been successfully applied in solving diverse problems of 2D wave diffraction and wave propagation ([41]). In this thesis, we give preference to an equivalent approach which transforms equations (2.33) to a pair of coupled dual series equations with trigonometric functions. Our purpose is to re-cast the form of the dual series equations to be solved so that the methods of [42] may be employed. This uses the same approach of conversion to trigonometric form as employed in [43]. First, we separate sums as follows. Writing

$$\sum_{n=-\infty}^{\infty} b_n = b_0 + \sum_{n=1}^{\infty} (b_n + b_{-n}),$$

and using the well known identities

$$e^{in\theta} = \cos n\theta + i \sin n\theta,$$

$$e^{-in\theta} = \cos n\theta - i \sin n\theta,$$

we decouple (2.33) into a pair of dual series equations with trigonometric kernels;

$$\sum_{n=1}^{\infty} n x_n \cos n\vartheta + \sum_{n=1}^{\infty} \left\{ \sum_{m=1}^{\infty} \left(\frac{1}{2} \mathcal{K}_{0,m}^{(+,+)} + \mathcal{K}_{n,m}^{(+,+)} \right) x_m \right\} \cos n\vartheta$$

$$+ \sum_{n=1}^{\infty} \left\{ \sum_{m=1}^{\infty} \left(\frac{1}{2} \mathcal{K}_{0,m}^{(-,-)} + \mathcal{K}_{n,m}^{(-,-)} \right) y_m \right\} \cos n\vartheta$$

$$= F(\vartheta) \xi_0 + f_0 + \sum_{n=1}^{\infty} f_n^{(+)} \cos n\vartheta, \qquad \vartheta \in [0, \vartheta_0], \qquad (2.34)$$

$$\sum_{n=1}^{\infty} x_n \cos n\vartheta = -\xi_0, \qquad \vartheta \in (\vartheta_0, \pi], \qquad (2.35)$$

and

$$\sum_{n=1}^{\infty} n y_n \sin n\vartheta + \sum_{n=1}^{\infty} \sum_{m=1}^{\infty} \mathcal{K}_{n,m}^{(+,-)} y_m \sin n\vartheta$$

$$+ \sum_{n=1}^{\infty} \sum_{m=1}^{\infty} \mathcal{K}_{n,m}^{(-,+)} x_m \sin n\vartheta$$

$$= G(\vartheta)\,\xi_0 + \sum_{n=1}^{\infty} f_n^{(-)} \sin n\vartheta, \qquad \vartheta \in [0,\vartheta_0] \qquad (2.36)$$

$$\sum_{n=1}^{\infty} y_n \sin n\vartheta = 0, \qquad\qquad \vartheta \in (\vartheta_0,\pi] \qquad (2.37)$$

where

$$x_n = \xi_n + \xi_{-n}, \quad y_n = \xi_n - \xi_{-n}, \quad f_n^{(\pm)} = f_n \pm f_{-n}, \qquad (2.38)$$

and

$$\mathcal{K}_{n,m}^{(+,+)} = \left(\kappa_{n,-m} + \kappa_{-n,m}\right) + \left(\kappa_{n,m} + \kappa_{-n,-m}\right),$$

$$\mathcal{K}_{n,m}^{(-,-)} = \left(\kappa_{n,-m} - \kappa_{-n,m}\right) - \left(\kappa_{n,m} - \kappa_{-n,-m}\right),$$

$$\mathcal{K}_{n,m}^{(+,-)} = \left(\kappa_{n,-m} - \kappa_{-n,m}\right) + \left(\kappa_{n,m} - \kappa_{-n,-m}\right),$$

$$\mathcal{K}_{n,m}^{(-,+)} = \left(\kappa_{n,-m} + \kappa_{-n,m}\right) - \left(\kappa_{n,m} + \kappa_{-n,-m}\right),$$

$$\mathcal{K}_{0,m}^{(+,+)} = 2\left(\kappa_{0,-m} + \kappa_{0,m}\right),$$

$$\mathcal{K}_{0,m}^{(-,-)} = 2\left(\kappa_{0,-m} - \kappa_{0,m}\right), \qquad (2.39)$$

$$\mathcal{K}_{n,0}^{(+,-)} = 2\left(\kappa_{n,0} - \kappa_{-n,0}\right),$$

$$F(\vartheta) = -2\left(\kappa_{00} + \sum_{n=1}^{\infty} \kappa_{n,0} \cos n\vartheta\right),$$

$$G(\vartheta) = -\sum_{n=1}^{\infty} \mathcal{K}_{n,0}^{(+,-)} \sin n\vartheta.$$

The edge condition (2.5) defines the solution class for the infinite sequences of the unknown coefficients $\{x_n\}_{n=0}^{\infty} \in l_2(1)$ and $\{y_n\}_{n=1}^{\infty} \in l_2(1)$, where by $l_2(\mu)$ we denote the space of sequences $\{z_n\}_{n=0}^{\infty}$ satisfying the condition $\sum_{n=0}^{\infty} n^\mu |z_n|^2 < \infty$.

Various solution methods of dual series equations are well developed and their detailed review can be found in [42] where in addition to the existing approaches, a new mathematically justified method is presented. In this method, the initial dual series equations with trigonometric kernels are converted into dual series equations with Jacobi polynomials $P^{\alpha,\beta}(\cos\vartheta)$ as kernels. This conversion is based on the well-known relations between trigonometric functions and

Jacobi polynomials below:

$$\cos n\vartheta = \sqrt{\pi}\frac{\Gamma(n+1)}{\Gamma\left(n+\frac{1}{2}\right)}P_n^{\left(-\frac{1}{2},-\frac{1}{2}\right)}(\cos\vartheta); \quad \sin n\vartheta = \frac{\sqrt{\pi}}{2}\frac{\Gamma(n+1)}{\Gamma\left(n+\frac{1}{2}\right)}\sin\vartheta P_{n-1}^{\left(\frac{1}{2},\frac{1}{2}\right)}(\cos\vartheta). \quad (2.40)$$

Using relations in equation (2.40) one can transform the dual series equations in (2.34)-(2.37) to the equivalent dual series equations with Jacobi polynomials $P_n^{\left(-\frac{1}{2},\frac{1}{2}\right)}(u)$ and $P_{n-1}^{\left(\frac{1}{2},\frac{1}{2}\right)}(u)$, as follows:

$$\begin{cases} \sum_{n=1}^{\infty} x_n \frac{\Gamma(n+1)}{\Gamma\left(n+\frac{1}{2}\right)}P_n^{\left(-\frac{1}{2},-\frac{1}{2}\right)}(u) = -\frac{1}{\sqrt{\pi}}\xi_0, \quad u \in (-1, u_0) \\[2mm] \sum_{n=1}^{\infty} nx_n \frac{\Gamma(n+1)}{\Gamma\left(n+\frac{1}{2}\right)}P_n^{\left(-\frac{1}{2},-\frac{1}{2}\right)}(u) + \sum_{n=1}^{\infty}\left\{\sum_{m=1}^{\infty}\left(\frac{1}{2}\mathcal{K}_{0,m}^{(+,+)} + \mathcal{K}_{n,m}^{(+,+)}\right)x_m\right\}\frac{\Gamma(n+1)}{\Gamma\left(n+\frac{1}{2}\right)}P_n^{\left(-\frac{1}{2},-\frac{1}{2}\right)}(u) \\[2mm] + \sum_{n=1}^{\infty}\left\{\sum_{m=1}^{\infty}\left(\frac{1}{2}\mathcal{K}_{0,m}^{(-,-)} + \mathcal{K}_{n,m}^{(-,-)}\right)y_m\right\}\frac{\Gamma(n+1)}{\Gamma\left(n+\frac{1}{2}\right)}P_n^{\left(-\frac{1}{2},-\frac{1}{2}\right)}(u) = \frac{1}{\sqrt{\pi}}\left(f_0 - 2\kappa_{00}\xi_0\right) \\[2mm] -2\xi_0 \sum_{n=1}^{\infty}\kappa_{n,0}\frac{\Gamma(n+1)}{\Gamma\left(n+\frac{1}{2}\right)}P_n^{\left(-\frac{1}{2},-\frac{1}{2}\right)}(u) + \sum_{n=1}^{\infty}f_n^{(+)}\frac{\Gamma(n+1)}{\Gamma\left(n+\frac{1}{2}\right)}P_n^{\left(-\frac{1}{2},-\frac{1}{2}\right)}(u), \quad u \in [u_0, 1] \end{cases} \quad (2.41)$$

$$\begin{cases} \sum_{n=1}^{\infty} y_n \frac{\Gamma(n+1)}{\Gamma\left(n+\frac{1}{2}\right)}P_{n-1}^{\left(\frac{1}{2},\frac{1}{2}\right)}(u) = 0, \quad u \in (-1, u_0) \\[2mm] \sum_{n=1}^{\infty} ny_n \frac{\Gamma(n+1)}{\Gamma\left(n+\frac{1}{2}\right)}P_{n-1}^{\left(\frac{1}{2},\frac{1}{2}\right)}(u) + \sum_{n=1}^{\infty}\sum_{m=1}^{\infty}\left(\mathcal{K}_{n,m}^{(+,-)}y_m + \mathcal{K}_{n,m}^{(-,+)}x_m\right)\frac{\Gamma(n+1)}{\Gamma\left(n+\frac{1}{2}\right)}P_{n-1}^{\left(\frac{1}{2},\frac{1}{2}\right)}(u) \\[2mm] = -\xi_0\sum_{n=1}^{\infty}\frac{\Gamma(n+1)}{\Gamma\left(n+\frac{1}{2}\right)}\mathcal{K}_{n,0}^{(+,-)}P_{n-1}^{\left(\frac{1}{2},\frac{1}{2}\right)}(u) + \sum_{n=1}^{\infty}f_n^{(-)}\frac{\Gamma(n+1)}{\Gamma\left(n+\frac{1}{2}\right)}P_{n-1}^{\left(\frac{1}{2},\frac{1}{2}\right)}(u), \quad u \in [u_0, 1] \end{cases} \quad (2.42)$$

The method for solving equations of type (2.41) and (2.42) is given in [42]. The key idea of the solution process is the transformation of the dual series equations into a single unique piece-wise continuous function defined on the complete interval of variation of the variable $u \in [-1, 1]$. The transformation employs the Abel's integral transform, which is a special case of an operator of fractional integration and differentiation. Following [42], we arrive at the transformed equations in the form:

$$F(u) = \begin{cases} F_1(u), u \in (-1, u_0), \\[2mm] F_2(u), u \in (u_0, 1). \end{cases}$$

Explicitly, we obtain

$$(1-u)\sum_{n=1}^{\infty}\frac{1}{n}\hat{x}_n\hat{P}_{n-1}^{(1,0)}(u) = \begin{cases} 2\xi_0, & u \in [-1, u_0), \\[2mm] -(1-u)\sum_{n=1}^{\infty}\left\{\sum_{m=1}^{\infty}\left(\frac{1}{2}\mathcal{K}_{0,m}^{(+,+)} + \mathcal{K}_{n,m}^{(+,+)}\right)\hat{x}_m\right\}\frac{1}{\sqrt{nm}}\frac{1}{n}\hat{P}_{n-1}^{(1,0)}(u) \\[2mm] -(1-u)\sum_{n=1}^{\infty}\left\{\sum_{m=1}^{\infty}\left(\frac{1}{2}\mathcal{K}_{0,m}^{(-,-)}\mathcal{K}_{n,m}^{(-,-)}\right)\hat{y}_m\right\}\frac{1}{\sqrt{nm}}\frac{1}{n}\hat{P}_{n-1}^{(1,0)}(u) \\[2mm] -2\left(f_0 - 2\kappa_{00}\xi_0\right)\log\frac{1+u}{2} - 2\xi_0(1-u)\sum_{n=1}^{\infty}\hat{\kappa}_{n,0}\frac{1}{n^2}\hat{P}_{n-1}^{(1,0)}(u) \\[2mm] +(1-u)\sum_{n=1}^{\infty}\hat{f}_n^{(+)}\frac{1}{n^2}\hat{P}_{n-1}^{(1,0)}(u), u \in [u_0, 1]. \end{cases}$$

$$(2.43)$$

$$\sum_{n=1}^{\infty}\hat{y}_n\hat{P}_{n-1}^{(1,0)}(u) = \begin{cases} 0, & u \in [-1, u_0) \\[2mm] -\sum_{n=1}^{\infty}\sum_{m=1}^{\infty}\left(\hat{\mathcal{K}}_{n,m}^{(+,-)}\hat{y}_m + \hat{\mathcal{K}}_{n,m}^{(-,+)}\hat{x}_m\right)\hat{P}_{n-1}^{(1,0)}(u) \\[2mm] -\xi_0\sum_{n=1}^{\infty}\hat{\mathcal{K}}_{n,0}^{(+,-)}\hat{P}_{n-1}^{(1,0)}(u) + \sum_{n=1}^{\infty}\hat{f}_n^{(-)}\hat{P}_{n-1}^{(1,0)}(u), & u \in [u_0, 1] \end{cases}$$

$$(2.44)$$

where

$$\left\{\hat{x}_n, \hat{y}_n, \hat{f}_n^{(+)}, \hat{f}_n^{(-)}\right\} = \sqrt{2n}\left\{x_n, y_n, f_n^{(+)}, f_n^{(-)}\right\},$$

$$\left\{\hat{\mathcal{K}}_{n,m}^{(+,-)}, \hat{\mathcal{K}}_{n,m}^{(-,+)}\right\} = \frac{1}{\sqrt{nm}}\left\{\mathcal{K}_{n,m}^{(+,-)}, \mathcal{K}_{n,m}^{(-,+)}\right\},$$

$$(2.45)$$

$$\left\{\hat{\mathcal{K}}_{n,0}^{(+,-)}\right\} = \sqrt{\frac{2}{n}}\left\{\mathcal{K}_{n,0}^{(+,-)}\right\},$$

and $\hat{P}_{n-1}^{(1,0)}(u) = \dfrac{P_{n-1}^{(1,0)}(u)}{\left\|P_{n-1}^{(1,0)}(u)\right\|} = \sqrt{\dfrac{n}{2}}P_{n-1}^{(1,0)}(u)$ are the normalised Jacobi polynomials which form

a complete orthogonal system on the interval $[-1, 1]$ with respect to the weighting function $(1-u)$:

$$\int_{-1}^{1}(1-u)\hat{P}_{n-1}^{(1,0)}(u)\hat{P}_{s-1}^{(1,0)}(u)\,du = \delta_{ns} = \begin{cases} 1, & n = s, \\ 0, & n \neq s. \end{cases}$$

$$(2.46)$$

It should be noted that to obtain equations (2.43) both equations in (2.41) have been integrated using Rodrigues' formula

$$-2n(1-z)^{\alpha}(1+z)^{\beta}P_n^{(\alpha,\beta)}(z) = \frac{d}{dz}\left\{(1-z)^{\alpha+1}(1+z)^{\beta+1}P_{n-1}^{(\alpha+1,\beta+1)}(z)\right\}$$

where we set $\alpha = \beta = -\dfrac{1}{2}$. This integration is a necessary step since direct enforcement of the Abel's integral transform on equations (2.41) is not feasible due to the restriction imposed on values α and β (for details, see [42]).

Using notations (2.45), we transform equations (2.43) and (2.44) to the following coupled infinite systems of linear algebraic equations of the second kind:

$$\hat{x}_s = 2\xi_0 \mathcal{R}(u_0)(1+u_0)\hat{P}_{s-1}^{(0,1)}(u_0) - \sum_{n=1}^{\infty}\left\{\sum_{m=1}^{\infty}\left(\frac{1}{2}\mathcal{K}_{0,m}^{(+,+)} + \mathcal{K}_{n,m}^{(+,+)}\right)\hat{x}_m\right\}\frac{1}{\sqrt{nm}}\frac{s}{n}\hat{Q}_{s-1,n-1}^{(1,0)}(u_0)$$

$$+2f_0\left\{(1+u_0)\log\frac{1+u_0}{2}\hat{P}_{s-1}^{(0,1)}(u_0) + \frac{1-u_0}{s}\hat{P}_{s-1}^{(0,1)}(u_0)\right\}$$

$$-4\kappa_{00}\xi_0\frac{1-u_0}{s}\hat{P}_{s-1}^{(0,1)}(u_0) - (1-u_0)(1+u_0)\hat{P}_{s-1}^{(0,1)}(u_0)\sum_{n=1}^{\infty}\hat{f}_n^{(+)}\frac{1}{n^2}\hat{P}_{n-1}^{(1,0)}(u_0)$$

$$+\sum_{n=1}^{\infty}\hat{f}_n^{(+)}\frac{1}{n}\hat{Q}_{s-1,n-1}^{(0,1)}(u_0) - 2\xi_0\sum_{n=1}^{\infty}\hat{\kappa}_{n,0}\frac{1}{n}\hat{Q}_{s-1,n-1}^{(0,1)}(u_0)$$

$$(2.47)$$

where

$$\mathcal{R}(u_0) = 1 - 2\kappa_{00}\log\frac{1+u_0}{2} + (1-u_0)\sum_{n=1}^{\infty}\hat{\kappa}_{n,0}\frac{1}{n^2}\hat{P}_{n-1}^{(1,0)}(u_0), \qquad (2.48)$$

and

$$\hat{y}_s + \sum_{n=1}^{\infty}\sum_{m=1}^{\infty}\left(\hat{\mathcal{K}}_{n,m}^{(+,-)}\hat{y}_m + \hat{\mathcal{K}}_{n,m}^{(-,+)}\hat{x}_m\right)\hat{Q}_{s-1,n-1}^{(1,0)}(u_0) =$$

$$-\xi_0\sum_{n=1}^{\infty}\hat{\mathcal{K}}_{n,0}^{(+,-)}\hat{Q}_{s-1,n-1}^{(1,0)}(u_0) + \sum_{n=1}^{\infty}\hat{f}_n^{(-)}\hat{Q}_{s-1,n-1}^{(1,0)}(u_0). \quad (2.49)$$

In equation (2.47), the notation $\hat{Q}_{kp}^{(\alpha,\beta)}(u_0)$ stands for the incomplete scalar product of Jacobi polynomials $\hat{P}_k^{(\alpha,\beta)}(u)$ and $\hat{P}_p^{(\alpha,\beta)}(u)$, defined as

$$\hat{Q}_{kp}^{(\alpha,\beta)}(u_0) = \int_{u_0}^{1}(1-u)^{\alpha}(1+u)^{\beta}\hat{P}_k^{(\alpha,\beta)}(u)\hat{P}_p^{(\alpha,\beta)}(u)\,du. \qquad (2.50)$$

It can be seen from equation (2.47) that for an arbitrary value ξ_0 the infinite set of coefficients $\{\hat{x}_s\}_{s=1}^{\infty}$ does not necessarily belong to the solution class $l_2(0) \equiv l_2$, which is defined by condition (2.5). The following relations can be used to clarify this assertion:

$$\hat{Q}_{s-1,n-1}^{(1,0)}(u_0) = -(1-u_0)\frac{1}{s}\hat{P}_{s-1}^{(0,1)}(u_0)\hat{P}_{n-1}^{(1,0)}(u_0) + \frac{n}{s}\hat{Q}_{s-1,n-1}^{(0,1)}(u_0) \qquad (2.51)$$

In fact, $\hat{Q}_{s-1,n-1}^{(1,0)}(u_0) = O(s^{-1})$, as $s \to \infty$. Hence, $s\hat{Q}_{s-1,n-1}^{(1,0)}(u_0) = O(1)$, $s \to \infty$. It implies that $\hat{x}_s = O(1)$ as $s \to \infty$. The proper choice of ξ_0 ensuring the required solution class is based

on the well-known correlation between smoothness of the function and the asymptotic behaviour of its Fourier coefficients. Therefore, the constant ξ_0 is defined by requiring the continuity of the function $F(u)$ at the point $u = u_0$. From equation (2.43):

$$
\begin{aligned}
\xi_0 = &- \frac{1 - u_0}{2\mathcal{R}(u_0)} \sum_{n=1}^{\infty} \left\{ \sum_{m=1}^{\infty} \left(\frac{1}{2} \mathcal{K}_{0,m}^{(+,+)} + \mathcal{K}_{n,m}^{(+,+)} \right) \hat{x}_m \right\} \frac{1}{\sqrt{nm}} \frac{1}{n} \hat{P}_{n-1}^{(1,0)}(u_0) \\
&- \frac{1 - u_0}{2\mathcal{R}(u_0)} \sum_{n=1}^{\infty} \left\{ \sum_{m=1}^{\infty} \left(\frac{1}{2} \mathcal{K}_{0,m}^{(-,-)} + \mathcal{K}_{n,m}^{(-,-)} \right) \hat{y}_m \right\} \frac{1}{\sqrt{nm}} \frac{1}{n} \hat{P}_{n-1}^{(1,0)}(u_0) \\
&- \frac{f_0}{\mathcal{R}(u_0)} \log \frac{1 + u_0}{2} + \frac{1 - u_0}{2\mathcal{R}(u_0)} \sum_{n=1}^{\infty} \hat{f}_n^{(+)} \frac{1}{n^2} \hat{P}_{n-1}^{(1,0)}(u_0),
\end{aligned}
\tag{2.52}
$$

Substituting relation (2.52) into (2.45) leads to the correct asymptotic $(s \to \infty)$ behaviour $O(s^{-1})$ for coefficients $\{\hat{x}_s\}_{s=1}^{\infty}$.

$$
\begin{aligned}
\hat{x}_s = &- \sum_{n=1}^{\infty} \left\{ \sum_{m=1}^{\infty} \left(\frac{1}{2} \mathcal{K}_{0,m}^{(+,+)} + \mathcal{K}_{n,m}^{(+,+)} \right) \hat{x}_m \right\} \frac{1}{\sqrt{nm}} \hat{Q}_{s-1,n-1}^{(0,1)}(u_0) \\
&- \sum_{n=1}^{\infty} \left\{ \sum_{m=1}^{\infty} \left(\frac{1}{2} \mathcal{K}_{0,m}^{(-,-)} + \mathcal{K}_{n,m}^{(-,-)} \right) \hat{y}_m \right\} \frac{1}{\sqrt{nm}} \hat{Q}_{s-1,n-1}^{(0,1)}(u_0) \\
&+ 2f_0 \frac{1 - u_0}{s} \hat{P}_{s-1}^{(0,1)}(u_0) - 4\kappa_{00}\xi_0 \frac{1 - u_0}{s} \hat{P}_{s-1}^{(0,1)}(u_0) \\
&+ \sum_{n=1}^{\infty} \hat{f}_n^{(+)} \frac{1}{n} \hat{Q}_{s-1,n-1}^{(0,1)}(u_0) - 2\xi_0 \sum_{n=1}^{\infty} \hat{\kappa}_{n,0} \frac{1}{n} \hat{Q}_{s-1,n-1}^{(0,1)}(u_0)
\end{aligned}
\tag{2.53}
$$

The coefficients $\{\hat{x}_s\}_{s=1}^{\infty}$ in equation (2.53) now belong to the functional class of square summable sequences: $\{\hat{x}_s\}_{s=1}^{\infty} \in l_2$. Keeping in mind equation (2.43), where the coefficients $\{x_s\}_{s=1}^{\infty}$ are replaced by $\{\hat{x}_s\}_{s=1}^{\infty}$, we may assert that the solution for $\{x_s\}_{s=1}^{\infty}$ satisfies (2.5), and it can be shown that $\{x_s\}_{s=1}^{\infty} \in l_2(1)$, which provides the asymptotic behaviour $x_s = O\left(s^{-\frac{3}{2}}\right)$, $s \to \infty$. In the coupled equations (2.53) and (2.49), we keep the constant ξ_0 as a multiplier before terms which possess asymptotic behaviour $O(s^{-1})$, $s \to \infty$. It is possible to eliminate the constant ξ_0 completely, but it will lead to bulky expressions for the matrix elements in (2.49) and (2.53). Thus, the discussed problem is reduced to the solution of coupled infinite systems of linear algebraic equations of the second kind (2.49) and (2.53), with the constant ξ_0 defined by (2.52).

2.2.1   Complex Frequencies and Spectral Theory of Open Cavities

We stated in the introduction that from a physical point of view the presence of a slit leads to the leakage of acoustic (or electromagnetic) energy through the slit to external space, i.e. leads to dissipation of energy from the interior of a cylinder, and hence to the radiation losses. Therefore the spectrum of real eigenvalues, which is characteristic for a closed cylinder, is replaced by a spectrum of complex eigenvalues. From the point of view of the classic L_2 spectral theory this means discrete eigenvalues are replaced with a continuous spectrum of the real positive axis of frequencies. A rigorous treatment of the propagation and diffraction of waves having complex frequencies has been studied in [39, 56, 57].

The principles of the general theory of waves with complex wavenumbers require an outer domain in the vicinity of infinity Ω_∞ , where the Svechnikov-Reihardt partial radiation condition is used. The Riemann surface S_R of analytical continuation of the function $H_0^1(z)$ is a natural choice. It is similar to $ln(z)$ with a cut along the real negative semi-axis, where z contains complex values. Let us use the following notations to express the domains:

$$D^0 = C[0, \infty), D^{(+)} = \left\{ z \in D^0 : Im > 0 \right\}, D^{(-)} = \left\{ z \in D^0 : Im < 0 \right\} \tag{2.54}$$

here D^0 denotes "physical" sheet of S_R and its open upper and lower half-planes $D^{(+)}$ and $D^{(-)}$. The Svechnikov-Reihardt partial radiation condition provides point-wise restriction on the scattered field $u^s(q)$ for every point $q \in \Omega_\infty$ while the Sommerfeld radiation condition restricts the asymptotic behaviour of $u^s(q)$ for $q \to \infty$.

It is shown in [56] that this additional restriction is necessary and sufficient to prove the correctness of our method using the Green's function in an open domain for every wavenumber $k \in S_R$, and the following statements can be made:

- There is a one to one correspondence between solutions of Neumann BVP and the solutions of equation (2.49) for any fixed value of $k \in D^0$.

- The set of $\sigma = k_1, k_2, k_3, ...k_j, ... \subset D^0$ of eigenvalues of the Neumann BVP is a countable subset in $\overline{D^{(-)}} = D^{(-)} \bigcup (0, \infty)$ for non-trivial solutions.

- The standard Green function $G(kR)$ of the Neumann BVP is analytical for $k \in D^{(+)}$ and has analytical continuation for $k \in D^{(-)}$.

- The operator function $A(k) = (I + H)(k)$ is an analytical matrix-operator function in l_2

and it is invertible in $D^{(+)}$. The inverse operator $A^{-1}(k)$ is meromorphic operator function in l_2 for $k \in \overline{D^{(-)}}$.

- The characteristic values of $A(k)$ correspond to the eigenvalues of Neumann BVP for real and complex values of k.

2.3   Aspects of Numerical Implementation of the Solution

In operator form, the solution obtained in the previous section can be represented as

$$
\begin{cases}
(I + H_{11})\,\hat{x} + H_{12}\hat{y} & = b_1 \\
H_{21}\hat{x} + (I + H_{22})\,\hat{y} & = b_2,
\end{cases}
\tag{2.55}
$$

where $\{\,\hat{x}, \hat{y}\,\} \in l_2$ are infinite sequences of the Fourier coefficients to be found, I is the identity operator, H_{ij} $(i, j = 1, 2)$ are completely continuous (compact) matrix operators in l_2, and $\{b_1, b_2\}$ are known right-hand sides, also belonging in the functional class l_2. Properties of such types of equations which arise as result of the MAR, are well-studied (see, for example the review [58]). They are efficiently solved by a truncation method which is characterised by a fast convergence rate. Computation of the matrix elements mostly requires the usage of recurrence formulas and the Fast Fourier Transform (FFT) which makes filling the matrix a fast and efficient procedure.

2.3.1   Object Oriented Programming for the Solution Using MATLAB

The codes to run numerical simulation are developed in MATLAB using Object Oriented Programming (OOP) principles. It is important to note that an "object" does not necessarily refer to scatterers which will be investigated, rather to parts of the codes that are described as a "class". Examples of classes are as follows; Incident Field, Scatterer (Physical Object), Solver (a class that sets up the algebraic system and solves the resulting matrix), Scattering (a class to calculate scattered field) etc. This approach has been found to be beneficial as it allows for properties to be modified without changing the rest of the numerical implementation. For example once a system is set up for calculation of the complex eigenvalues for a rectangle, we can repeat the calculation by changing its slot width, wavenumber or the type/direction of incident

field without changing any code. The numerical implementation can be briefly described as follows;

1. Define the scatterer.

   A scatter is realised using tgeometry class in Matlab. For each physical object a number of parameters will be passed on to a child class of tgeometry, required to define the boundary and the opening size in radians. As it can be seen in snippets 2.1 and 2.2, parameters for a circle are a radius and an opening used in analytical formulation to set up the object while for a rectangle it will be number of parameters passed in to a numerical interpolation algorithm explained in the next chapter. The important part here is once the scatterer object is created, its property of opening can be changed without recreating the object from the beginning.

   Code Snippet 2.1: A circle object.

```matlab
classdef tcircle < tgeometry
  properties
    a
    theta
  end
  methods
    function self = tcircle(a,theta)
      % if the parameters are not passed on assume a unit circle
      % without opening
        if nargin < 2; theta = 0;
          if nargin < 1; a=1;
          end
        end
      % call parent constructor
      self = self@tgeometry(theta);
      self.a = a;
      self.theta=theta;
    end
  % calculate return parameters
  function [x,y,dx,dy,d2x,d2y,d3x,d3y] = geom(self,tgrid)
    x = self.a.*cos(tgrid);
    y = self.a.*sin(tgrid);
    dx = -self.a*sin(tgrid);
    dy = self.a*cos(tgrid);
    d2x = -self.a*cos(tgrid);
    d2y = -self.a*sin(tgrid);
    d3x = self.a*sin(tgrid);
    d3y = -self.a*cos(tgrid);
  end
  end % end of methods
end
```

2. Define incident field.

   The incident field class is coded for 3 options and the parameters they take is given below:

- Planewave incident field: Requires wavenumber k and direction along z axis

- Point source: Requires wavenumber k and location in $x - y$ coordinates

- Complex point source: Requires wavenumber k, location in $x - y$ coordinates, parameters b, β (aperture width and orientation angle respectively).

As they are object classes, one or more of the parameters can easily be changed which is useful in searching a solution for a spectrum of k for while keeping all other parameters fixed. It should also be noted that the incident field can be left empty for modal field analysis which does not require the right hand side of the equation to be constructed.

Code Snippet 2.2: A rectangle object using interpolation.

```matlab
classdef trectangle < tgeometry
  properties
    a % longer side
    b % sharter side
    w % slot width
    h_mol % mollifier ratio
  end
  methods
    function self = trectangle(a,b,w,h_mol)
      % if mollifying ratio is not given, set it to 2%
      if nargin < 4 ; h=0.02; end
      % calculate the opening with respect to total length
      screen = a/2+b+(a/2-w/2);
      opening = w/2;
      tau0 = (opening / (opening + screen))*pi;
      % call parent constructor
      self     = self@tgeometry(tau0);
      self.a   = a;
      self.b   = b;
      self.w   = w;
      self.h_mol = h_mol;
    end
    function [x,y,dx,dy,d2x,d2y,d3x,d3y] = geom(self,tgrid)
      % set known points
      known_points = [self.a/2,0; self.a/2,self.b/2;
        -self.a/2,self.b/2; -self.a/2,-self.b/2;
        self.a/2,-self.b/2; self.a/2,0];
      % call Interpolation with Sobolev approximation
      [A,B]=hermitmollifier(known_points,tgrid,self.h_mol,1);
      x   = A(1,:);
      dx = A(2,:);
      d2x = A(3,:);
      d3x = A(4,:);
      y   = B(1,:);
      dy = B(2,:);
      d2y = B(3,:);
      d3y = B(4,:);
    end
  end % end of methods
end
```

3. Define truncation number N.

4. Pass scatterer object, incident field (including wavenumber) and system size to solver class which solves the problem to find the unknown coefficient of surface distribution using the algorithm:

   (a) First, the solver is initialised: passed parameters are assigned to the object "solverNeumann" in Matlab.

   (b) Then setup method is called. As a result, the matrix of the system is calculated/filled following below steps:

      • Initial parametrization of the scatterer which returns $x, y, \partial x, \partial y, \partial^2 x, \partial^2 y$ and $\partial^3 x, \partial^3 y$.

      • Then a mesh grid R is created based on the $x - y$ axes. Using the meshgrid, and the standard Matlab method *besselj*, the Green's function and the coefficients of D_0 are calculated.

      • Next step is the calculation of the coefficients of K_s which is done in two parts: first all elements except the diagonal which corresponds to the singularity, then the diagonal using the analytical expression found.

      • Once the coefficients of K_s is found, they are expanded into their Fourier series. Combined with Fourier transform of the function $l(\theta)\dfrac{l(\tau)}{2}log\left(2sin\left(\dfrac{(\theta-\tau)}{2}\right)\right)$ this step contributes the vast majority of computation time of the algorithm. This is due to the need for nested for-loops (see code snippet 2.3) which can not be vectorized and are very time-consuming operations. This step has been improved with a C++ implementation (see code snippet 2.4), as a result, computation time for root finding algorithm with a system size $N = 1028$ dropped from 142 seconds minutes to 48 second, while for a system size $N = 2048$ the change was more significant, from 13.2 minutes to 2.8 minutes.

      • Then rescaling sequences are initialised depending on a problem type whether the boundary is open or closed.

      • Calculation of elements of the matrix Q, including incomplete scalar products of needed order, leads to solution matrix A of the system.

   (c) After the matrix of the system is defined, "solve" method is called. As a result,

Fourier coefficients of the unknown surface density distribution are obtained. The method works in the following way:

- First, the incident field is checked, if it is not provided it means modal field representation is being solved, which doesn't require the right hand side. Therefore, the standard Matlab function $x = eigs(A, 1, sm)$ returns the first smallest magnitude eigenvalues vector of the corresponding solution matrix.

- If an incident field is provided then the right hand side of the problem B is calculated. Then the system is solved using the standard Matlab backslash operator $x = A\backslash b$

- Then the back rescaling is performed, to obtain original surface density distribution depending on the problem type (whether the boundary is open or closed).

Code Snippet 2.3: Matlab nested loop for arclength.

```matlab
function [Lsn] = coefFourier_ll_log(k,ll)
  N=length(ll);
  ll_n=coefFourier1(k*ll);
  lambda=zeros(1,N-1); lambda(N/2+1:N-1)=-0.5./(1:N/2-1);
  lambda(N/2-1:-1:1) = lambda(N/2+1:N-1);
  M  = N/2-1; Lsn = zeros(N-1, N-1,'like', ll_n);
  M1 = M+1;
  for n = -M:M
    c = min(M-n, M);
    d = max(-M, -M-n);
    for s = -M:M
      rmin = max(s-M, d);
      rmax = min(s+M, c);
      Lsn(s+M1, n+M1) = Lsn(s+M1, n+M1) + ...
      sum(ll_n(s-rmin+M1:-1:s-rmax+M1) .* ...
      ll_n(n+rmin+M1:n+rmax+M1) .* ...
      lambda(rmin+M1:rmax+M1));
    end
  end
  Lsn=0.5*Lsn;
```

5. Once the surface density distribution is known, we can search for the roots or complex roots of the system, continue with calculation of scattering characteristics of interest, such as backscattering cross-section, field distribution, radiation resistance etc.

6. At this stage we can also check the truncation error, and increase the system size (truncation number), repeat the procedure until a desired accuracy is obtained.

Code Snippet 2.4: C++ nested loop for arclength.

```cpp
#include "mex.h"
#include <iostream>
#include <stdlib.h>
#include <complex>
using namespace std;

/* computational subroutine */
void myMexFunction(const mxArray * lambda,const mxArray * ll_n, mxArray *
    ↪ output,
int N)
{
  mwSignedIndex n,s,r;
  mwSignedIndex M = N/2-1;
  mwSignedIndex N1 = N-1;
  mwSignedIndex c,d,rmin,rmax;

  /* get pointers to the arrays */
  mxDouble      * lam = mxGetDoubles(lambda);
  mxComplexDouble * lln = mxGetComplexDoubles(ll_n);
  mxComplexDouble * out = mxGetComplexDoubles(output);

  /* perform the nestedloop op */
  for(s = -M; s <= M; s++){
    c = max(-M,s-M);
    d = min(M,s+M);
    for(n = -M; n <= M; n++){
      rmin=max(-M-n,c);
      rmax=min(M-n,d);
      for(r= rmin; r<=rmax; r++){
        out[N1*(s+M)+(n+M)].real =
        out[N1*(s+M)+(n+M)].real + (lln[s-r+M].real * lln[n+r+M].real -
            ↪ lln[s-r+M].imag * lln[n+r+M].imag)*lam[r+M];
        out[N1*(s+M)+(n+M)].imag =
        out[N1*(s+M)+(n+M)].imag + (lln[s-r+M].real * lln[n+r+M].imag +
            ↪ lln[s-r+M].imag * lln[n+r+M].real)*lam[r+M];}
    }
  }
}

/* The gateway routine. */
void mexFunction( int nlhs, mxArray *plhs[],
int nrhs, const mxArray *prhs[] )
{
  int N = (int) mxGetScalar(prhs[3]);

  /* coppy array and set the output pointer to it */
  plhs[0] = mxDuplicateArray(prhs[2]);

  /* call the C subroutine */
  myMexFunction(prhs[0], prhs[1], plhs[0], N);

  return;
}
```

Critical parts of the solverNuemann class setup and solve functions, as well as auxiliary functions created for easily accessing parameters such as current, far field are summarized

below.

Code Snippet 2.5: Setup function in solverNeumann class.

```matlab
function setup(self)

  self.tgrid = 2*pi*(0:self.N-1)/self.N;
  self.nk = self.N/2-1;
  [self.x,self.y,self.dx,self.dy,self.d2x,self.d2y,self.d3x,self.d3y] =
      ↪ self.scatterer.geom(self.tgrid);
  self.ll=sqrt(self.dx.^2+self.dy.^2);

  % Initialize
  R=sqrt((self.x'*ones(1,self.N)-ones(self.N,1)*self.x).^2 +
      ↪ (self.y'*ones(1,self.N)-ones(self.N,1)*self.y).^2);
  R1=R+eye(self.N);
  H01=besselj(0,self.kwave*R1)+1i*bessely(0,self.kwave*R1);
  H11=besselj(1,self.kwave*R1)+1i*bessely(1,self.kwave*R1);
  U=1./(self.kwave*R1).*H11; V=2*U-H01;
  A_=(self.x.'*ones(1,self.N)-ones(self.N,1)*self.x).*
      ↪ (ones(self.N,1)*self.dy)-(self.y.'*ones(1,self.N)-
      ↪ ones(self.N,1)*self.y).*(ones(self.N,1)*self.dx);
  B_=(self.x.'*ones(1,self.N)-ones(self.N,1)*self.x).*
      ↪ (self.dy.'*ones(1,self.N))-(self.y.'*ones(1,self.N)-
      ↪ ones(self.N,1)*self.y).*(self.dx.'*ones(1,self.N));
  C_=(self.dx.'*ones(1,self.N)).*(ones(self.N,1)*self.dx)+
      ↪ (self.dy'*ones(1,self.N)).*(ones(self.N,1)*self.dy);
  D0=-1i/4*1./((self.ll.'*ones(1,self.N)).*(ones(self.N,1)*self.ll)).*
      ↪ (self.kwave^2*U.*C_-self.kwave^4*A_.*B_.*V./((self.kwave*R1).^2));

  % Ksmooth without the diagonal
  stt=2*(sin(toeplitz(0:self.N-1)*pi/self.N)+eye(self.N));
  Ktt=2*pi*(self.ll.'*ones(1,self.N)).*(ones(self.N,1)*self.ll).*D0+
      ↪ 1./(stt.^2);
  Ksmooth=Ktt-self.kwave^2/2*(self.ll.'*ones(1,self.N)).*
      ↪ (ones(self.N,1)*self.ll).*log(abs(stt));

  % Diagonal of Ksmooth
  P13=self.dx.*self.d3x+self.dy.*self.d3y; P22=self.d2x.^2 +self.d2y.^2;
  M12=self.dx.*self.d2y-self.d2x.*self.dy;
  diagonalKs=0.5*(self.kwave*self.ll).^2.*log(self.kwave*self.ll*0.5)-
      ↪ (self.kwave^2/6*P13-self.kwave^2/4*P22)./((self.kwave*self.ll).^2)
  -0.5*(self.kwave^2*M12).^2./((self.kwave*self.ll).^4)-
  (self.kwave*self.ll).^2.*(1i*pi/4-0.5*0.57721566490153+0.25)+1/12;

  % Ksmooth with the diagonal
  Kd=diag(Ksmooth);
  Ksmooth=Ksmooth-diag(Kd)+diag(diagonalKs);

  % Fourier coefficients of K
  Ksmooth_sn=coefFourier2(Ksmooth);
  L_sn=coefFourier_ll_log_v3(self.kwave,self.ll);
  K_sn=Ksmooth_sn+L_sn;
  self.tau=sqrt([self.nk:-1:1,1,1:self.nk]);
  Kreg_sn=zeros(self.N-1,self.N-1);
  Kreg_sn(:,self.N/2+1:self.N-1)=fliplr(K_sn(:,1:self.N/2-1));
  Kreg_sn(:,1:self.N/2-1)=fliplr(K_sn(:,self.N/2+1:self.N-1));
  Kreg_sn(:,self.N/2)=K_sn(:,self.N/2);
  Kreg_sn=2*Kreg_sn;
```

```matlab
    % Scale Close Problem
    if self.scatterer.tau0==0
      Kreg_sn(self.N/2,self.N/2)=Kreg_sn(self.N/2,self.N/2)-1;
      Kreg_sn=(((1./self.tau)')*(1./self.tau)).*Kreg_sn;
      self.A=eye(self.N-1)+Kreg_sn;
    % Scale Open Problem
    else
      self.mig=(-1).^(-self.nk:self.nk);
      Kreg_sn=(((self.mig./self.tau)')*(self.mig./self.tau)).*Kreg_sn;
      t0 = cos(self.scatterer.tau0);
      self.D=zeros(self.N-1,self.N-1);
      self.D(1,1)=sqrt(2)-1;
      [self.q10,self.q01,self.p01]=in_sc_pr10(t0,self.nk-1);
      self.pn=(1+t0)./(1:self.nk).*self.p01;
      self.C=zeros(self.N-1,self.N-1);
      self.C(1:self.nk+1,1)=-sqrt(2)*[log((1-t0)/2), self.pn].';
      self.C(1,2:self.nk+1)=-self.pn;
      self.C(2:self.nk+1,2:self.nk+1)=self.q10;
      self.C(self.nk+2:self.N-1,self.nk+2:self.N-1)=self.q01;

      hnp=0.5*(Kreg_sn+fliplr(Kreg_sn)+flipud(Kreg_sn)+rot90(Kreg_sn,2));
      hpp=hnp(self.nk+1:self.N-1,self.nk+1:self.N-1);
      hpp(1,:)=0.5*hpp(1,:);
      Kpp=hpp;

      hnp=0.5*(Kreg_sn-fliplr(Kreg_sn)+flipud(Kreg_sn)-rot90(Kreg_sn,2));
      hpm=hnp(self.nk+1:self.N-1,self.nk+2:self.N-1);
      hpm(1,:)=0.5*hpm(1,:);
      Kpm=hpm;

      hnp=0.5*(Kreg_sn+fliplr(Kreg_sn)-flipud(Kreg_sn)-rot90(Kreg_sn,2));
      hmp=hnp(self.nk+2:self.N-1,self.nk+1:self.N-1);
      Kmp=hmp;

      hnp=0.5*(Kreg_sn-fliplr(Kreg_sn)-flipud(Kreg_sn)+rot90(Kreg_sn,2));
      hmm=hnp(self.nk+2:self.N-1,self.nk+2:self.N-1);
      Kmm=hmm;
      Kr=[Kpp,Kpm;Kmp,Kmm];

      self.A=eye(self.N-1)+self.D+self.C*Kr;
    end
end
```

Code Snippet 2.6: Solve function in solverNeumann class.

```matlab
function solve(self)
  if isempty(self.A)
    error('Must call setup() first')
  end
  if isempty(self.incidentField{1})
    % calculate eigenvalues
    [self.X,~] = eigs(self.A,1,'sm');
  else
    % solve system with incident field
    self.B = get_rhs(self);
    self.X = self.A\self.B;
  end
  if self.scatterer.tau0 == 0
  % Scale back coefficients for closed problem
```

```matlab
        self.X_kappa=self.X./self.tau';
        self.ksi0=self.X_kappa(self.nk+1);
        self.ksin=self.X_kappa(self.nk+2:self.N-1);
        self.ksi_n=flipud(self.X_kappa(1:self.nk));
        self.Ksi = [flip(self.ksi_n);self.ksi0;self.ksin];
    else
        % Scale back coefficients for open problem
        self.ksi0=self.X(1);
        self.ksin=0.5*((-1).^(1:self.nk)').*((self.X(2:self.nk+1)+
        self.X(self.nk+2:2*self.nk+1))./sqrt((1:self.nk)'));
        self.ksi_n=0.5*((-1).^(1:self.nk)').*((self.X(2:self.nk+1)-
        self.X(self.nk+2:2*self.nk+1))./sqrt((1:self.nk)'));
        self.Ksi = [flip(self.ksi_n);self.ksi0;self.ksin];
    end
end
```

Code Snippet 2.7: Current function in solverNeumann class.

```matlab
function current = get_current(self)
    current =self.ksi0+exp(1i*(self.tgrid-pi)'*(1:self.nk))*self.ksin+
        ↪ exp(1i*(self.tgrid-pi)'*(-1:-1:-self.nk))*self.ksi_n;
end
```

Code Snippet 2.8: Far field function in solverNeumann class.

```matlab
function farfield = getFarField(self,points,index)
  if nargin<3 || isempty(index)
    index = 1:self.numIncidentField;
  end
  points = points(:);
  farfield = zeros(length(points),self.numIncidentField);
  for j = 1:self.numIncidentField
    F = exp( -1i * self.kwave * ((self.x.') * cos(self.tgrid) +
        ↪ (self.y.' * sin(self.tgrid))).*
        ↪ (self.dy.'*cos(self.tgrid)-self.dx.'*sin(self.tgrid)));
    wf = fftshift( fft2(F) / (self.N * self.N));
    beta = wf( 2:self.N, 2:self.N);
    fullcurr = [flipud(self.ksin(:,j));self.ksi0(:,j);self.ksi_n(:,j)];
    fullprod = (fullcurr.') * beta;
    sums = fullprod * exp( 1i * ((-self.nk:1:self.nk).') * points.');
    tmp = abs(sums);
    farfield(:,j) = tmp(:);
  end
end
```

A number of helper functions are also created for fast and easy numerical implementation. The helper functions are used for calculation of system condition number and determinant, finding the eigenvalues (roots), complex eigenvalues (complex roots), for evaluation and plotting field distribution, radiation patterns and radar cross sections.

Code Snippet 2.9: Calculation of system determinant.

```matlab
function detA = detNeumann(scatterer,n_tr,kwave)
  s_mar = solverNeumann(scatterer,kwave,[],n_tr); % initialising the
      ↪ problem
  s_mar.setup();
  detA = det(s_mar.A);
end
```

Code Snippet 2.10: Evaluate scattered field.

```matlab
% Evaluate Scattered Field
function evaluate(self,s_mar)
  Usc_v = zeros(1,size(self.XY,2));
  XY_masked = self.XY(:,self.mask);
  nk = s_mar.N/2-1;
  self.J = s_mar.ksi0+exp(1i*(s_mar.tgrid)'*(1:nk))*s_mar.ksin+
      ↪ exp(1i*(s_mar.tgrid)'*(-1:-1:-nk))*s_mar.ksi_n;

  v = zeros(1,size(XY_masked,2));
  ind = self.scatterer.getIndices(s_mar.tgrid);
  % normal derivatives to the contour
  nx=s_mar.dy./s_mar.ll; ny=s_mar.dx./s_mar.ll;

  for i = 1:length(v)
    % calculate the distance for each point
    R = sqrt((XY_masked(1,i)-s_mar.x).^2 + (XY_masked(2,i)-s_mar.y).^2);
    if min(R(ind)) > self.eps_prec
      dH = -s_mar.kwave * besselh(1,s_mar.kwave*R) .*
          ↪ ((XY_masked(1,i)-s_mar.x).*nx - (XY_masked(2,i)-s_mar.y).*ny
          ↪ )*1./R;
      U_int = 1i/4*dH.*self.J.';
      v(i) = (trapz(s_mar.tgrid,U_int.'));
    elseif min(R(ind)) <= self.eps_prec
      U_int = ((s_mar.d2x.*s_mar.dy - s_mar.d2y.*s_mar.dx)).*self.J.';
      v(i) = (trapz(s_mar.tgrid,U_int.'))/(4*pi);
    end
    % insert values into the return array
    Usc_v(:,self.mask) = v;
    Usc_v(:,~self.mask) = 0;
    self.Usc = reshape(Usc_v,self.ngrid,self.ngrid);
    if ~isempty(s_mar.incidentField{1})
      Uinc_v = s_mar.incidentField{1}.evaluate(self.XY(1,:)+
          ↪ 1i*self.XY(2,:),self.mask);
      self.Uinc = reshape(Uinc_v(1,:),self.ngrid,self.ngrid);
    end
  end
end
```

Before proceeding to detailed results, we will give a brief summary of the plots used in this thesis and why they are preferred. First, the calculations of eigenvalues, especially complex eigenvalues require a very close initial approximation. This is true whether we use Matlab's standard root finding algorithm "fsolve" or our root finding algorithm (see Algorithm 1) based on derivative estimated iterative functions ([59]). We use a log scaled line plot of system condition number against the wavenumber k where the peaks correspond to locations of roots and gives

us initial approximations (see figure 2.4).

Next, field representation plots are provided as colourmaps using Matlab "surf" plots. The only exception is the use of contour lines to highlight the effect of necks in Helmholtz resonators. Matlab "contourf" plots provided more informative visuals where the resonators are illuminated with an incident field, which are also used for phase plots; these are calculated only for Helmholtz resonators.

Finally, we have opted for line plots for radiation patterns which can often be presented as polar plots, as it presents better visuals for comparison of patterns for different parameters.

Wrapping up the the discussion about the numerical code, it must be noted that in a mathematical sense, the implementation of the MAR for solving the problem for a slotted arbitrary rigid cylinder is much more complex than the analogous problem for a sound-soft cylinder (see [46], [48], and [52]). It is, thus, of interest to start the numerical implementation by evaluating the convergence rate of the solution for truncated systems as truncation number increases. For this purpose we may use the duct-like structure, described in [52]. This cavity is characterised by the following parameterisation involving parameters a and q:

$$x(\phi) = a \cos \phi, \quad y(\phi) = a \left[\tan^{-1} \left(\frac{3}{2} \cos \phi \right) + q \sin \phi \right], \quad a = 1, \, 0 < q < 1,$$

and the aperture of the duct is defined by the angle ϕ_1.

To measure the convergence rate, we calculate the normalised truncation error $e(N)$ as a function of system size N, treated in the maximum l_2-norm sense [60] defined by

$$e(N_i) = \frac{\left\| \bar{z}^{N_{i+1}} - z^{N_i} \right\|}{\left\| z^{N_i} \right\|}, \quad i = 1, 2, \ldots, \tag{2.56}$$

where $N_i < N_{i+1}$ are two successive truncation numbers and $\bar{z}^{N_{i+1}}$ is a projection of the solution vector $z^{N_{i+1}}$ on the $\mathbb{C}^{N_i}$ space consisting of the first N_i coordinates.

The geometry of the duct-like structures with parameters $\phi_1 = 30°$ and $q = 0.3$ is shown in Figure 2.2. We investigate two cavities with parameters $\phi_1 = 5°$ and $\phi_1 = 15°$ excited by plane wave with incident angle $\alpha = 0°$. The relative wavenumber ka takes three values $ka = 5, 20, 50$. The dependencies of $e(N)$ upon system size N are shown in Figures 2.3a and 2.3b, respectively. It is clear that $e(N)$ exhibits fast convergence, which is characteristic of MAR ([61, 62]).

It should be noted that the parameters $ka = 5, 20, 50$ have been chosen somewhat arbitrarily.
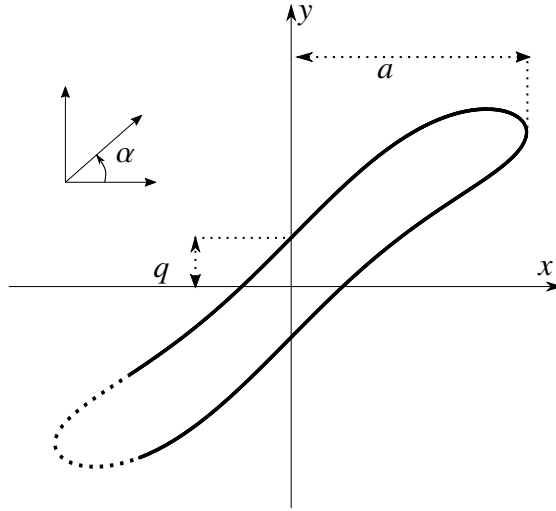
Figure 2.2: Duct-like structure ($\phi_1 = 30°, q = 0.3$) excited by a plane wave at the incidence angle α.

The following question may arise: what happens when the incidence frequency (or parameter ka) coincides with one of the real parts of the complex eigenvalues from the spectrum of complex oscillations which may be excited in the considered structure? To answer this question, first we need to find the complex eigenvalues. How the MAR solution can be used for this purpose was shown in [54]. Having in hand the solution for the scattering problem given by equations (2.55), we null their right-hand sides, assuming $b_1 = b_2 \equiv 0$. Then, we use the well-known result of linear algebra: non-trivial (non-zero) solutions of the homogeneous linear algebraic equations exist if and only if the corresponding determinant equals to zero. Thus, the characteristic (dispersion) equation for finding the complex eigenvalues has the form

$$\det A_N = 0 \tag{2.57}$$

where A_N is the matrix of the truncated joint system of equations (2.55) with truncation number N. Consequently, extraction of the complex eigenvalues is reduced to finding the complex roots of equation (2.57). Finding the complex roots of an arbitrary matrix equation of the type (2.57) is in general a very challenging task. However, one of the strengths of the method presented in this thesis is that even for arbitrary domains the approach of [54] is effective, especially for cavities with moderate to high Q-factors, i.e., cavities in which the imaginary part of the complex eigenvalue is small compared to the real part, This relies on the fact that the real part of

(a) $\phi_1 = 15°$

(b) $\phi_1 = 5°$
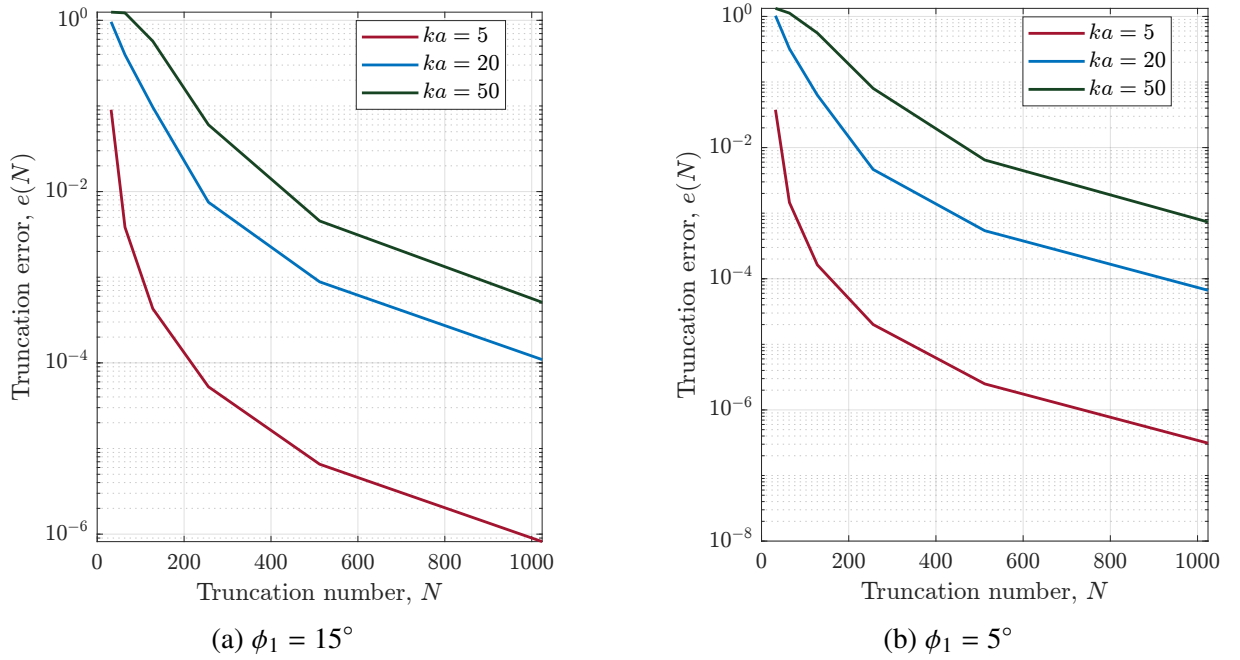
Figure 2.3: Truncation error $e(N)$ for duct-like cavity, $ka = 5, 20, 50$.

such a complex eigenvalue under investigation is well approximated by the real value at which condition number $\kappa(A_N(ka))$ of the matrix A_N has a local maximum.

In Chapter 4, we will examine the peculiarities around complex eigenvalues arising from mode splitting (for which modes double roots occur). We will demonstrate that the accuracy of the approach used allows us to investigate without limitations the fine structure of the spectra, resolve problems of mode competition and separate higher modes, the complex eigenvalues of which may differ only in the fifth or sixth significant decimal place. Any prescribed accuracy of calculations is achievable by increasing the truncation number N until the desired number of significant decimal digits is reached in both real and imaginary parts of the complex eigenvalues.

In case of a cavity of non-canonical geometry, it is practically impossible to make prior predictions of the spectrum composition and location of its individual components. The unique feature of the matrices generated by the MAR is its capability to cope with this problem and furthermore to obtain the detailed spectrum map on any frequency interval. Such map (or spectrum "portrait") appears as the result of calculating the frequency dependence of condition number $\kappa(A_N(ka))$ of the matrix A_N. We illustrate this by finding $\kappa(A_N(ka))$ for the duct-like structure with parameters $q = 0.3$ and $\phi_1 = 15°$. Let us introduce the following notations $\gamma_n = \gamma'_n - i\gamma''_n, n = 0, 1, 2, \ldots$ for the real and imaginary parts of complex eigenvalues.

The corresponding unloaded Q-factor of each complex oscillation is defined by the well-known formula $Q_n = \dfrac{-\gamma_n'}{2\gamma_n''}$. Intrinsically, the reduction of slot width should lead to a reduced imaginary part of γ_n, and consequently, to an increase in Q_n since $\gamma_n' \gg \gamma_n''$. Hence, the condition number $\kappa\left(A_N\left(ka\right)\right)$ becomes highly sensitive to the case when $\gamma_n'' \ll 1$ and $|ka - \gamma'| = \delta \ll 1$. Under this condition, the dependence on $\kappa\left(A_N\left(ka\right)\right)$ is expected to exhibit sharp peaks, as shown in figure 2.4.
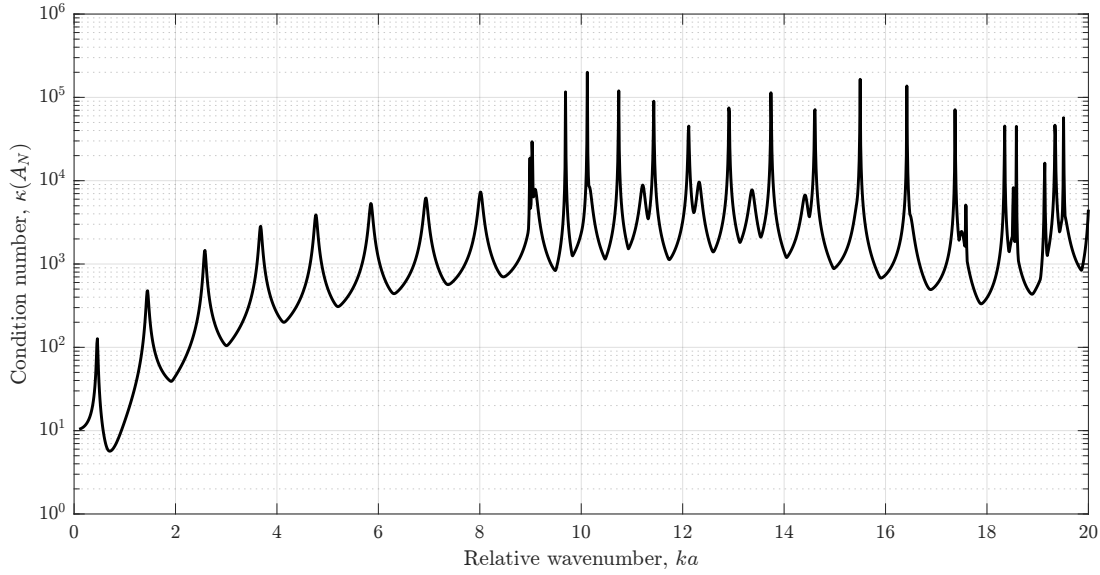
Figure 2.4: Condition number $\kappa\left(A_N\left(ka\right)\right)$ against relative wavenumber ka for a duct-like cavity with the parameters: $q = 0.3$ and $\phi_1 = 5^0 \left(\dfrac{d}{2q} \approx 0.097\right)$, $N = 256$.

The spectral dependence of condition number $\kappa\left(A_N\left(ka\right)\right)$, $N = 256$ demonstrates the presence of complex oscillations (modes), which may emerge near the frequencies corresponding to the peaks of the function $\kappa\left(A_N\left(ka\right)\right)$. In Table 2.1, we have collected the results for selected complex eigenvalues $\gamma_0, \gamma_4, \gamma_{10}$ of two duct-like structures characterised by values of relative slot width $\dfrac{d}{2q} \approx 0.28$ ($\phi_1 = 15°$) and $\dfrac{d}{2q} \approx 0.097$ ($\phi_1 = 5°$). The low-frequency oscillations represent the mode special to Helmholtz resonators where the complex eigenvalues are $\gamma_0 = 0.49543092 - 0.01381610\,i \left(\phi_1 = 15^0\right)$ and $\gamma_0 = 0.45737160 - 0.01104749\,i \left(\phi_1 = 5^0\right)$. The tabulated results illustrate rapid convergence as truncation number increases, also as shown in Figure 2.3. Calculation of the complex eigenvalues starts with an initial approximation using a truncation number $N = 64$. The calculated value is then used as an initial approximation for the next step ($N = 128$) of the recursive algorithm. This procedure continues until the desired accuracy is achieved. The number of digits stabilised after each step is highlighted in Table 2.1.

Table 2.1: Selected complex eigenvalues calculated for increasing truncation numbers for a duct-like structure. The bold digits indicate convergence to the exact value.

γ_n	N	$\vartheta_0 = 165°$	$\vartheta_0 = 175°$
	64	**0.4952**914151 − **0.0649**950669i	**0.4572**203430 − **0.0110**384464i
	128	**0.4954306**135 − **0.0138160**668i	**0.4573713**370 − **0.0110474**689i
γ_0	256	**0.4954308**890 − **0.0138161**007i	**0.4573715**761 − **0.0110474**947i
	512	**0.4954309**237 − **0.0138161**049i	**0.4573716**063 − **0.0110474**980i
	1024	**0.4954309**280 − **0.0138161**054i	**0.4573716**101 − **0.0110474**984i
	64	**4.86**94667580 − **0.0649**950669i	**4.76**67972705 − **0.0298**953143i
	128	**4.8700**204157 − **0.0650**836917i	**4.7673**150804 − **0.0299**434674i
	256	**4.8700**821262 − **0.0650**939449i	**4.7673**723993 − **0.0299**491106i
γ_4	512	**4.8700**896905 − **0.0650**951954i	**4.7673**794568 − **0.0299**498063i
	1024	**4.8700**906326 − **0.0650**953511i	**4.7673**803347 − **0.0299**498927i
	2048	**4.8700**907501 − **0.0650**953705i	**4.7673**804443 − **0.0299**499035i
	128	**9.69**12309912 − **0.0002**487920i	**9.69**00803968 − **0.0000028**950i
	256	**9.692**5527640 − **0.0002**491026i	**9.691**3999381 − **0.0000024**459i
γ_{10}	512	**9.6927**162254 − **0.0002**491979i	**9.6915**631197 − **0.0000024**452i
	1024	**9.6927**366025 − **0.0002**492107i	**9.6915**834619 − **0.0000024**460i
	2048	**9.6927**391479 − **0.0002**492123i	**9.6915**860030 − **0.0000024**461i

Analysis of the spectral dependence $\kappa(A_N(ka))$ in Figure 2.4 reveals two groups of resonances. The first group occupies the interval $0.45 \leq ka \leq 9$ while the second is characterised by $ka > 9$. The half-beam width of resonances populating the first group significantly exceeds that of the second, where one can observe significantly sharper resonance peaks. It indicates different formation mechanisms of the standing waves in each group. In fact, this phenomenon can be explained by simple physical arguments. The considered structure can be characterised by an approximate relative length $\frac{L}{a} = 2\sqrt{2}$ and varying relative thickness $\frac{t}{a} \simeq 0.33 - 0.35$. The average distance between neighbouring peaks of the condition number graph $\kappa(A_N(ka))$ is $\Delta ka \approx 1.1$. Hence, $\Delta kL \approx 1.1 \times 2.83 = 3.11 \approx \pi$, i.e. $\Delta kL \approx \frac{\lambda}{2}$. It simply means that each peak is separated from the preceding one by a half-wave distance in the interval $0.45 \leq ka \leq 9$. Considering

the fact that inside this interval the parameter kt is less than π, i.e., $t < \dfrac{\lambda}{2}$, conditions for standing waves to emerge in the "transverse" direction do not exist. We arrive at the conclusion: the maxima of the condition number $\kappa\left(A_N\left(ka\right)\right)$, lying in the interval $0.45 \le ka \le 9$ represents only one-dimensional "longitudinal" acoustic oscillations in the form of standing waves along the duct of length L. When parameter ka crosses the "threshold" value of $ka \approx 9$, the transverse size t approaches a half-wave length $kt = \dfrac{t}{a}ka = (0.33 - 0.35) \times 9 \approx \pi$. This gives rise to the emergence of the first lower "transverse" oscillation. Further increase in ka generates the spectrum of higher transverse oscillations. These oscillations dominate the longitudinal oscillations since the amount of acoustic energy leakage through the slot is significantly smaller than that for longitudinal oscillations. With further increase in acoustic size (bigger relative wavenumber ka), the spectrum complexity increases, reflecting emergence of complex oscillations containing systems of transverse and longitudinal standing waves. This complication is accurately described by the spectral dependence of condition number $\kappa\left(A_N\left(ka\right)\right)$.

(a) $\phi_1 = 15°$

(b) $\phi_1 = 5°$
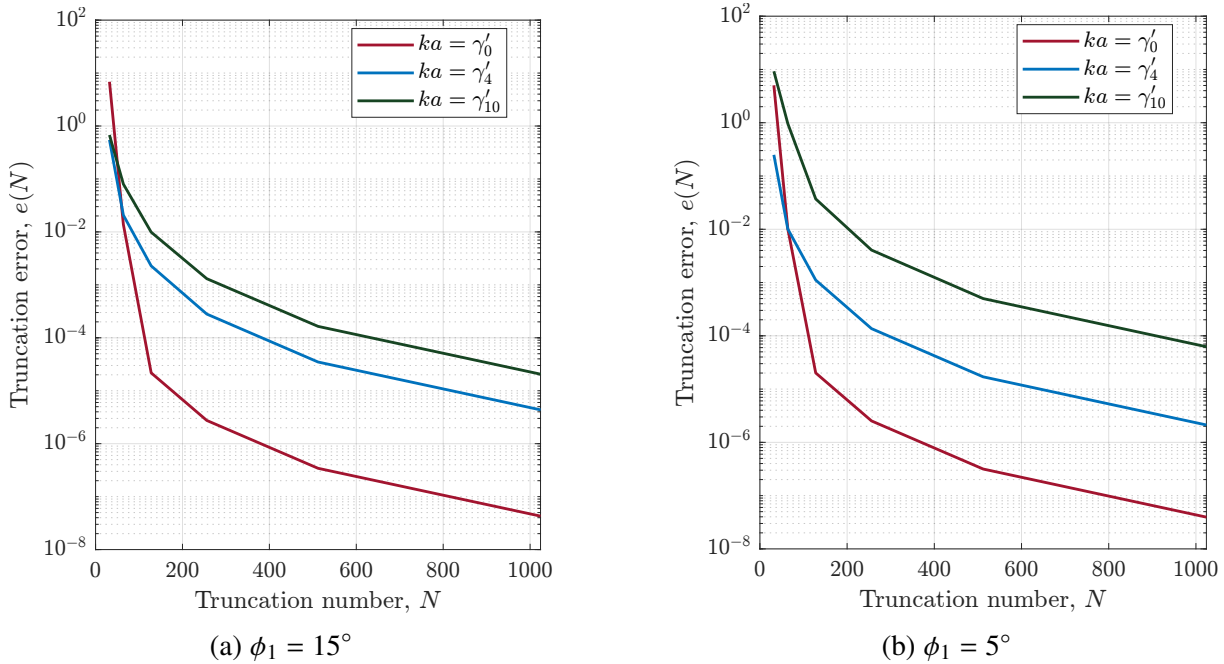
Figure 2.5:   Truncation error $e\left(N\right)$ for duct-like cavity at the resonant frequencies $ka = Re(\gamma_n), n = 0, 4, 10$.

We complete this subsection by investigating the relative error $e(N)$ when the parameter ka coincides with the real part γ'_n of the complex eigenvalue γ_n, i.e. $ka = Re(\gamma_n)$. It can be clearly seen that application of the MAR avoids the well known "numerical catastrophe" encountered by other methods in the vicinity of resonance. The convergence rate of the complex roots of the determinant against the truncation number N is reflected in Table 2.1. Using this data,

the relative error $e(N)$ is presented in Figure 2.5 at the points $ka = Re(\gamma_n)$, $n = 0, 4, 10$ for the structures with parameters $q = 0.3$, $\phi_1 = 15^0$ and $q = 0.3$, $\phi_1 = 5^0$. Comparison of the plots in Figure 2.5a and 2.5b for the same complex eigenvalues $ka = Re(\gamma_n)$, $n = 0, 4, 10$ shows that decreasing the slot width from $\dfrac{d}{2q} \approx 0.28$ ($\phi_1 = 165°$) to $\dfrac{d}{2q} \approx 0.097$ ($\phi_1 = 175°$) results in a smaller system size required to reach to the same values of $e(N)$.

2.4   Practical Modelling of Arbitrary Surfaces

The assumption about the capability of the developed approach to be applied to the analysis of arbitrarily shaped cylindrical cavities should be supported by a reliable simulation mechanism modelling various surfaces without undue limitations. While simple shapes such as circles and ellipses can be expressed analytically, a generalisation of the superellipse formula ([63]) (superformula) is often used for parametrisation of various canonical shapes (see [64–67]):

$$r(\phi) = \left[\left(\left| \frac{1}{a} \cos \frac{m\phi}{4} \right| \right)^{n_2} + \left(\left| \frac{1}{b} \sin \frac{m\phi}{4} \right| \right)^{n_3} \right]^{-\frac{1}{n_1}}, \qquad (2.58)$$

and

$$x = r(\phi) \cos(\phi), \quad y = r(\phi) \sin(\phi),$$

where r is the radius and ϕ is the angle in polar coordinates, a and b describe the structure size, m represents the symmetry of the structure while parameters n_1, n_2, n_3 define sharpness of its corners.

Although the superellipse formula extends the number of structures that can be investigated, more complex cross sections are required for special problems. Analytical parametrisation of those structures and calculation of derivatives up to the third order is a challenging task in itself, if not impossible. In this thesis we investigate Cubic Spline Interpolation ([68]) which has been successfully applied to the Dirichlet value problems using the MAR (see [69] and [70]), Piecewise Cubic Hermite Interpolation ([71]) and Sobolev space approximation by the Friedrich's mollifier ([72]) for parametrisation of arbitrarily shaped canonical and polygonal structures with closed and open/slotted boundaries.

2.4.1 Interpolation Techniques

A number of interpolating functions and spline approximation methods described in literature are used for representing complex boundaries arising in antenna and waveguide problems ([73–75]).

Let us assume that a set of points $p_i = (x_i, y_i)$ for $i = 0, 1, 2, ..., n$ is known. Let l_i be the arc length of p_i from the starting point, with L defining the total length of the curve, and set $\theta_i = -\pi + \frac{2\pi}{L} l_i$; then it is possible to map each of those known points p_i to a set of knots $-\pi = \theta_0 < \theta_1 < \theta_2 < ... < \theta_n = \pi$.

A cubic spline function is a real-valued function $S(\theta) : [-\pi, \pi] \to \mathbb{R}$ with the following properties:

- $S(\theta)$ is twice continuously differentiable on $[-\pi, \pi] :\in [-\pi, \pi]$;

- On each subinterval $[\theta_i, \theta_{i+1}]$ for $i = 0, 1, 2, ..., n - 1$, $S(\theta)$ is a third degree polynomial;

- For all knots $\theta_i \in [-\pi, \pi]$, $S(\theta_i) = p_i$.

Let us define the following notation;

$$S(\theta) = \begin{cases} s_1(\theta), \theta_0 \leq \theta < \theta_1 \\ ... \\ s_i(\theta), \theta_{i-1} \leq \theta < \theta_i \\ ... \\ s_n(\theta), \theta_{n-1} \leq \theta \leq \theta_n \end{cases}$$

where

$$s_i(\theta) = a_i(\theta - \theta_i)^3 + b_i(\theta - \theta_i)^2 + c_i(\theta - \theta_i) + d_i \tag{2.59}$$

is the cubic on the ith interval defined by constants a_i, b_i, c_i, d_i.

During investigation of polygonal cross sections, where ensuring that an applied approach preserves the structure's shape is critical, cubic spline interpolation can "over-smooth" the edges to attain a continuous second derivative. In [76], this problem is described in terms of the trade-off between interpolation of the data in order to preserve monotonicity, or of monotonicity in order to preserve interpolation. Monotone piecewise cubic interpolation is suggested in order

to derive necessary and sufficient conditions for a cubic interpolation function to be monotone in an interval thus preventing "bumps" and "wiggles" near the connections of curves. We now declare a second approach known as Piecewise Cubic Hermite Interpolation (PCHIP). Using the same parametrisation defined above, let $-\pi = \theta_0 < \theta_1 < \theta_2 < ... < \theta_n = \pi$ be the knots for a given set of points $p_i = (x_i, y_i)$, $i = 0, 1, 2, ..., n$. It is desired to construct a piece-wise cubic interpolation function $P(\theta)$ such that $P(\theta_i) = p_i$ for $i = 0, 1, 2, ..., n$ on each subinterval $[\theta_i, \theta_{i+1}]$ for $i = 0, 1, 2, ..., n - 1$. $P(\theta)$ can be represented as follows:

$$P(\theta) = p_i H_1(\theta) + p_{i+1} H_2(\theta) + d_i H_3(\theta) + d_{i+1} H_4(\theta), \tag{2.60}$$

where

$$d_i = p'(\theta_i) \qquad\qquad H_1(\theta) = \phi\left((\theta_i - \theta)/h_i\right)$$

$$\phi(t) = 3t^2 - 2t^3 \qquad\qquad H_2(\theta) = \phi\left((\theta - \theta_i)/h_i\right)$$

$$\psi(t) = t^3 - t^2 \qquad\qquad H_3(\theta) = -h_i \psi\left((\theta_{i+1} - \theta)/h_i\right)$$

$$h_i = \theta_{i+1} - \theta_i \qquad\qquad H_4(\theta) = h_i \psi\left((\theta - \theta_i)/h_i\right)$$

and the $H_k(\theta)$ are known as the Hermite basis functions.

Figure 2.6 represents two different functions modelled with standard MATLAB libraries ([77]) to compare the behaviour of the two methods above. It can be clearly seen that the choice of the technique leads to a different level of "shape closeness".
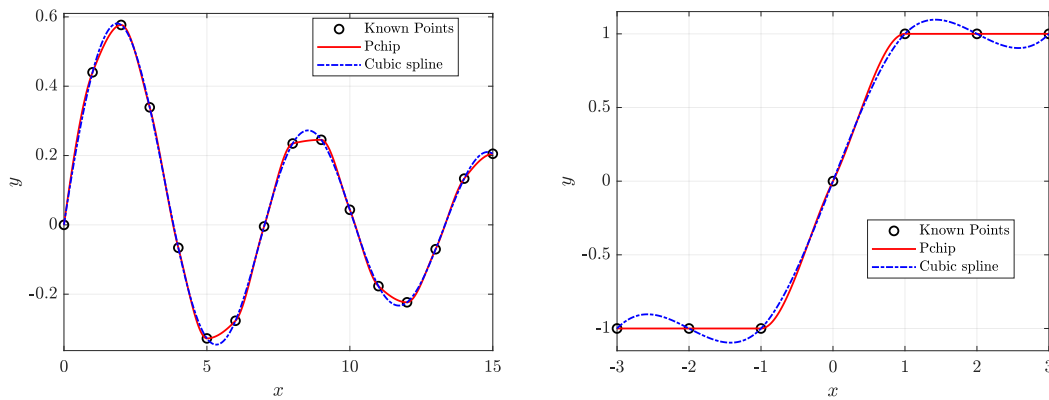
Figure 2.6: Examples of shape preserving and smoothing interpolation functions.

2.4.2 Sobolev Approximation

In this thesis we deal with various polygonal structures and as such PCHIP is preferred for parametrisation of the bounding contours. Our implementation of the MAR requires second and third derivatives of the contour defining the scatterer to be continuous but PCHIP only ensures continuity of the first derivative. Therefore, we need to smooth the function's sharp edges while ensuring that the smoothed contour remains close to the original shape. The Friedrich's mollifier arising in the Sobolev approximation ([72]) can be used to address this problem. Let us define the function $\psi \in C^\infty(\mathbb{R})$ by

$$\psi(t) = \begin{cases} c \cdot e^{-\frac{1}{1-|t|^2}}, & |t| < 1 \\ 0, & |t| \geq 1 \end{cases}$$

where $c > 0$ is chosen so that

$$\int_{\mathbb{R}} \psi(t)\, dt = 1.$$

For $\varepsilon > 0$, set

$$\psi_\varepsilon(t) = \frac{1}{\varepsilon} \psi\left(\frac{t}{\varepsilon}\right).$$

The function ψ_ε is known as Friedrich's mollifier. For $\varepsilon > 0$, let us use the change of variable $u = \dfrac{t}{\varepsilon}, du = \varepsilon dt$ to obtain

$$\int_{\mathbb{R}} \psi_\varepsilon(t) dt = \frac{1}{\varepsilon} \int_{\mathbb{R}} \psi\left(\frac{t}{\varepsilon}\right) dt = \frac{1}{\varepsilon} \int_{\mathbb{R}} \psi(u)\, \varepsilon du = \int_{\mathbb{R}} \psi(t)\, dt.$$

If $f \in L^1$ then its convolution mollification f_ε on $(-\infty, \infty)$ is given by

$$f_\varepsilon(x) = (f * \psi_\varepsilon)(x) = \int_{-\infty}^{\infty} f(t)\psi_\varepsilon(x-t)dt = \int_{x-\varepsilon}^{x+\varepsilon} f(t)\psi_\varepsilon(x-t)dt. \tag{2.61}$$

The function f_ε is infinitely differentiable which follows from the same property of ψ_ε. In this formula, parameter ε is used as the mollifier coefficient.

Let us demonstrate the effect of convolution mollification on a parametrised contour and its derivatives using a rectangular boundary as an example in Figure 2.7. We note that straight line segments are transformed to straight line segments at all points except near the corners. Rather than the mollifier coefficient itself, we use a dimensionless mollifying ratio $d = \varepsilon/L$ which depends on the characteristic length L of the structure. In general, L is chosen as

the longest side of the scatterer. We demonstrate the effect of rounding using two mollifying ratios $d = 0.001$ and $d = 0.01$. This helps one visually distinguish the change on the boundary. We also demonstrate the variation on the third derivative as a function of the parameter θ, recalling the contour is parametrised by $\eta(\theta) = (x(\theta), y(\theta))$. As a result, the trade-off between "closeness" to the original shape and its "smoothness" can be easily seen in figure 2.7.
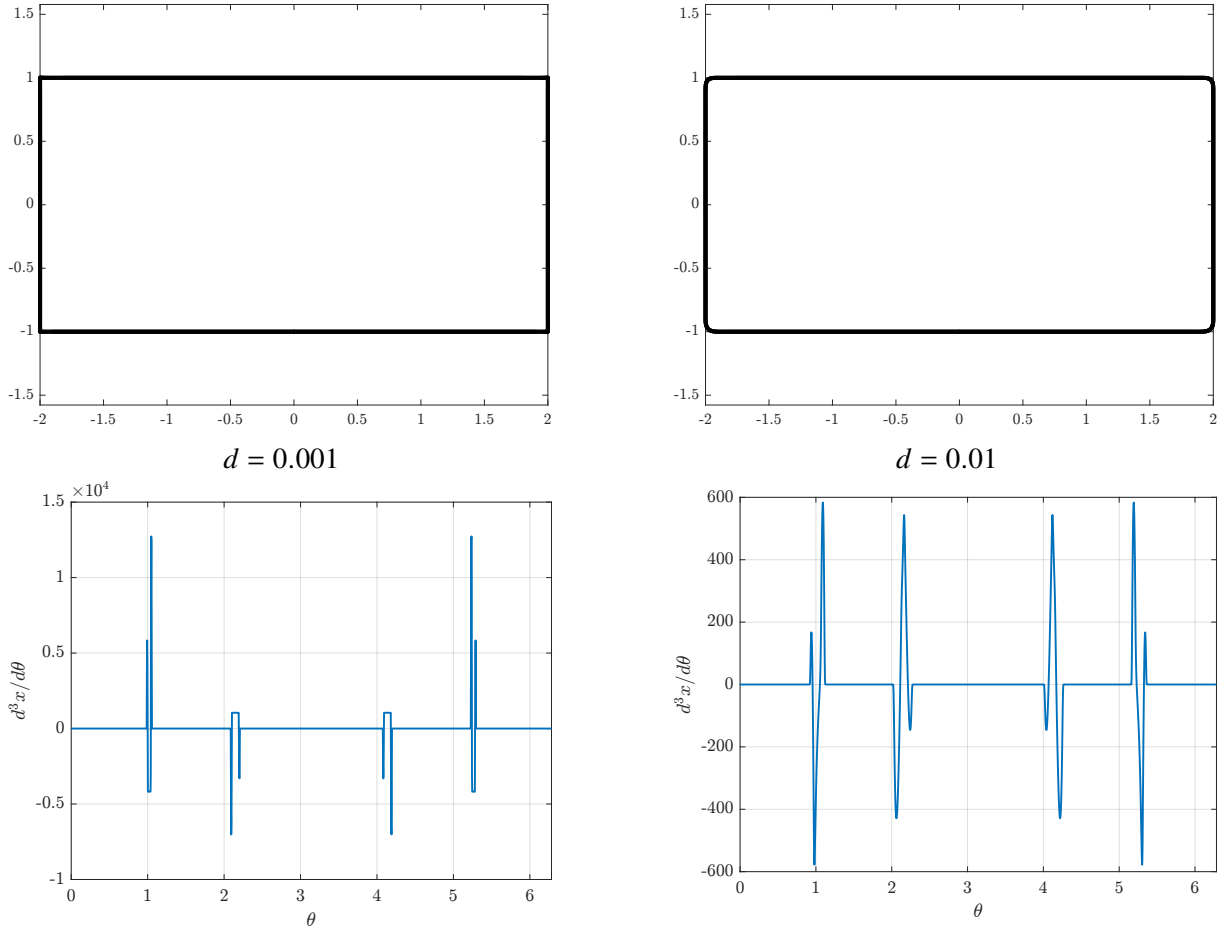
Figure 2.7: Effect of mollifier on the contour parameterisation and its third derivative: a) $d = 0.001$, b) $d = 0.01$.

As we switch from boundaries that can be expressed analytically (circles, ellipses, superellipses) to contours that are approximated (by splines or otherwise), we introduce another source of numerical error that also should be investigated. In the following chapters we demonstrate that solutions with 5-6 digits accuracy can be obtained by proper approximation methods. We also compare the results for arbitrary shapes with those available in literature to show the accuracy of the solution obtained by the MAR.

It is worth mentioning that in the thesis we have used a number of different methods for obtaining the set of known point coordinates (i.e. knots) to construct interpolation/mollification

geometries. Naturally, more known points on the contour will generate an interpolating surface that is closer to the desired shape, especially for complex boundaries. For example, a triangle contour can be generated and parametrised, using only the corner points given in the following format:$[(x_n, y_n)] = [(0, 0), (1, 0), (0, 1), (0, 0)]$. For arbitrary non-canonical shapes, such as the boundary of a submarine, CAD (computer-aided design) tools are used to create a contour that can be imported into MATLAB. Standard libraries in MATLAB also allow for importing image files and translating bounding contours into sets of coordinate points. This is a method used often to analyse x-ray images.

2.5 The MAR Solution for Arbitrarily Shaped Cross Sections

In this section, we demonstrate the excellent agreement between numerical results obtained by the MAR for polygonal contours generated and smoothed by use of PCHIP and Sobolev's approximation technique and the analytical/numerical results available in literature.

For the classical rectangular waveguide shown in Figure 2.8a, relative cut-off wavenumbers $(k_c a)_{mn}$ can be calculated analytically ([78]), using the readily deducible formula

$$(k_c)_{mn} b = \pi \sqrt{\left(\frac{b}{a}\right)^2 m^2 + n^2} \tag{2.62}$$

where $m, n = 0, 1, 2, \dots$ and $m^2 + n^2 \neq 0$.
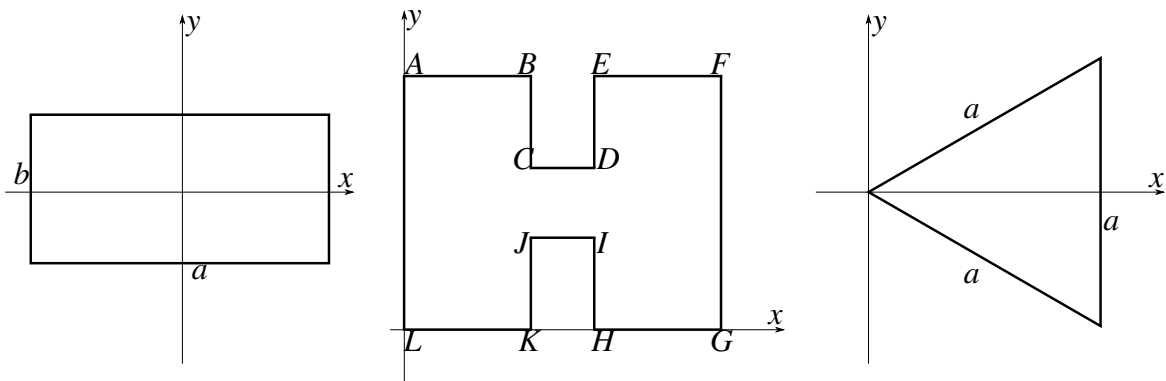
(a) Rectangular waveguide.   (b) Double-ridge waveguide.   (c) Equilateral triangle waveguide.

Figure 2.8: Cross sections of polygonal structures.

The exact values of the first 6 cut-off wavenumbers for a rectangular waveguide with sides $a = 2$ and $b = 1$ are shown in Table 2.2. To analyse the same waveguide by the MAR, we

Table 2.2: The cut-off wavenumbers for a rectangular waveguide.

m	n	$(k_c a)_{mn}$
1	0	1.57079632
0,(2)	1,(0)	3.14159226
1	1	3.51240736
2	1	4.44288293
3	0	4.71238898
3	1	5.66358669

need to start with a parametrisation of the contour. As demonstrated in Figure 2.7, the mollifier coefficient defines the degree of the "closeness" of the generated structure to the desired shape. Naturally, taking a smaller mollifier ratio and adding more points on the contour will result in a shape closer to the desired polygonal structure. As a result, increased system size will then provide higher accuracy in numerical simulations.

Using a mollifier ratio of $d = 0.02$ and a system size $N = 128$, we calculated the spectral dependence of the condition number of the resulting matrix. The choice of the mollifying ratio of 2% is based on the standard production tolerances of waveguides ([79]). The locations of the spikes in the graph shown in Figure 2.9 gives us the first approximation for calculation of the roots where the equation $\det(A) = 0$ defines cut-off wavenumbers of a rectangular waveguide. We follow the same approach (described earlier for finding the roots of a duct-like cavity) of the recursive root finding algorithm. Using each calculated root as the initial approximation for the next step, and fine tuning the mollifier coefficient, we calculate the roots (cut-off wavenumbers) with increased accuracy, and show digits stabilisation as the truncation number increases in Table 2.3.

Table 2.3: The fundamental mode against increasing system size for a rectangular waveguide.

d	N	$k_c a$	Computation Time
2.5%	128	**1.57**188349	1.2 sec
2.1%	256	**1.5707**0692	4.5 sec
1.8%	512	**1.57079**083	18.7 sec
1.4%	1024	**1.57079**311	62.3 sec
1.2%	2048	**1.570796**55	337.6 sec
Analytical	-	1.57079632	-
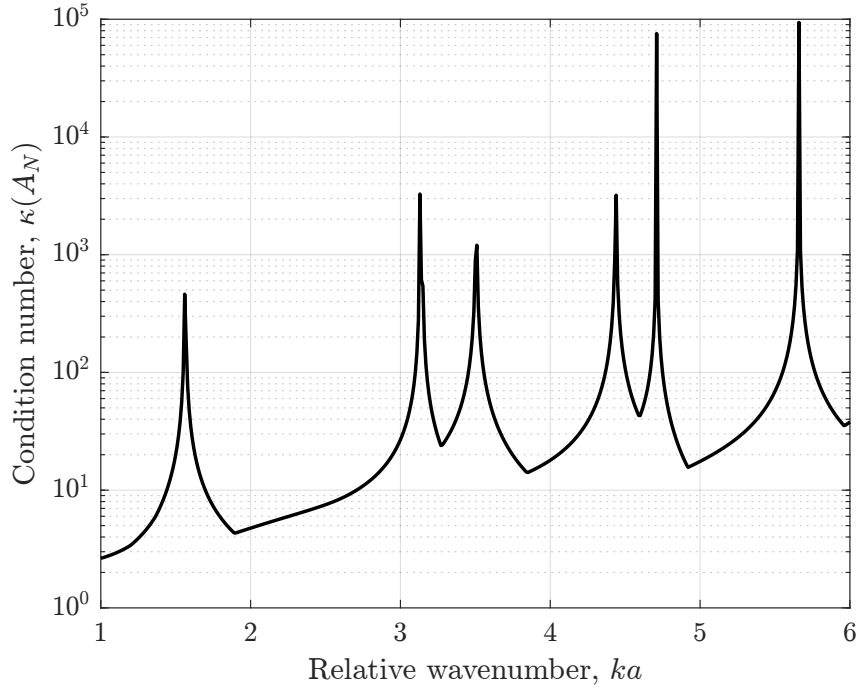
Figure 2.9: Condition number $\kappa\left(A_N\left(ka\right)\right)$ against relative wavenumber ka for a rectangular waveguide.

It is important to note here that to offset computing resources introduced by numerical implementation of an arbitrary contour, we use an improved root finding algorithm (see Algorithm 1) based on derivative estimated iterative functions ([59]) developed using the following set of relations:

$$
\begin{aligned}
f'(x) &= \frac{f(x+h) - f(x-h)}{2h} \\
f''(x) &= \frac{f(x+h) - 2f(x) + f(x-h)}{h^2} \\
\Delta &= f'(x) \mp \sqrt{(f''(x))^2 - 4f(x)f'(x)} \\
\delta &= \frac{-2f(x)}{\Delta}
\end{aligned}
\tag{2.63}
$$

where $f(ka) = \det\left(A_N(ka)\right)$ and h is a sufficiently small step size $\left(10^{-6}\right)$. The computation time required for the root finding algorithm on a personal computer (Intel(R) Core(TM) i7-8750H CPU @ 2.20GHz, 16.0 GB RAM, Geforce GTX 1050 Ti 4GB) is presented in Table 2.3. It is shown that roots with 5 digits accuracy are obtained for a system size $N = 512$ and computation time of 18.7 seconds. We would like to demonstrate that the calculation of higher frequency cut-off wavenumbers and simulation of high frequency field distribution H_z can also be achieved without any modification to the algorithm. To highlight this capability, we present the frequency

---

Algorithm 1 Modified Troub Root Finder

1: **procedure**
2:     $x_0, x_{new} \leftarrow$ *initial guess*
3:     *maxit* $\leftarrow$ *maximum number of iterations*
4:     $h \leftarrow$ *step size for derivative*
5:     **repeat**
6:         $x_{old} \leftarrow x_{new}$
7:         $i \leftarrow i + 1$
8:         calculate $f(x_{old}), f'(x_{old}), f''(x_{old}), \Delta, \delta$
9:         **if** $i > maxit$ **then**
10:            no convergence
11:        $x_{new} \leftarrow x_{new} + \delta$
12:        calculate $f(x_{new})$
13:    **until** $|f(x_{old})| \geq |f(x_{new})|$ **and** $i > maxit$

---

dependence of the condition number in Figure 2.10 and normalised modal field distribution for selected modes in Figure 2.11. We also note that unless otherwise stated we use truncation size $N = 512$ for the rest of the calculations in this thesis.
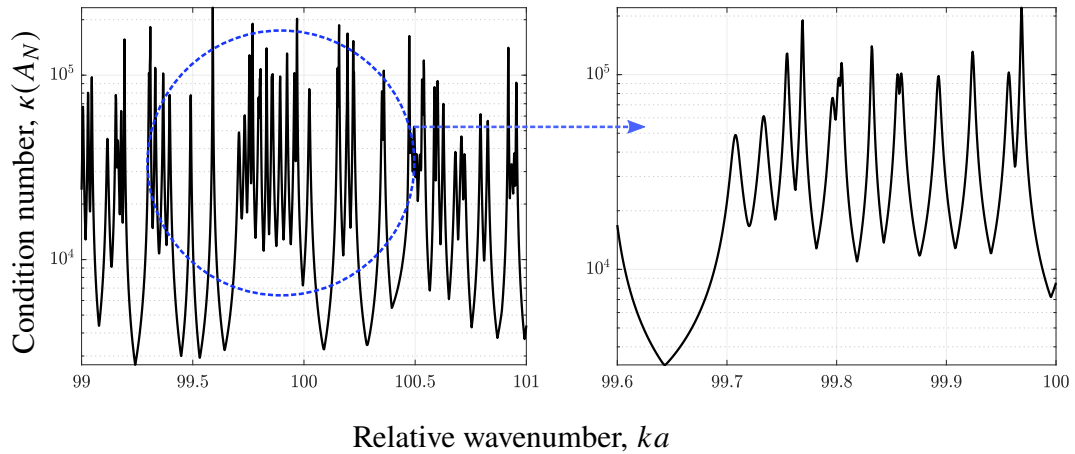
Figure 2.10: Condition number $\kappa (A_N (ka))$ against relative wavenumber ka for a rectangular waveguide − high frequency region.

Closed-form exact analytical solutions for calculation of cut-off wavenumbers for triangular waveguides for various cross sections (including equilateral and isosceles right) are available in the literature. It can be seen that in [80, 81] some fundamental modes are missed while in [82] complete exact results are available for equilateral waveguides. In [83], one can find the ratio of cut-off wavenumbers against fundamental modes for four different triangular waveguide construction. Cut-off wavenumber calculations are presented in Table 2.4 and the modal field distribution plots in Figure 2.12 shows a very good agreement with the results available in [82].

(a) $m=10, n=10, ka=35.1240$

(b) $m=10, n=20, ka=64.765$

(c) $m=10, n=40, ka=126.641$

(d) $m=20, n=10, ka=44.428$

(e) $m=20, n=20, ka=70.248$

(f) $m=20, n=40, ka=129.531$
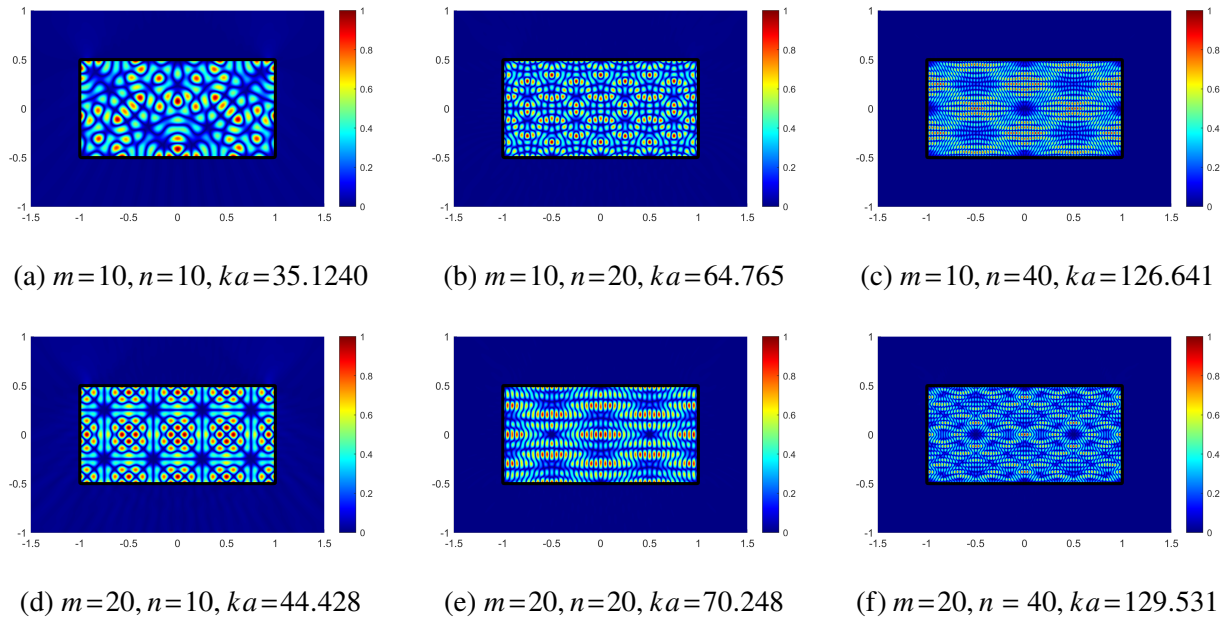
Figure 2.11: Normalised modal field representation of selected high frequency modes for a rectangular waveguide.

(a) TE_1T

(b) TE_1H

(c) TE_2

(d) TE_3T

(e) TE_3H

(f) TE_4T

(g) TE_4H

(h) TE_4T

(i) TE_5H

(j) TE_6

(k) TE_7T

(l) TE_7H
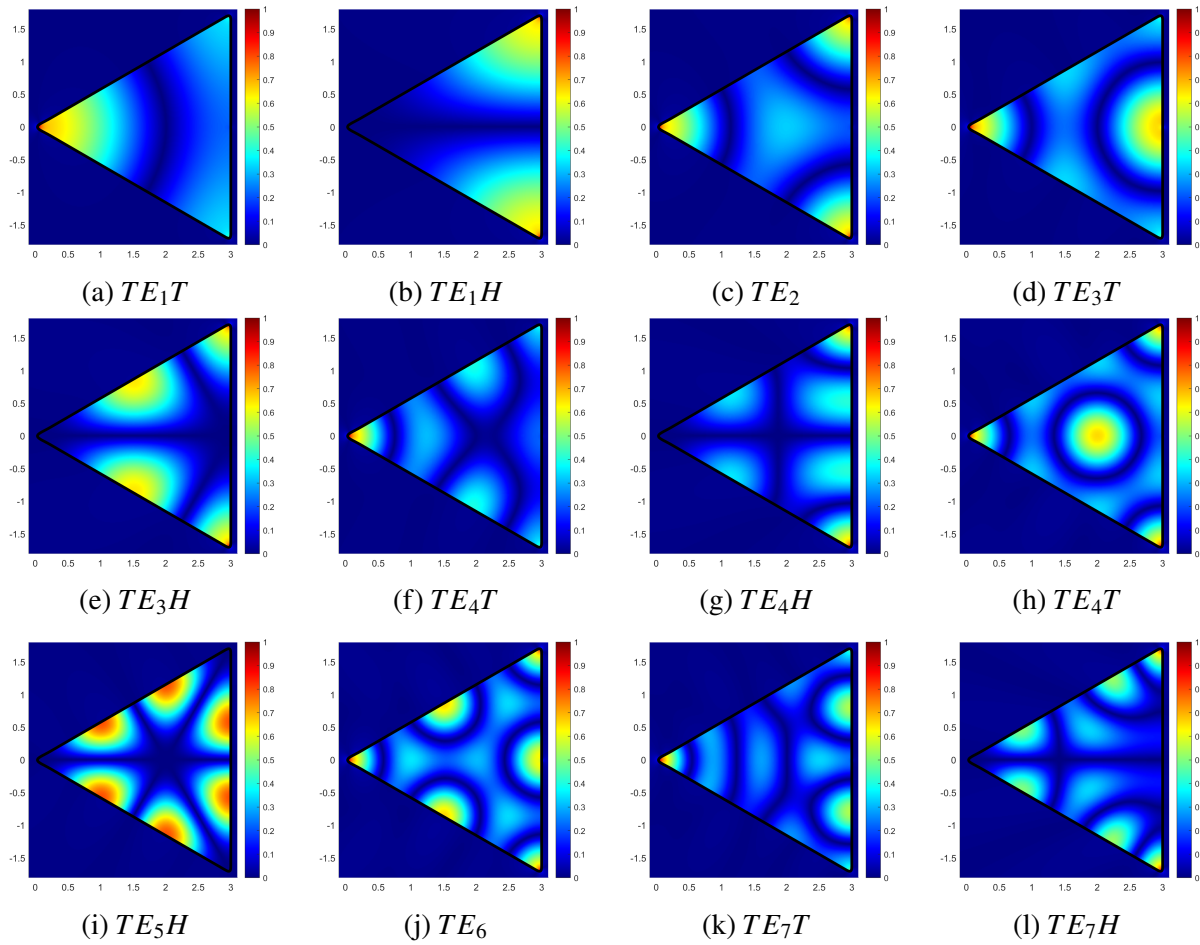
Figure 2.12: Normalised modal field representation of the first 7 modes for a triangular waveguide.

Table 2.4: The cut-off wavenumbers for triangular waveguides.

Cross Section	Modes(mn)	k_c MAR	[83]	[82]
equilateral	TE$_{01}$	1.209257	1.20920	1.2092
	TE$_{10}$	2.094406	2.094334	2.0944
	TE$_{11}$, TE$_{02}$	2.418413	2.418392	2.4184
	TE$_{12}$	3.199255	3.199542	3.1992
isosceles right	TE$_{01}$	3.141592	3.141593	
	TE$_{11}$	4.442260	4.442212	
	TE$_{02}$	6.283275	6.283115	
	TE$_{12}$	7.024832	7.024601	

Next we turn our attention to arbitrary shaped ridge waveguides which are extensively used in various applications due to their numerous advantages including smaller size and weight, wider operating frequency range, larger cut-off wavenumbers, lower impedance characteristics and higher Q factor of resonators based on such shapes. As it is one of the most common cross sections, we investigate double-ridge waveguides shown in figure 2.8b where AB = EF = GH = KL = 0.508cm, BC = DE = HI = JK = 0.3863cm, CD = IJ = 0.254cm, and FG = LA = 1.016cm. Its corresponding condition number plot with a system size $N = 128$ can be seen in Figure 2.13, which provides us with an initial approximation for the cut-off wavenumber calculation with a bigger system size for higher accuracy. The results are validated against [84], while [85],
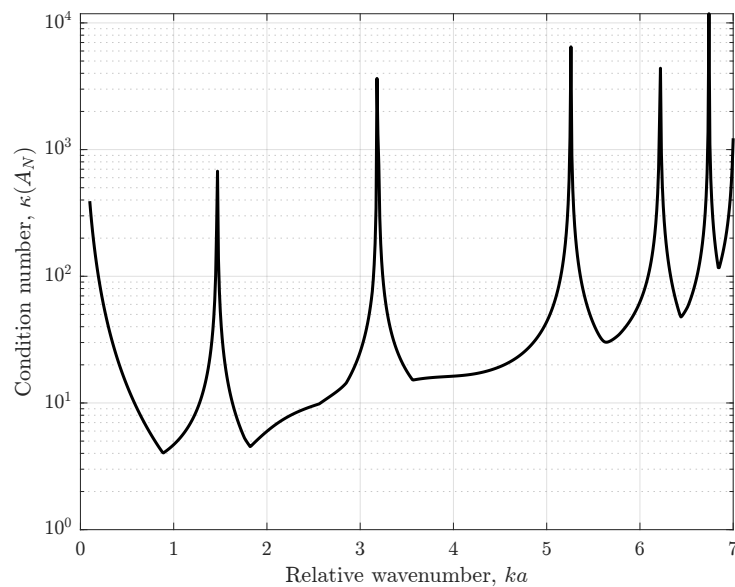
Figure 2.13: Condition number $\kappa\left(A_N\left(ka\right)\right)$ against relative wavenumber ka for double-ridge waveguide.
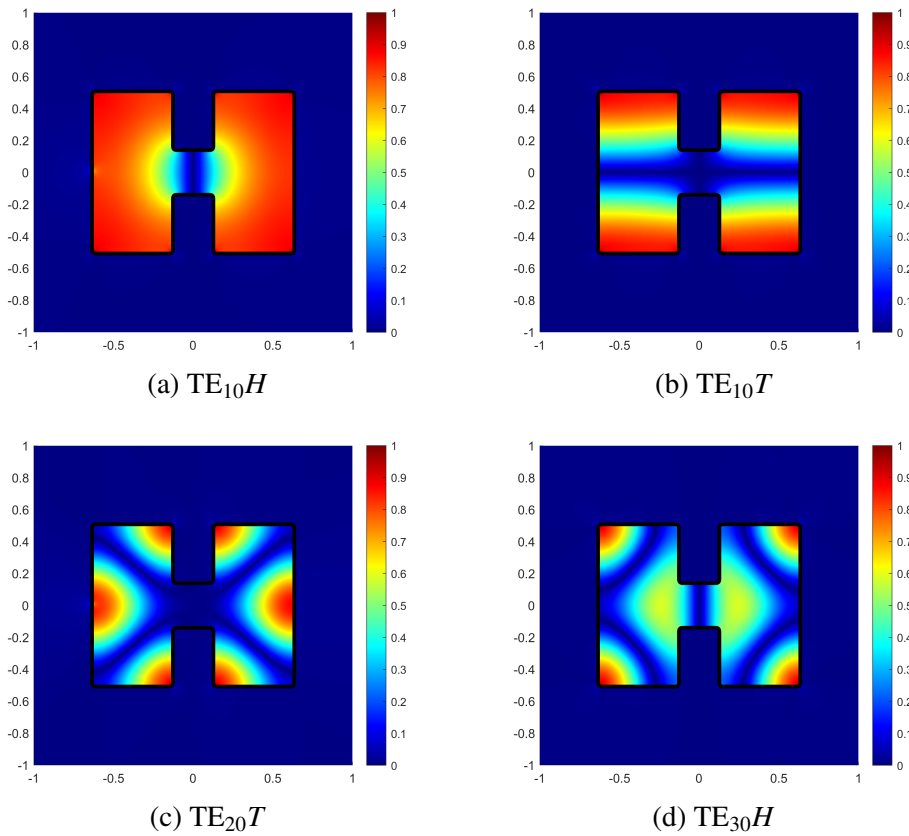
Figure 2.14: Normalised modal field representation of double-ridge waveguide for selected modes.

[86] and [87] are used for the comparison. The cut-off wavenumbers collected in Table 2.5, shows good agreement with other numerical methods where an exact solution is not available. In Figure 2.14, modal field H_z distribution for the cut-off modes TE_{10H}, TE_{10T}, TE_{20T}, TE_{30H} which are validated against [84] is presented. A similar approach is followed in naming the waveguide modes, i.e. the suffixes H and T stand for Hybrid (a basic ridged waveguide mode) and Through (a rectangular waveguide-type mode existing in the connecting region), respectively.

Table 2.5: The cut-off wavenumbers for a double-ridge waveguide.

Modes(mn)	k_c MAR	[85]	[86]	[87]	[84]
TE_{10H}	1.4568	1.434	1.5097	1.4849	1.4843
TE_{10T}	3.1713	3.168	3.1931	3.2015	3.1570
TE_{20T}	6.2055	6.192	6.2218	6.2065	6.1916
TE_{30H}	6.7265	6.705	6.7629	6.7230	6.7112
TE_{11T}	6.9916	6.975	7.0123	7.0021	6.9745

(a) The relative error.

(b) The condition number.
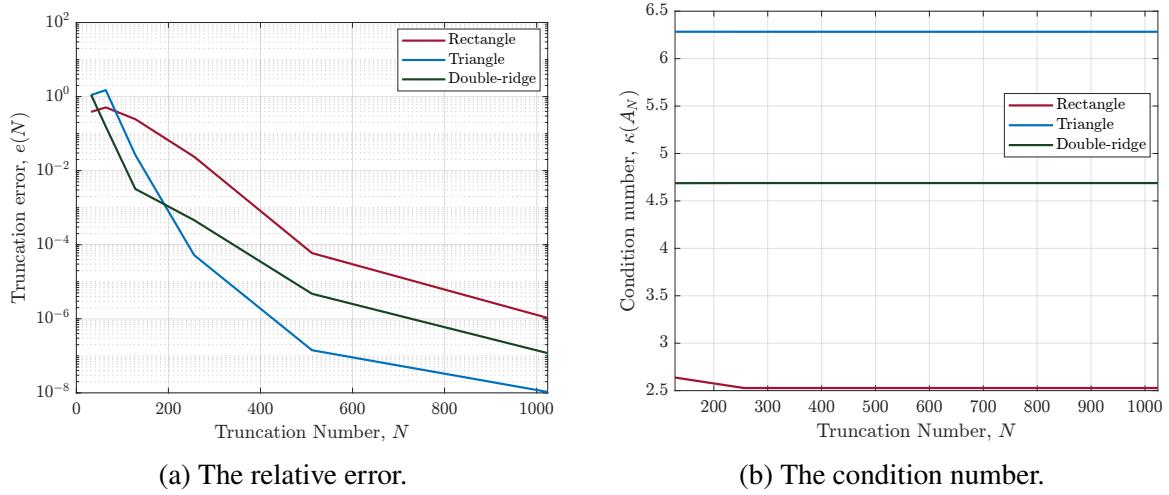
Figure 2.15: Accuracy of the solution and the condition number of the truncated systems for rectangular, triangular and double-ridge waveguides.

Prior to finalising this chapter, we would like to further demonstrate the accuracy of the obtained results when analytical parametrisation is replaced with interpolation/mollifier functions. The truncation error function against the system truncation number is shown in Figure 2.15a for the geometries investigated: rectangular, equilateral triangular and double-ridge waveguides. We also present the fast convergence of system's condition number to its limiting value for each geometry in Figure 2.15b.

3

2D Helmholtz Resonators

In this chapter, we investigate Helmholtz resonators and present accurate numerical results obtained by the application of the MAR. We collect all material related to emergence of the Helmholtz modes so as to avoid repetition of comments regarding this phenomenon in the following chapters. We consider various shapes of resonators to demonstrate the effectiveness of the MAR-based approach which can be easily extended for numerical simulation of different practical and theoretical problems.

In solving the Neumann problem for an slotted arbitrary cylinder, one inevitably encounters a resonance phenomenon in the low-frequency region ($ka \ll 1$, where a is the characteristic linear size of the cross section), when the relative wavenumber ka of incident radiation approaches the real part γ'_H of the complex eigenvalue $\gamma_H = \gamma'_H - i\gamma''_H$, of the Helmholtz mode. This simply means that when the slit is relatively narrow, any slotted cylinder may be regarded as a Helmholtz resonator. The Helmholtz mode for each structure is unique, in a sense that equation (2.57) can only have a single root and a single field distribution pattern. Examples of modes and cases where we have double roots resulting in symmetric and anti-symmetric modes, are provided in the following chapters. The unloaded $Q-$factor, denoted by Q_H of the Helmholtz mode is one of the key characteristic properties of a Helmholtz resonator and is used in the analysis of various types and structures. We use the standard definition of this value, $Q_H = -\dfrac{\gamma'_H}{2\gamma''_H}$. Our focus on the extraction of the Helmholtz mode from the complete spectrum of the complex oscillations

(complex modes) is explained by two reasons: a) the widespread application of the Helmholtz resonators in diverse areas of practical acoustics and electro-engineering; and b) the possibility of individual study of the unique features arising in excitation of the Helmholtz mode in cylinders of various cross sections and configurations with various neck lengths and sizes.

Practical applications of Helmholtz resonator are well described in literature; we mention only some technical areas where the usage of Helmholtz resonators is most promulgated. Helmholtz resonators find most applications in acoustics in amplification or attenuation of sound waves, for example in musical instruments, to amplify certain frequencies to produce a desired tone, or in internal combustion engines to attenuate high noise levels produced by the combustion engine ([88]). In addition, the Helmholtz resonator is one of the devices most-exploited in sound-energy harvesters ([89]). 2D arrays of Helmholtz resonators with optimised absorption properties are frequently used at low frequencies in order to improve sound diffusion in the audible regime. Furthermore, flow-excited Helmholtz resonators are used as flow control devices ([90]). Other applications may be found also in electromagnetics ([91]).

Production of devices based on distinctive properties of Helmholtz resonators requires estimation of their characteristic parameters. In general, this is achieved by approximation methods. The use of such methods can be justified by a clear understanding of the physical process and non-complex geometry of most devices in creating the phenomenon of low-frequency resonance. The classical view on these processes is well described, in particular, in [92, 93], where the Helmholtz resonator is treated as the archetypical system exhibiting resonance with distributed parameters. From a physical point of view, it is reasonable to postulate that all the kinetic energy of the system is concentrated in the column of air in the neck that moves as a plunger. On the other hand, the potential energy of the system is stored through the process of elastic deformation of the air contained in the cavity. Periodic transformation of one type of energy to the other is the key point in explaining emergence of the Helmholtz mode. In this sense, the Helmholtz resonator may be regarded as an acoustic system analogous to a simple harmonic oscillator, and hence may be described by the general postulates of classical oscillation theory.

Furthermore, a close analogy can be established between the propagation of sound in pipes or chambers and electrical circuits, which is a great aid in acoustical problems of many kinds, since all the theory related to the electrical circuit theorems may be applied and it is possible to substitute a complex acoustic system by a systematic circuit of its analogous electrical system. It
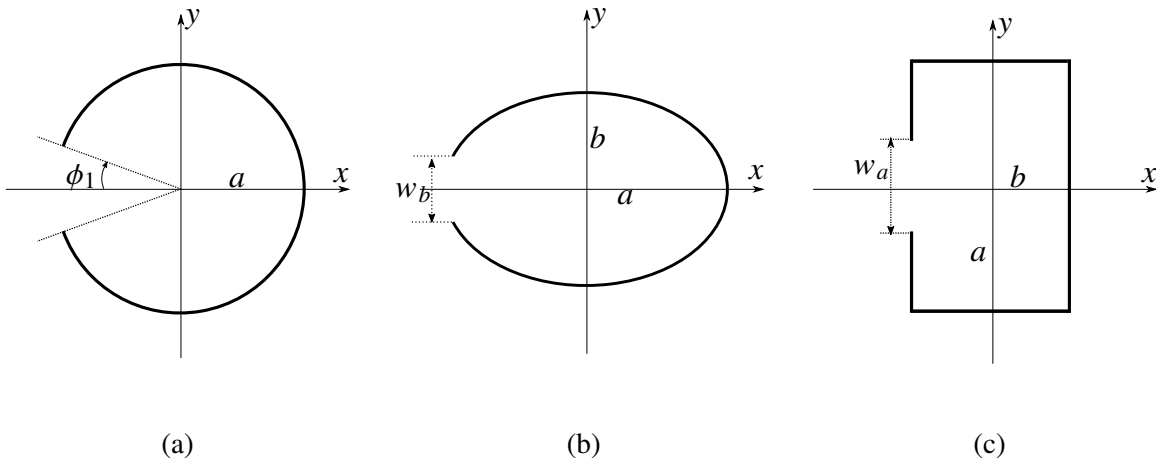
Figure 3.1: Geometry of simple cavities as Helmholtz resonators.

is evident that we can even have equivalent mechanical, electrical, and acoustic expressions for resonance frequency. The classic lumped approach approximates this resonator as an equivalent spring (cavity) and mass (neck) system and yields the expressions for the resonator frequency and the transmission loss. In other words, the classical approach in modelling these resonators is to neglect the spatial distribution leading to an equivalent spring–mass system ([94]). An extensive review of the lumped-elements approach (the spring-mass damper model) can be found in [95].

The methods based on explanation of emergence of the Helmholtz mode by common physical properties characteristic for oscillating systems with lumped parameters are widely used for primary estimates in the design of the systems incorporating Helmholtz resonators in practical use. Nevertheless, the accuracy of such approximations is validated mostly by experiments, which, sometimes, are rather resource consuming. Thus it is highly desirable to replace experiments by numerical models where possible, taking advantage of a reliable and accurate theoretical approach. Once developed, such an approach provides an independent external estimate for the validity and accuracy of existing approximate methods.

3.1 Circular Helmholtz Resonators

A slotted infinitely long rigid circular cylinder may be regarded as a 2D analogy of the classical Helmholtz resonator, usually presented as a rigid spherical shell with a small circular aperture, see [92, 93] . The diffraction problem for a circular slotted metallic cylinder, irradiated by an H−polarised plane wave, was rigorously solved using the MAR, in 1971 ([96]). The low-frequency approximation of the solution including the case of an electromagnetic Helmholtz

Table 3.1: Complex eigenvalue γ_H of the Helmholtz mode for a slotted circular cylinder.

ϕ_1	Approximate (eq. (3.1))	Accurate (MAR)
1°	0.324737-i0.0292825	0.309491-i0.012457
2°	0.351438-i0.0342960	0.332487-i0.0157361
5°	0.399536-i0.0443259	0.372456-i0.0229525
10°	0.452673-i0.0569003	0.414270-i0.0329788
15°	0.495537-i0.0681865	0.446178-i0.0426394
30°	0.608214-i0.1027207	0.523018-i0.0740877

resonator was investigated in [97] and [98]. In these publications, the authors derived the following approximate formula for the complex eigenvalue of the Helmholtz mode for small slit widths $d = 2a \sin \phi_1$, $\phi_1 \ll 1$, where ϕ_1 denotes angular semi-width (see Figure 3.1a), when $ka \ll 1$:

$$\gamma_H = \left(-2 \log \sin \frac{\phi_1}{2} \right)^{-\frac{1}{2}} \left\{ 1 + i \frac{\pi}{16} \left(\log \sin \frac{\phi_1}{2} \right)^{-1} \right\}. \tag{3.1}$$

The derivation of this formula may be found in [99].

The extraction of the complex eigenvalue γ_H from the complete spectrum is obtained by solving the dispersion equation $\det(A_N) = 0$. The predetermined accuracy of calculation is achieved by proper choice of truncation number N; we calculated value γ_H with accuracy of 5-6 significant decimal places. The approximate values of γ_H obtained from equation (3.1) and their accurate values obtained via the MAR are collected in Table 3.1. Comparison shows that equation (3.1) has limited applicability, only for exceedingly small angular sizes of a slit, when $\phi_1 \ll 1$.

The distributions of the resonance field (absolute value of the total potential velocity, $\left| U^{tot}(x, y) \right|$, in logarithmic scale) for $ka = Re\gamma_H \equiv \gamma'_H$ in the vicinity of "classical" Helmholtz resonators as well as other basic shapes (ellipse and rectangle) shown in Figure 3.1, are presented in Figure 3.2. The vertical slit ratio $\frac{w_b}{2b}$ and eccentricity $e = \sqrt{1 - q^2}$ $\left(q = \frac{b}{a} \right)$ for the parametrisation of the elliptic cavity and the vertical slit ratio of $\frac{w_a}{2a}$ is used for the rectangular cavity, where a and b stand for major and minor semi-axes.

(a) $\phi_1 = 5°$, $ka = 0.372456$

(b) $\phi_1 = 15°$, $ka = 0.446178$

(c) $e = 0.5$, $w_b = 0.2$, $ka = 0.447637$

(d) $e = 0.9$, $w_b = 0.2$, $ka = 0.550138$

(e) $a/b = 2$, $w/a = 0.1$, $ka = 0.486802$

(f) $a/b = 2$, $w/a = 0.25$, $ka = 0.566795$
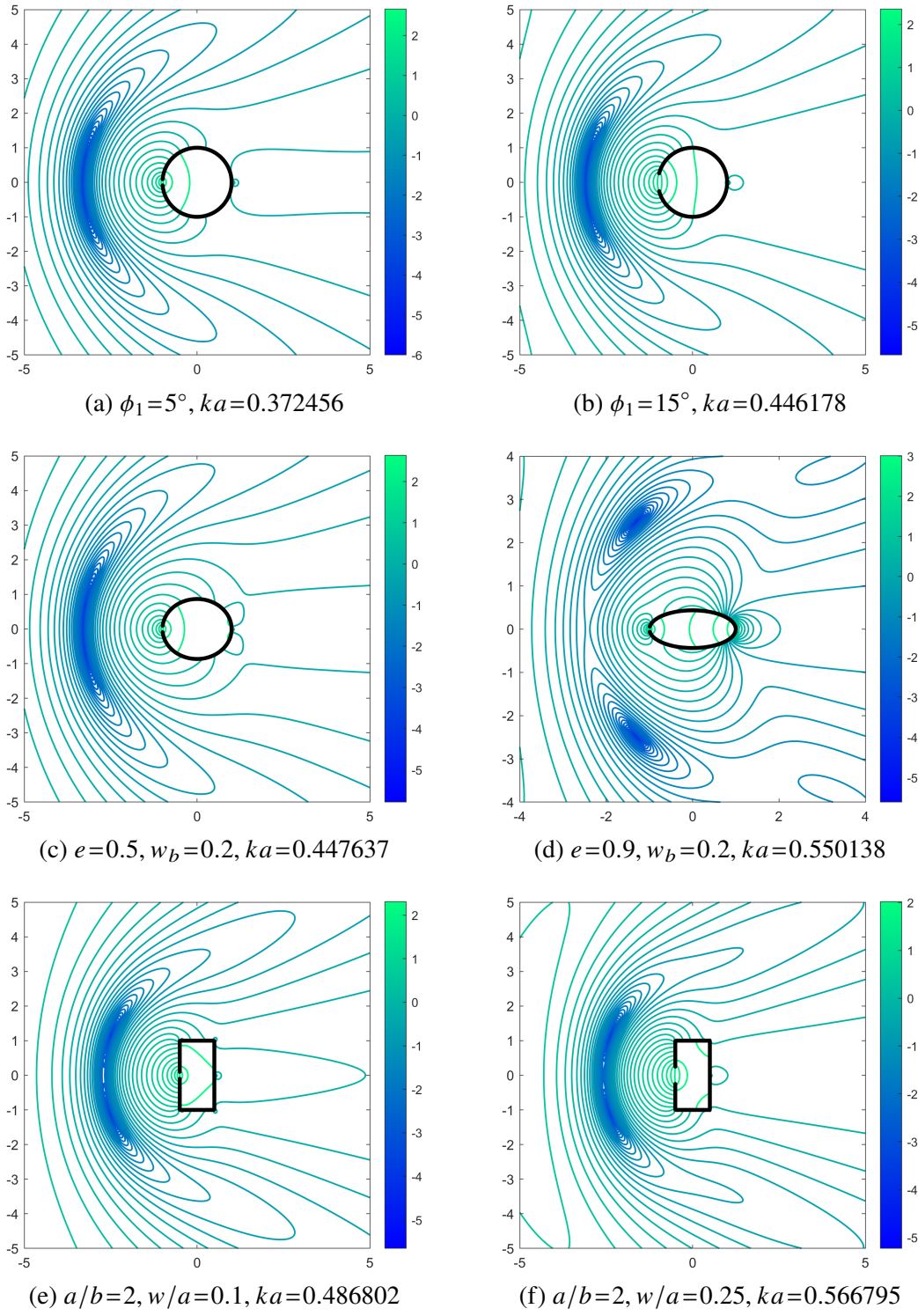
Figure 3.2: Distribution of $\left| U^{tot}(x,y) \right|$ in logarithmic scale in the vicinity of circular, elliptic and rectangular Helmholtz resonators, $ka = \gamma'_H$, incident angle $\alpha = 0°$.

(a)   (b)
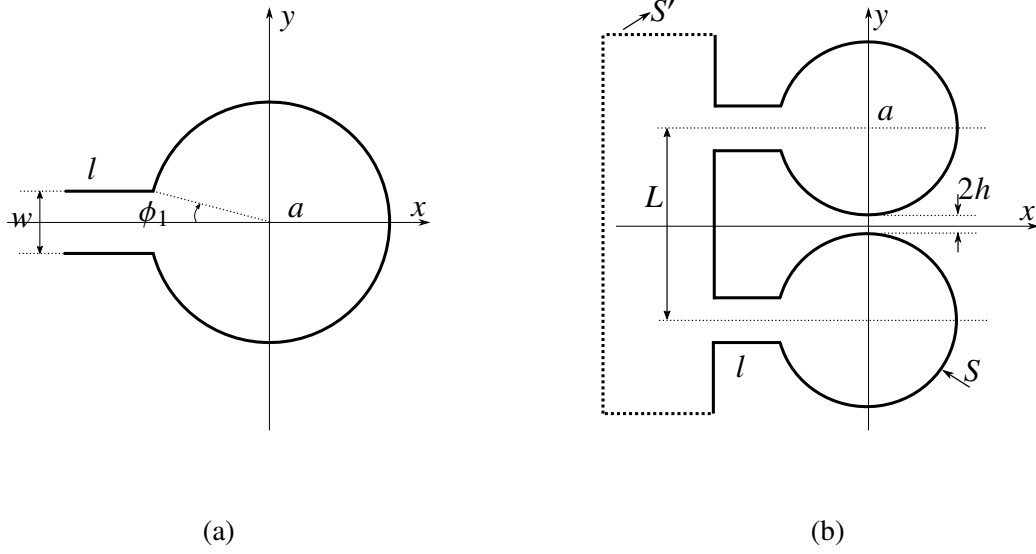
Figure 3.3: Circular Helmholtz resonator: a)with attached neck; b)paired.

3.2 Influence of the Neck on the Helmholtz Mode for Slotted Circular Cylinders

A more realistic shape for a Helmholtz resonator is shown in 3.3a, where a neck with a length of l is attached to the entry (slit) of a slotted cylinder. For optimal characterisation of such Helmholtz resonators, it is convenient to use dimensionless length $l_r = l/d$, where $d = 2a \sin \phi_1$ is the slot width. From a physical point of view, it is obvious that for a fixed slit width one may predict that the longer the neck, the higher the value of the Q−factor. This qualitative argument is supported by accurate numerical calculations for three values of angular slit semi-width $\phi_1 = 5°, 10°, 15°$, where the relative neck length l_r varies from $l_r = 0$ to $l_r = 2.5$. The calculations are collected in Table 3.2.

The results show agreement with the basic features characteristic for Helmholtz resonators with attached necks: as relative length l_r increases, the resonance relative wavenumber $ka \equiv Re\gamma_H$ decreases and radiation losses diminish which is reflected in the decrease of the values $Im\gamma_H$. This phenomenon has a notable impact on the significant growth of the unloaded quality factor $Q_H = \frac{-Re\gamma_H}{2Im\gamma_H}$. For the "classical" Helmholtz resonator ($l_r = 0$), the values of Q_H for $\phi_1 = 5°$ and $\phi_1 = 15°$ are 8.1138 and 5.2320, respectively, but for the Helmholtz resonator with attached neck length $l_r = 2.5$, $Q_H = 39.1548$ and $Q_H = 14.5878$, respectively. The influence of the neck length on the distributions of the total potential velocity $\left|U^{tot}(x, y)\right|$ at resonance frequencies ($ka = \gamma'_H$) is also analysed for various relative neck length l_r; the results

Table 3.2: Complex eigenvalue γ_H of the Helmholtz mode for a circular cylinder with attached neck.

l_r	$\phi_1 = 5°$	$\phi_1 = 10°$	$\phi_1 = 15°$
0	0.372457-i0.022953	0.414271-i0.032979	0.446178-i0.042639
0.05	0.369495-i0.022366	0.410492-i0.031992	0.441310-i0.041106
0.1	0.367206-i0.021907	0.406885-i0.031055	0.436065-i0.039494
0.5	0.345282-i0.017885	0.373884-i0.023545	0.393964-i0.028555
1	0.319073-i0.013869	0.339773-i0.017432	0.352736-i0.020459
1.5	0.297233-i0.011085	0.312189-i0.013465	0.320232-i0.015454
2	0.277855-i0.008987	0.289052-i0.010700	0.294846-i0.012247
2.5	0.263590-i0.007644	0.271611-i0.008920	0.273641-i0.009969

are presented in Figure 3.4. To understand the distribution $\left|U^{tot}(x,y)\right|$ across the neck better,

(a) $l_r=0.5$, $ka=0.373884$ (b) $l_r=2.5$, $ka=0.271611$
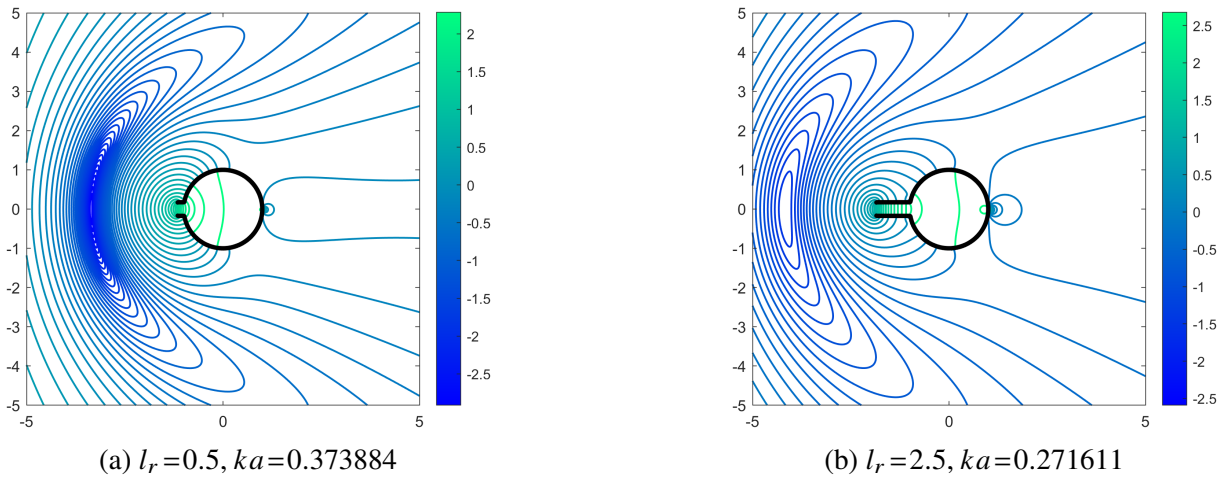
Figure 3.4: Distribution of $\left|U^{tot}(x,y)\right|$ in logarithmic scale in the vicinity of a circular Helmholtz resonator with various relative neck lengths, $ka = \gamma'_H$, incident angle $\alpha = 0°$.

we demonstrate the resonance distribution for a slotted circular Helmholtz resonator ($\phi_1 = 10°$) with a longer neck ($l_r = 5$) and a magnified view near the neck in Figure 3.5. It can be seen that the distribution of the velocity vector is concentrated inside the resonance cavity. Another important and illustrative image is the amplitude-phase distribution of the total potential velocity $U^{tot}(x,y) = \left|U^{tot}(x,y)\right|e^{i\psi}$. The phase distribution $\psi(x,y)$ in Figure 3.6b reveals the distortion of the phase front of the propagating plane wave as an empty arc; this distortion makes the Helmholtz resonator appear a bigger obstacle than its real physical size. Because of this reason, the total and sonar cross sections become resonant quantities.
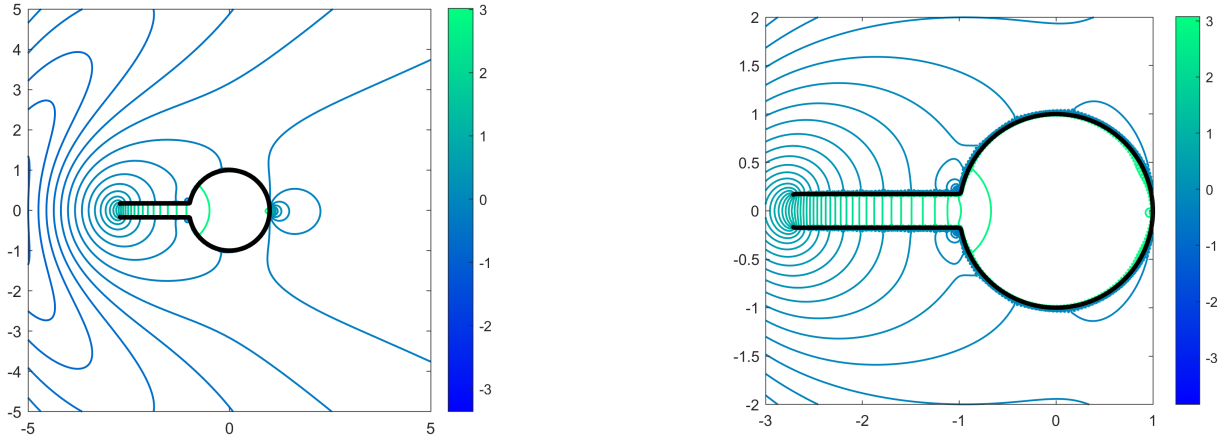
Figure 3.5: Distribution of $\left|U^{tot}(x, y)\right|$ in logarithmic scale in vicinity of a circular Helmholtz resonator $\left(\phi_1 = 15°, l_r = 5, ka = \gamma'_H = 0.207895\right)$, incident angle $\alpha = 0°$.

(a) $\log(\left|U^{tot}(x, y)\right|)$ (b) $\log(\left|\psi(x, y)\right|)$
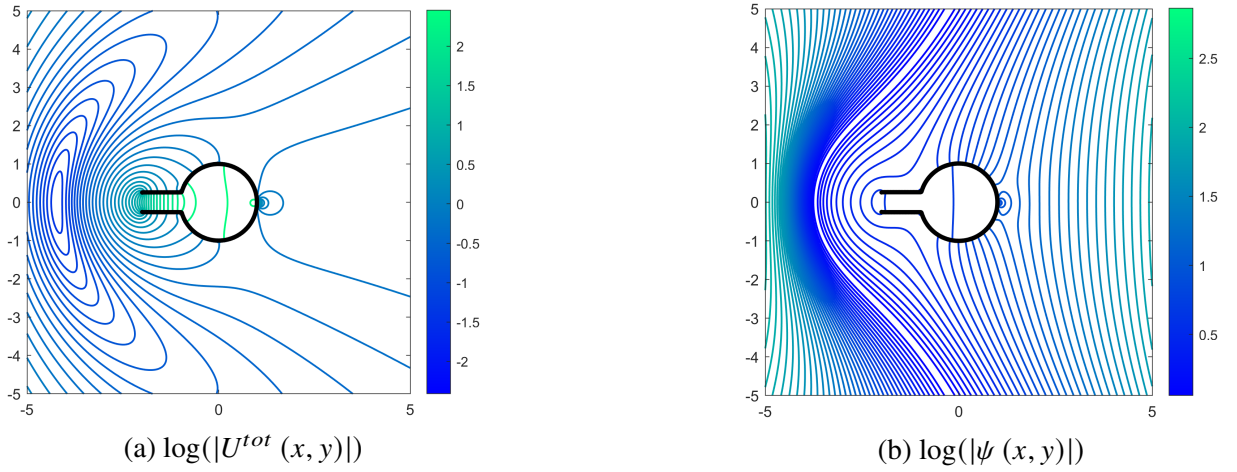
Figure 3.6: Amplitude-phase distribution $\left|U^{tot}(x, y)\right| e^{i\psi}$ in the vicinity of a circular Helmholtz resonator $\left(\phi_1 = 15°, l_r = 2, ka = \gamma'_H = 0.292612\right)$, incident angle $\alpha = 0°$.

3.3   Paired Cylindrical Helmholtz resonators

In practice, low-frequency noise attenuation and sound absorption is achieved by implementation of arrays of Helmholtz resonators (see, for example, [95]). A minimal fragment of such an array consisting of two identical resonators is shown in Figure 3.3b. Although resulting array of resonators will have multiple openings the screen S is continuous and complementary surface S' is arbitrary.

A pair of Helmholtz resonators present a multi-parameter system, described by four parameters: a is the radius of a cylinder; $d = 2a \sin \phi_1$ width of a slot; l is the length of the neck; and L is distance between resonance entry points. The distance L between resonators is measured by the relative value $L_r = \dfrac{L}{2(a + h)}$. From the variety of parameters available, we choose two values of the neck width: $d = 2a \sin 10° \approx 0.3473$ and $d = 2a \sin 20° \approx 0.6840$; two values
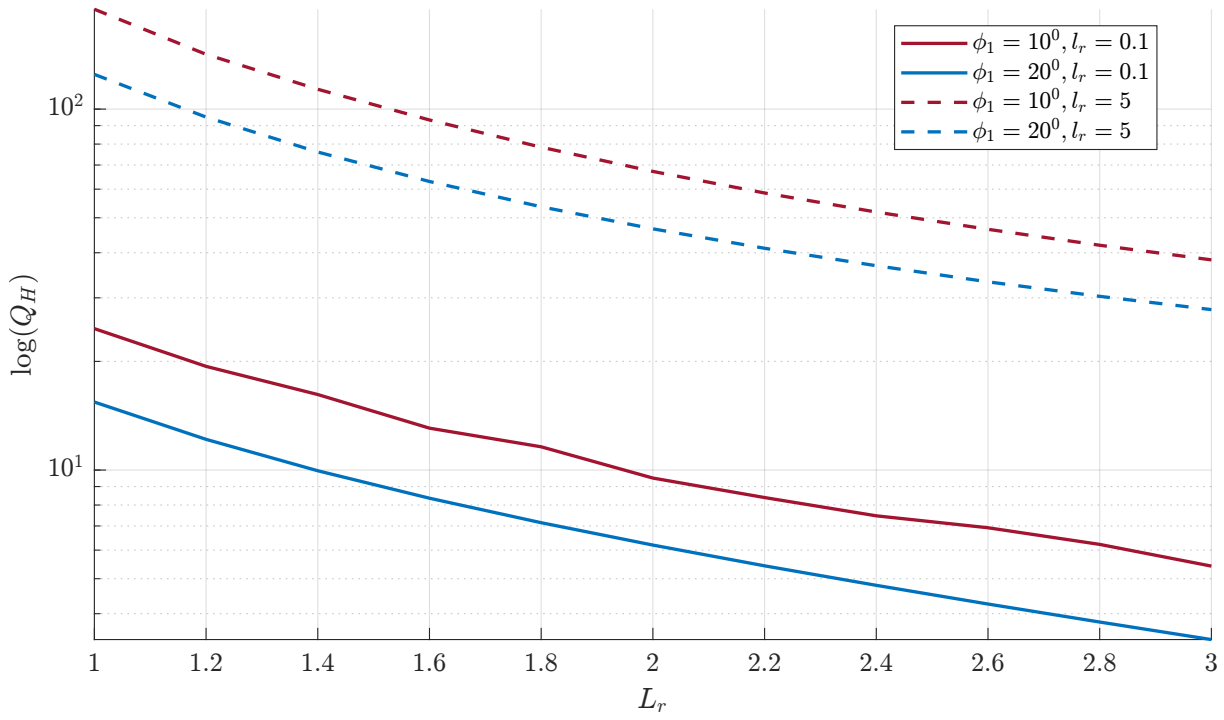
Figure 3.7: Quality factor of a paired cylindrical Helmholtz resonator with various neck width and length.

of neck length: $l_r = l/d = 0.1$ (Helmholtz resonator with minimal neck) and $l_r = 5$ ("long" neck); and the relative distance varies in the range $1 \le L_r \le 3$. The change of the quality factor $Q_H(L_r)$ against distance L_r at fixed parameters $\phi_1 = 10°, 20°$ and $l_r = 0.1, 5$ is shown in Figure 3.7.

Before analysing numerical results and the graphs, it is possible to predict the scale of acoustic (electromagnetic) coupling between two Helmholtz resonators for different sets of parameters. Close co-location of resonators ($L_r = 1 + \delta$, $\delta \ll 1$) should provide the maximum coupling. This is due to significant radiation through the slits into the free space. As can be seen in Figure 3.7 the closeness of their location is limited by the geometry. Strongest coupling is only possible when Helmholtz resonators are oriented in such a way that they form "slit-to-slit" configuration. As such a configuration is not implementable, each of Helmholtz resonators will practically operate independently. Thus, we may predict rather weak coupling between them.

We verify this expectation by two sets of accurate numerical calculations. First, in Figure 3.8, the modal field ($|H(x, y)|$) is presented for two extreme relative locations of the resonators. One location may be called "neighbouring" ($L_r = 1.1$); the other may be qualified as "distanced" ($L_r = 2.5$). In both cases we use also the parameters $\phi_1 = 15°, l_r = 0.1, 2.5$. The family of space distributions $|U^{tot}(x, y)|$ have been calculated for the forced oscillations induced by a normally

propagating sound plane wave ($\alpha = 0°$) in Figure 3.9, for the same set of parameters. It can be seen that in each case the Helmholtz mode is excited by the incident field.

(a) $l_r = 0.1, L_r = 1.1, ka = 0.422697$ (b) $l_r = 0.1, L_r = 2.5, ka = 0.391943$

(c) $l_r = 2.5, L_r = 1.1, ka = 0.268497$ (d) $l_r = 2.5, L_r = 2.5, ka = 0.261009$
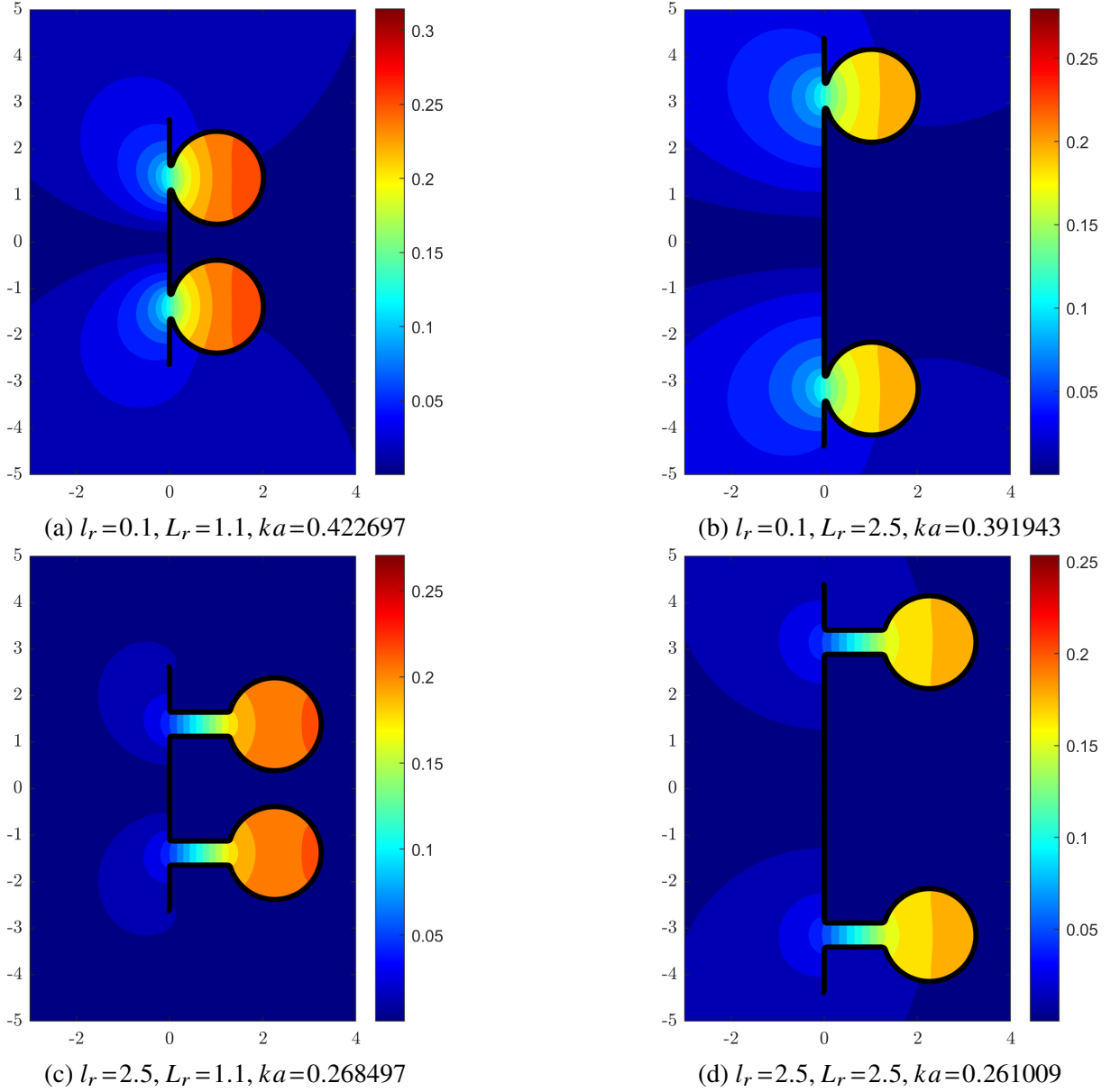
Figure 3.8: Modal field distribution for various parameters of paired Helmholtz resonators $(\phi_1 = 15°)$, $ka = \gamma'_H$.

Let us revisit Figure 3.7 and use the unloaded Q−factor as indicator of the effectiveness of the coupling of the paired Helmholtz resonators. Considering different values of the parameters (ϕ_1, l_r, L_r), it is possible to investigate the following: a) the effect of L_r by fixing (ϕ_1, l_r), b) the effect of l_r by fixing (ϕ_1, L_r), and c) the effect of ϕ_1 by fixing (L_r, l_r). The dependency of $Q_H(L_r)$ demonstrates the qualitatively predicted behaviour. At fixed L_r increase in neck length leads to increased coupling which is reflected in higher Q_H. At fixed l_r (or ϕ_1) increased

(a) $l_r = 0.1$, $L_r = 1.1$, $ka = 0.422697$

(b) $l_r = 0.1$, $L_r = 2.5$, $ka = 0.391943$

(c) $l_r = 2.5$, $L_r = 1.1$, $ka = 0.268497$

(d) $l_r = 2.5$, $L_r = 2.5$, $ka = 0.261009$
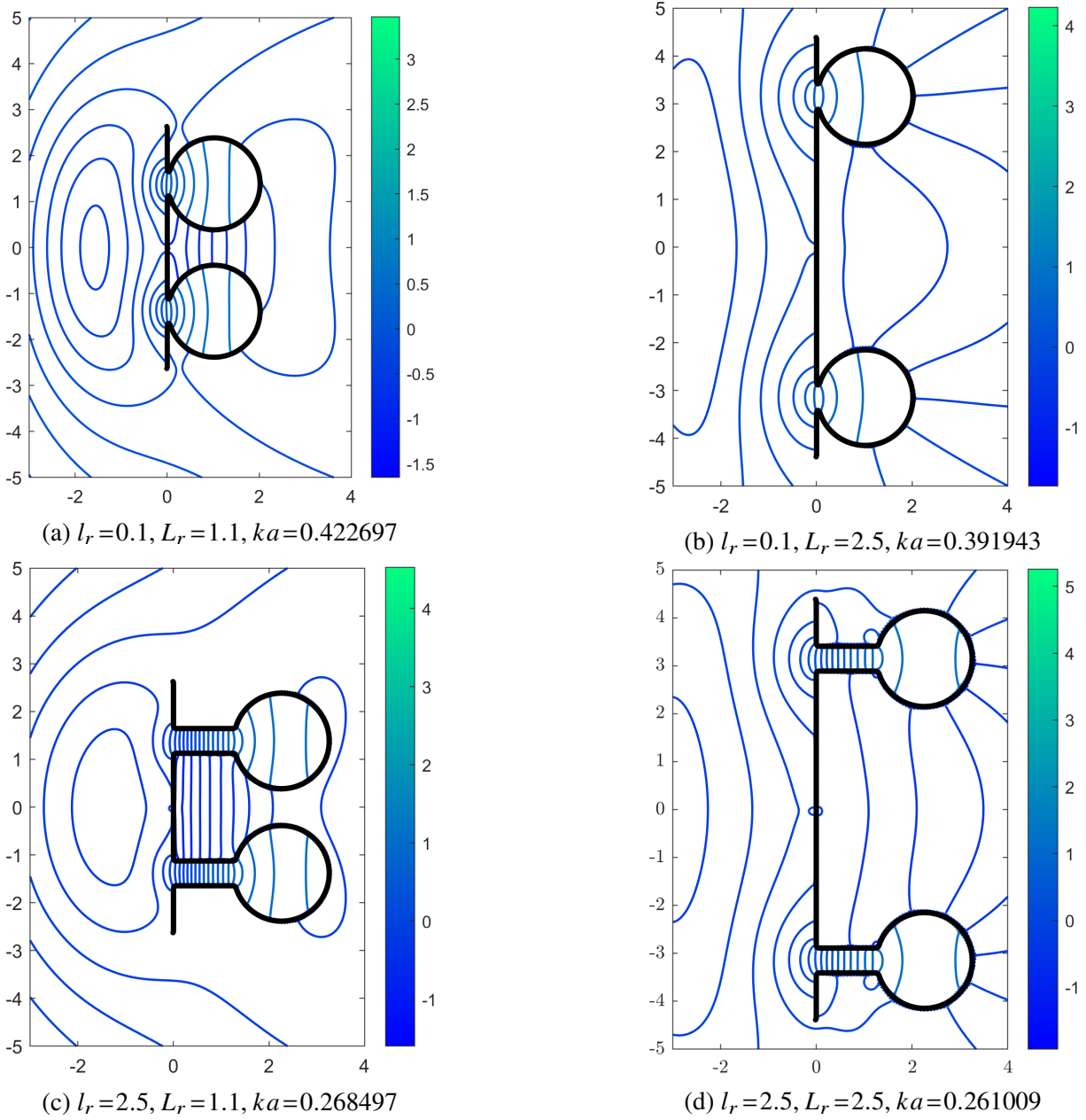
Figure 3.9: Distribution of $\left| U^{tot}(x, y) \right|$ in logarithmic scale in the vicinity of a paired circular Helmholtz resonator, $ka = \gamma'_H$, incident angle $\alpha = 0°$.

separation (L_r) of resonators weakens their coupling which leads to a decrease in the overall performance (lower Q_H).

3.4 Rectangular Helmholtz Resonators

One of the most promulgated shapes of Helmholtz resonators used in industry is a finite hollow rectangular cylinder with circular aperture cut in one of the lids and neck attached

to the aperture. Usually, the neck presents a pipe of circular cross section. Depending on the technical problem to be solved, variously shaped necks are designed ([96–98]). In this section, we restrict ourselves to the examination of 2D analogues of the axisymmetric Helmholtz resonators shown in Figure 3.10. This structure is an infinite slotted rectangular cylinder with sides a and b, cut by a slot of width w, with attached neck of length l and flanges of width f as indicated in Figure 3.10a. As before, we examine the minimal part of array, consisting of two Helmholtz resonators, with the cross section shown in Figure 3.10b. The following parameters are chosen for the analysis of the single resonator: $a/b = 0.5, 2$; $w/a = 0.1, 0.2, 0.5$; $l/w = 1, 2, 5$; $f/a = 0.75$. For the analysis of the paired resonators, the same parameters as for the single one are selected, with the addition of the distance parameter $L/a = 1, 2, 5$.

(a) Classical   (b) Array of resonators
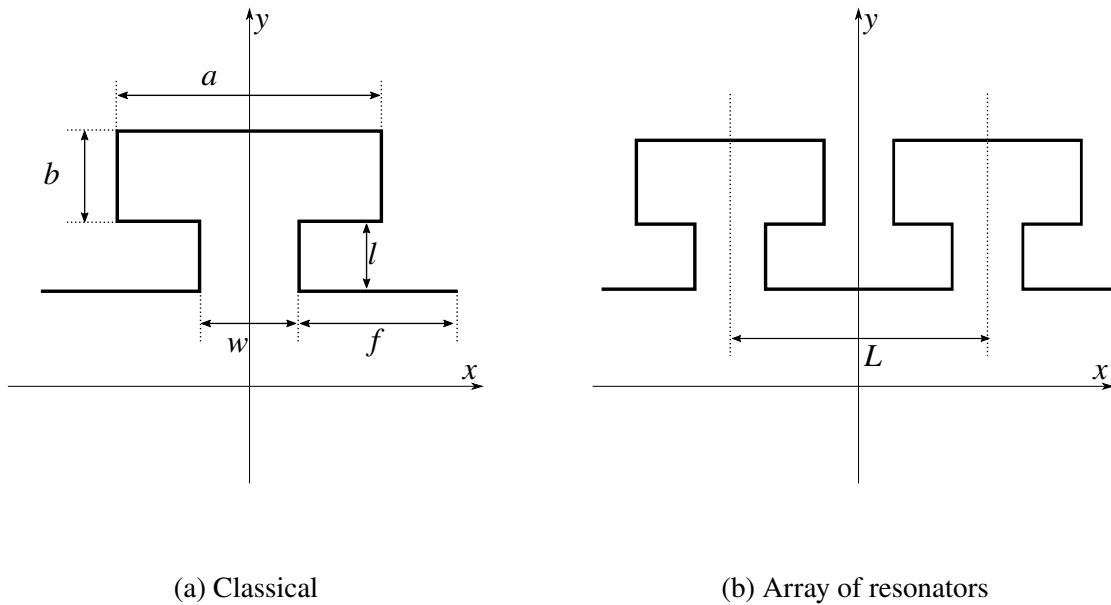
Figure 3.10: Rectangular Helmholtz resonator types

It should be noted that when operating in the low-frequency region, where the size of a structure is small compared to the wavelength λ, its precise form becomes immaterial since the incident field "does not sense" the finer details of a scatterer. For this reason, whether a Helmholtz resonator is shaped as a circular or rectangular cylinder, its performance, at least qualitatively, will be the same. Therefore we provide only a brief analysis along with the numerical results for selected rectangular Helmholtz resonators to complete this chapter. First, we demonstrate (quantitatively) the growth of the $Q-$factor as relative neck length increases: the dependence $Q_H (l_r)$ is shown in Figure 3.11b for resonators with two aspect ratios $a/b = 0.5, 2$ and three values of relative slit widths $w/a = 0.1, 0.2, 0.5$.

(a) $a/b = 2$ (b) $a/b = 0.5$
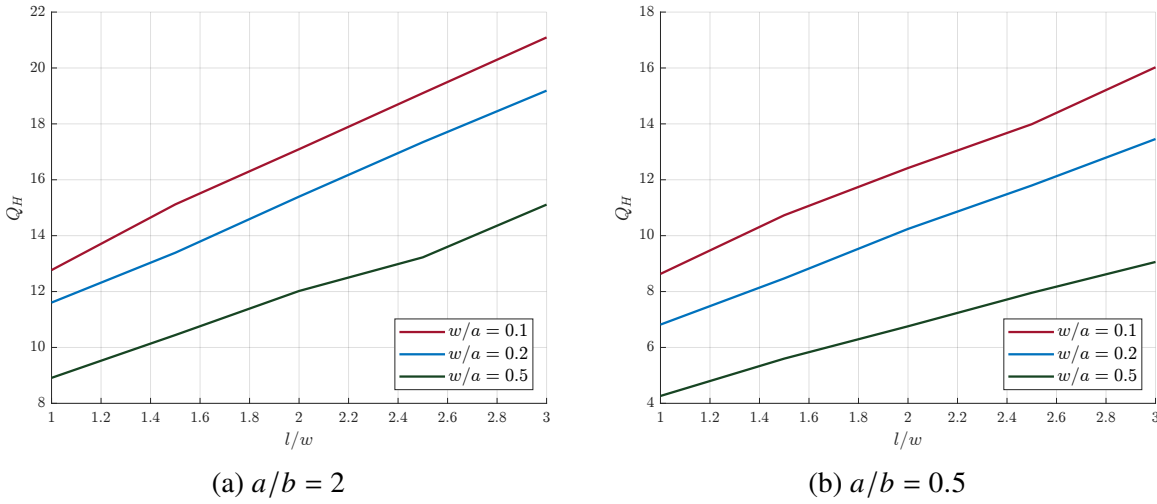
Figure 3.11: Quality factor Q_H for a single rectangular resonator against relative neck length l_r for various slot width.

Table 3.3: Q−factors for various w/a, l_r, and L_r ratios for coupled rectangular resonator of $a/b = 2$, $f/a = 0.75$.

w/a	L_r	$Q_h(l_r = 1)$	$Q_h(l_r = 2)$	w/a	L_r	$Q_h(l_r = 1)$	$Q_h(l_r = 2)$
0.1	1	13.79	23.34	0.2	1	10.92	18.64
0.1	2	10.35	12.26	0.2	2	10.24	12.01
0.1	3	6.30	12.05	0.2	3	5.18	10.68

Table 3.4: Q−factors for various w/a, l_r, and L_r ratios for coupled rectangular resonator of $a/b = 0.5$, $f/a = 0.75$.

w/a	L_r	$Q_h(l_r = 2)$	$Q_h(l_r = 3)$	w/a	L_r	$Q_h(l_r = 2)$	$Q_h(l_r = 3)$
0.2	1	50.79	64.99	0.5	1	33.92	48.36
0.2	2	16.08	21.41	0.5	2	15.08	21.56
0.2	3	6.40	7.69	0.5	3	6.31	8.42

Turning to a pair of rectangular resonators with varying parameters $a/b, w/a, l/w, L/a$, a tabulated view is preferred to demonstrate the relations between the parameters and the Q−factors; the results are collected in Tables 3.3 and 3.4. A similar behaviour to the circular paired resonators can be observed: for fixed ratios of a/b, the slit width w/a, and relative distance L_r, larger neck length magnifies the coupling which leads to an increase in the overall performance (higher Q_H). Also, as in the case of a circular pair, for fixed ratios of a/b, slit width w/a and neck length l_r, increased separation (L_r) of resonators weakens their coupling which leads to a decrease in the overall performance (lower Q_H).

Finally, we demonstrate the modal field ($|H(x, y)|$) in Figure 3.12 and the space distribution $|U^{tot}(x, y)|$ in Figure 3.13 for externally forced oscillations for two different separations of resonators. A comparison of the plots presented in these figures with their circular counterparts (see Figures 3.8 and 3.9) shows a high level of similarity, thus reinforcing the remarks made regarding the precise shape of the resonators.

(a) $l_r = 1, L_r = 0.5, ka = 0.434439$

(b) $l_r = 1, L_r = 1.2, ka = 0.411260$

(c) $l_r = 3, L_r = 0.5, ka = 0.318195$

(d) $l_r = 3, L_r = 1.2, ka = 0.310402$
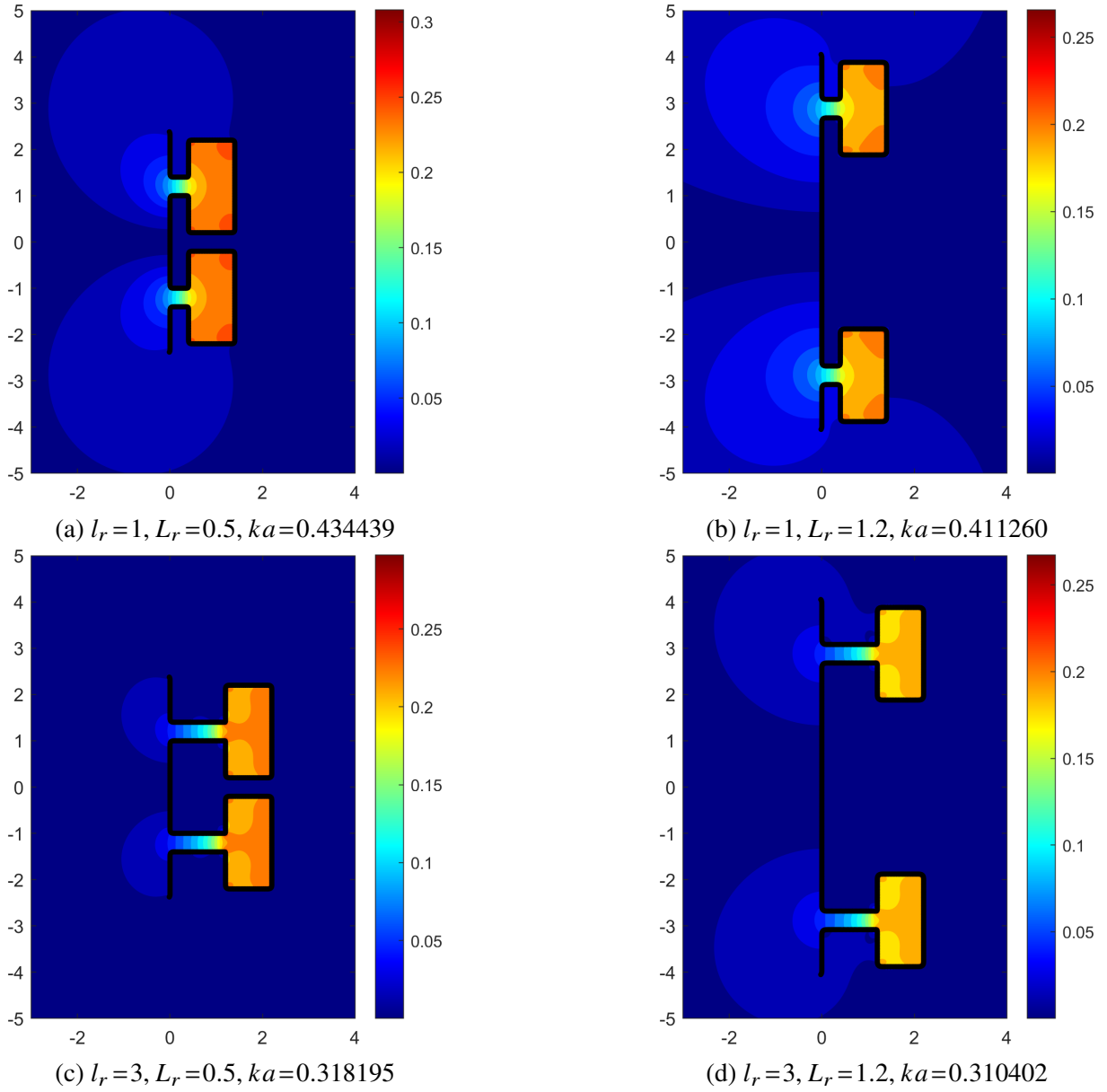
Figure 3.12: Modal field distribution for various parameters of paired rectangular Helmholtz resonators $(a/b = 2, f/a = 0.5, w/a = 0.2)$, $ka = \gamma'_H$.

(a) $l_r = 1, L_r = 0.5, ka = 0.434439$

(b) $l_r = 1, L_r = 1.2, ka = 0.411260$

(c) $l_r = 3, L_r = 0.5, ka = 0.318195$

(d) $l_r = 3, L_r = 1.2, ka = 0.310402$
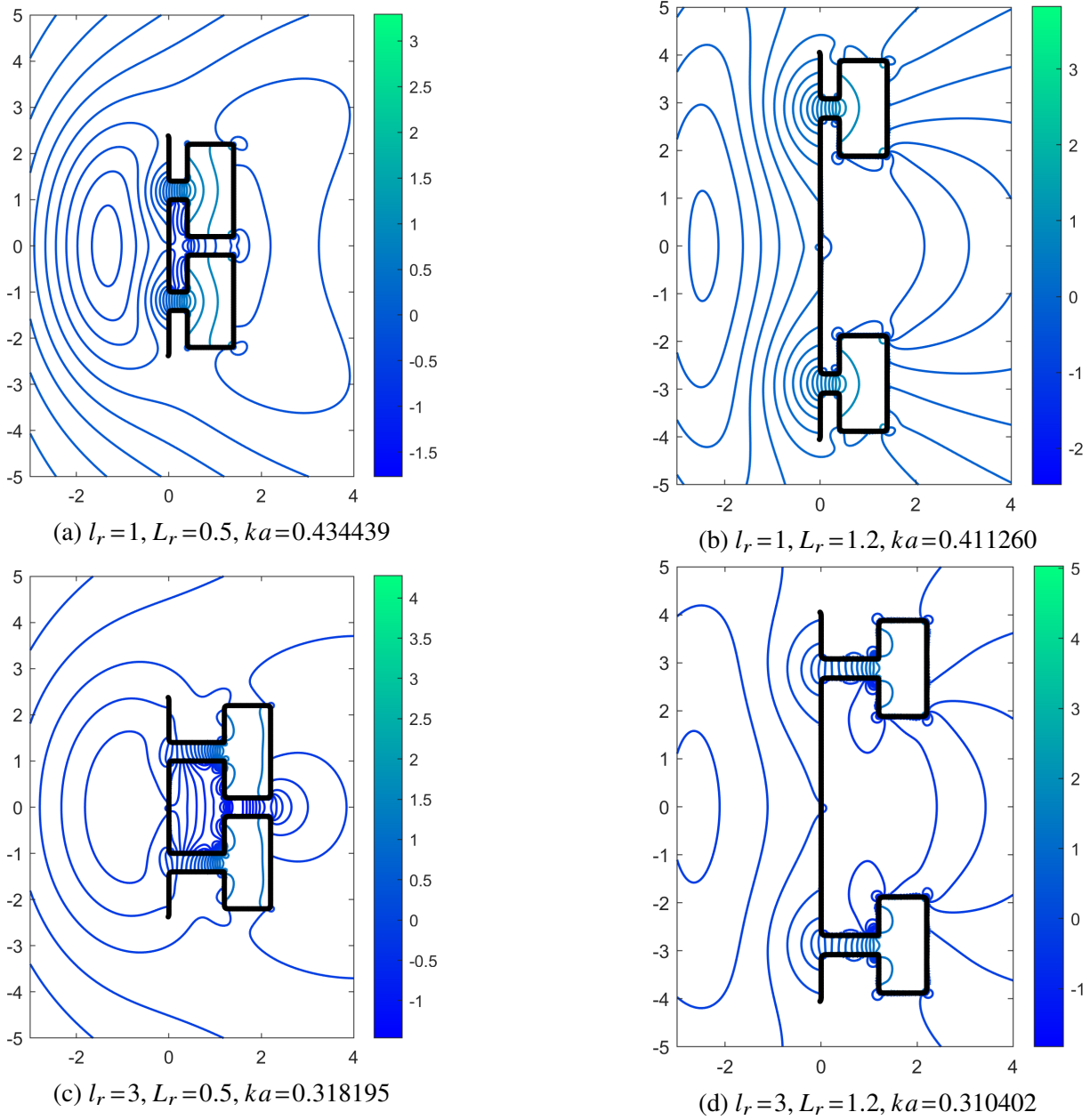
Figure 3.13: Distribution of $\left| U^{tot}(x, y) \right|$ in logarithmic scale in the vicinity of a paired rectangular Helmholtz resonators $(a/b = 2, f/a = 0.5, w/a = 0.2)$, $ka = \gamma'_H$, incident angle $\alpha = 0$.

4

Spectral Studies of Slotted Cavities

In this chapter, the generalised MAR is applied to find the spectrum of complex eigenvalues for a selection of 2D slotted cavities: circular, elliptic, and rectangular cylinders, and cylinders of arbitrary cross section (for example, corrugated cylinders). We present highly accurate (5-6 significant decimal places) extended tables of complex eigenvalues for circular and elliptic cylinders with variably placed slits.

In addition, we briefly consider slotted rectangular and polygonal (pentagon, heptagon, nonagon) cavities, computing the few first complex eigenvalues. Furthermore, taking advantage of the developed approach, we also conduct a preliminary examination of topologically more complex slotted cavities. They include sinusoidally corrugated circular cylinders and cavities used in design of magnetron resonators.

Finding the spectrum of acoustic complex oscillations in 2D open arbitrary cavities is of practical interest in diverse areas of acoustic- and electro-engineering. This stimulated development of purely numerical and semi-analytical techniques for extraction of the natural eigenvalues in closed cavities and the complex eigenvalues in open cavities. It should be noted that the values of "cavity resonances" and "cut-off frequencies" for 2D arbitrary cylinders are numerically identical. It simply means that any investigation of the spectrum of standing waves in 2D cavities is at the same time the investigation of cut-off wavenumbers (frequencies) for propagating modes in waveguides ([100]).

In many cases, electromagnetic waveguide theory may serve as a source to borrow solutions for acoustic problems and vice versa. This interdisciplinary link is based on the appearance of identical boundary value problems when formulating acoustic and electromagnetic scattering problems for obstacles in 2D space. This observation has been discussed in Introduction; nevertheless, since in this chapter we only address the acoustic problem, it is useful to recall this equivalence. The Dirichlet problem for the Helmholtz equation, posed for a 2D obstacle, simultaneously describes acoustic scattering by a sound-soft obstacle and electromagnetic scattering of E−polarised radiation by a PEC cylinder. The Neumann problem describes acoustic scattering by a sound-hard (rigid) obstacle or electromagnetic scattering of H−polarised radiation by the same obstacle with a PEC surface.

Theoretical approaches to solving the corresponding wave scattering problem by real closed or open cavities assume some idealisation. When posing the idealised boundary conditions at the surface of an obstacle, generally neither acoustic losses in the cavity walls nor defects of its manufacturing are considered. Similarly, in this thesis we consider idealised 2D open arbitrary cylindrical cavities with absolutely reflecting (sound-hard or rigid) walls: the actual walls of finite thickness are replaced by their mathematical (non-physical) model of infinitesimally thin surfaces. Without focusing on detail of the well-studied problem of acoustic waves penetration into solids, we simply state that the condition $\lambda \gg d$ (where d denotes thickness of the walls) justifies our assumption. The most idealised structure is a closed lossless cavity. Its eigenvalues of natural oscillations are real valued, leading to the infinite values of Q−factor. Using the idealised boundary conditions at the surface of a cavity with openings provides more realistic modelling of radiation loss emergence, caused by leakage of the acoustic energy to external space through the opening in the cavity. In this case, the total losses consist of losses in the walls and radiation losses. The balance of these two contributions is the decisive factor in arguments on the closeness of the mathematical model of wave scattering by a cavity with openings to its practical counterpart. In practice, radiation losses exceed the losses in the walls significantly, even for small openings.

The vast majority of publications (for example, see [101–103]) devoted to extraction of real and complex eigenvalues by various methods in both acoustics and electromagnetics provide 3-4 significant digits accuracy in their calculations; which is usually sufficient for practical needs. In many cases, it is challenging to make external estimates of the accuracy of these mainly purely numerical techniques due to the absence of benchmark studies. Additionally, these techniques

only work properly for extraction of the eigenvalues for lower frequency oscillations (since they are well separated). However, spectrum compression (which occurs at higher frequencies when neighbouring oscillations are separated by small frequency gap) prevents the use of numerical techniques due to their restricted frequency resolution.

Let us illustrate this assertion by an example for a closed elliptical cavity with sound-soft walls with extracted two natural oscillations S_{c21} and S_{s21} from the spectrum ([54]), when eccentricity $e = 0.1$. The corresponding eigenvalues $\gamma_{c21} = 5.148339$ and $\gamma_{s21} = 5.148569$ differ only in the fourth decimal place. It means that the accuracy of any applied method should be, at least, no less than 10^{-4}. We may conclude that there is a strong need for a universal, reliable algorithm which provides a tool for the calculation of real eigenvalues (closed cavities) and complex eigenvalues (cavities with openings) with the predetermined and proven accuracy.

4.1 Complex Eigenvalues of Slotted Circular Cylinder

Although there are number of publications ([104–107]) where MAR based solutions have been obtained for electromagnetic diffraction from slotted PEC cylinders, systematic investigation of the spectrum of the complex oscillations for these structures has not been conducted. It is well-known that, in closed sound-hard cylinders, the natural oscillations $\Psi_{mn}(\rho, \phi)$ are doubly degenerate except those oscillations $\Psi_{0n}(\rho, \phi)$. The indices m and n stand for the number of oscillations along coordinates ϕ and ρ, respectively, which can be approximated using following relation:

$$\Psi_{mn} \sim A_{mn} J'_m \left(\chi_{mn}^{(0)} \frac{\rho}{a} \right) \cdot \begin{cases} \cos(m\phi) \\ \sin(n\phi) \end{cases}, \tag{4.1}$$

where $m, n = 0, 1, 2...$ and $m^2 + n^2 \neq 0$, $\chi_{mn}^{(0)}$ are zeros of the derivative of the Bessel function of first kind and order m $\left(J'_m \left(\chi_{mn}^{(0)} \right) = 0 \right)$, representing the eigenvalues of natural oscillations Ψ_{mn}. The degeneracy is removed as soon as any surface or volume inhomogeneity is introduced. The longitudinal slit is of such nature and it leads to splitting of the eigenvalues $\chi_{mn}^{(0)}$ into two complex eigenvalues $\chi_{cmn} = Re\chi_{cmn} - i \cdot Im\chi_{cmn}$ and $\chi_{smn} = Re\chi_{smn} - i \cdot Im\chi_{smn}$, where the indices c (cosine) and s (sine) indicate symmetric or asymmetric oscillations, respectively. The lowest oscillation Ψ_{c00} is characterised by the complex eigenvalue χ_{c00}, originating from the "non-physical" value $\chi_{00}^{(0)} = 0$. This value becomes "physical" $(\chi_{00}^{(0)} \rightarrow \chi_{c00})$ for a slotted cylinder and characterises the low-frequency mode of the Helmholtz resonator, which has been

analysed extensively in Chapter 3.

We have calculated the first 21 complex eigenvalues $\chi_{c(s)mn}$ from the spectrum of the complex oscillations $\Psi_{c(s)mn}$ for a slotted circular cylinder. They are formed by the splitting of 9 of the first 12 oscillations and by 3 remaning oscillations $\Psi_{c00}, \Psi_{c01}, \Psi_{c02}$ which cannot be split since the phenomenon of degeneracy is absent for $m = 0$. Calculations were performed with 5-6 significant decimal places accuracy and a truncation size $N = 512$. The results are collected in the Table 4.1 and Table 4.2 and Figures 4.1 - 4.5. We also provide a magnified view of the complex oscillations $\Psi_{c(s)41}$ and $\Psi_{c(s)12}$ in Figure 4.4 due to their non-trivial coupling when the slit width ϕ_1 exceeds some threshold value ($\phi_1 \geq 4.5°$).

Table 4.1 contains complex oscillations for small relative slit widths $\dfrac{d}{a} \simeq 0.035, 0.087$ where d is slit semi-width, defined by $d = a \sin \phi_1$, with $\phi_1 = 2°, 5°$. Calculations for wider slits are presented in Table 4.2 for $\frac{d}{a} \simeq 0.174 \left(\phi_1 = 10° \right), 0.258 \left(\phi_1 = 15° \right), 0.5 \left(\phi_1 = 30° \right)$. It can be seen from both tables that non-symmetric complex oscillations Ψ_{smn} greatly dominate over symmetric oscillations Ψ_{cmn}, even when the longitudinal slit is small ($\phi_1 = 2°, 5°$). Overall, despite the small values of the imaginary parts $Im\chi_{smn} \sim 10^{-5} - 10^{-7}$, they significantly exceed those of the imaginary pats $Im\gamma_{smn}$ which can be attributed to complex oscillations S_{smn} arising in corresponding slotted sound-soft circular cylinders ([51]). For example, the values of $Im\chi_{smn}$ at $\phi_1 = 2°$ become comparable with the values $Im\gamma_{smn}$ only when the slit cut in the sound-soft circular cylinder is of angular size $\phi_1 = 10°$.

To explain the difference, it is pertinent to make use of the electromagnetic analogy of the discussed problem. Formally, the solution for a sound-soft cylinder is the same as for a perfectly electric conductor (PEC) cylinder supporting E-polarised (E_z, H_ρ, H_ϕ) oscillations, while the solution for a sound-hard cylinder coincides with that of a PEC cylinder supporting H-polarised (H_z, E_ρ, E_ϕ) oscillations. Since the surface current density $\vec{j}$ (defined by the formula $\vec{j} = \dfrac{c}{4\pi} \left[\vec{n} \times \vec{H} \right]$ where $\vec{n}$ is the outward normal unit vector ($\vec{n} \equiv \vec{e}_\rho$)) in the case of E−polarised oscillations has only the longitudinal component j_z ($\vec{j} = j_z \vec{e}_z$), the current is continuous and it flows parallel to the sharp edges of the slit, resulting in minimal radiation. In the case of H−polarisation, the only component of the surface current is transverse to the edges of the slit ($\vec{j} = j_\phi \vec{e}_\phi$); the current flow is interrupted at the slit edges which leads to significant radiation into exterior space and, hence, to enhancement of radiation losses.

Table 4.1: Complex oscillations $\Psi_{c(s)mn}$ of a slotted circular cylinder with a small slit.

$\Psi_{c(s)mn}$	$\phi_1 = 0°$	$\phi_1 = 2°$	$\phi_1 = 5°$
Ψ_{c00}	0	$0.332487 - i0.0157361$	$0.372456 - i0.0229525$
Ψ_{s11}	1.841183	$1.841417 - i0.0000002$	$1.842628 - i0.0000091$
Ψ_{c11}	1.841183	$1.944838 - i0.0197959$	$1.976698 - i0.0344412$
Ψ_{s21}	3.054236	$3.054929 - i0.0000017$	$3.058442 - i0.0000648$
Ψ_{c21}	3.054236	$3.141488 - i0.0198596$	$3.171731 - i0.0368628$
Ψ_{c01}	3.831705	$3.850878 - i0.0042552$	$3.857797 - i0.0078444$
Ψ_{s31}	4.201188	$4.202500 - i0.0000060$	$4.208997 - i0.0002133$
Ψ_{c31}	4.201188	$4.286133 - i0.0229348$	$4.319625 - i0.0464755$
Ψ_{s41}	5.317553	$5.319603 - i0.0000154$	$sup.$
Ψ_{c41}	5.317553	$5.326771 - i0.0001061$	$sup.$
Ψ_{s12}	5.331442	$5.331509 - i0.0000010$	$5.332988 - i0.0002152$
Ψ_{c12}	5.331442	$5.436038 - i0.0324721$	$5.319625 - i0.0684192$
Ψ_{s51}	6.415616	$6.418543 - i0.0000299$	$6.432228 - i0.0009514$
Ψ_{c51}	6.415616	$6.483909 - i0.0179212$	$6.508308 - i0.0323522$
Ψ_{s22}	6.706133	$6.706328 - i0.0000021$	$6.707324 - i0.0000768$
Ψ_{c22}	6.706133	$6.743357 - i0.0135434$	$6.764459 - i0.0336951$
Ψ_{c02}	7.015586	$7.030840 - i0.0053676$	$7.039694 - i0.0142906$
Ψ_{s61}	7.501266	$7.505157 - i0.0000534$	$7.522850 - i0.0016170$
Ψ_{c61}	7.501266	$7.575477 - i0.0241361$	$7.605953 - i0.0524352$
Ψ_{s32}	8.015236	$8.015620 - i0.0000059$	$8.017461 - i0.0001864$
Ψ_{s32}	8.015236	$8.045693 - i0.0104212$	$8.062563 - i0.0258332$

In acoustics, the velocity of sound flow at the surface of a sound-soft or sound-hard obstacle serves as an analogue of electromagnetic surface current. At the surface of a sound-hard slotted cylinder the normal component of the velocity $v_n \equiv v_\rho = -\dfrac{\partial U}{\partial \rho}$ is continuous, including the points on the slit and the screen. At the same time, the azimuthal component of the velocity $v_\phi = -\dfrac{\partial U}{\partial \phi}$, being perpendicular to the sharp edges of the slit, becomes discontinuous. In this case, the edges may be treated as a secondary source of acoustic radiation, which leads to

an increase in radiation losses. They are substantially higher than those which arise for a sound-soft slotted cylinder since the sound flow in the sound-soft case is provided by the non-zero normal component of sound velocity only.

Table 4.2: Complex oscillations $\Psi_{c(s)mn}$ of a slotted circular cylinder with a large slit.

$\Psi_{c(s)mn}$	$\phi_1 = 0°$	$\phi_1 = 10°$	$\phi_1 = 15°$	$\phi_1 = 30°$
Ψ_{c00}	0	$0.414270 - i0.0329788$	$0.446178 - i0.0426394$	$0.523018 - i0.0740877$
Ψ_{s11}	1.841183	$1.846809 - i0.0001360$	$1.853482 - i0.0006306$	$1.887305 - i0.0075861$
Ψ_{c11}	1.841183	$2.016813 - i0.0588688$	$2.053178 - i0.0862410$	$2.170014 - i0.1961900$
Ψ_{s21}	3.054236	$3.070059 - i0.0008905$	$3.087733 - i0.0038033$	$3.172912 - i0.0376045$
Ψ_{c21}	3.054236	$3.210826 - i0.0671188$	$3.246292 - i0.1017330$	$sup.$
Ψ_{c01}	3.831705	$3.868933 - i0.0148153$	$3.883423 - i0.0243156$	$3.976368 - i0.0794217$
Ψ_{s31}	4.201188	$4.229510 - i0.0026995$	$4.259327 - i0.0107286$	$4.396182 - i0.0916456$
Ψ_{c31}	4.201188	$4.363267 - i0.0937152$	$4.400263 - i0.1545040$	$sup.$
Ψ_{s51}	6.415616	$6.470959 - i0.0100675$	$6.520301 - i0.0330158$	$sup.$
Ψ_{c51}	6.415616	$6.533104 - i0.0477940$	$sup.$	$sup.$
Ψ_{s22}	6.706133	$6.711240 - i0.0011841$	$6.720196 - i0.0073419$	$sup.$
Ψ_{c22}	6.706133	$6.808787 - i0.0821690$	$6.892990 - i0.1102620$	$6.875355 - i0.2609700$
Ψ_{c02}	7.015586	$7.056628 - i0.0485843$	$sup.$	$sup.$
Ψ_{s61}	7.501266	$7.570811 - i0.0161372$	$7.629342 - i0.0520732$	$7.719149 - i0.1265100$
Ψ_{c61}	7.501266	$sup.$	$sup.$	$sup.$
Ψ_{s32}	8.015236	$8.023997 - i0.0022879$	$8.038230 - i0.0111522$	$sup.$
Ψ_{s32}	8.015236	$8.095068 - i0.0684827$	$8.135462 - i0.1266600$	$sup.$

For acoustic waveguides with narrow slits, the wave propagation and modal acoustic field distribution is expected to be similar to that in a closed waveguide. It can be seen that while that is true for asymmetric complex modes Ψ_{smn}, it is not the case for symmetric modes Ψ_{cmn}. In fact, the notations we use for complex oscillations Ψ_{smn} and Ψ_{cmn} borrowed from the natural oscillations of closed cylinder, are directly applicable only to asymmetric complex oscillations Ψ_{smn} when the slit width is relatively small. The symmetric oscillations Ψ_{cmn} are exposed to such significant distortions that notation Ψ_{cmn} simply characterise their provenance. This is especially clear for the complex modes Ψ_{cmn} with an even number of the radial oscillations $n = 2p$, $p = 1, 2, \ldots$, and a non-zero number of azimuthal oscillations $m \geq 1$. The oscillations

Ψ_{c12}, Ψ_{c22}, and Ψ_{c32} provide concrete examples as can be seen in Table 4.1.

To make the classification of oscillations unambiguous, we used an additional means: namely, the calculation of the resonance distribution of the velocity jump $\Delta U(\phi)$ at the surface of the cylinder. The slotted cylinder is excited by an obliquely propagating sound plane wave characterised by an incidence angle α. In the idealised problem statement, the sound pressure p is proportional to the velocity potential U ($p = -i\omega\rho_0 U$), where ω is angular frequency, ρ_0 is constant fluid density. We calculated the jump of the sound pressure at the surface of cylinder using the formula $|U(\rho, \phi)| = \frac{1}{\omega\rho_0} |\Delta p(a, \phi)|$ where $\Delta U(a, \phi) = U(a - 0, \phi) - U(a + 0, \phi)$ and $\Delta p(a, \phi) = p(a - 0, \phi) - p(a + 0, \phi)$.

As can be seen in Table 4.2, the introduction of a slit leads to a positive shift $\delta_{c(s)mn}$ in the values $Re\chi_{c(s)mn} = \chi_{c(s)mn}^{(0)} + \delta_{c(s)mn}$. Compared to the distance Δka between neighbouring eigenvalues $\chi_{c(s)mn}^{(0)}$ this value is relatively small, especially if they are well separated. As a result, verifying which complex eigenvalue belongs to which complex oscillation $\Psi_{c(s)mn}$ is a straightforward process as it is likely that the complex oscillation $\Psi_{c(s)mn}$ can be identified with an appropriate oscillation of the closed cylinder $\Psi_{c(s)mn}^{(0)}$.

Nevertheless, we verified the complex oscillations by calculating the function $|\Delta p(a, \phi)|$ at resonances, that is when $ka = Re\chi_{c(s)mn}$. The results are presented in Figure 4.1 for the 9 asymmetric complex oscillations Ψ_{smn} emerging in the slotted cylinder with angular semi-width $\phi_1 = 2°$ under excitation by a plane wave ($\alpha = 20°$). It should be noted that asymmetrical excitation occurs only when the incidence angle $\alpha \neq 0$. Furthermore, the interval for the optimal excitation is found to be $10° \leq \alpha \leq 45°$. Each distribution $|\Delta p(a, \phi)|$ displayed in Figure 4.1 shows the ideal shape and correct number of azimuthal variations characteristic of the corresponding complex oscillation Ψ_{smn}. In contrast, a high level of radiation losses for symmetric oscillations Ψ_{cmn} occurring even for geometrically small ($\phi_1 = 2°$) slits leads to pronounced distortion of the (un-perturbed) natural oscillations $\Psi_{cmn}^{(0)}$ which may emerge in the closed cylindrical cavity. The distortion can be clearly seen in Figure 4.2 for selected distributions of complex oscillations Ψ_{cmn}, which also leads to suppression of some modes as the slit width passes a corresponding threshold value; these are denoted as "sup." in the tables. In all cases the excitation is symmetrical ($\alpha = 0°$), since it is the optimal angle for emergence of high-amplitude symmetrical complex oscillations Ψ_{cmn}.

It is not surprising that the maxima of $|\Delta p(a, \phi)|$ in Figure 4.2 are of significantly lower level. The data for the complex eigenvalues χ_{cmn}, collected in Table 4.1 reveals high values of

Figure 4.1: Distribution of the jump of the velocity potential function $|\Delta p\,(a, \phi)|$ at the surface of a slotted cylinder for various complex eigenvalues Ψ_{smn} at resonant frequencies ($ka = Re\,\chi_{smn}$) against observation angle ϑ, incident angle $\alpha = 20°$.

the imaginary parts $Im\,(\chi_{cmn})$. This makes the unloaded quality factor $Q_{cmn} = -\dfrac{Re\,\chi_{cmn}}{2Im\,(\chi_{cmn})}$ for symmetric oscillations Ψ_{cmn} relatively small. For four of the six presented distributions $|\Delta p\,(a, \phi)|$ one can find the correct number of azimuthal variations (see plots for Ψ_{c00}, Ψ_{c11}, Ψ_{c51} and Ψ_{c61}), though the overall shape of distributions $|\Delta p\,(a, \phi)|$ is far from ideal. For distributions related to complex oscillations Ψ_{c01} and Ψ_{c02}, neither the number of variations m nor shape of distribution matches the canonical shape of the natural oscillations $\Psi_{c01}^{(0)}$ and $\Psi_{c02}^{(0)}$ in the closed cylindrical cavity.

Next, let us turn to our attention to emergence of the complex oscillations Ψ_{c41}, Ψ_{s41}, Ψ_{c12} and Ψ_{s12}. This is a non-trivial region as the values $\chi_{c(s)41}^{(0)} = 5.317553$ and $\chi_{c(s)12}^{(0)} = 5.331442$ lie in very close proximity to each other. The introduction of a slit is expected to lead to
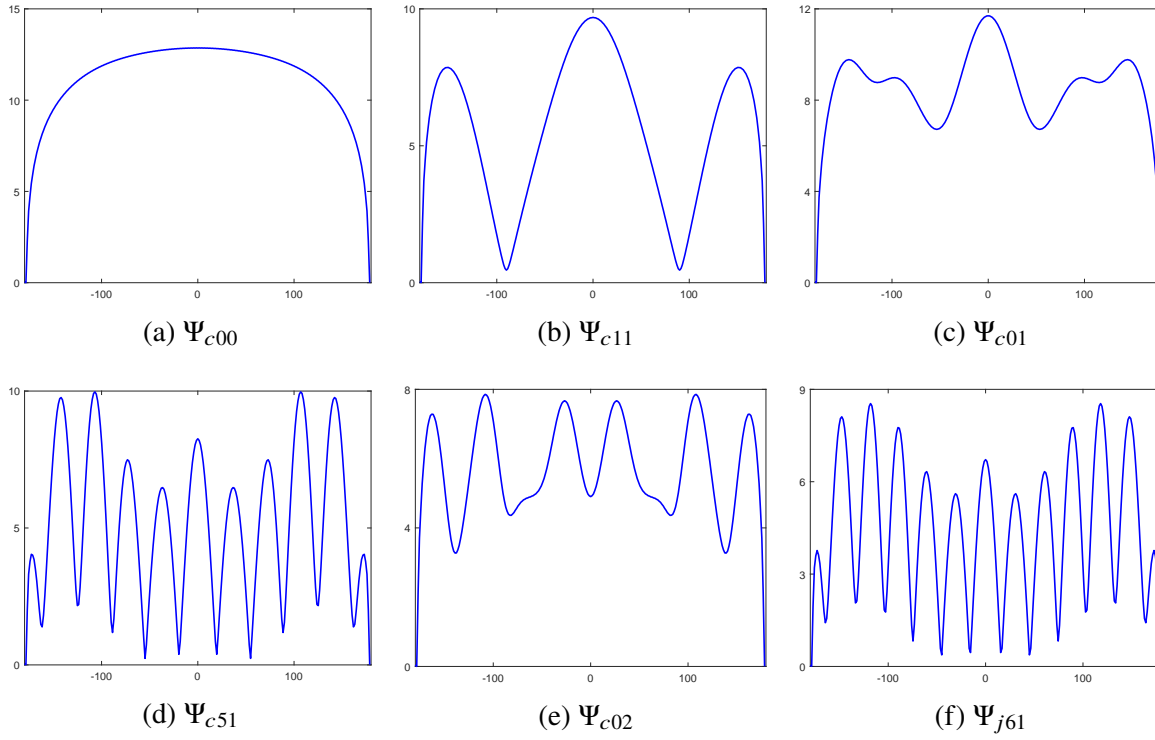
Figure 4.2: Distribution of the jump of the velocity potential function $|\Delta p\,(a,\phi)|$ at the surface of a slotted cylinder for various complex eigenvalues Ψ_{cmn} at resonant frequencies ($ka = Re\chi_{smn}$) against observation angle ϑ, incident angle $\alpha = 0°$.

the emergence of four complex oscillations. The preliminary calculation of the frequency dependence of the condition number $\kappa\,(A_N\,(ka))$ inside the interval $0.001° \leq \phi_1 \leq 20°$ reveals the general pattern of the complex mode competition. Considering these preliminary data, it was found that the most clear picture of the investigated phenomenon is given by the dependencies $Re\chi_{c(s)mn}\,(\phi_1)$, where $m = 4, n = 1$ and $m = 1, n = 2$, and the angular semi-width of slit varies from $\phi_1 = 0.1°$ to $\phi_1 = 20°$. The graphs $|\Delta p\,(a,\phi)|$ for $\phi_1 = 0.1°$ are shown in Figure 4.3. Two distributions $|\Delta p\,(a,\phi)|$ undoubtedly belong to the asymmetric complex oscillations Ψ_{s41} and Ψ_{s12}. The other two are of symmetric oscillations and may be identified with a highly distorted complex oscillation Ψ_{c41}. To distinguish them, we introduce the notation $\Psi_{c41}^{(+)}$ for the "strong" oscillation ($\chi_{c41}^{(+)} = 5.326357 - i0.000114316$) and $\Psi_{c41}^{(-)}$ for the "weak" oscillation ($\chi_{c41}^{(-)} = 5.378501 - i0.0074323$). As a result of the mode competition by the counterpart of Ψ_{s12}, the complex oscillation Ψ_{c12} does not emerge at all, even when the angular semi-width ϕ_1 is as low as $\phi_1 = 0.001°$. It is useful to compare the real parts of the complex eigenvalues $\chi_{s41} = 5.317558 - i9.7 \cdot 10^{-11}$ and $\chi_{s12} = 5.331442 - i2.7 \cdot 10^{-12}$. The process of transformation of the complex oscillations $\Psi_{s41}, \Psi_{c41}^{(+)}, \Psi_{s12}$ for increasing angular semi-width ϕ_1 is demonstrated in Figure 4.4. Being separated from the real parts of the complex

(a) Ψ_{s41}

(b) Ψ_{c41}^{+}

(c) Ψ_{s12}

(d) Ψ_{c41}^{-}

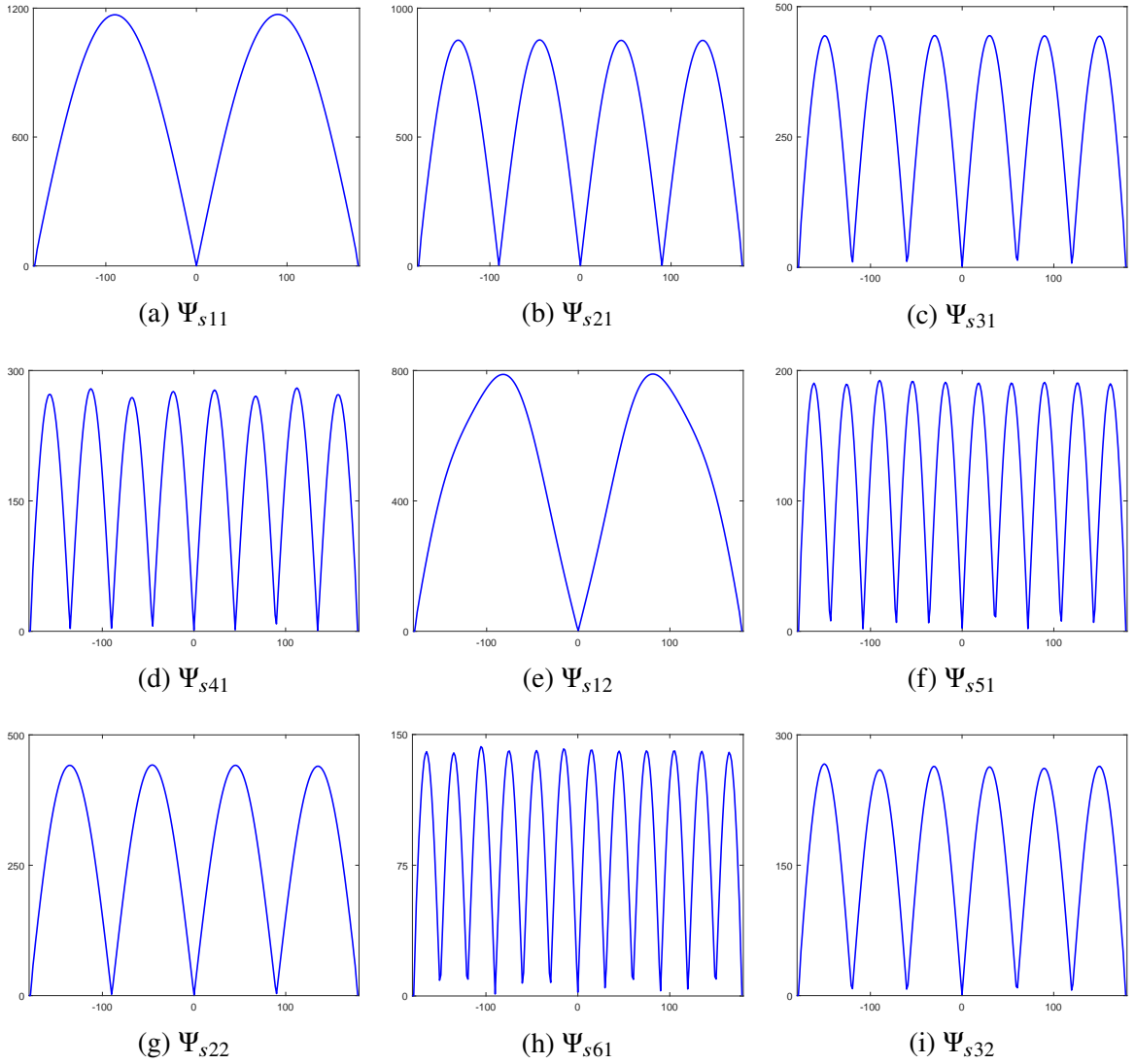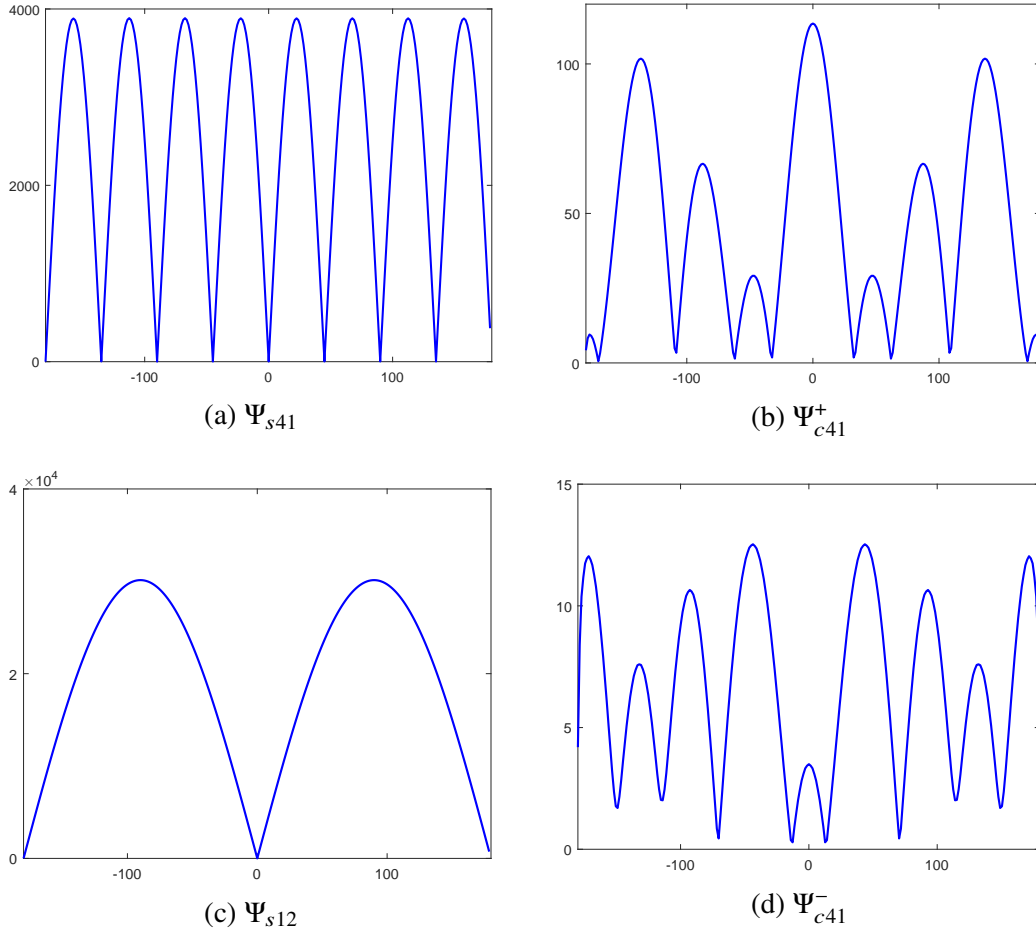Figure 4.3: Distribution of the jump of the velocity potential function $|\Delta p(a, \phi)|$ at the surface of a slotted cylinder with narrow longitudinal slit ($\phi_1 = 0.1°$) for complex oscillations $\Psi_{s41}, \Psi_{c41}^{(+)}, \Psi_{s12}, \Psi_{c41}^{(-)}$.

eigenvalues χ_{s41}, χ_{s12}, and $\chi_{c41}^{(+)}$, the oscillation $\Psi_{c41}^{(-)}$ does not pass through the process of merging oscillations, and hence, the curve $Re\chi_{c41}^{(-)}(\phi_1)$ is absent in Figure 4.4. Another reason for the absence of the curve $Re\chi_{c41}^{(-)}(\phi_1)$ is that it possesses a much higher Q−factor. Let us illustrate this assertion by a few numerical results: a) $\phi_1 = 1°, \chi_{c41}^{(-)} = 5.414574 - i0.0209421$ $\left(Q_{c41}^{(-)} = 129.2749\right)$; b) $\phi_1 = 5°, \chi_{c41}^{(-)} = 5.483889 - i0.0684186 \left(Q_{c41}^{(-)} = 40.0760\right)$; and c) $\phi_1 = 10°, \chi_{c41}^{(-)} = 5.552421 - i0.1459716 \left(Q_{c41}^{(-)} = 19.0188\right)$. The mutual interchange of oscillations Ψ_{s41} and Ψ_{s12}, when the dependencies $\chi_{s41}(\phi_1)$ and $\chi_{s12}(\phi_1)$ approach each other in the interval $4° < \phi_1 < 6°$ whilst the dependence $\chi_{c41}^{(+)}$ reveals an independent behaviour within the entire range $0.1° < \phi_1 \leq 20°$, can be seen in Figure 4.4.

The oscillation $\Psi_{c41}^{(+)}$ becomes coupled with the oscillation Ψ_{s12} at two crossing points: $\phi_1 = 4.4883°$ and $\phi_1 = 15.8684°$. The calculated complex eigenvalues $\chi_H^{(1)}$ and $\chi_H^{(2)}$ describing the emerging complex hybrid oscillations, are equal to $\chi_H^{(1)} = 5.326808 - i0.000104593$ ($\phi_1 = 4.4883°$) and $\chi_H^{(2)} = 5.330893 - i0.0000258039$ ($\phi_1 = 15.8684°$). The first hybrid oscillation
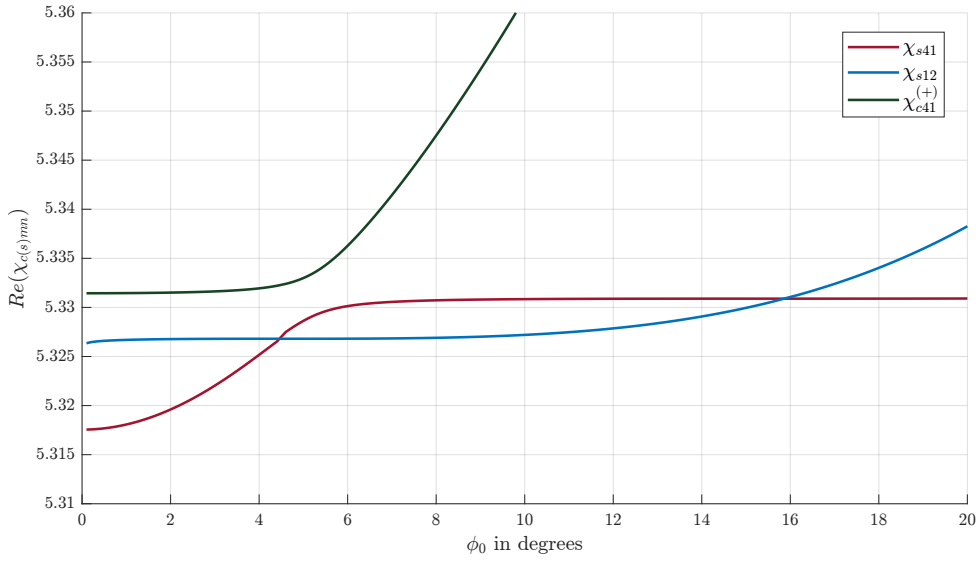
Figure 4.4: Evolution of complex eigenvalues χ_{s41}, χ_{s12} and $\chi_{c41}^{(+)}$ relative to the slit width.

(a) $ka = 5.326808$, $\phi_1 = 4.4883°$

(b) $ka = 5.330893$, $\phi_1 = 15.8684°$
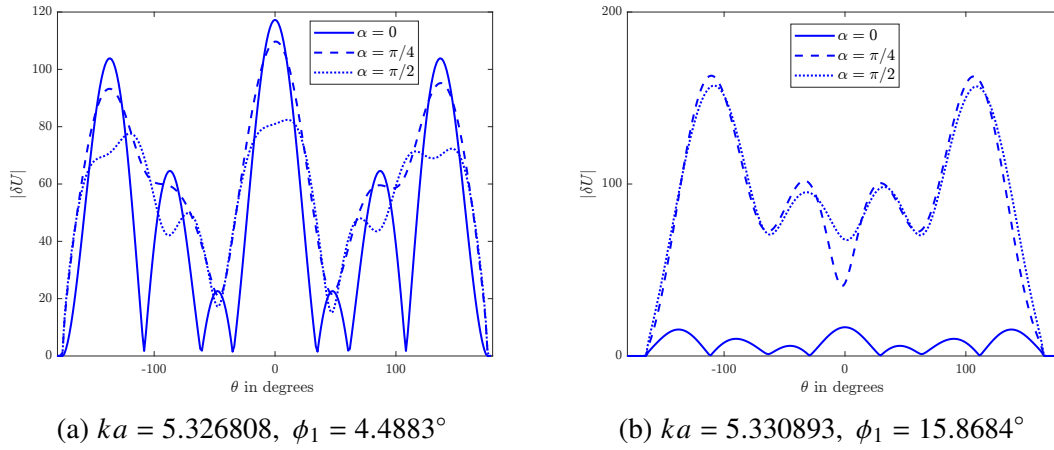
Figure 4.5: Patterns of the velocity jump function $|\Delta p (a, \phi)|$ for hybrid oscillations $\Psi_H^{(1)}$.

is of symmetrical type: at the incidence angle $\alpha = 0°$ the function $|\Delta p (a, \phi)|$ has the shape of the distorted oscillation $\Psi_{c41}^{(+)}$ (with 3 variations instead of 4). Surprisingly, at the incidence angles $\alpha > 0°$ ($\alpha = 45°, 90°$) we may observe the "revival" of the totally suppressed oscillation Ψ_{c12}, albeit slightly distorted. It should be observed that the excitation effectiveness of this so-called "Janus oscillation" is comparable with that at $\alpha = 0°$ (tentatively, $\Psi_{c41}^{(+)}$) and within the interval $10° \leq \alpha < 45°$ (tentatively, Ψ_{c12}). The shape of the function $|\Delta p (a, \phi)|$ for the second hybrid oscillation developing at $ka = Re\chi_H^{(2)} = 5.330893(\phi_1 = 15.8684°)$ also depends on excitation angle α. When $\alpha = 0°$, the shape $|\Delta p (a, \phi)|$ matches that of the distorted oscillation $\Psi_{c41}^{(+)}$. When α lies in the interval $0° < \alpha \leq 90°$, the shape $|\Delta p (a, \phi)|$ may be described as a result of coupling of the oscillations Ψ_{s12} and Ψ_{c12} (distorted oscillation Ψ_{s12} or distorted oscillation Ψ_{c12}). Irrespective of the interpretation of the shape of this oscillation, it is

rather tentative since the semi-width of the slit is too wide to maintain the same shape as that for the cylinder with a narrow slit, for example, $\phi_1 = 0.1°$ (see Figure 4.3, oscillation Ψ_{s12}).

4.2   Complex Oscillations of Sound-hard Elliptic Cylinder with Variably Placed Slit

Complex oscillations in an elliptic sound-soft cylinders with longitudinal slit have been studied in [54]. We complete the analysis for sound-hard cylinder, which is possibly more valuable for acoustic problems. A closed sound-hard cylinder, treated as an acoustic waveguide, possesses the fundamental (lowest) mode $\Psi_{c11}^{(0)}$, the eigenvalue $\chi_{c11}^{(0)}$ of which depends on eccentricity e. For example, $\chi_{c11}^{(0)} = 1.84155996 \, (e = 0.1)$, $\chi_{c11}^{(0)} = 1.85100194 \,\, (e = 0.5)$. As before,
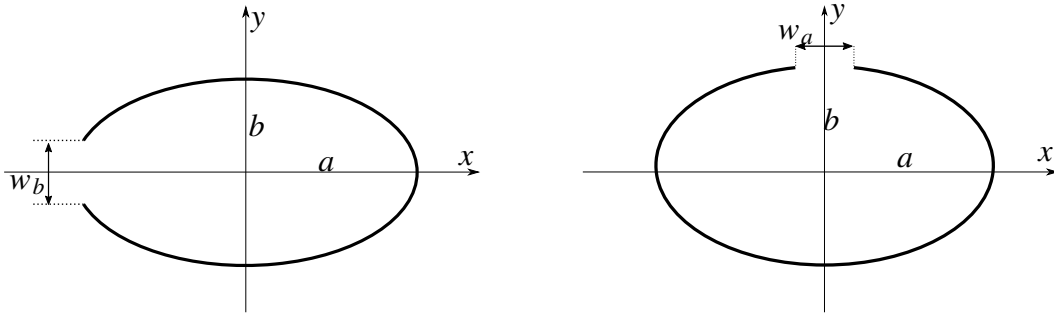
(a) Vertical slit of relative width w_b (b) Horizontal slit of relative width w_a

Figure 4.6: Slotted elliptic cylinders.

we use the dimensionless slit width ratios: $\dfrac{w_b}{2b}$ and $\dfrac{w_a}{2a}$ for vertical and horizontal slit location, respectively, as shown in Figure 4.6, where b and a stand for minor and major semi-axes of the ellipse. For the calculation of the complex eigenvalues $\chi_{c(s)mn}$ we use three values of eccentricity $e = \sqrt{1 - q^2} \, (q = \frac{b}{a})$: $e = 0.1 \, (q \simeq 0.995)$, $e = 0.5 \, (q \simeq 0.886)$, $e = 0.9 \, (q \simeq 0.436)$, and three values of slit width $w_b, w_a = 0.05, 0.1, 0.2$. The eigenvalues $\chi_{c(s)mn}^{(0)}$ of a closed sound-hard elliptic cylinder have been calculated in [108] by the direct calculation of the roots of the radial Mathieu function's derivative with an accuracy of 8 significant decimal places. Using the MAR based solution, with large truncation system sizes $N = 4096$ we verified these results and found excellent agreement: see Table 4.3, containing the first 8 eigenvalues (the expanded list of eigenvalues may be found in [108]).

Table 4.3: Eigenvalues $\chi^{(0)}_{c(s)mn}$ of natural oscillations $\Psi^{(0)}_{c(s)mn}$.

$\Psi^{(0)}_{c(s)mn}$	$e = 0.1$	$\Psi^{(0)}_{c(s)mn}$	$e = 0.5$	$\Psi^{(0)}_{c(s)mn}$	$e = 0.9$
$\Psi^{(0)}_{c11}$	1.84155996	$\Psi^{(0)}_{c11}$	1.85100194	$\Psi^{(0)}_{c11}$	1.87658638
$\Psi^{(0)}_{s11}$	1.85007877	$\Psi^{(0)}_{s11}$	2.11236405	$\Psi^{(0)}_{c21}$	3.43585287
$\Psi^{(0)}_{c21}$	3.06184719	$\Psi^{(0)}_{c21}$	3.22266147	$\Psi^{(0)}_{s11}$	4.01493082
$\Psi^{(0)}_{s21}$	3.06193336	$\Psi^{(0)}_{s21}$	3.29315820	$\Psi^{(0)}_{c31}$	4.96528375
$\Psi^{(0)}_{c01}$	3.84143455	$\Psi^{(0)}_{c01}$	4.19049573	$\Psi^{(0)}_{s21}$	5.11153824
$\Psi^{(0)}_{c31}$	4.21172636	$\Psi^{(0)}_{c31}$	4.47916938	$\Psi^{(0)}_{s31}$	6.29196435
$\Psi^{(0)}_{s31}$	4.21172701	$\Psi^{(0)}_{s31}$	4.49470665	$\Psi^{(0)}_{c41}$	6.47912399
$\Psi^{(0)}_{c41}$	5.33089546	$\Psi^{(0)}_{c41}$	5.68162430	$\Psi^{(0)}_{s41}$	7.53400165

Table 4.4: Complex eigenvalues $\chi_{c(s)mn}$ (Elliptic cylinder: $e = 0.1$; vertical slits).

$\Psi_{c(s)mn}$	$w_b = 0.05$	$w_b = 0.1$	$w_b = 0.2$
Ψ_{c00}	$0.347333 - i0.0180628$	$0.380538 - i0.02451743$	$0.425526 - i0.0359268$
Ψ_{s11}	$1.850554 - i0.0000010$	$1.851961 - i0.00001562$	$1.857446 - i0.0002332$
Ψ_{c11}	$1.956127 - i0.0242096$	$1.983919 - i0.03794990$	$2.028913 - i0.0668496$
Ψ_{s21}	$3.063338 - i0.0000072$	$3.067399 - i0.00010935$	$3.082486 - i0.0014850$
Ψ_{c21}	$3.159994 - i0.0250437$	$3.186833 - i0.04144180$	$3.231214 - i0.0779270$
Ψ_{c01}	$3.862053 - i0.0051049$	$3.868126 - i0.00845494$	$3.881192 - i0.0168233$
Ψ_{s31}	$4.214379 - i0.0000248$	$4.221843 - i0.00035614$	$4.248236 - i0.0044077$
Ψ_{c31}	$4.308090 - i0.0296133$	$4.337871 - i0.05277462$	$4.386733 - i0.1107514$

It should be noted that the data in Table 4.3 is presented in increasing order of $\chi^{(0)}_{c(s)mn}$ in each column. In a case of small eccentricity $e = 0.1$ ($q \simeq 0.995$), an elliptic cylinder may be treated as a slightly deformed circular cylinder. In general, this deformation should lead to disappearance of degeneracy, and result in the splitting of the eigenvalues. But some oscillations keep the degeneracy if the deformation is not sufficient. This phenomenon is observed, when $e = 0.1$ ($q \simeq 0.995$), for two pairs of degenerate oscillations: $\left(\Psi^{(0)}_{c41}, \Psi^{(0)}_{s41} \right)$ and $\left(\Psi^{(0)}_{c51}, \Psi^{(0)}_{s51} \right)$ for which $\chi^{(0)}_{c41} = \chi^{(0)}_{s41} = 5.33089546$ and $\chi^{(0)}_{c51} = \chi^{(0)}_{s51} = 6.43171653$, respectively. It is important to mention that this assertion is based on our calculation of the eigenvalues $\chi^{(0)}_{c(s)mn}$ with accuracy of 8 significant decimal places. In contrast, introduction of an exceedingly small slit immediately removes degeneracy. For example, the vertical slit with the relative width $w_b = 0.001$ splits oscillations Ψ_{c41} and Ψ_{s41}: $\chi_{s41} = 5.330897 - i1.05 \cdot 10^{-11}$ and $\chi_{c41} = 5.335432 - i2.5776 \cdot 10^{-5}$.

Let us explain why we opt for tabulated results instead of more compact graphical forms such as shown in Figure 4.4. The first reason is the loss of accuracy in presentation since the high accuracy of computations (8 significant digits) is masked by low graphical accuracy of 1%. The second reason is convenience in using the accurate tabulated results in practice and, in addition, to have accurate *benchmark* data for comparison with those obtained by other methods.

Table 4.5: Complex eigenvalues $\chi_{c(s)mn}$ (Elliptic cylinder: $e = 0.5$; vertical slits).

$\Psi_{c(s)mn}$	$\chi^0_{c(s)mn}$	$w_b = 0.1$	$w_b = 0.2$
Ψ_{c00}	0	$0.401569 - i0.0246131$	$0.447637 - i0.0354677$
Ψ_{s11}	1.85100194	$2.003705 - i0.0377619$	$2.050495 - i0.0652908$
Ψ_{c11}	2.11236405	$2.113873 - i0.0000128$	$2.118307 - i0.0001921$
Ψ_{s21}	3.22266147	$3.297815 - i0.0000850$	$3.310883 - i0.0011755$
Ψ_{c21}	3.29315820	$3.373973 - i0.0479814$	$3.428919 - i0.0903767$
Ψ_{c01}	4.19049573	$4.197202 - i0.0017604$	$4.200457 - i0.0033164$
Ψ_{s31}	4.47916938	$4.503750 - i0.0002845$	$4.527914 - i0.0036150$
Ψ_{c31}	4.49470665	$4.627725 - i0.0566036$	$4.686973 - i0.1146210$

Table 4.6: Complex eigenvalues $\chi_{c(s)mn}$ (Elliptic cylinder: $e = 0.9$; vertical slits).

$\Psi_{c(s)mn}$	$\chi^0_{c(s)mn}$	$w_b = 0.1$	$w_b = 0.2$
Ψ_{c00}	0	$0.504926 - i0.0230244$	$0.550138 - i0.0301307$
Ψ_{c11}	1.87658638	$2.098288 - i0.0334506$	$2.152062 - i0.0510938$
Ψ_{c21}	3.43585287	$3.641781 - i0.0421754$	$3.704696 - i0.0699540$
Ψ_{s11}	4.01493082	$4.015090 - i0.0000017$	$4.015601 - i0.0000267$
Ψ_{s21}	4.96528375	$5.112319 - i0.0000119$	$5.114754 - i0.0001793$
Ψ_{c31}	5.11153824	$5.169117 - i0.0505311$	$5.241350 - i0.0891116$
Ψ_{s31}	6.29196435	$6.294052 - i0.0000437$	$6.300383 - i0.0006243$
Ψ_{c41}	6.47912399	$6.685584 - i0.0590294$	$6.767492 - i0.1094960$

Tables 4.4 – 4.7 contain the complex eigenvalues $\chi_{c(s)mn}$ for various slotted elliptic cylinders created by a selection of the parameters: three values of eccentricity $e = 0.1$ ($q \simeq 0.995$), $e = 0.5$ ($q \simeq 0.886$), $e = 0.9$ ($q \simeq 0.436$), three values of relative slit width $w_b = 0.05, 0.1, 0.2$, and two types of slits: vertical and horizontal. This way we cover a range of options in eccentricity, slit size, and orientation. We conclude that the tendency of suppression of the complex

Table 4.7: Complex eigenvalues $\chi_{c(s)mn}$ (Elliptic cylinder: $e = 0.5$; horizontal slits).

$\Psi_{c(s)mn}$	$\chi^0_{c(s)mn}$	$w_a = 0.1$	$w_a = 0.2$
Ψ_{c00}	0	$0.405314 - i0.0261481$	$0.452213 - i0.0382128$
Ψ_{c11}	1.85100194	$1.852968 - i1.204 \cdot 10^{-5}$	$1.858692 - i1.8196 \cdot 10^{-4}$
Ψ_{s11}	2.11236405	$2.257540 - i0.0390177$	$2.301937 - i0.0677287$
Ψ_{c21}	3.22266147	$sup.$	$sup.$
Ψ_{s21}	3.29315820	$3.298616 - i9.338 \cdot 10^{-5}$	$3.313633 - i1.2788 \cdot 10^{-3}$
Ψ_{c01}	4.19049573	$4.244796 - i0.0142567$	$4.266110 - i0.0236603$
Ψ_{c31}	4.47916938	$4.488283 - i2.720 \cdot 10^{-4}$	$4.511992 - i3.4213 \cdot 10^{-3}$
Ψ_{s31}	4.49470665	$4.619391 - i0.0556689$	$4.667695 - i0.119558$

symmetric oscillations Ψ_{cmn} observed for the slotted circular cylinder is also observed for the elliptic cylinder with a longitudinal slit. Moreover, vertical or horizontal placement of the slit does not change the phenomenon.

4.3 Slotted Rectangular and Polygonal Cylinders

Since the MAR-based approach for calculation of complex eigenvalues is explained in detail in earlier sections, we focus here on numerical results and only highlight important points and distinctive aspects in this section. First, we consider a rectangular cavity with aspect ratio $a/b = 2$ and a longitudinal slit symmetrically placed in the wider wall of the waveguide (see Figure 4.7).
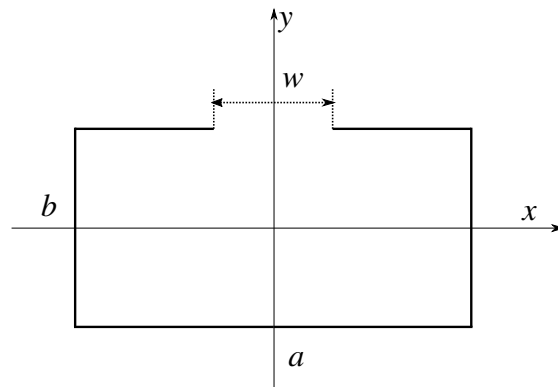

Figure 4.7: Slotted rectangular cylinder.

For classical rectangular waveguides, the relative cut-off wavenumbers $(k_c)_{mn}$ can be found

in the exact form, using the slightly rearranged well-known formula

$$(k_c)_{mn} = \pi\sqrt{\left(\frac{b}{a}\right)^2 m^2 + n^2} \tag{4.2}$$

where the indices $m, n = 0, 1, 2..., m^2 + n^2 \neq 0$, describe the number of variations of the electro-magnetic waves between the narrow and broad walls of the waveguide. According to this formula, there are two degenerate modes, TE_{01} and TE_{20}, in the frequency range of our interest charac-terised by the same cut-off wavenumber: $(k_c)_{01} = (k_c b)_{20} = \pi$. It can be reasonably assumed that any irregularity in the walls geometry should lead to disappearance of the mode degeneracy, which is the case when we introduce an infinite longitudinal slit. The first eight complex eigen-values calculated for a rectangular cavity with parameters $a/b = 2$ and $w/a = 0.1, 0.25, 0.5$, are collected in Table 4.8. The disappearance of the degeneracy is observed in modes TE_{01} and TE_{20}. It should be noted that mode TE_{01} is significantly less distorted in its electromagnetic field structure by the slit than mode TE_{20} which is suppressed rapidly when slit takes values $w/a > 0.14$. In general, suppression of certain complex oscillations occurs when the cylinder is cut by a slit of a sufficiently large width. This phenomenon is clearly observed in the frequency dependence of condition number as peaks for certain modes, present for smaller slit widths, vanish. Depending on the oscillation type, the suppression occurs when the $Q-$factor drops to 2.5-3.5, as a result of widening the slit.

Table 4.8: Complex eigenvalues in a slotted ($w/a = 0.1, 0.25, 0.5$) rectangular ($a/b = 2$) cavity.

TE_{mn}	$w/a = 0.1$	$w/a = 0.25$	$w/a = 0.5$
TE_{00}	$0.486802 - i0.0386621$	$0.566795 - i0.069984$	$0.651299 - i0.127871$
TE_{10}	$1.576784 - i0.0000192$	$1.606806 - i0.000752$	$1.698781 - i0.010946$
TE_{01}	$3.141727 - i0.0000001$	$3.144431 - i0.000005$	$3.183191 - i0.001291$
TE_{20}	$3.353183 - i0.0681991$	$sup.$	$sup.$
TE_{11}	$3.517790 - i0.0001287$	$3.542604 - i0.003945$	$3.634609 - i0.055512$
TE_{21}	$4.624361 - i0.0943883$	$sup.$	$sup.$
TE_{30}	$4.728786 - i0.0005732$	$4.783138 - i0.012113$	$4.841085 - i0.064734$
TE_{31}	$5.691209 - i0.0015848$	$5.793825 - i0.038782$	$5.936111 - i0.239491$

Next, we investigate the effect of varying the rectangular cavity ratio a/b at the fixed slit widths $w/b = 0.1, 0.25, 0.5$. We calculate the complex eigenvalues

$\gamma_{mn}(kb) = \gamma'_{mn}(kb) - i\gamma''_{mn}(kb)$ for the range $1.1 \leq a/b \leq 2$ ($b = 1$). The results of the calculations for complex eigenvalues $\gamma_{00}, \gamma_{01}, \gamma_{10}$ are plotted in Figures 4.8 - 4.10, for various values of the slit width. Overall, with growth of the ratio $\dfrac{a}{b}$ the real part of the relevant complex eigenvalue decreases while the imaginary part increases.

| (a) γ_{00} | (b) γ_{10} | (c) γ_{01} |

Figure 4.8: Complex eigenvalues γ_{mn} of the complex natural oscillations TE$_{mn}$ in a rectangular cavity with $w/b = 0.1$ and varying ratio a/b.

| (a) γ_{00} | (b) γ_{10} | (c) γ_{01} |

Figure 4.9: Complex eigenvalues γ_{mn} of the complex natural oscillations TE$_{mn}$ in a rectangular cavity with $w/b = 0.25$ and varying ratio a/b.

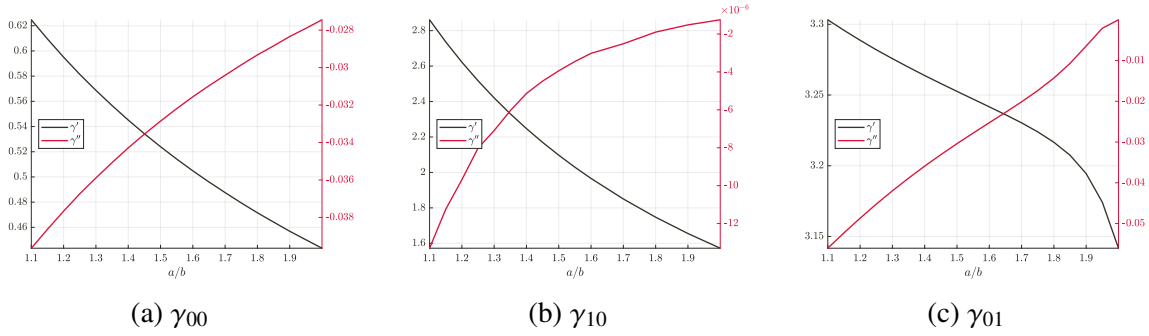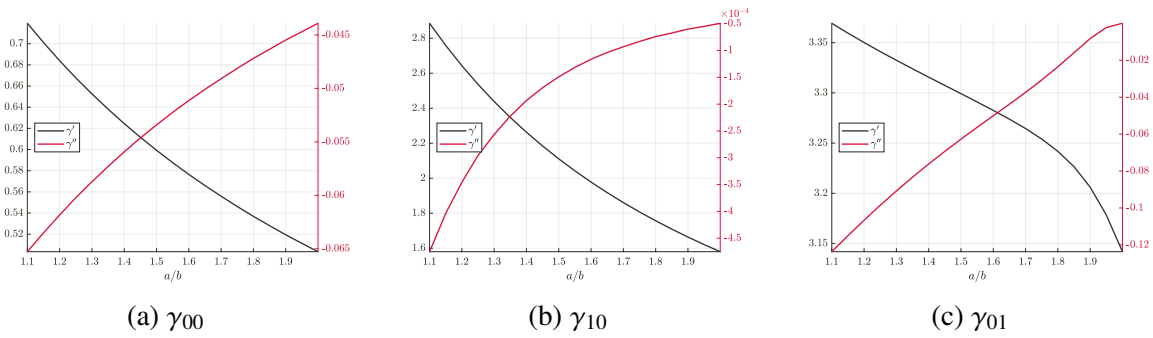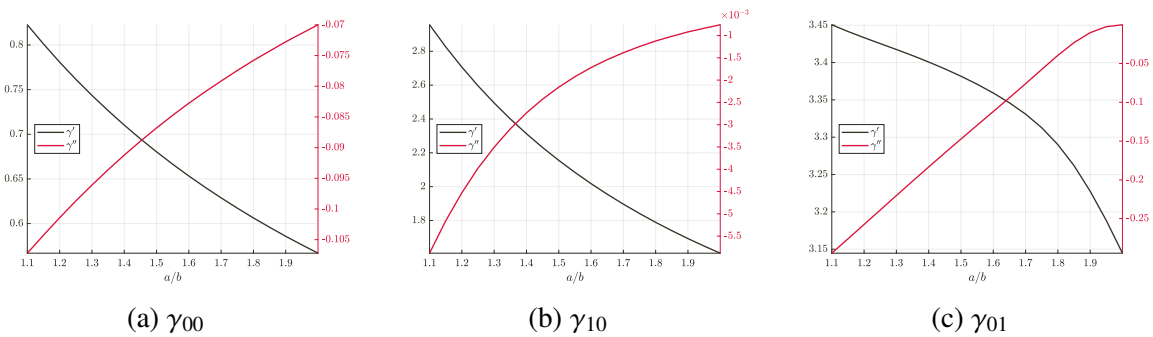| (a) γ_{00} | (b) γ_{10} | (c) γ_{01} |

Figure 4.10: Complex eigenvalues γ_{mn} of the complex natural oscillations TE$_{mn}$ in a rectangular cavity with $w/b = 0.5$ and varying ratio a/b.
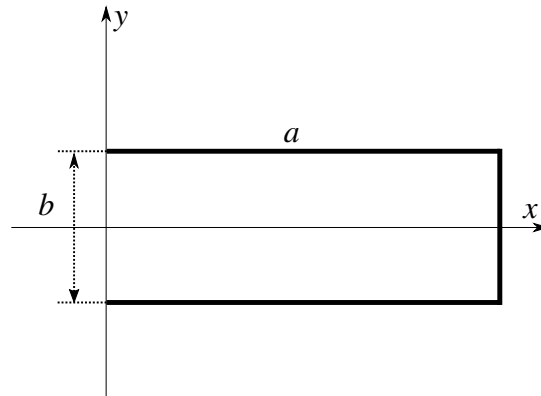
Figure 4.11: Open rectangular cavity formed by the removal of the left narrow wall.

Duct-like systems as shown in Figure 4.11 (that can be modelled by removal of one of the narrow walls of a rectangular waveguide, $a \gg b$) are widely used in electromagnetic and acoustic applications ([109]). We show that the MAR can be used effectively to calculate complex eigenvalues of these rectangular ducts without a limitation on the ratio a/b. We start our investigation by presenting the complete spectral portrait in the interval of $0 < kb \leq 10$ obtained by calculating condition number $\kappa \left(A_N \left(kb \right) \right)$ presented in Figure 4.12. This plot reveals an increasing number of complex natural oscillations as the open rectangular cavity elongates, successively taking the values $a/b = 2, 5, 10, 20$. From the behaviour of the dependence $\kappa \left(A_N \left(kb \right) \right)$, it can be seen that the oscillations $TE_{0n}, n = 1, 2, \ldots$ dominate over the oscillations $TE_{mn}, m > 0, n = 1, 2, \ldots$ This phenomenon is readily explained: with steady elongation of the open rectangular cavity the formation of standing waves between the right narrow wall and the edges of the opening becomes less pronounced in comparison with the transverse oscillations between the upper and lower wall (of length a). In other words, the longer an open cylinder is, the closer its spectral properties are to a resonator composed of two parallel planes which is characterised by a system of vertical standing waves only. From the complete spectrum of the complex eigenvalues (the approximate location of their real parts $Re\gamma_{mn} \equiv \gamma'_{mn}$ can be deduced from Figure 4.12) we extract those which are relevant to the modes $\left(TE_{01}, TE_{11} \right), \left(TE_{02}, TE_{12} \right), \left(TE_{03}, TE_{13} \right)$.

The results of calculation of the complex eigenvalues $\left(\gamma_{01}, \gamma_{11} \right), \left(\gamma_{02}, \gamma_{12} \right), \left(\gamma_{03}, \gamma_{13} \right)$ for steadily elongating open rectangular cylinder with parameter $a/b = 2, 5, 10, 20$, are collected in Table 4.9. To make the effect of removal of the left narrow wall on eigenvalues more visible, we have included in the table the real-valued eigenvalues $\gamma_{mn}^{(0)} \equiv \left(k_c b \right)_{mn}$ of the corresponding
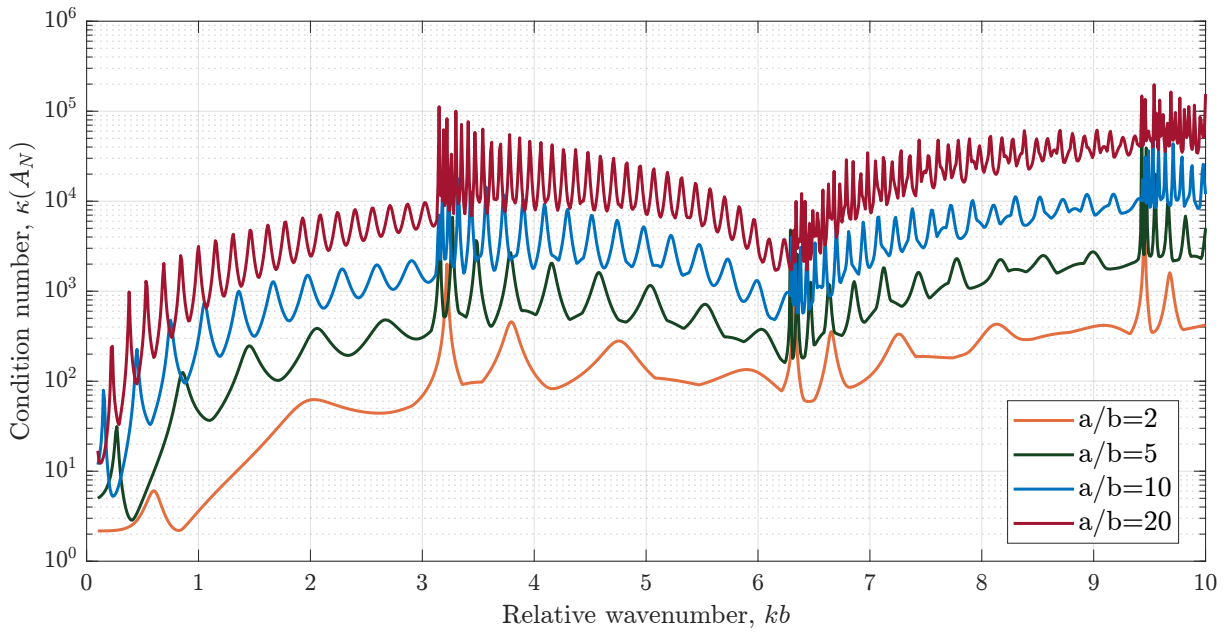
Figure 4.12: Condition number $\kappa\left(A_N\left(kb\right)\right)$ against relative wavenumber kb for an open rectangular resonator with one narrow wall removed for aspect ratios $a/b = 2, 5, 10, 20$.

natural oscillations for the closed rectangular cavity (calculated using equation (4.3)). The numerical data confirm the dominance of standing waves in the space between the broad walls over the standing waves between the right narrow wall and edges of the cavity entry. As $a/b \to \infty$ the complex eigenvalues γ_{mn} converge to the real-valued eigenvalues $\gamma_{mn}^{(0)}$, with $\gamma'_{mn} \to \gamma_{mn}^{(0)}$ and $\gamma''_{mn} \to 0$.

Having considered a rectangular cross section, we turn our attention to regular polygonal cylinders formed by n straight equilateral sides. Regular (equilateral) polygonal waveguides (PW) with n denoting the number of side walls ($3 \leq n \leq 8$), find wide application in microwave engineering ([110]). In a brief description on applications of PW contained in ([111]), the author asserts that the least studied shape is the heptagonal waveguide (HPW). Cut-off frequencies of both fundamental TE- and TM-modes in a regular PW have been obtained in [112] using the perturbation method. From a variety of polygon shapes, we choose the pentagon ($n = 5$), heptagon ($n = 7$) and nonagon ($n = 9$). The opening in each of these polygonal cylinders is formed by removal of one of its sides as shown in Figures 4.13a-4.13c.

Table 4.9: Complex eigenvalues γ_{mn} ($m = 0, 1; n = 1, 2, 3$) of oscillations TE$_{mn}$ in an open elongated rectangular cavity.

a/b	$\gamma_{01}^{(0)}$	γ_{01}	$\gamma_{11}^{(0)}$	γ_{11}
2	3.141592	$3.219752 - i0.006391$	3.512407	
5	3.141592	$3.155113 - i0.000498$	3.203808	$3.268287 - i0.004407$
10	3.141592	$3.146513 - i0.000082$	3.157261	$3.176594 - i0.000601$
20	3.141592	$3.142693 - i0.000011$	3.145517	$3.150445 - i0.000080$

a/b	$\gamma_{02}^{(0)}$	γ_{02}	$\gamma_{12}^{(0)}$	γ_{12}
2	6.283185	$6.325649 - i0.003824$	6.476559	
5	6.283185	$6.290767 - i0.000290$	6.314523	$6.345881 - i0.002336$
10	6.283185	$6.285984 - i0.000076$	6.291034	$6.301363 - i0.000250$
20	6.283185	$6.282999 - i0.000026$	6.285148	$6.287141\text{-}i0.000037$

a/b	$\gamma_{03}^{(0)}$	γ_{03}	$\gamma_{13}^{(0)}$	γ_{13}
2	9.424777	$9.453659 - i0.002560$	9.554781	
5	9.424777	$9.430410 - i0.000193$	9.445698	$9.470321 - i0.001241$
10	9.424777	$9.426178 - i0.000065$	9.430012	$9.436832 - i0.000174$
20	9.424777	$9.419334 - i0.000043$	9.426086	$9.423705 - i0.000143$

(a) Pentagon ($n = 5$)   (b) Heptagon ($n = 7$)

(c) Nonagon ($n = 7$)   (d) Partially removed side wall
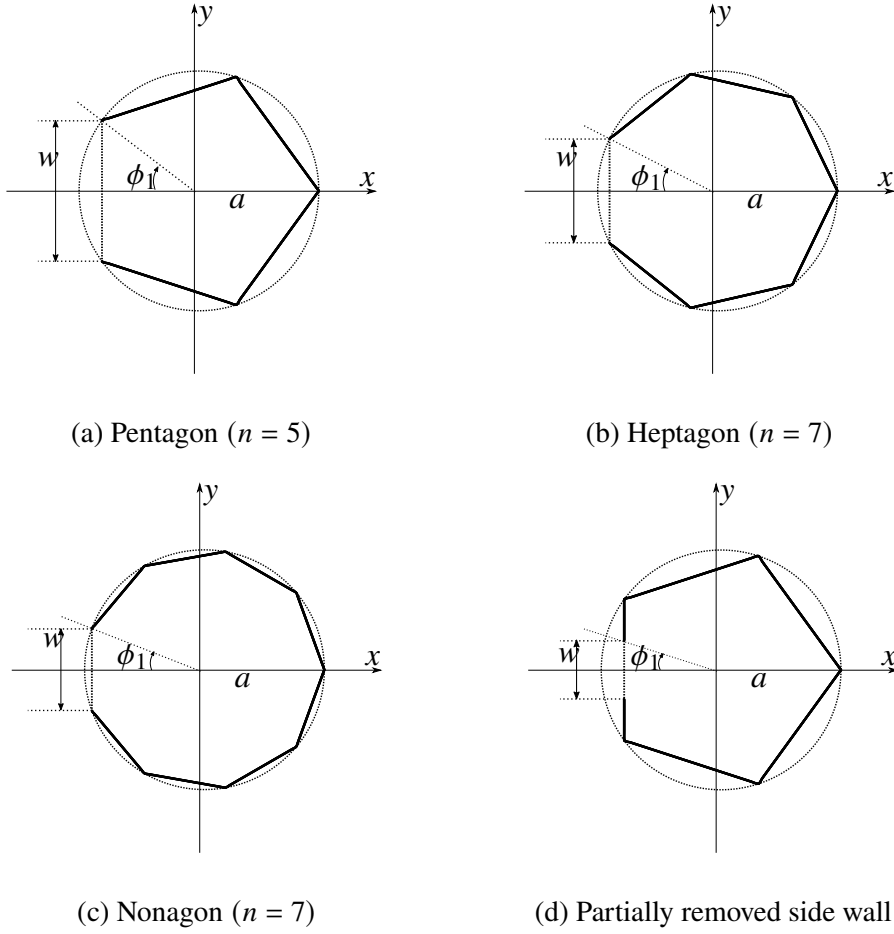
Figure 4.13: Slotted polygonal cylinders.

It is also possible to form an opening by incomplete (or partial) removal of the side, as shown in Figure 4.13d. We restrict ourselves to spectral studies of the interval $0 < ka \leq 5$, where a is the radius of the circle in which the polygons are inscribed. The aperture may be defined by the indicated angle ϕ_1. First, we calculate the frequency dependence of condition number $\kappa(A_N(ka))$, $N = 128$, $0 < ka \leq 5$ for each of the open polygonal cylinders shown in Figure 4.13. In case of an incomplete removal of a side wall (for example when $\phi_1 = 5°$), the dependence $\kappa(A_N(ka))$, $N = 128, N = 5, 7, 9$ is shown in Figure 4.14. From the resonance peaks of the function $\kappa(A_N(ka))$ presented in this figure, we extract five values of ka as initial approximations for further accurate calculation of the complex eigenvalues of the corresponding complex oscillations TE_{mn}. It is of interest to compare those complex eigenvalues γ_{mn} of the open polygonal cylinders with the corresponding values $\chi_{c(s)mn}$ of the circular cylinder with a slot of the same angular semi-width ϕ_1. The results for apertures $\phi_1 = 5°$ and $\phi_1 = 10°$ are collected in Tables 4.10 and 4.11, respectively. We have included the complex eigenvalues for the slotted circular cylinder in the last columns of both tables (labelled $n \to \infty$ since the circular

Figure 4.14: Condition number $\kappa\left(A_N\left(ka\right)\right)$ against relative wavenumber ka for open ($\phi_1 = 5°$) polygonal cylinders.

cylinder is the limiting case of a polygonal cylinder). It can be seen that the real parts of the complex eigenvalues $Re\gamma_{c(s)mn}$ monotonically approach their circular cylinder counterparts as the parameter n increases. The behaviour of the comp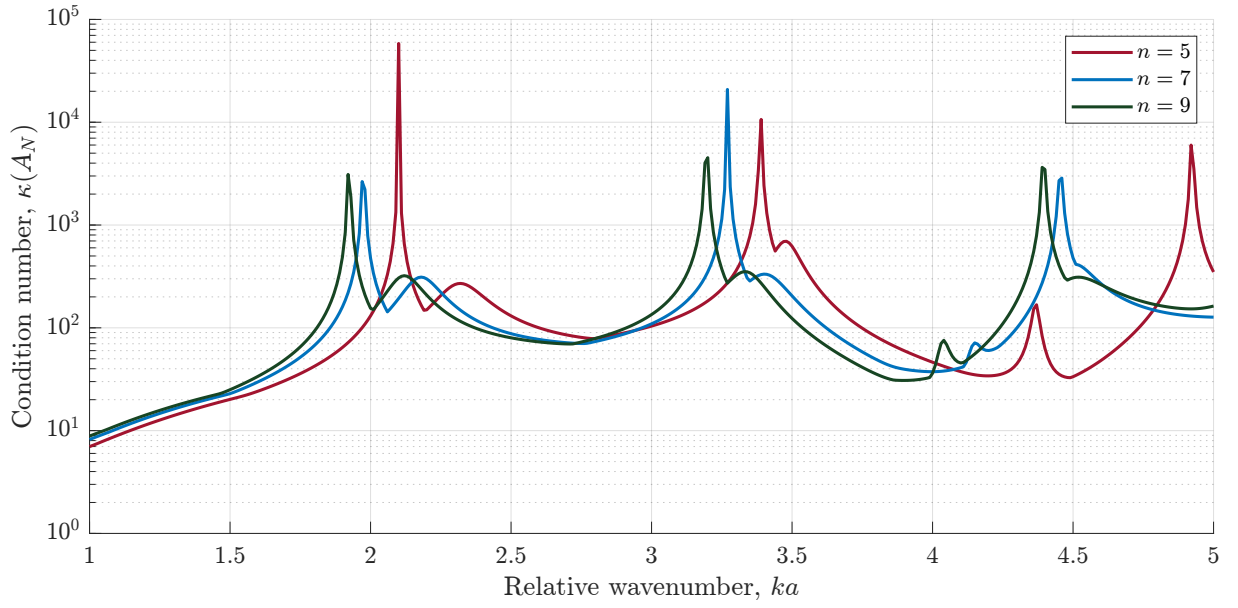lex parts $Im\gamma_{c(s)mn}$ is not of monotonic character. The peculiarities in the behaviour of $Im\gamma_{c(s)mn}$ may be explained by the different influence of the structure walls and slit (under increasing n) on the anti-nodes in the standing waves which are specific for each complex natural oscillation $TE_{c(s)mn}$.

If one wall is removed completely, the slit width w measured in terms of angular semi-width ϕ_1 is significantly larger: in fact $\phi_1 = 36°$ ($n = 5$), $\phi_1 \simeq 25.7°$ ($n = 7$), $\phi_1 = 20°$ ($n = 9$). This fact makes radiation losses through the slit more significant. As a result, the values of $Im\gamma_{c(s)mn}$ increases and unloaded Q−factors significantly decrease. This physically evident phenomenon is well illustrated by calculations shown in Table 4.12.

Table 4.10: Complex eigenvalues for polygonal cylinders $\chi_{c(s)mn}$, ($\phi_1 = 5°$).

| $TE_{c(s)mn}$	$n = 5$	$n = 7$	$n = 9$	$n \to \infty$
TE_{00}	$0.513528 - i0.036720$	$0.458188 - i0.031238$	$0.430316 - i0.028454$	$0.372457 - i0.022953$
TE_{s11}	$2.086311 - i3.23 \cdot 10^{-8}$	$1.965051 - i4.52 \cdot 10^{-8}$	$1.915731 - i1.48 \cdot 10^{-7}$	$1.841417 - i2.033 \cdot 10^{-7}$
TE_{s21}	$3.341879 - i7.98 \cdot 10^{-8}$	$3.242407 - i1.39 \cdot 10^{-7}$	$3.172253 - i4.56 \cdot 10^{-7}$	$3.058442 - i6.5 \cdot 10^{-5}$
TE_{c01}	$4.341781 - i0.00108$	$4.112456 - i0.001918$	$4.005527 - i0.001679$	$3.857797 - i0.007844$
TE_{s31}	$4.903779 - i5.23 \cdot 10^{-8}$	$4.391686 - 1.65 \cdot 10^{-7}$	$4.351629 - i9.13 \cdot 10^{-7}$	$4.208996 - i0.213 \cdot 10^{-4}$

Table 4.11: Complex eigenvalues for polygonal cylinders $\chi_{c(s)mn}$, $(\phi_1 = 10°)$.

$TE_{c(s)mn}$	$n = 5$	$n = 7$	$n = 9$	$n \to \infty$
TE_{00}	$0.560412 - i0.049869$	$0.501652 - i0.042834$	$0.472653 - i0.039424$	$0.414271 - i0.032979$
TE_{s11}	$2.099883 - i1.94 \cdot 10^{-4}$	$1.974553 - i1.63 \cdot 10^{-4}$	$1.923758 - i1.5 \cdot 10^{-4}$	$1.846809 - i0.000136$
TE_{s21}	$3.388374 - i0.002187$	$3.270413 - i0.001019$	$3.195333 - i9.59 \cdot 10^{-4}$	$3.007005 - i0.000890$
TE_{c01}	$4.367170 - i0.012683$	$4.145138 - i0.025930$	$4.035392 - i0.020587$	$3.868933 - i0.014815$
TE_{s31}	$4.923339 - i0.002335$	$4.455207 - i0.005152$	$4.394785 - i0.002901$	$4.229510 - i0.002699$

Table 4.12: Complex eigenvalues for polygonal cylinders with one side removed.

$TE_{c(s)mn}$	$n = 5$	$n = 7$	$n = 9$
TE_{00}	$0.706302 - i0.114857$	$0.591198 - i0.077050$	$0.531879 - i0.059942$
TE_{s11}	$2.183621 - i0.012418$	$2.008343 - i0.004461$	$1.940655 - i0.001826$
TE_{s21}	$3.504750 - i0.216623$	$3.363242 - i0.020537$	$3.241184 - i0.009959$
TE_{c01}	$4.669968 - i0.178820$	$4.265923 - i0.091300$	$4.078391 - i0.047294$
TE_{s31}	$5.075525 - i0.095449$	$4.265923 - i0.091300$	$4.475217 - i0.024658$

To conclude our investigation of complex eigenvalues of polygonal cylinders, we use the values $Re(\gamma_{mn})$ in Tables 4.10-4.12 to calculate the modal field distribution for a pentagon with a partially removed wall ($\theta_1 = 5°$), a heptagon with a partially removed wall ($\theta_1 = 10°$), and a nonagon with a completely removed wall ($\theta_1 = 20°$). The resulting plots are presented in Figures 4.15 - 4.17. It is evident that the modal structure inside the cavity is similar for all three polygons.

(a) TE_{00} (b) TE_{s11} (c) TE_{s21} (d) TE_{c01}
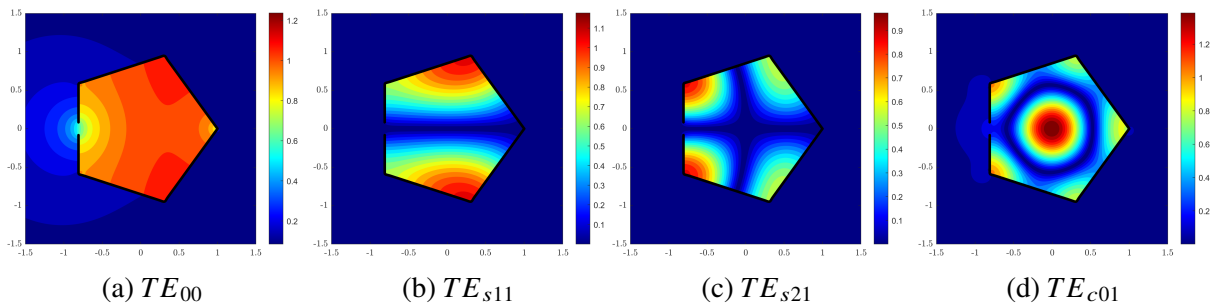
Figure 4.15: Modal field distribution for four complex natural oscillations in an open cylinder ($n = 5, \phi_1 = 5°$).

(a) TE_{00} (b) TE_{s11} (c) TE_{s21} (d) TE_{c01}

Figure 4.16: Modal field distribution for four complex natural oscillations in an open cylinder ($n = 7, \phi_1 = 10°$).
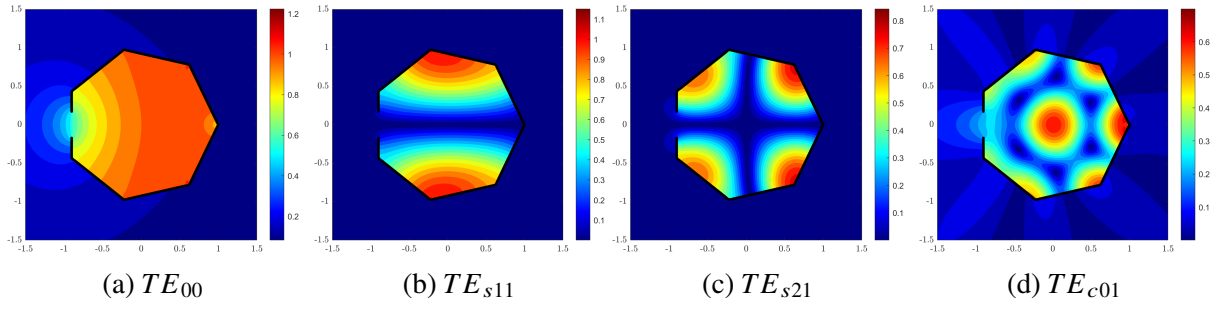

(a) TE_{00} (b) TE_{s11} (c) TE_{s21} (d) TE_{c01}
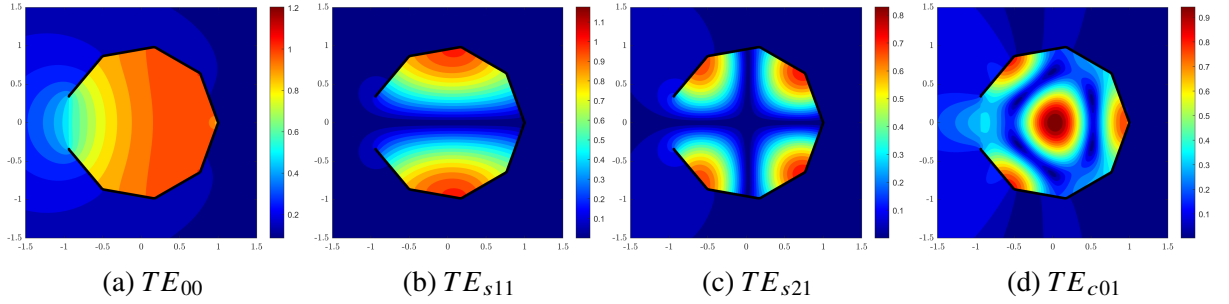
Figure 4.17: Modal field distribution for four complex natural oscillations in an open cylinder ($n = 9, \phi_1 = 20°$).

4.4 Slotted Cylinders of Arbitrary Cross Section

4.4.1 Sinusoidally Corrugated Circular Cylinder

The term "corrugated waveguide" is usually associated with periodic (or non-periodic) circumferential corrugation of its walls. Electromagnetic propagation in transversely corrugated cylindrical waveguides finds application in microwave engineering, in particular, in horn antennas. They are used in radio-astronomy and satellite communications due to their excellent characteristics such as low side lobe levels, low cross-polarisation, and pattern symmetry ([113]). Longitudinally corrugated waveguides are utilised as cluster feeds of reflector antennas due to their high aperture efficiencies. Quasi-TEM modes with near uniform aperture field distribution supported by such axially grated hard-walled waveguides have also been proposed as effective elements in multifunction interlaced arrays and vital components in quasi-optical grid amplifiers ([114–116]). Other applications of hard corrugated waveguides include mode converters, polarisation transformers, as well as resonant cavities.

Consequently, prior research on these structures may be divided into transversely or longitudinally corrugated waveguides. In this section, we focus on preliminary studies of longitudinally corrugated open 2D circular cavities (waveguides), targeting purely theoretical aspects of

the modal analysis. Before discussing numerical results, one reservation should be made. Both sinusoidally and magnetron-type corrugated open circular cavities (cylinders) are characterised by a number of parameters. Thus, the full examination of such cavities for obtaining the optimal solution is only practical for strictly defined problems. Therefore, we restrict our attention to several examples that reveal the MAR's ability and effectiveness. First, a sinusoidally corrugated open circular cylinder, parametrised by equation (4.3) and shown in Figure 4.18 is considered.

$$\rho\left(\phi\right) = a + b \sin \phi, \quad x = \rho(\phi) \cos\left(c\phi\right), \quad y = \rho(\phi) \sin\left(c\phi\right) \tag{4.3}$$

(a) $b = 0.05, c = 15$ (b) $b = 0.15, c = 10$ (c) Open
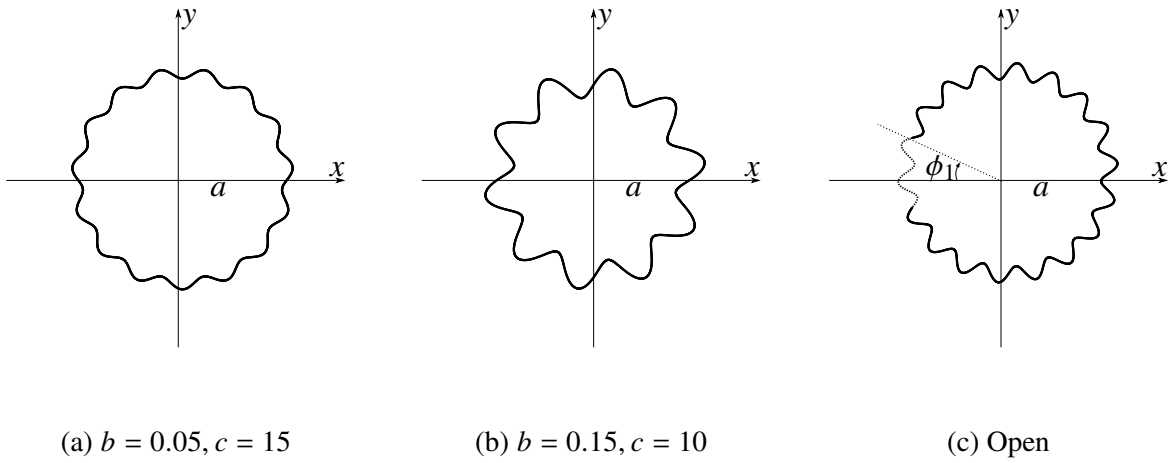
Figure 4.18: Circular cylinders of a mean radius a with sinusoidal corrugation (closed and open).

As usual, our study of spectral features of open corrugated circular cylinders start from the frequency dependence $\kappa\left(A_N\left(ka\right)\right)$, which immediately clarifies the nature of the spectral portrait in a given range of variation ka, set to $0 < ka \leq 5$. We investigate two corrugated cylinders shown in Figure 4.18 with parameters $b = 0.05, c = 15$ and $b = 0.15, c = 10$, where b is the relative amplitude of the sinusoid and c is the number of variations along the circle. For both cylinders the angular semi-width of slot ϕ_1 is set to $\phi_1 = 10°$, and the mean radius $a = 1$. The frequency dependence of the condition number $\kappa\left(A_N\left(ka\right)\right)$ is presented in Figure 4.19.

Three calculated complex eigenvalues $\gamma_{00}, \gamma_{s11}, \gamma_{s21}$ of the complex natural oscillations $TE_{00}, TE_{s11}, TE_{s21}$, are compared with the non-corrugated (smooth) circular cylinder of equal slot width ($\phi_1 = 10°$). The result are collected in Table 4.13. The comparison of the data for corrugated and non-corrugated slotted cylinders shows that when the depth of corrugation is small ($b \ll a$ or $b = 0.05 \ll 1$), its influence on the complex eigenvalues is insignificant. By enlarging the modulation parameter b, one can find a threshold value beyond which the influence
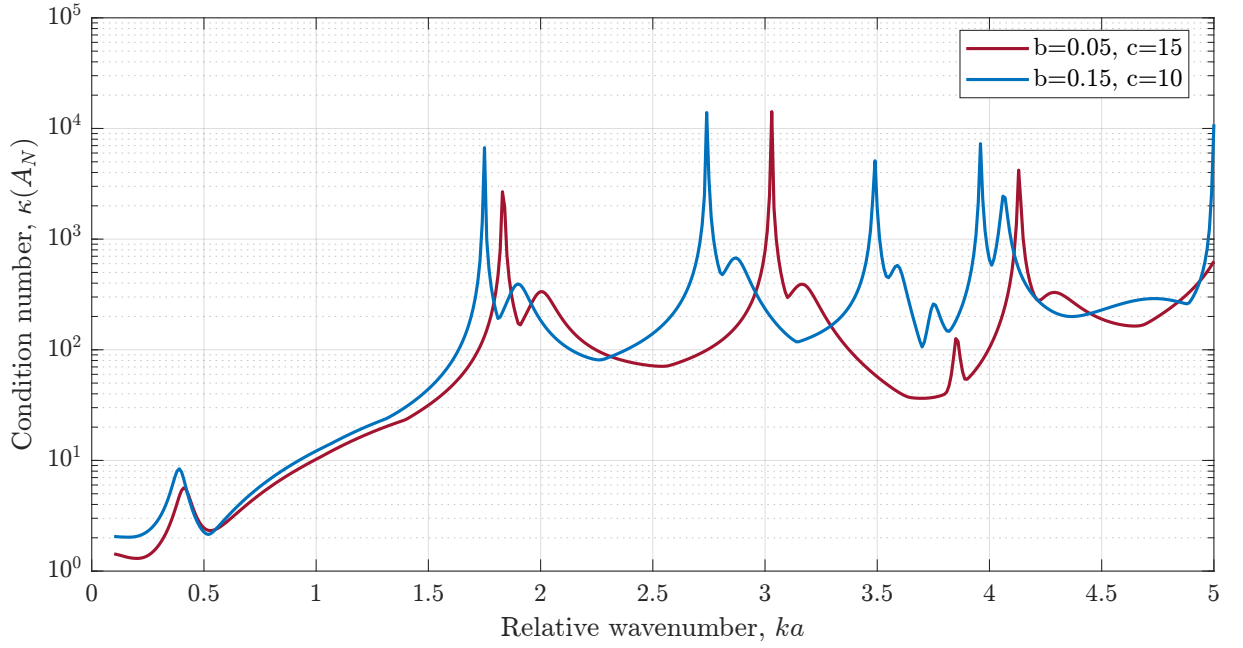
Figure 4.19: Condition number $\kappa\left(A_N\left(ka\right)\right)$ against relative wavenumber ka for sinusoidal corrugated slotted cylinders ($\phi_1 = 10°$).

of corrugation renders unrecognisable the family of complex eigenvalues. The effect of increasing the depth from $b = 0.05$ to $b = 0.15$ can be seen in the data as distortion of the complex oscillations becomes more visible. Finally, we conclude this section with modal field plots of the distribution of electromagnetic field $|H_z(x, y)|$ shown in Figure 4.20, based on the data provided in Table 4.13.

Table 4.13: Comparison of the first three complex oscillations in a corrugated against non-corrugated circular cylinder.

$TE_{c(s)mn}$	Non-corrugated	$b=0.05, c=10$	$b=0.15, c=10$
TE_{00}	$0.446178 - i0.042639$	$0.442153 - i0.041674$	$0.420014 - i0.036630$
TE_{s11}	$1.853482 - i0.000630$	$1.841401 - i0.000548$	$1.758827 - i0.000270$
TE_{s21}	$3.087733 - i0.003803$	$3.047906 - i0.003599$	$2.902398 - i0.076619$

4.4.2   Magnetron-type Cavity with Longitudinal Slit

Cavity magnetrons are high-power sources of radiation and are commonly used in applications such as microwave ovens, radar systems, medical line accelerators, and historically, in lighting systems. Normally, a cavity magnetron is made up of a solid metallic cylinder acting as anode. Small resonator cavities are placed inside the cylinder, interacting with a source placed
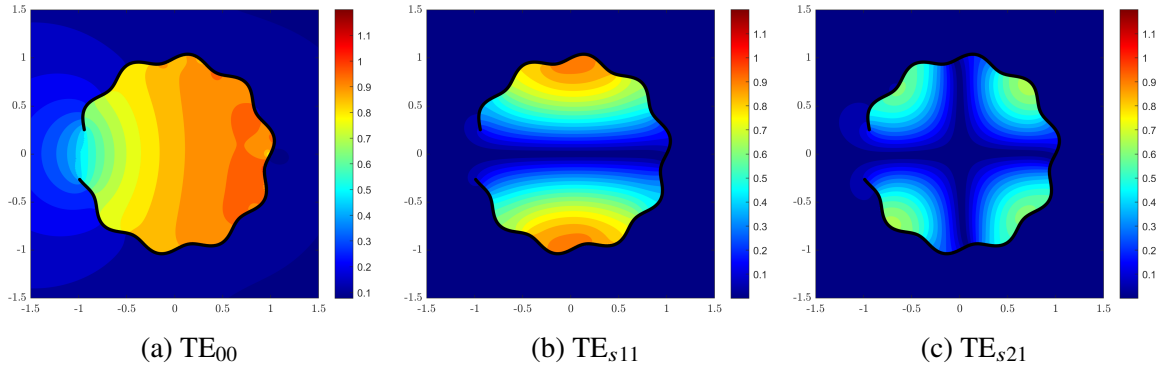
(a) TE$_{00}$ (b) TE$_{s11}$ (c) TE$_{s21}$

Figure 4.20: Modal field distribution in an open sinusoidally corrugated cylinder $a = 1$, $b = 0.05$, $c = 10$, $\phi_1 = 10°$.
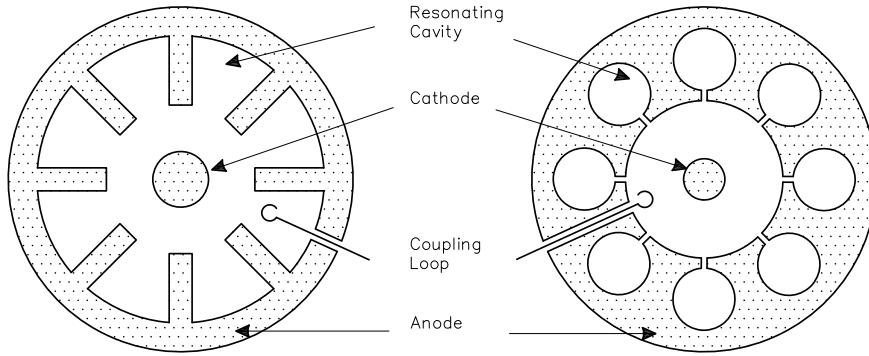
Figure 4.21: Common diagrams of a resonant magnetron cavity.

in the centre as a cathode. Common cross sectional diagrams of a resonant magnetron cavity are presented in Figure 4.21.

In this section we model a 2D version of a magnetron-type cavity. The parametrisation of the contour for a magnetron-type cavity is very similar to the parametrisation of the radial ridge waveguides. We use the number of "ridges" as a parameter which enables us to investigate dual-ridge, quad-ridge and octo-ridge geometries before proceeding to magnetron-type cavities. The parametrisation of a ridge waveguide can be created by constructing one quarter of the contour, and then using the symmetry across the $x-$ and $y-$axis, this process allows to obtain the complete contour. As demonstrated in Figure 4.22, the height and width of the ridge can be adjusted via parameters h_r and w_r, respectively.

The main motivation in developing radial ridge waveguides lies in their usage in antenna feed systems [117]. As stated in the previous sections, irregularities in the waveguide walls result in the disappearance of degenerate modes. This can affect the bandwidth in varying degrees for
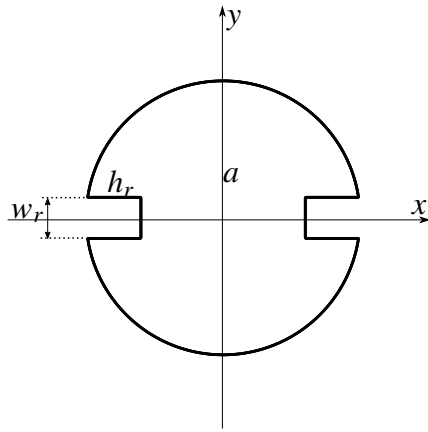
(a) dual-ridge, $n=2$, $h_r=0.4$, $w_r=0.3$
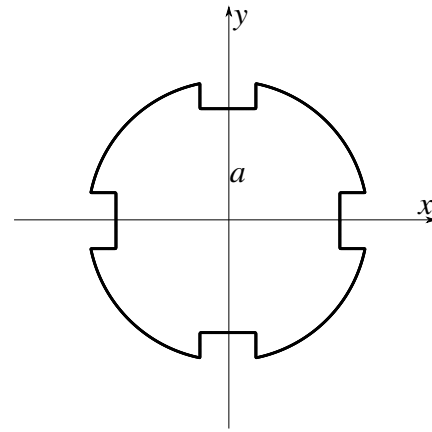
(b) quad-ridge, $n=4$, $h_r=0.2$, $w_r=0.4$
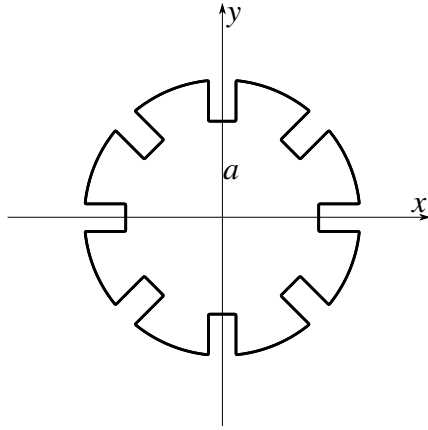
(c) octo-ridge, $n=8$, $h_r=0.3$, $w_r=0.2$
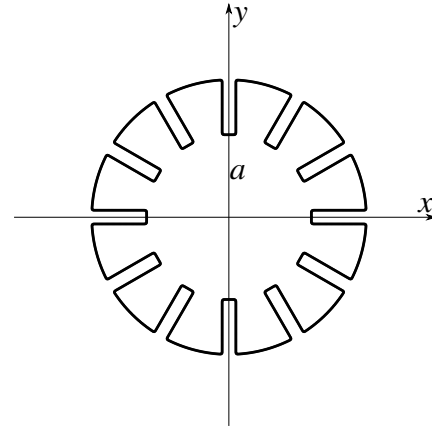
(d) magnetron, $n=12$, $h_r=0.4$, $w_r=0.1$

Figure 4.22: Various ridge and magnetron-type structures.

different modes. For lower modes, where ratio $\dfrac{\text{TE}_{nm}}{\text{TE}_{11}} < 3$, degenerate modes and their effect on bandwidth has been investigated in [118]. Using the MAR, excellent agreement with these numerical results is obtained.

We use parameters similar to those in [118]: $w_r = w/r$ and $h_r = h/r$ where $w_r = 0.1$ and $h_r = 0.1, 0.2, \ldots, 0.8$ to analyse the effect of increasing ridge height on the mode characteristics. Starting with a dual-ridge waveguide in Figure 4.22a, we calculate the cut-off wavenumbers for varying h_r. The introduction of the ridge removes degeneration of different modes in different ridge configurations. We will denote a mode with subscripts R and W as in TE_{11R}, TE_{11W}. The subscript W indicates that the mode is not significantly affected by the ridge and is similar to the modes of a simple circular waveguide while the subscript R denotes that the mode is heavily affected by the inclusion of ridges. The cut-off wavenumbers, normalised by TE_{11} mode, are presented in Figure 4.23: the inclusion of ridge splits the degenerate modes for both TE_{11} and

TE_{21}. Effect of a degenerate mode splitting is also seen in the modal field representations shown in Figure 4.24.

Figure 4.23: Normalised cut-off wavenumbers TE_{mn}/TE_{11} as functions of h_r for a dual-ridge cylindrical waveguide ($w_r = 0.1$).

(a) TE_{11W} (b) TE_{11R}
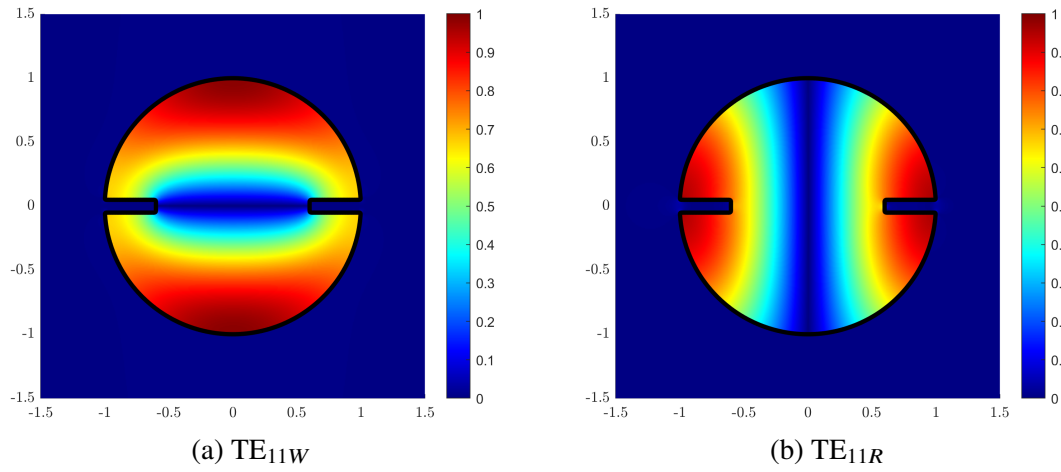
Figure 4.24: Normalised modal field distribution in a dual-ridge waveguide ($w_r = 0.1$, $h_r = 0.4$).
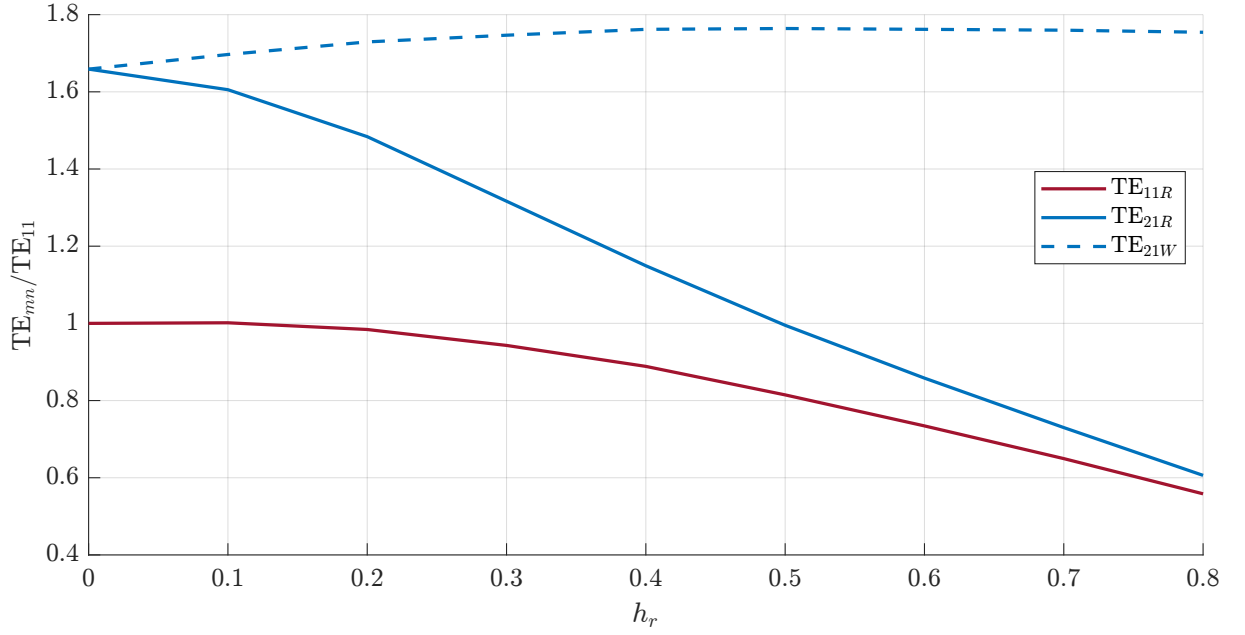
Figure 4.25: Normalised cut-off wavenumbers $\text{TE}_{mn}/\text{TE}_{11}$ as functions of h_r for a quad-ridge cylindrical waveguide ($w_r = 0.1$).

(a) TE_{21W}

(b) TE_{21R}
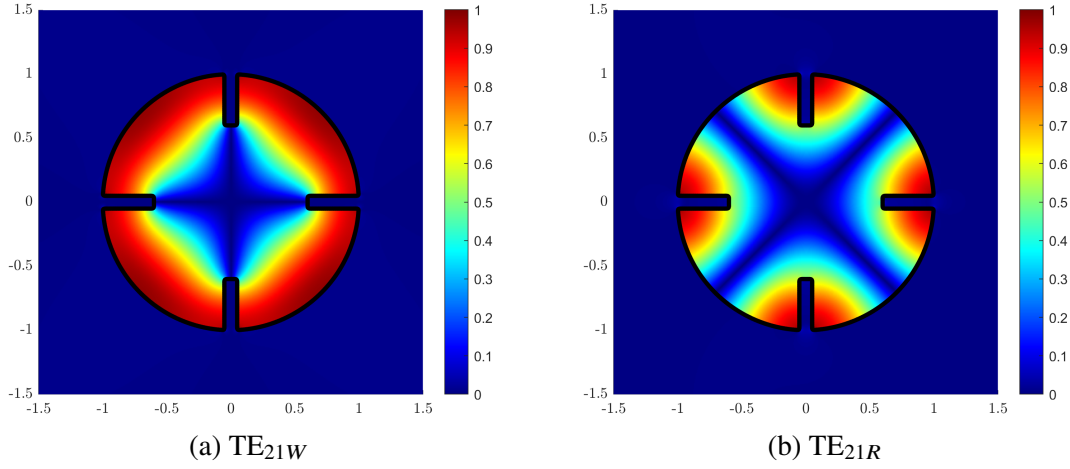
Figure 4.26: Normalised modal field distribution in quad-ridge waveguide $w_r = 0.1$, $h_r = 0.4$.

Due to $x-$ and $y-$axis symmetry the TE_{11} mode is still a degenerate mode in quad-ridge waveguides, but a split of degenerate mode TE_{21} can be observed in Figure 4.25 and 4.26. Before turning to the magnetron-type cavity, we consider an octo-ridge waveguide. As shown in Figure 4.27, the first degenerate mode that splits is TE_{41} and adding ridges results in the disappearance of TE_{21W}. The field plots representing the split degenerate modes are provided in Figure 4.28.

To summarise, while the introduction of ridges is helpful where broad bandwidth and high power are required, when the ridge height h approaches the radius of the simple circular waveguide, the operating bandwidth is dramatically reduced for some modes. As can be seen
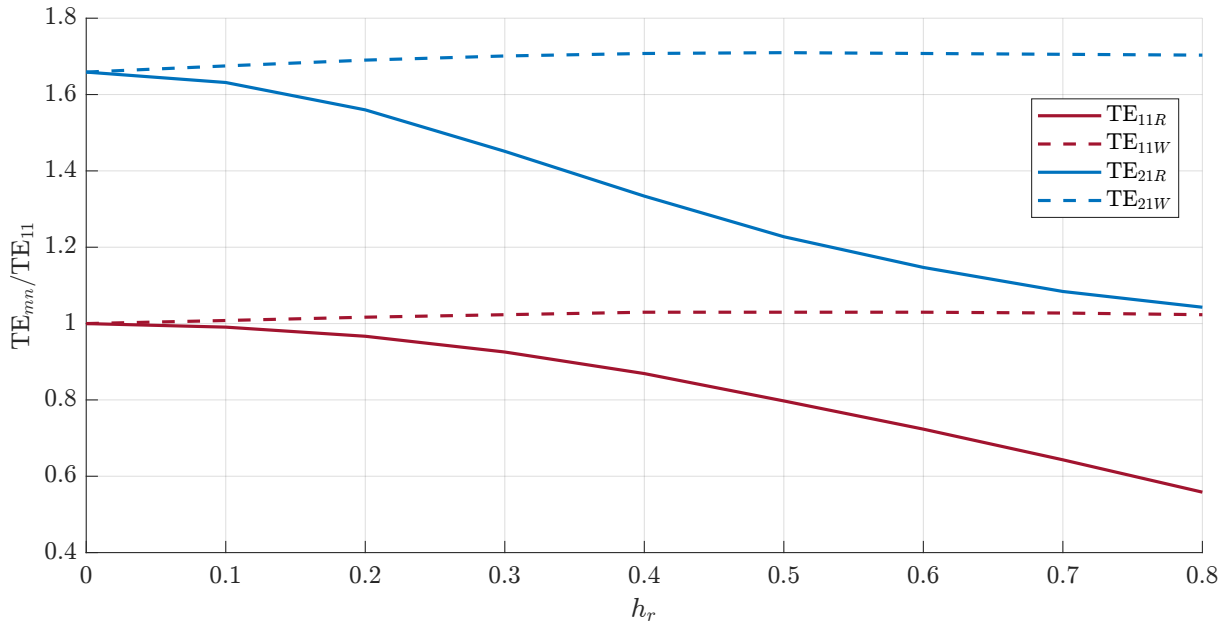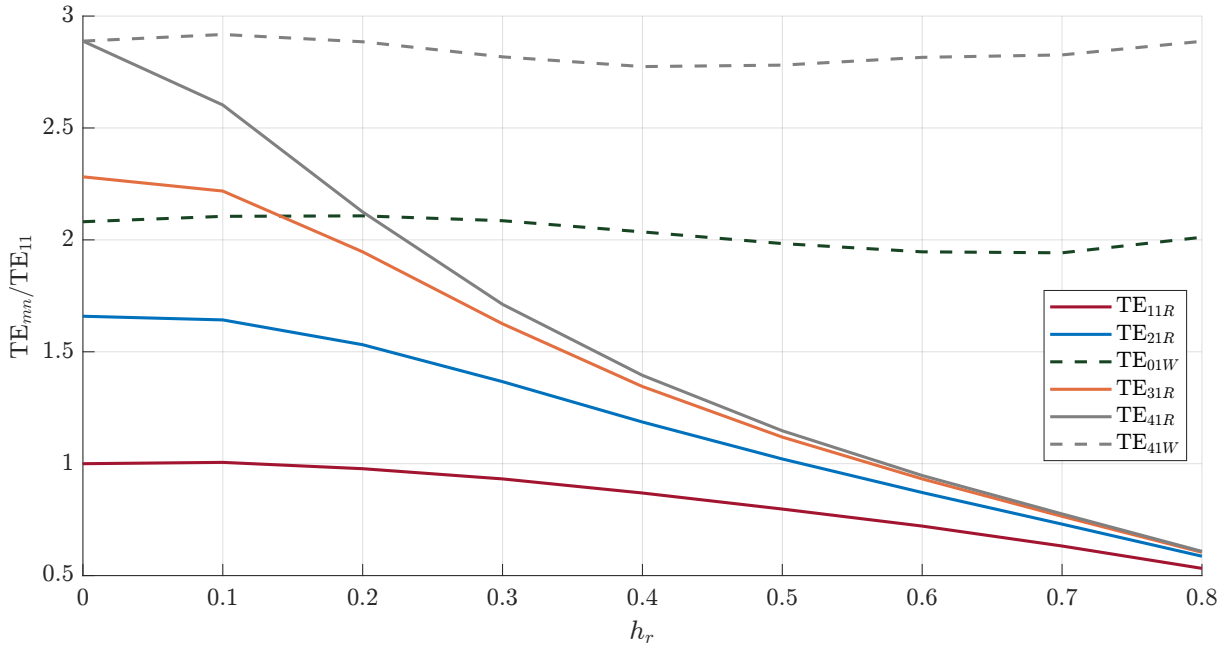
Figure 4.27: Normalised cut-off wavenumbers TE_{mn}/TE_{11} as functions of h_r for an octo-ridge cylindrical waveguide ($w_r = 0.1$).


(a) TE_{41W} (b) TE_{41R}
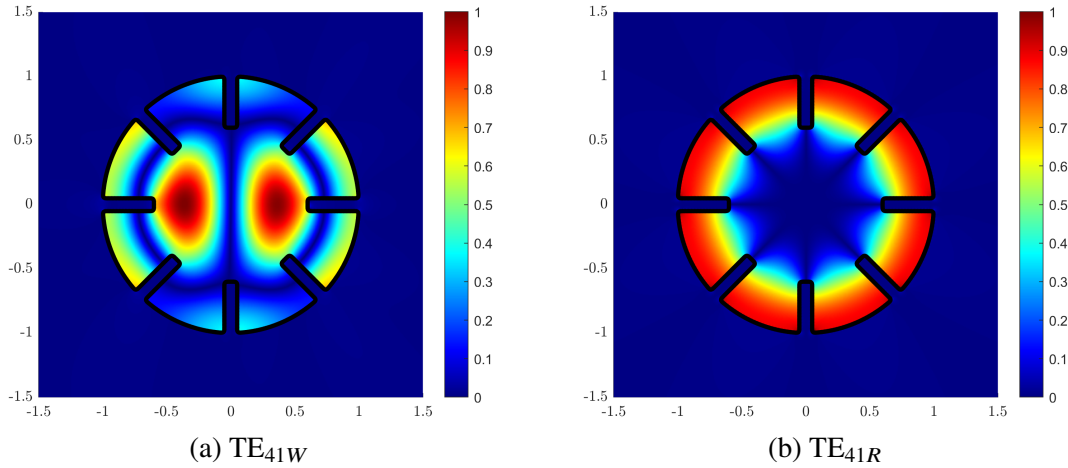
Figure 4.28: Normalised Modal field ($|H_z(x,y)|$) in octo-ridge waveguide $w_r = 0.1$, $h_r = 0.4$.

from Figure 4.25 and 4.27, $h_r \approx 0.2$ provides an optimum ratio for quad- and octo-ridge waveguides.

Finally, we turn our attention to magnetron type slotted cavities shown in Figure 4.29 with an opening that represents the output coupling loop. In cavity magnetrons, the oscillations around the inner resonator cavities generate radio frequency energy. The slot is then used for removing the output power from the anode by a probe which is connected to a coupling waveguide or antenna ([119]. Our brief analysis is limited to the effect of corrugation width and depth for different slot sizes.
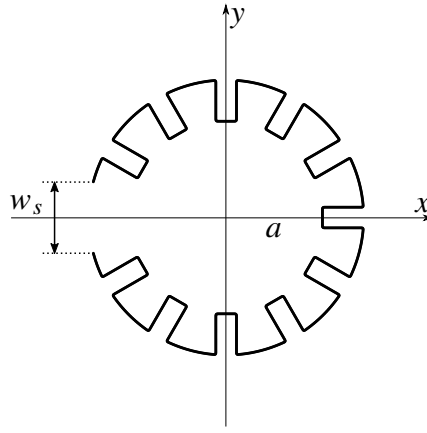
Figure 4.29: Magnetron type cavity with a longitudinal slit w.

Employing the frequency dependence of the condition number $\kappa\left(A_N\left(ka\right)\right)$ for $0 < ka \leq 5$, shown in Figure 4.30, we analyse the spectral portrait of selected magnetron-type cavities to see the influence of parameters h_r, w_r (height and width of corrugation), and w_s (width of slot) on the complex eigenvalues. Two complex eigenvalues $\gamma_{00}, \gamma_{s11}$ of the complex natural oscillations TE_{00}, TE_{s11} are calculated and presented in Table 4.14 for structures with $w_r = 0.15, h_r = 0.3, w_s = 0.2$ and $w_r = 0.1, h_r = 0.5, w_s = 0.2$. As explained in [120], mode conversion should be carefully considered in the design of magnetron cavities, as well as the effect of corrugation (both in height and width) on bandwidth between operating and competing modes. The MAR enables one to calculate complex eigenvalues effectively with any chosen set of parameters, which in turn gives the capability of extended calculations for a deep analysis of specific structures. TE_{00} and TE_{s11} modes are selected for such a further analysis of the mode dependence on corrugation depth and width. In Tables 4.15 and 4.16, we present the complex eigenvalues for two sets of parameters: $w_r = 0.15, h_r = 0.3, 0.4, 0.5, 0.6$, and $h_r = 0.5, w_r = 0.1, 0.14, 0.18, 0.2$ for a fixed slit width $w_s = 0.2$.

Table 4.14: Complex eigenvalues $\gamma_{00}, \gamma_{s11}, \gamma_{s21}$ of the complex natural oscillations TE_{00}, TE_{s11}, TE_{s21} for magnetron-type open cavity.

$TE_{c(s)mn}$	$w_r = 0.15, h_r = 0.3$	$w_r = 0.1, h_r = 0.5$
TE_{00}	$0.376418 - i0.021659$	$0.239477 - i0.011731$
TE_{s11}	$1.807131 - i0.000018$	$1.544956 - i0.002930$
TE_{s21}	$2.633786 - i0.000010$	$1.975477 - i0.009056$

As seen in Tables 4.15 and 4.16 increasing the height (h_r) of corrugation for fixed width w_r decreases the real part of the complex eigenvalues for both TE_{00} and TE_{s11} modes, while
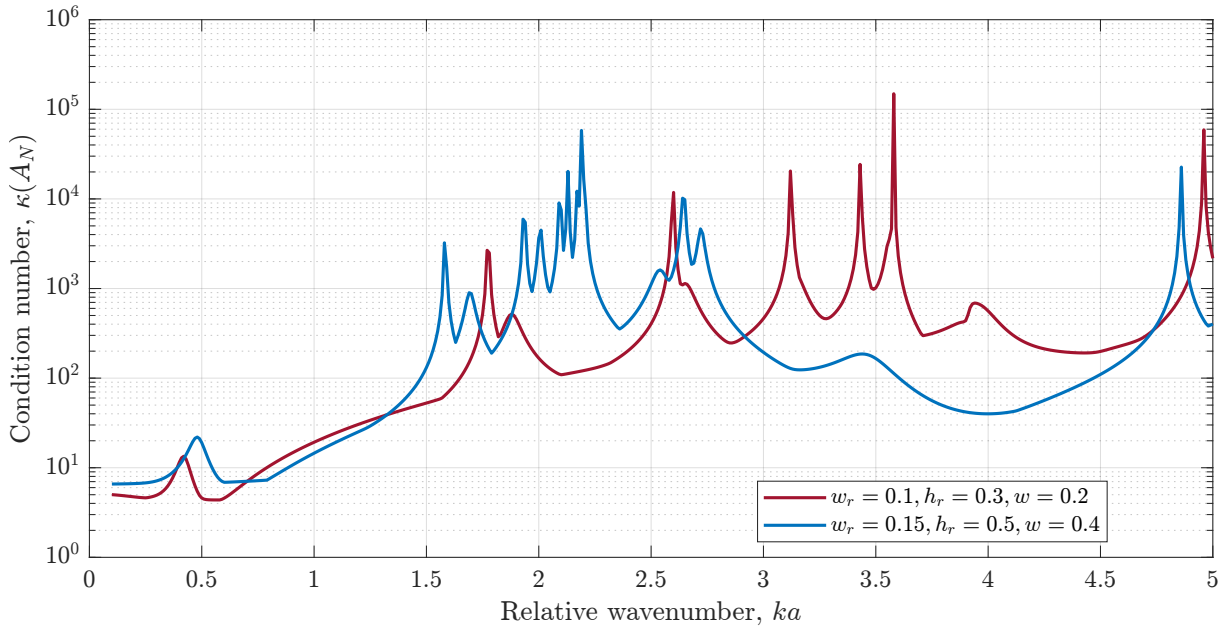
Figure 4.30: Condition number $\kappa\left(A_N\left(ka\right)\right)$ against relative wavenumber ka for magnetron type open cavity

Table 4.15: Complex eigenvalues $\gamma_{00}, \gamma_{s11}$ for a magnetron-type open cavity with $w_r = 0.15$, $w = 0.2$ and varying h_r.

h_r	TE_{00}	TE_{s11}
0.3	$0.376418 - i0.021659$	$1.807131 - i0.000018$
0.4	$0.369609 - i0.019509$	$1.722889 - i0.000021$
0.5	$0.347186 - i0.017181$	$1.587197 - i0.000087$
0.6	$0.262625 - i0.010494$	$1.409153 - i0.000291$

the imaginary part of the eigenvalues are affected in different ways. As addressed in earlier sections, this may be explained by the differing influence of the corrugations of the structure on the anti-nodes of the standing waves, which are specific for each complex natural oscillation. We see similar behaviour on the imaginary part of complex eigenvalues when w_r increases for a fixed value of h_r. In contrast, the real parts of complex eigenvalues gradually increase for both complex modes. In Figure 4.31, the modal field distribution of the magnetron-type cavity for selected degenerate modes is presented. The plots reveals different levels of field intensity between the directions radial and normal to the slit.

Table 4.16: Complex eigenvalues $\gamma_{00}, \gamma_{s11}$ for a magnetron-type open cavity with $h_r = 0.5$, $w = 0.2$ and varying w_r.

w_r	TE_{00}	TE_{s11}
0.1	$0.239477 - i0.011731$	$1.544956 - i0.002930$
0.14	$0.341705 - i0.018821$	$1.581022 - i0.000177$
0.18	$0.396849 - i0.021145$	$1.605345 - i0.000006$
0.2	$0.428533 - i0.023943$	$1.623482 - i0.000013$

(a) TE$_{s11}$

(b) TE$_{c11}$

(c) TE$_{s21}$

(d) TE$_{c21}$
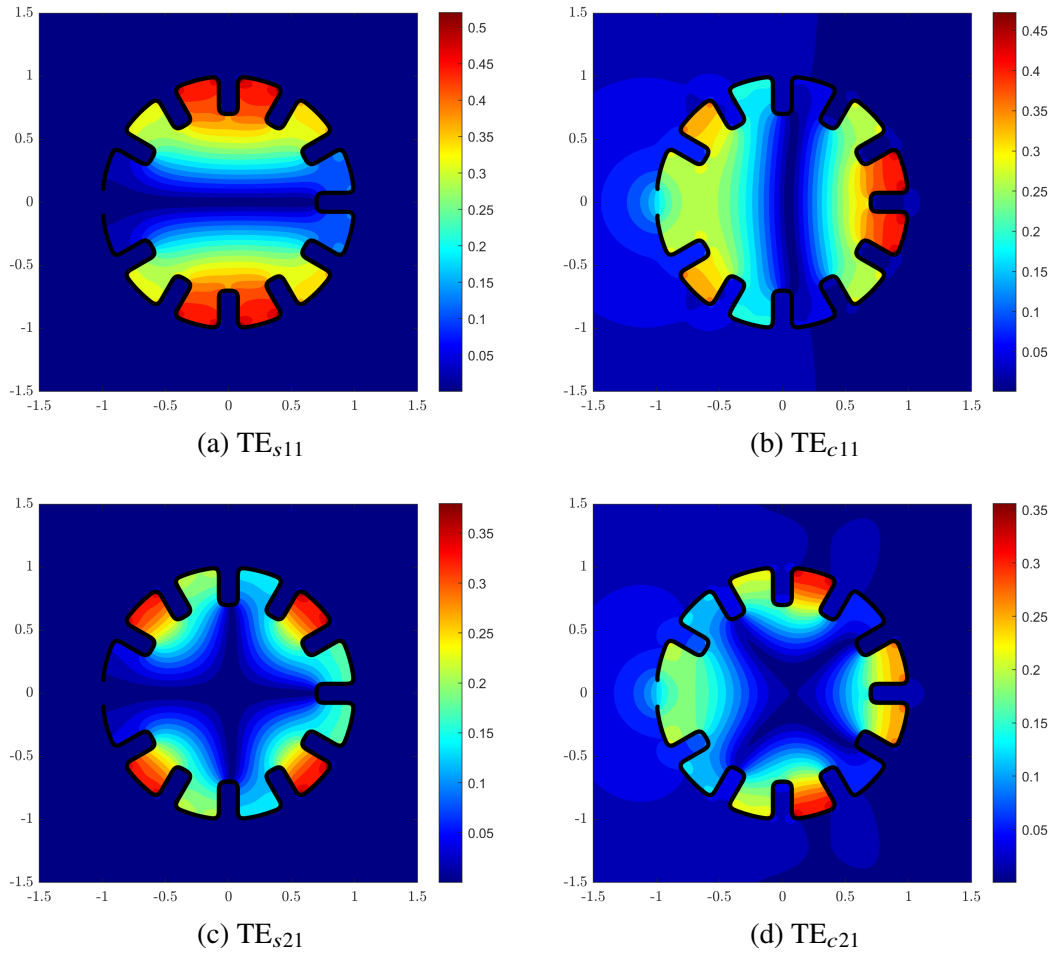
Figure 4.31: Modal field distribution in magnetron-type open cavity ($w_r = 0.15$, $h_r = 0.3$).

5

Resonance Wave Scattering and Radiation
from Slotted Cylinders

In this chapter, we present far field analysis of resonance wave scattering for open cylinders at frequencies close to the real parts of complex eigenvalues. When a scatterer is illuminated by a plane wave, three quantities are mainly employed to characterise far field: a) radiation pattern, $S(\vartheta)$; b) bistatic cross section (properly normalised value of $|S(\vartheta)|^2$); and c) radar (or sonar) cross section, σ_B, which is the properly normalised value of $|S(\pi + \alpha)|^2$. In practice σ_B is often called the monostatic cross section and the radiation pattern and bistatic cross section are presented in the decibel-scaled normalised form.

The Neumann problem for open cylinders, being equally applicable to electromagnetic or acoustic wave scattering, requires us to make choice between these two wave processes. In this chapter, we consider electromagnetic scattering of the $H-$polarised waves; all obtained results can be used in acoustics by a simple redefinition of the physical characteristics.

The chapter is organised as follows. Section 5.1 is of introductory character in which the characteristics of the scattered field in the far-field zone and formulas obtained in terms of the MAR solution are presented. We also verify the correctness of computational formulas by using known results for circular cylinders. In Section 5.2, the investigation of resonance scattering of an obliquely incident $H-$polarised plane wave by slotted PEC cylinders of classical

shape is presented. Numerical results are provided for circular, elliptic, and rectangular cylinders in a wide frequency band, which covers the Rayleigh scattering ($\lambda \gg a$), resonance scattering ($\lambda \sim a$) and the quasi-optics regime ($\lambda \ll a$). In Section 5.3, we briefly examine three examples of plane wave scattering by elongated, open, duct-like structures: semi-elliptical, rectangular,and rectangular bent cavities.

5.1   Definition of Basic Characteristics of the Scattered Field in the Far-field Zone

Let us recall that the scattered field $H_z^{sc}(q)$ is given by the following relation (see equation (2.6)):

$$U^{sc}(q) \equiv H_z^{sc}(q) = -\frac{i}{4} \int\limits_L \frac{\partial}{\partial n_p} H_0^{(1)}(k\,|q - p|) \cdot Z(p)\,dl_p, \quad q \in R^2. \qquad (5.1)$$

Using the parametrisation $\left(dl_p = l(\tau)\,d\tau, \ R = |p - q| = \sqrt{[x(\tau) - x(\vartheta)]^2 + [y(\tau) - y(\vartheta)]^2} \right)$ and the unknown function

$$z(\tau) = \begin{cases} Z(\tau) & , \quad \tau \in [-\vartheta_0, \vartheta_0], \\ 0 & , \quad \tau \in [-\pi, -\vartheta_0] \cup [\vartheta_0, \pi], \end{cases} \qquad (5.2)$$

we transform equation (5.1) to

$$H_z^{sc} = -\frac{i}{4} \int\limits_{-\pi}^{\pi} \frac{\partial}{\partial n(\tau)} H_0^{(1)}\left(k\sqrt{[x(\tau) - x(\vartheta)]^2 + [y(\tau) - y(\vartheta)]^2} \right) z(\tau) l(\tau)\,d\tau. \qquad (5.3)$$

If the distance between the points p and q is significant, R can be rewritten:

$$R = \sqrt{\rho^2 - 2\rho\left[x(\tau)\cos\vartheta + y(\tau)\sin\vartheta + x^2(\tau) + y^2(\tau) \right]} \simeq \rho - [x(\tau)\cos\vartheta + y(\tau)\sin\vartheta], \qquad (5.4)$$

as $\rho \to \infty$ where we expressed point $\rho = \rho(\vartheta)$, $x(\vartheta) = \rho \cos \vartheta$, $y(\vartheta) = \rho \sin \vartheta$. As a result, equation ((5.3)) is simplified to

$$H_z^{sc}(\rho, \vartheta) = -\frac{i}{4} \int_{-\pi}^{\pi} \frac{\partial}{\partial n(\tau)} H_0^{(1)}(k\rho - k[x(\tau) \cos \vartheta + y(\tau) \sin \vartheta]) \cdot z(\tau)l(\tau)\, d\tau. \quad (5.5)$$

Taking advantage of the asymptotic behaviour of the Hankel function $H_0^{(1)}(z)$

$$H_0^{(1)}(z) \sim \sqrt{\frac{2}{\pi z}} e^{iz} \cdot e^{-i\frac{\pi}{4}}, \text{ as } z \to \infty$$

we obtain the expression for the longitudinal component of the magnetic field H_z^{sc} in the far-field zone as $\rho \to \infty$

$$H_z^{\infty} \sim \frac{e^{ik\rho}}{\sqrt{\rho}} \left\{ -\frac{i}{4} \sqrt{\frac{2}{\pi k}}\, e^{-i\frac{\pi}{4}} \right\} \int_{-\pi}^{\pi} \frac{\partial}{\partial n(\tau)} \left\{ e^{-ik[x(\tau) \cos \vartheta + y(\tau) \sin \vartheta]} \right\} \cdot z(\tau)\, l(\tau)\, d\tau. \quad (5.6)$$

Recalling that the unknown function $z(\tau)$ is expressed in Fourier coefficients by

$$z(\tau) = \sum_{n=-\infty}^{\infty} \xi_n e^{in\tau},$$

and defining

$$\left[\frac{\partial f}{\partial x} \cdot y'(\tau) - \frac{\partial f}{\partial y} x'(\tau) \right] = \sum_{m=-\infty}^{\infty} \beta_m(\vartheta)\, e^{im\tau}$$

where

$$f(x, y) = e^{-ik[x(\tau) \cos \vartheta + y(\tau) \sin \vartheta]},$$

equation (5.6) transforms to

$$H_z^{\infty} = \frac{e^{ik\rho}}{\sqrt{\rho}} \left\{ -\frac{k}{4} \sqrt{\frac{2}{\pi k}}\, e^{-i\frac{\pi}{4}} \right\} \sum_{m=-\infty}^{\infty} \beta_m(\vartheta) \sum_{n=-\infty}^{\infty} \xi_n \int_{-\pi}^{\pi} e^{i(m+n)\tau}\, d\tau \quad (5.7)$$

which can be re-arranged as

$$H_z^{\infty} = \frac{e^{ik\rho}}{\sqrt{\rho}} \left\{ i\sqrt{\frac{\pi k}{2}}\, e^{-i\frac{\pi}{4}} \sum_{n=-\infty}^{\infty} \beta_{-n}(\vartheta)\, \xi_n \right\}. \quad (5.8)$$

Consequently, the radiation pattern $S(\vartheta)$ is defined as

$$S(\vartheta) = \left| \sum_{n=-\infty}^{\infty} \beta_{-n}(\vartheta)\, \xi_n \right|, \tag{5.9}$$

the radar cross section (RCS) σ_B

$$\sigma_B = k\pi a^2 \left| \sum_{n=-\infty}^{\infty} \beta_{-n}(\pi + \alpha)\, \xi_n \right|^2.$$

Here ϑ denotes the observation angle. When normalised by the factor πa, it takes the form

$$\frac{\sigma_B}{\pi a} = ka \left| \sum_{n=-\infty}^{\infty} \beta_{-n}(\pi + \alpha)\, \xi_n \right|^2. \tag{5.10}$$

We use the dB scaled representation of the normalised radiation pattern $S^{(n)}(\vartheta)$:

$$S^{(n)}(\vartheta) = 20 \log_{10} \frac{|S(\vartheta)|}{max\, |S(\vartheta)|}, \quad dB \tag{5.11}$$

Verification of formula (5.10) is done by comparison of the frequency dependence $\sigma_B(ka)$ of a truncated system presented in Figure 5.1 with known results for the closed circular cylinder.
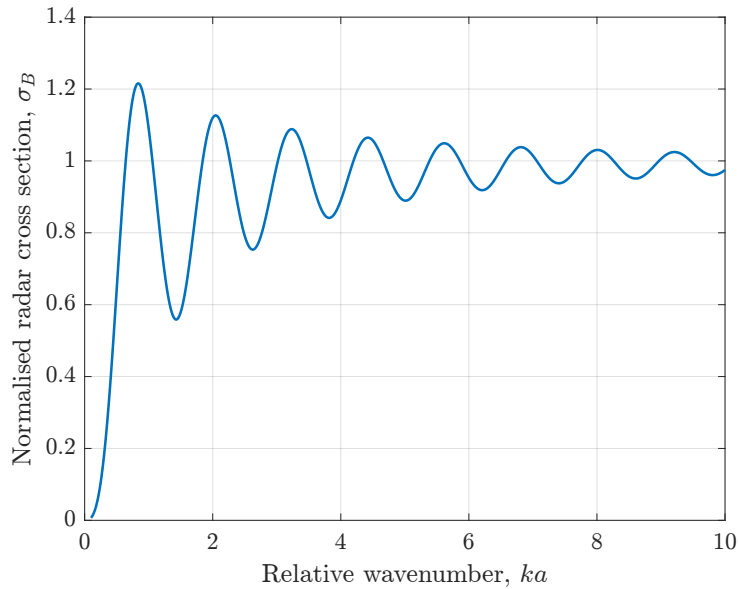

Figure 5.1: Frequency dependence of the normalised radar cross section for a closed circle.

5.2 Resonance Scattering by Slotted PEC Cylinders of Classical Shape

In this section, we study the resonance scattering of an obliquely incident $H-$polarised plane wave by various slotted cylinders. We limit our numerical investigation to calculations of frequency dependencies of the normalised radar cross section $\sigma_B(ka)$ and normalised radiation pattern $\left|S^{(n)}(\vartheta)\right|$. The parameter a stands for the maximum characteristic size of each considered cavity. For a circular cylinder, a is its radius; for an elliptic and rectangular cylinder, a is the major semi-axis as shown in Figure 5.2. The frequency dependence of the normalised radar
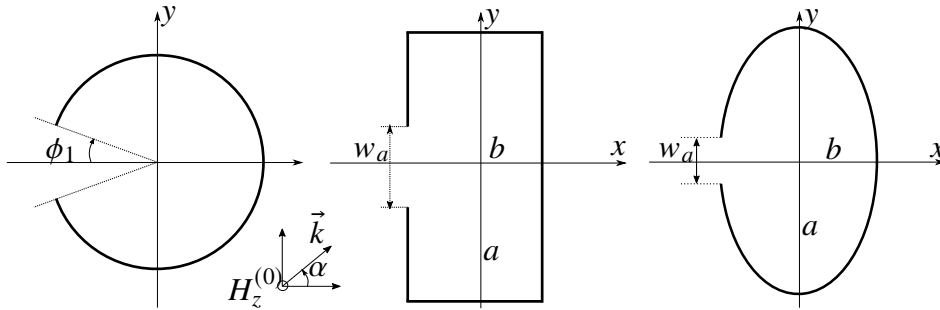
Figure 5.2: Excitation of slotted cylinders by obliquely incident $H-$polarised plane wave.

cross section is calculated for slotted-circular cylinders in the low frequency and resonance region of scattering. The plots are shown for various slot widths ($\phi_1 = 5°, 30\circ$) and different plane wave incident angles ($\alpha = 0°, 45°, 90°, 180°$) in Figures 5.3 and 5.4.

Observing the behaviour in these normalised radar cross section plots, it can be noted that the most effective excitation of the natural oscillations occurs at the incidence angle $\alpha = 0°$, i.e. when the plane wave strikes the slit normally. As the incident angle α increases, the effectiveness of excitation steadily weakens, completely vanishing at $\alpha = 180°$. In other words, the oscillations are excited with varying levels of effectiveness when slit the is directly illuminated by the plane wave ($0° \leq \alpha \leq 90°$). When the slit is in shadowed zone ($90° < \alpha \leq 180°$), the level of excitation dramatically drops, almost vanishing at $\alpha = 180°$.

We have previously asserted that the MAR-based numerical approach is universally applicable for arbitrary shapes in a wide frequency range. Figure 5.5 presents the normalised radar cross section in the high-frequency region for a semi-cylindrical cavity ($\phi_1 = 90°$) illuminated by a plane wave at $\alpha = 0$ where the radius a varies from a fraction of wavelength λ to $a = 50\lambda$ ($ka = 100\pi$).

(a) $\alpha = 0°$

(b) $\alpha = 45°$

(c) $\alpha = 90°$

(d) $\alpha = 180°$

Figure 5.3: Frequency dependence of the normalised radar cross section of a slotted circular cylinder ($\phi_1 = 5°$).

Returning to Figures 5.3 and 5.4, one can observe that the main distinctive feature of backscattering from slotted cylindrical cavities, which possesses a spectrum of high Q−factor complex oscillations, is the emergence of the so-called "resonance duplet" in the frequency dependence $\sigma_B(ka)$. This phenomenon is well-known in general theory of oscillations ([121]) and it appears in diverse areas of science and technology. In the context of resonance wave scattering, a detailed study can be found in [43].

For a detailed analysis of the resonance duplet, we have calculated and plotted magnified views of the normalised radar cross section σ_B in Figure 5.6. We have selected two resonance frequencies ($ka = Re\gamma_{c01}$ and $ka = Re\gamma_{c11}$) and narrowed the frequency range in order to observe the local minimum and maximum of the normalised radar cross section at these frequencies.

It is also useful to investigate how a small change in frequency affects the normalised radiation pattern $\left|S^{(n)}(\vartheta)\right|$ for values when the incidence frequency (defined by relative wavenumber

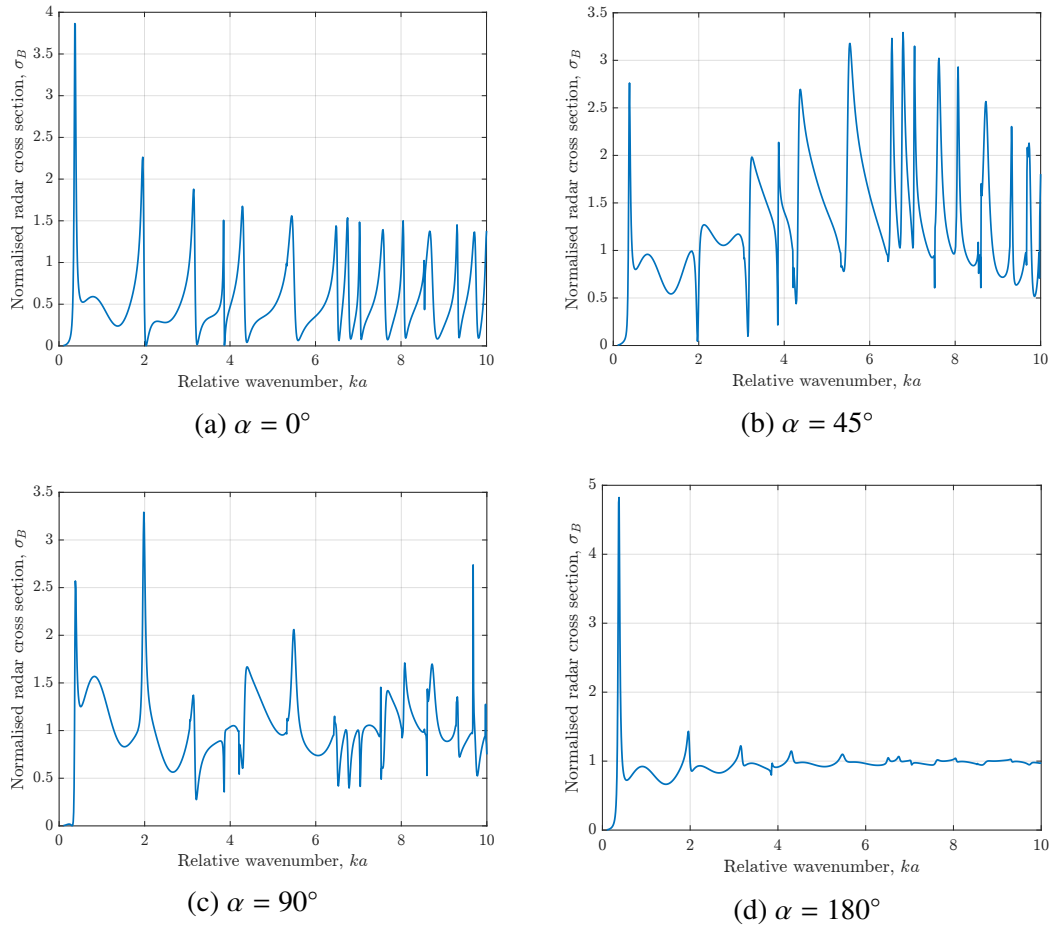(a) $\alpha = 0°$

(b) $\alpha = 45°$

(c) $\alpha = 90°$

(d) $\alpha = 180°$
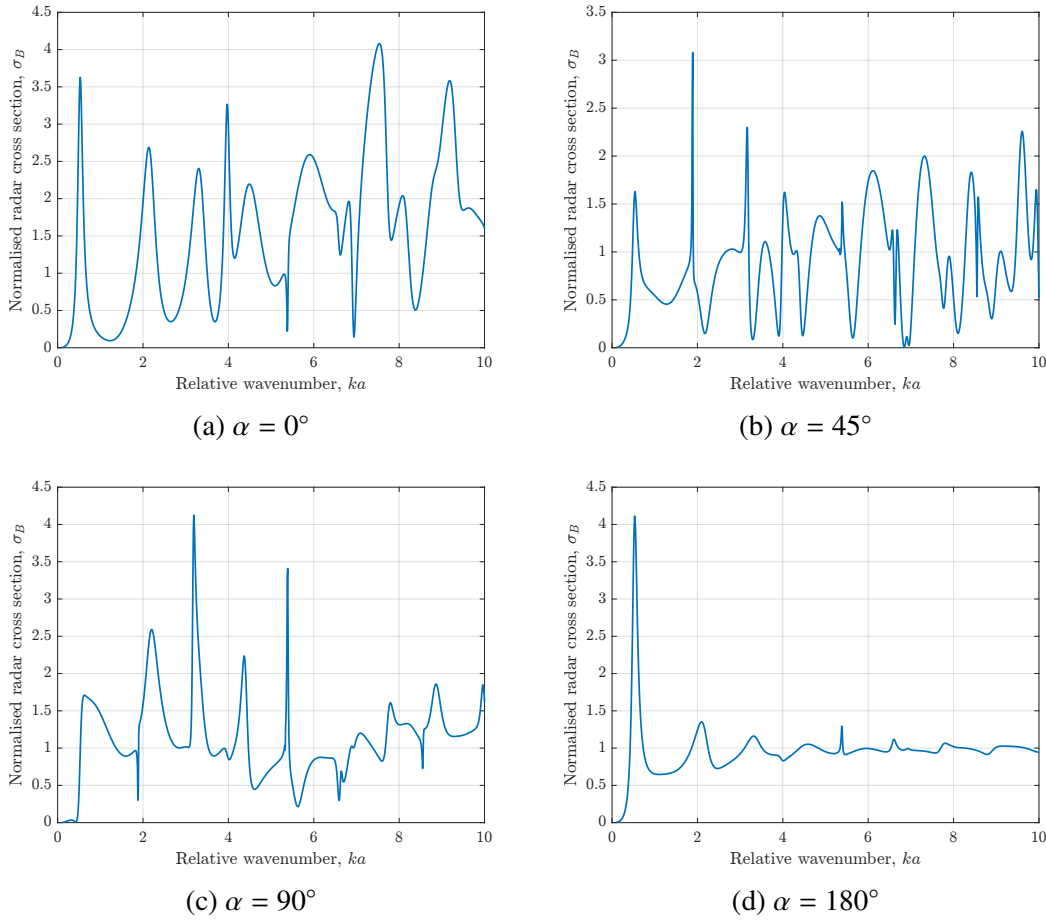
Figure 5.4: Frequency dependence of the normalised radar cross section of a slotted circular cylinder ($\phi_1 = 30°$).

ka) matches the values $ka = (ka)_{max}$, $ka = Re\gamma_{cm1}$ ($m = 0, 1$), and $ka = (ka)_{min}$. This gives characteristic information for backscattering. The results of calculations are shown in Figure 5.7. In the plots, all radiation patterns are normalised by the largest value of $\left|S^{(n)}(\vartheta)\right|$ across three frequencies. Analysing $\left|S^{(n)}(\vartheta)\right|$ in these two figures, one can observe a significant influence of the excited oscillations on the level of backscattering ($\vartheta = \pi$), and its near absence in forward ($\vartheta = 0$) scattering. A small negative shift of the incident frequency ka from $Re\gamma_{cm1}$ to $(ka)_{max}$ leads to a dramatic increase in the backscattering level. At the same time, a small positive shift from $ka = Re\gamma_{cm1}$ to $ka = (ka)_{min}$ delivers the minimum level of backscattering. The difference between backscattering at these frequencies exceeds $\sim 10dB$ in both of these narrow frequencies ranges where TE_{c01} and TE_{c11} oscillations are excited. The sharpness of the resonance duplets at each natural oscillation and its effect on the normalised radar cross section depends on the $Q-$factor.

The resonance duplet seen in the frequency dependence of the normalised radar cross section σ_B for slotted circular cylinders is universal and occurs for all possible shapes of slotted cylinders
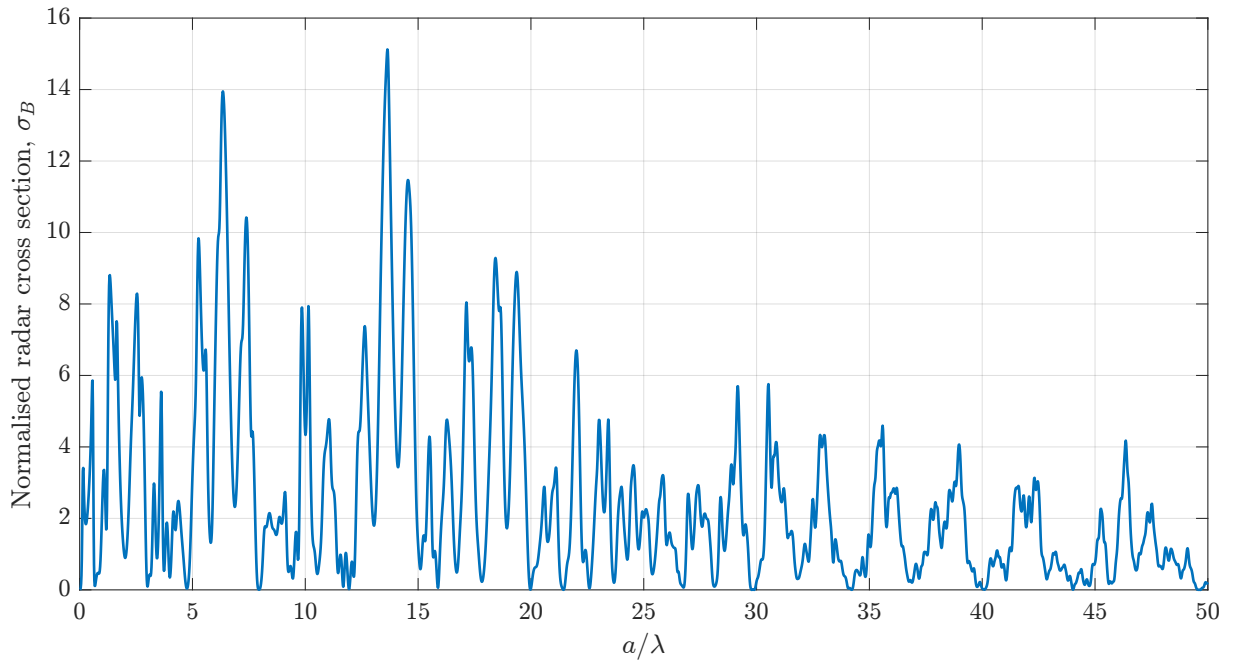
Figure 5.5: Frequency dependence of the normalised radar cross section of a semi-circular cavity ($\phi_1 = 90°$) in extended frequency range ($0 < ka \leq 100\pi$), incident angle $\alpha = 0$.

in which the complex oscillations possess sufficiently high $Q-$factors. Considering slotted cylinders of elliptical and rectangular shapes, we do not specifically focus on this phenomenon, but rather provide numerical results for selected sets of parameters which highlight the main distinctive features of resonance scattering. For slotted elliptic cylinders with $b/a = 0.5$, we examine both vertical and horizontal slits (Figure 5.8) with the following setups: for incident angles $\alpha = 0°, 90°$, we examine the slit widths of $w/a = 0.1, 0.5, 1$ and $w/b = 0.1, 0.5, 1$. This covers a variety of possible configurations related to the slit orientation and size.

We focus on one striking effect, which is present in many plots $\sigma_B (ka)$, but is especially pronounced for a slotted elliptic cylinder with relative slit width $w/a = 0.1$, which is excited by the normally incident ($\alpha = 90°$) plane wave (see 5.9a). This figure demonstrates the pronounced effect of the resonance duplet resulting in large fluctuations in the normalised radar cross section $\sigma_B (ka)$. In fact, at $ka = (ka)_{max} = 3.4451$ the value $\sigma_B ((ka)_{max}) = 3.21$ while at $ka = (ka)_{min} = 3.4498$ the value $\sigma_B ((ka)_{max}) = 0.32$.

Next, in a similar fashion, we consider resonance scattering from rectangular cavities of aspect ratio $a/b = 2$ with a small slit size $w/a = 0.1$, and large slit size $w/a = 1$ which is obtained by removing the broad wall a of the cavity completely. Resulting plots for incident angles $\alpha = 0°, 30°, 90°$ are collected in Figure 5.11.

We conclude the results for rectangular cylinders and this section by pointing out that

(a) $Re\gamma_{c01} = 1.9766$

(b) $Re\gamma_{c11} = 3.8577$
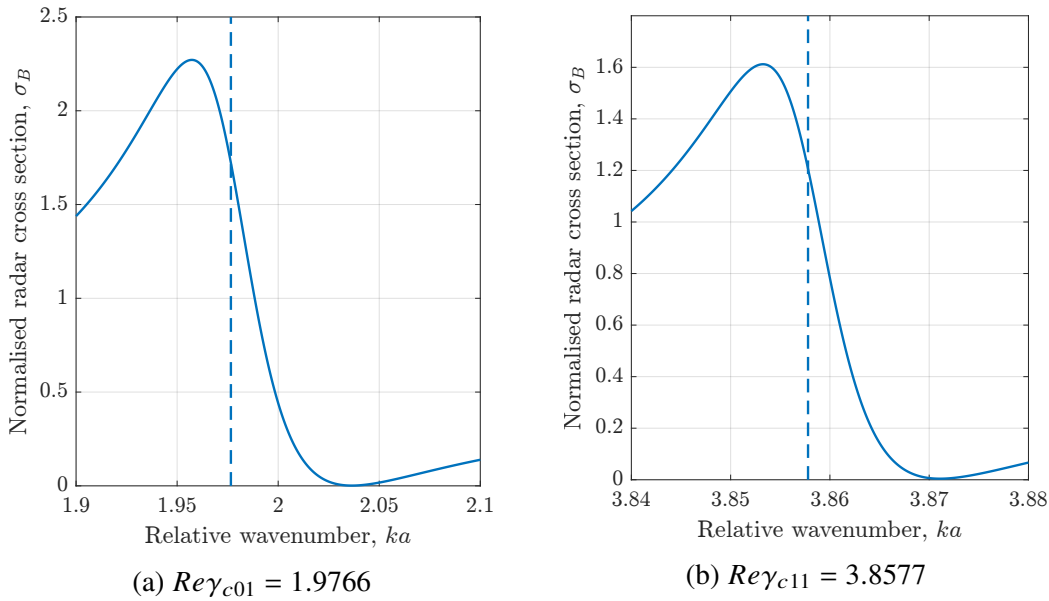
Figure 5.6: The normalised radar cross section for a slotted circular cylinder ($\phi_1 = 5°$) near the resonance frequency (blue dashed lines).

(a) TE_{c01}

(b) TE_{c11}
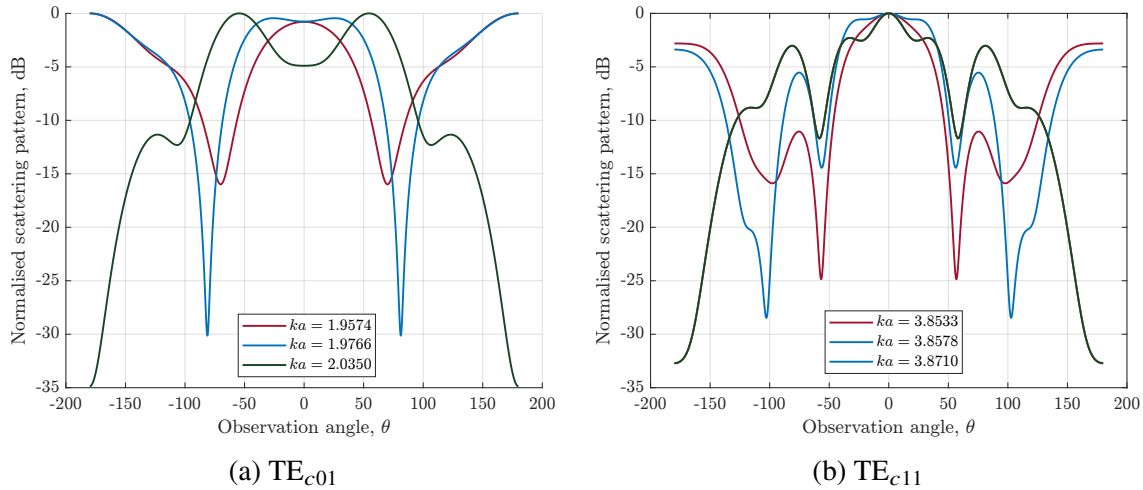
Figure 5.7: The normalised radiation pattern for a slotted circular cylinder ($\phi_1 = 5°$) at $Re\gamma_{cm1}$ and at a local minimum and maximum of radar cross section.

the qualitative behaviour of the normalised cross section is similar to that of circular and elliptic cavities. As shown in Figure 5.11 resonance response occurs at frequencies close to the real parts of the complex eigenvalues, and the response strength depends on the value of $Q-$factor and the incidence angle α.
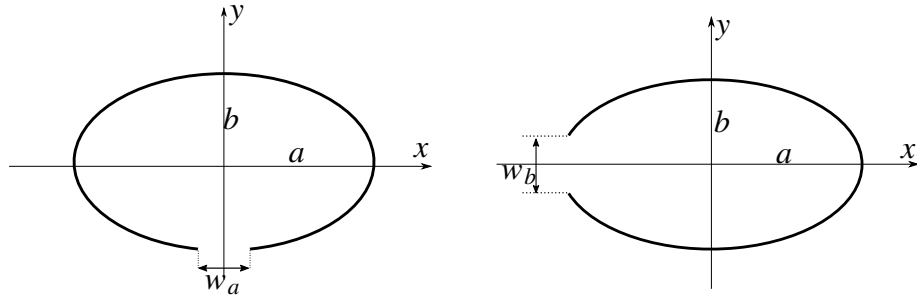
Figure 5.8: Elliptic slotted cylinders with variable slit placement.

5.3   Plane Wave Scattering from Duct-like Structures

In this section, we consider some examples of wave scattering problems for duct-like structures which are effectively solvable by the MAR. As a rule, studies of such type of structures are focused on specific geometries simulating for example, real shape of components in jet engine intakes. The ducts, abstracted from real geometries, are usually considered for testing, mostly with approximation techniques, to ensure their reliability for further application in studies of more complicated structures, the shape of which approaches that of a real duct. This explains the terminology "duct-like structures". In the context of this thesis, there is no practical reason to conduct an exhaustive spectral study for such duct-like structures, but rather to demonstrate the capability of the MAR to cope with such spectral and scattering problems. This has been partly shown in the earlier chapters of the thesis. Here, we focus on study of backscattering via computation of the normalised radar cross section for duct-like structures in a wide frequency band. The geometry and parameters of considered structures are shown in Figure 5.12.

In our systematic analysis of backscattering, we take a fixed geometrical size of the entry in each cavity. The other geometrical parameters may vary. Thus, the radar cross section σ_B in all cases is normalised by the same value πb, with b denoting the entry size. For an elliptic cavity entry $b = 2b_1$ is used, where b_1 is the minor semi-axis of the ellipse. The characteristics of scattering for semi-elliptic and rectangular ducts together with the normalised radar cross section and radiation patterns have already been considered using the MAR, when these structures are illuminated by $E-$polarised plane wave ([53, 55]). Open elongated semi-elliptical and rectangular cavities have a lot of similarities in the electromagnetic or acoustic sense. Let us recall the standard formula for rectangular cavities of sides a and b: the eigenfrequencies in
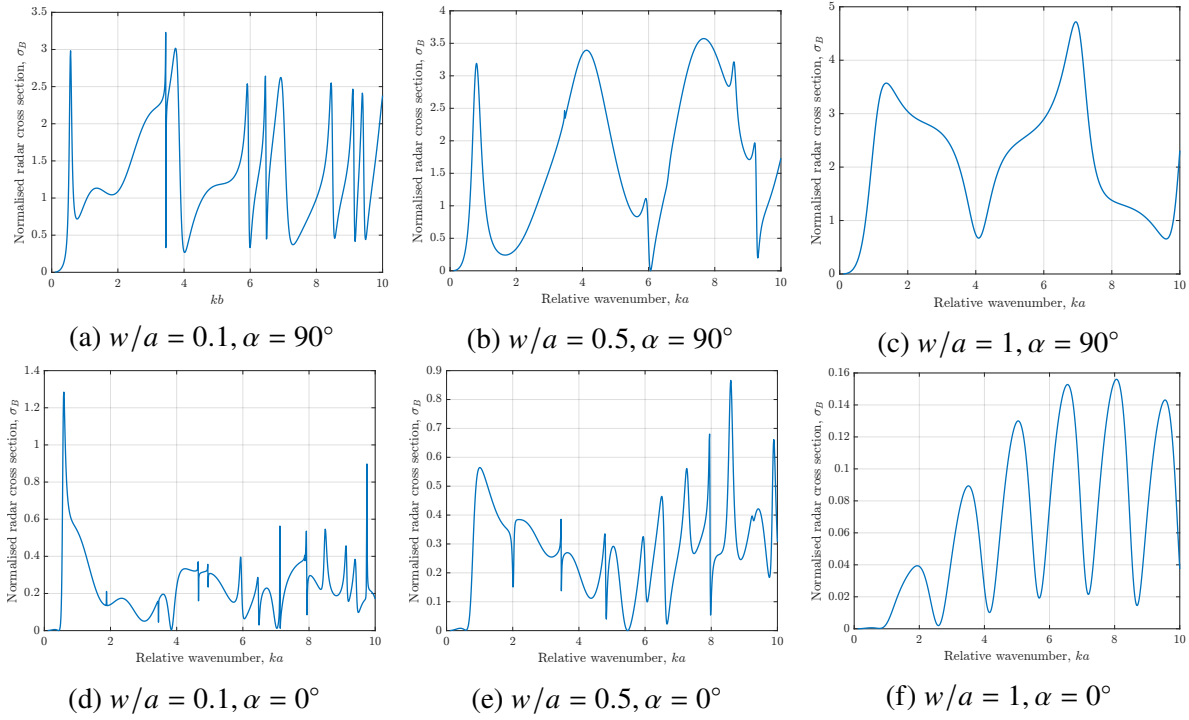
Figure 5.9: Frequency dependence of the normalised radar cross section of an elliptic cylinder with various vertical slit sizes and incident angles.
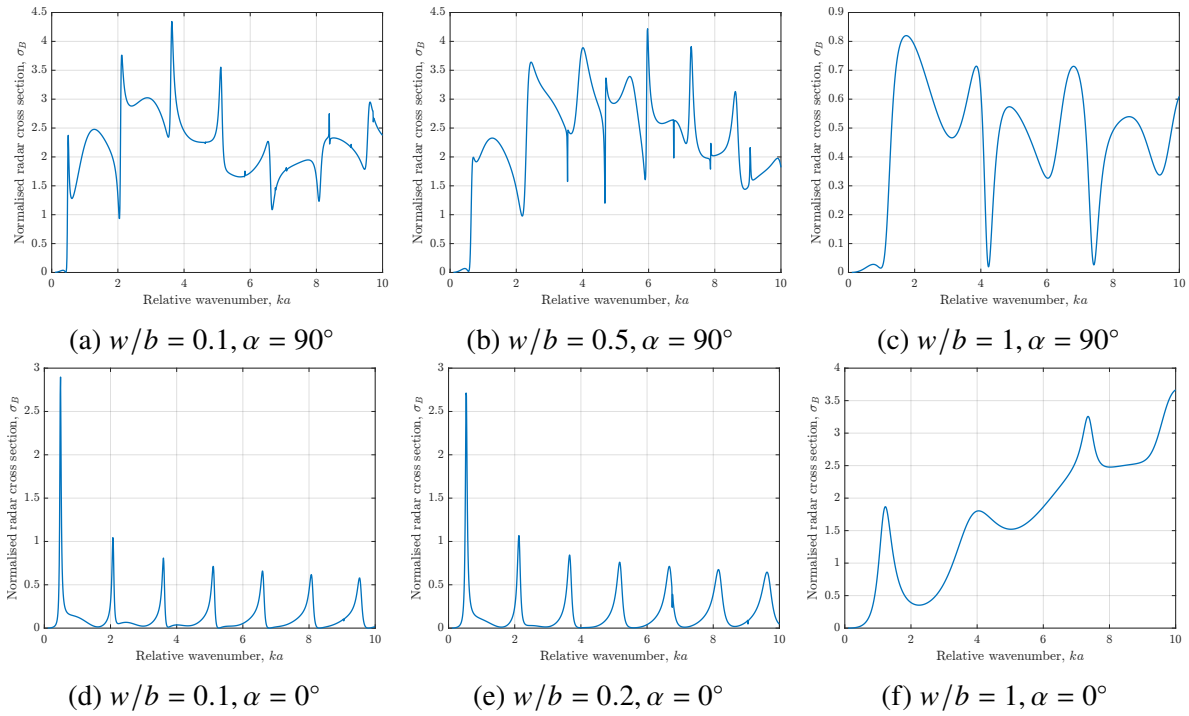
Figure 5.10: Frequency dependence of the normalised radar cross section of elliptic cylinder with various horizontal slit sizes and incident angles.

(a) $w/a = 0.1, \alpha = 0°$ (b) $w/a = 0.1, \alpha = 30°$ (c) $w/a = 0.1, \alpha = 90°$

(d) $w/a = 1, \alpha = 0°$ (e) $w/a = 1, \alpha = 30°$ (f) $w/a = 1, \alpha = 90°$
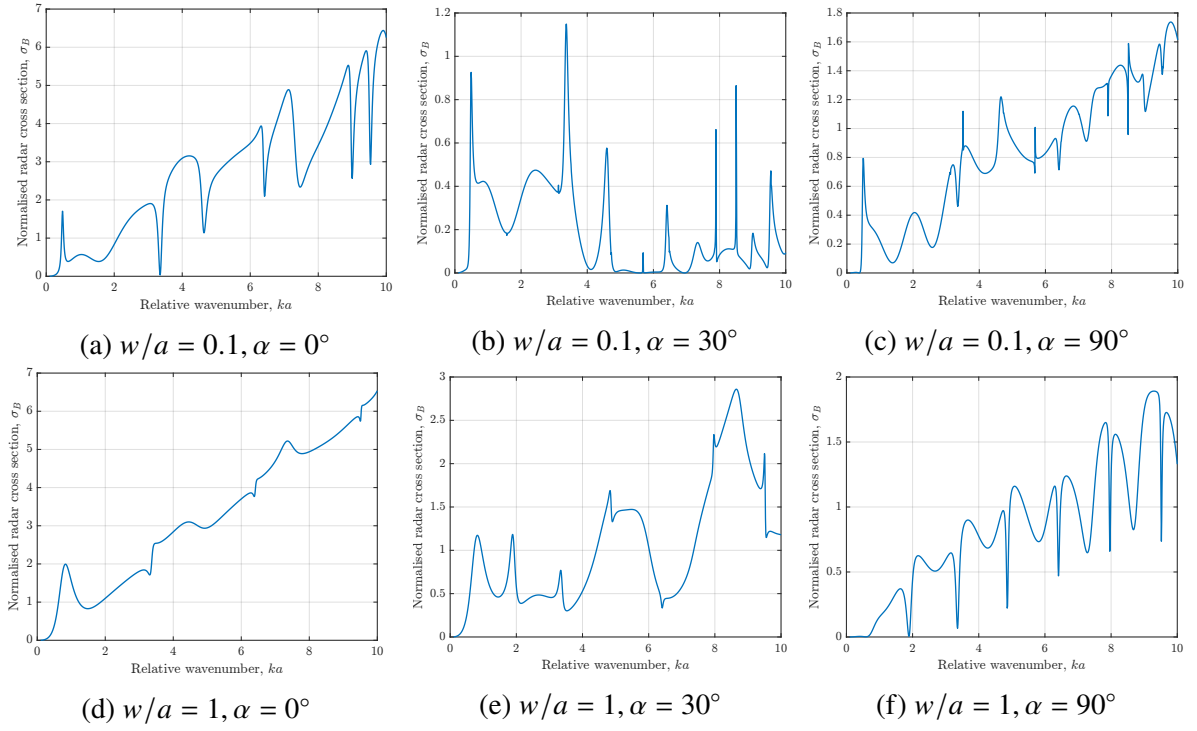
Figure 5.11: Frequency dependence of the normalised radar cross section of a slotted rectangular ($a/b = 2$) cylinder with slit sizes $w/a = 0.1, 1$ with various incident angles.

(a)   (b)   (c)
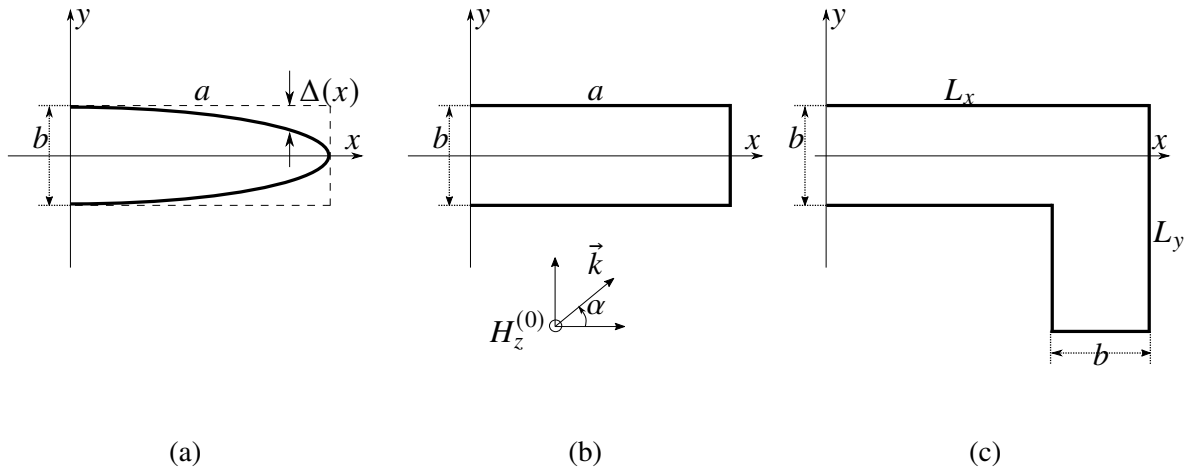
Figure 5.12: Geometry of duct-like cavities.

the form of relative wavenumbers $\gamma_{nm} = k_{nm}b$ are

$$\gamma_{nm} = n\pi\sqrt{1 + \left(\frac{m}{n}\right)^2\left(\frac{b}{a}\right)^2} \simeq n\pi\left\{1 + \frac{1}{2}\left(\frac{m}{n}\right)^2\left(\frac{b}{a}\right)^2, \quad \frac{b}{a} \ll 1\right\} \tag{5.12}$$

where indexes $m, n = 0, 1, 2...$, $m^2 + n^2 \neq 0$ describe the number of variations in the electromagnetic waves between narrow and broad walls of the waveguide, correspondingly. For an infinitely long resonator with parallel plates, when $b/a \to 0$, $\gamma_{nm} \to \gamma_n = n\pi$, $n = 1, 2, \ldots$.
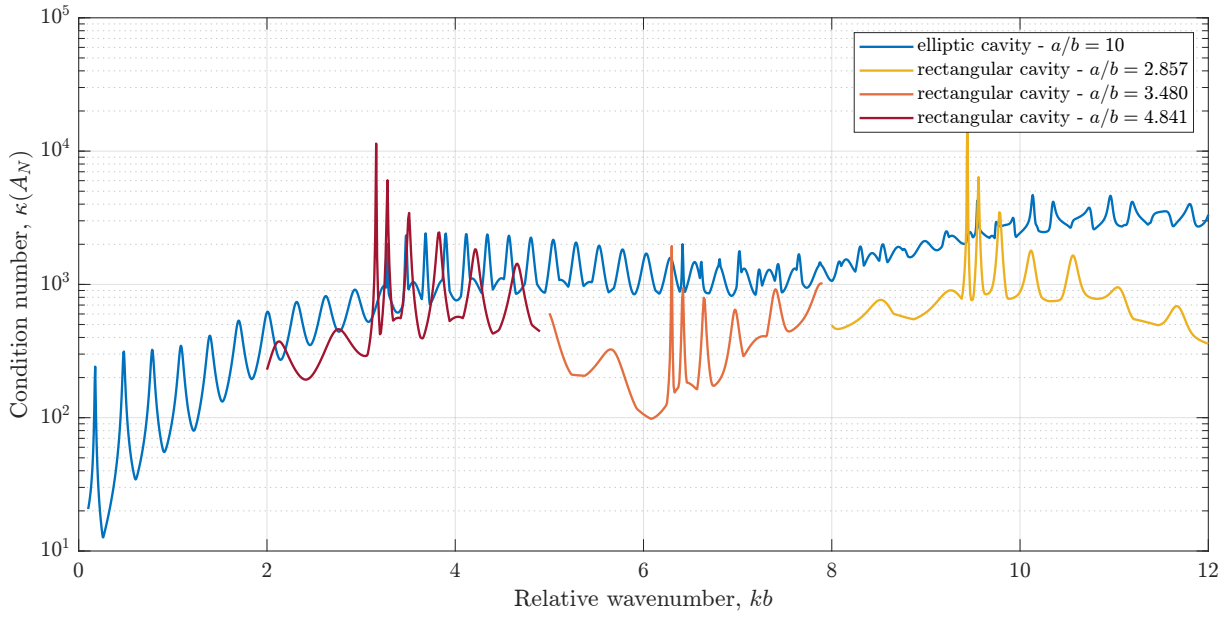
Figure 5.13: Combined condition number as a function of relative wavenumber for elliptic and rectangular ducts.

From a geometrical viewpoint, the semi-elliptic cavity inscribed into the open rectangular cavity is close to the shape of the rectangular cavity in the part adjoining the common entry of both cavities. In the electromagnetic sense, the part of the semi-elliptic cavity occupying the region bounded by the cavity entry ($x = 0$, $y = \pm b$) and the plane defined by the choice of some "critical" parameters $\left(x_c, y_c = \sqrt{1 - (x_c/a)^2}\right)$ cannot be distinguished from a rectangular cavity ($0 \leq x \leq x_c$, $|y| \leq y_c$). Total deviation of the elliptical shape from the rectangular one may be quantified by

$$2\Delta\left(x_c\right) = b\left(1 - \sqrt{1 - (x_c/a)}\right). \tag{5.13}$$

In antenna techniques, it is well known that, if a reflector surface deviates from ideal shape by a value of less than $\lambda/16$, then both surfaces (ideal and "deviated") are practically indistinguishable in an electrical sense. Fulfilment of the condition $2\Delta\left(x_c\right) \leq \lambda/16$, defines the critical value x_c/a:

$$\frac{x_c}{a} = \left(\frac{\pi}{2kb}\right)\sqrt{\frac{kb}{\pi} - \frac{1}{16}}. \tag{5.14}$$

Using a simple estimate $kb \approx \gamma_n \simeq n\pi$ for the resonance value kb in the highly elongated semi-elliptic cavities ($b/a \to 0$) we obtain the following approximate formula for the critical parameter: $(x_c/a) \simeq \left(\frac{1}{2n}\right)\sqrt{n - \frac{1}{16}}$. For $n = 1, 2, 3$, we obtain $x_c/a = 4.841, 3.480, 2.857$, respectively.

It can be assumed that the part of semi-elliptic cavity defined by $0 < x < x_c$ is the region

where the dominant complex oscillations are formed. The fragments of the spectral maps the for semi-elliptical cavity ($a/b = 10$) and three sizes of rectangular cavity obtained by multiplication of the aspect ratio $a/b = 10$ by the parameter x_c/a shown in Figure 5.13 reveal, in general, the consistency of our arguments. Due to the similarity in spectral maps of these two open cavities, a similar behaviour of the radar cross section $\sigma_B (kb)$ is expected at the resonance points when the variable kb matches the real part of one of the complex eigenvalues of the dominant oscillations. However, it is not the decisive factor in formation of the main backscattering mechanism. The nature of backscattering is defined by merely interference phenomenon between the field (or rays) reflected from the edges of cavities and the field which passes into the cavity, reflects from the cavity wall and returns to the entry with a certain phase change. Whether these two fields are in-phase or anti-phase determines the maximum or minimum of the normalised radar cross section $\sigma_B (kb)$, respectively.

(a) $a/b = 2$ (b) $a/b = 10$ (c) $a/b = 20$

Figure 5.14: The frequency dependence of the normalised radar cross section for deep rectangular cavities, incident angle $\alpha = 0°$.

This qualitative prediction is confirmed by the computed dependence $\sigma_B (kb)$ for an open rectangular cavity at the normal ($\alpha = 0°$) incidence for $a/b_1 = 2, 10, 20$, as shown in Figure 5.14. The plot $\sigma_B (kb)$ is of oscillatory character, where the wave distance between neighbouring maxima (and minima) Δa tends to $\lambda/2$ as the wave size a/λ of the cavity increases.

A different situation arises when a plane wave is normally incident on an elongated semi-elliptical cavity. Again, using the simplified geometrical optics (GO) concept, one may argue that the reflected field (array) from the edges is the same as for a rectangular cavity, but reflection from the terminating region is completely different. Ideally, at high frequencies the flat termination of the rectangular cavity reflects incoming rays normal to its surface and the reflected rays pass way back to the entry of cavity without repeated reflections. By contrast, reflection from the terminating surface of the semi-elliptical cavity occurs at various angles along the $x-$axis.

This leads to numerous repeated reflections from the walls of cavity before the rays finally reach the entry. Such complexity might be expected to be clearly seen in the dependence $\sigma_B(kb)$ for the semi-elliptical cavity. However, it is known that the GO approximation works surprisingly well even when the usual criteria for its use are not fulfilled. At least, the wavelength λ should be much smaller than the characteristic size D of the scatterer ($\lambda \ll D$) in order to use the ray tracing technique. Nevertheless, the computed plots $\sigma_B(kb)$ for deep semi-elliptical cavities confirm this practical observation. In Figure 5.15, where the plots $\sigma_B(kb)$ are presented for semi-elliptical cavities with the values of parameter $a/b = 2, 10, 20$, the transition of regular oscillations $\sigma_B(kb)$ to their complex pulsations occur after a threshold value $kb \approx 2\pi$ ($b \approx \lambda$) is observed for all values a/b.
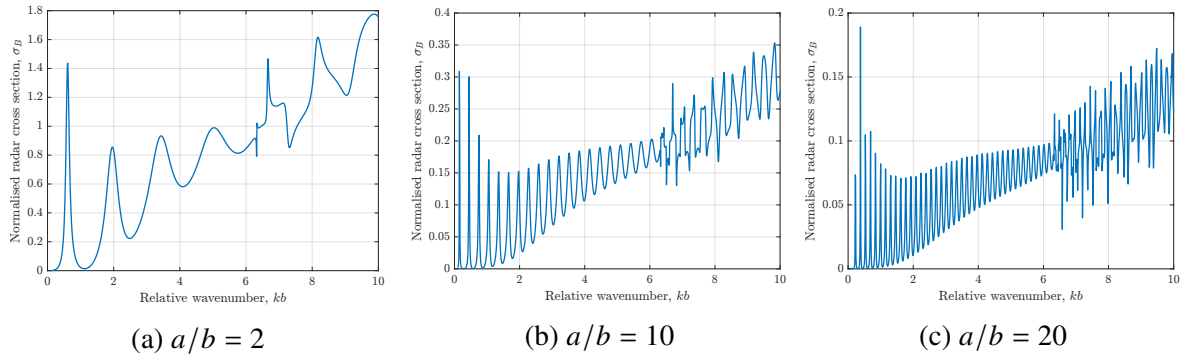

(a) $a/b = 2$ (b) $a/b = 10$ (c) $a/b = 20$
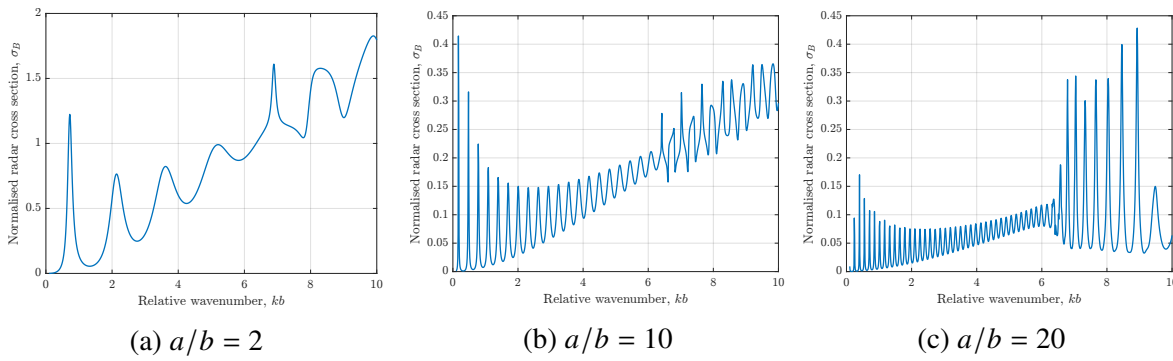
Figure 5.15: The frequency dependence of the normalised radar cross section for deep semi-elliptic cavities, incident angle $\alpha = 0°$.

(a) $\alpha = 45°$ (b) $\alpha = 90°$ (c) $\alpha = 135°$
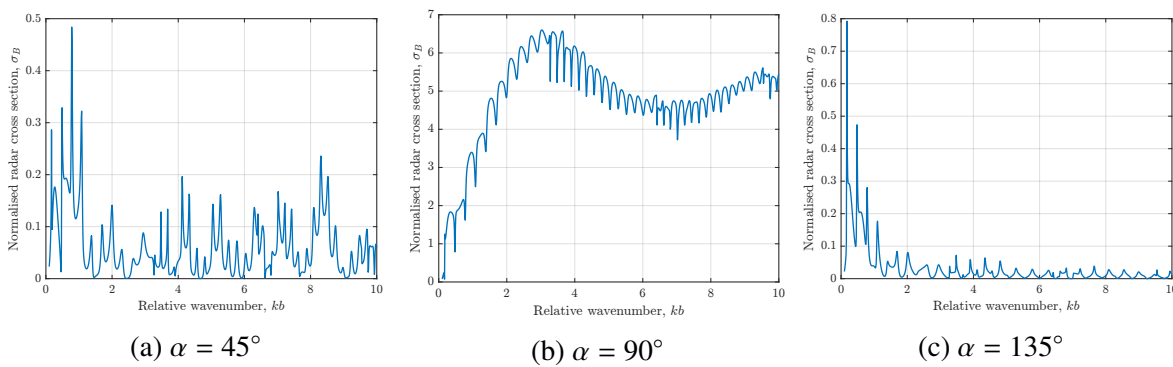
Figure 5.16: The frequency dependence of the normalised radar cross section for semi-elliptic cavity $a/b = 10$ with various incident angles.

We should comment on the high level of backscattering which is revealed in the normalised radar cross section plot for the deep semi-elliptic deep cavity with $a/b = 10$ and the incident angle $\alpha = 90°$ in Figure 5.16b. This is due to the normalisation of the radar cross section by πb which can be recalculated as follows: $\sigma_B/\pi a = 0.1\sigma_B/\pi b$ since $a/b = 10$. In fact,

the backscattering should be close to that of a plane strip when the incident angle is $\alpha = 90°$ or $\alpha = 270°$. The numerical results for $\sigma_B/\pi a$ (a plane wave incident on broad wall) and $\sigma_B/\pi b$ (plane wave incident on narrow wall) are in good agreement with asymptotic value ($ka_s \gg 1$) of the radar cross section for a strip of width a_s, since $\sigma_B/\pi a_s \simeq ka_s$.

In the final part of this chapter, we briefly analyse backscattering from bent duct cavities. In our parametrisation of this shape the bend angle is the variable shown in Figure 5.17.
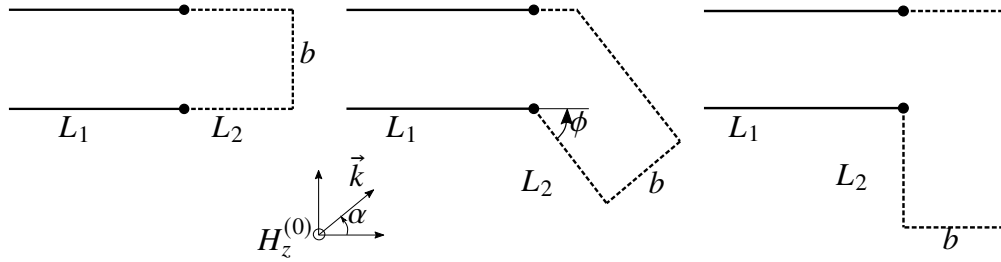
Figure 5.17: Excitation of slotted cylinders with a bend by obliquely incident $H-$polarised plane wave.

We limit ourselves to computation of the normalised radar cross section and compare backscattering for non-bent ($\phi = 0°$) and slightly bent ($\phi = 10°$) ducts. The non-bent duct is of course the already studied open straight rectangular cavity. The plots $\sigma_B(kb)$ for values $L_1 = 2, L_2 = 2, b = 1, \phi = 0°$ and $\phi = 10°$ are shown in Figure 5.18. For bigger ducts $L_1 = 5, L_2 = 5$ and, keeping rest of parameters the same ($b = 1, \phi = 0°$ and $\phi = 10°$), the dependence $\sigma_B(kb)$ is shown in Figure 5.19.
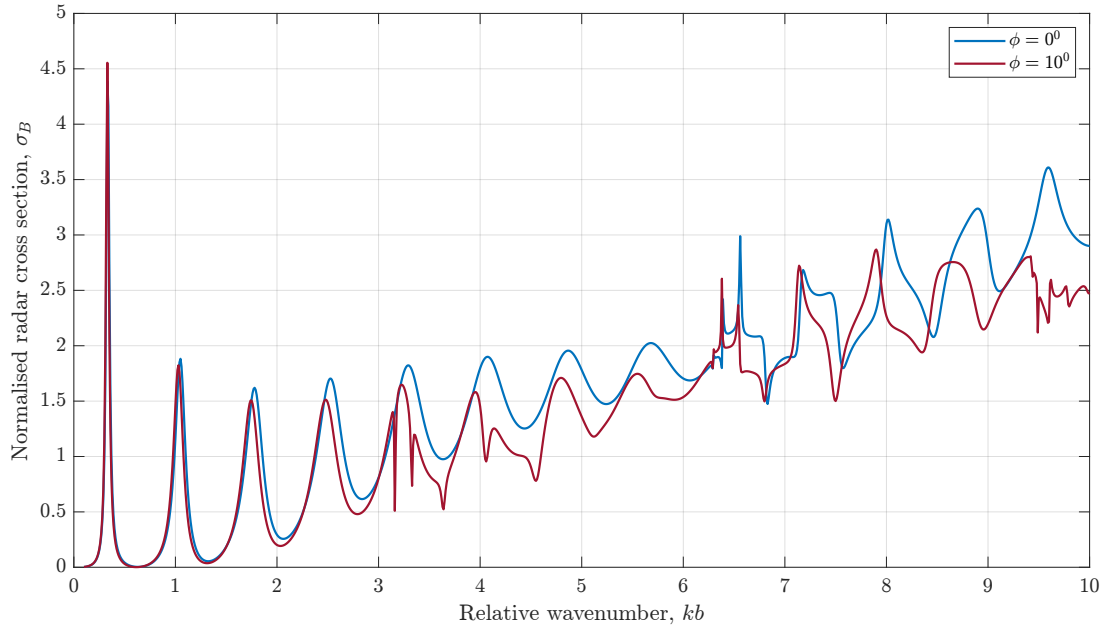
Figure 5.18: Frequency dependence of the normalised radar cross section for bend ducts, $L_1 = 2, L_2 = 2, b = 1, \phi = 0°$ and $\phi = 10°$, incident angle $\alpha = 0°$.
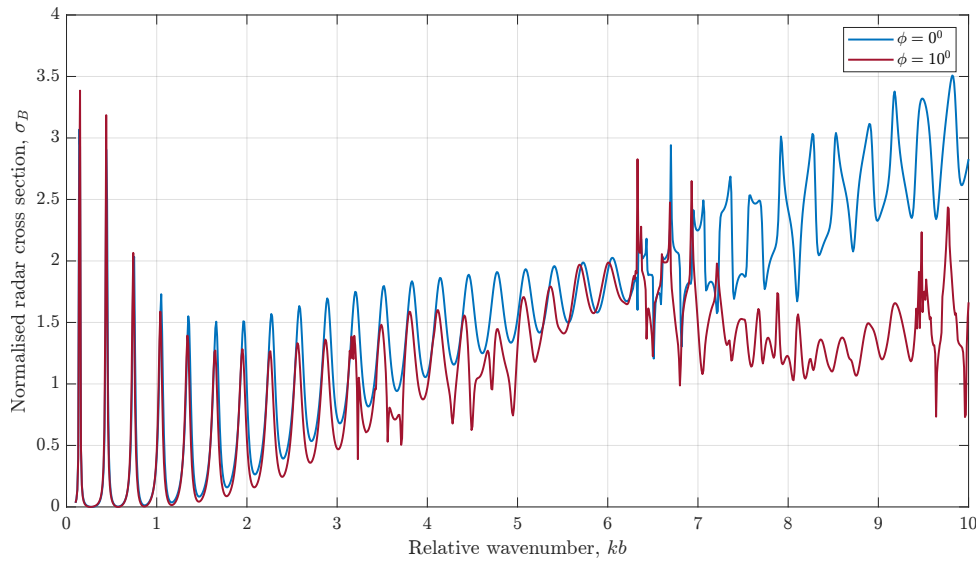
Figure 5.19: The frequency dependence of the normalised radar cross section for bend ducts, $L_1 = 5, L_2 = 5, b = 1, \phi = 0°$ and $\phi = 10°$, incident angle $\alpha = 0°$.

It can be clearly seen in both figures that for the first part of the frequency range the normalised radar cross section $\sigma_B(kb)$ for both bend angles $\phi = 0°$ and $\phi = 10°$ are quite similar. The divergence between the two plots starts to appear after the relative kb wavenumber passes a threshold value $kb \sim \pi$, i.e., when $b \sim \lambda/2$. When the bend angle $\phi = 90°$, the bent duct resembles a corner reflector of thickness b. One may expect that a plane wave striking the bent duct at incident angle $\alpha = 45°$ will initiate a very strong backscattering that is characteristic of a right-angled corner reflector. To confirm this assertion, we provide normalised radar cross

(a) $\alpha = 0°$ (b) $\alpha = 45°$
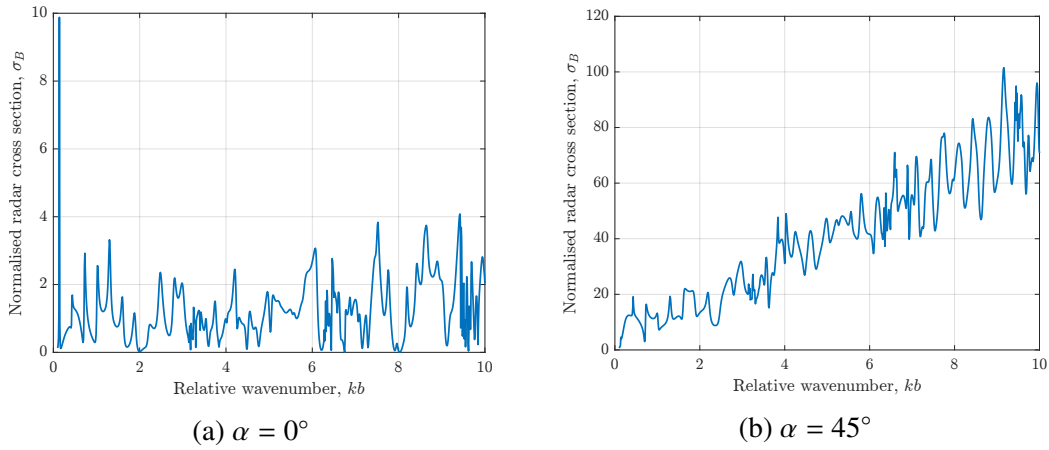
Figure 5.20: Frequency dependence of the normalised radar cross section for a bend duct with parameters $L_1 = 5, L_2 = 5, b = 1, \phi = 90°$, incident angles $\alpha = 0°$ and $\alpha = 45°$.

section plots for a bent duct with $L_1 = 5$, $L_2 = 5$, $b = 1, \phi = 90°$ and with incident plane wave angles $\alpha = 0°$ and $\alpha = 45°$ (Figure 5.20). The high level of back scattering $\sigma_B(kb)$ can easily be seen in the plot of $\sigma_B(kb)$.

6

A Selective Overview of Advanced Applications of the MAR

In this chapter, we further demonstrate the potential of the MAR for diverse advanced applications of wave scattering which are free from limitations on frequency range and geometry of the open structures often encountered by other methods. The demonstration is introductory and illustrative, since each problem listed in this chapter of necessity deserves investigations on a large scale and might be a subject of numerous publications or a separate thesis. It is our contention that the results presented here provides a clear guide on using the MAR for comprehensive studies of numerous problems arising in practice. In using the term diverse, we mean problems of a rather contrasting nature.

We start our analysis with two problems related to reflector antennas and usually considered in high-frequency region. First, we investigate the classical cylindrical parabolic antenna and its modified version with attached flanges. Then we move to another well-known type of reflector, the corner reflector. Both types of reflectors operate at such frequencies that the aperture size D significantly exceeds the wavelength λ of incident electromagnetic (or acoustic) field, i.e. $D/\lambda \gg 1$.

The next problem concerns finite sinusoidal gratings. Keeping in mind the multi-aspect nature of the considered problems and the illustrative character of this chapter, we concentrate

on two most important aspects that always arise in investigations of finite periodic structures. The first is the applicability of theoretical results obtained for infinite periodic structures to their finite counterparts. The second is to answer the question: to what extent is the grating formula, defining the radiating angles of the diffraction beams, accurate for finite gratings?

We conclude this chapter by demonstrating the application of the developed method for studies of the radar response of targets with complex shape. As an example, we consider simplified contours of a plane and a submarine. The calculations cover a wide frequency range with the target wave size L/λ where characteristic size L varying from low ($L/\lambda \ll 1$) to high ($L/\lambda \gg 1$) values. Calculations are carried out for both near- and far-field regions.

Before finishing this introduction, we note that fast convergence of the MAR allowed us to use truncation number $N = 512$ for calculations in this chapter, irrespective of their complex geometry and the frequency region we investigate. We have also performed some calculations with bigger system sizes to demonstrate high efficiency of the developed numerical algorithms along with the computation time. We must also note that the references made in this chapter do not necessarily reflect the paramount significance of the investigations presented in these sources but were chosen simply to help describe the-state-of-the-art of theoretical analysis.

6.1 Cylindrical Parabolic Reflector Antennas

We consider two types of cylindrical antennas of parabolic shape operating in the receiving regime: the classical parabolic cylindrical reflector (flange width $w_f = 0$) and a reflector with attached flanges ($w_f > 0$) shown in Figure 6.1. The cylindrical parabolic reflector in reduced Cartesian coordinates $x_F, y_F, (x_F = x/F, y_F = y/F)$, where F is the focal distance, is described by the parabola

$$y_F = -\frac{1}{4}x_F^2 + 1.$$

The reflector is characterised by the focal distance F and the aperture size D. In practice, there are two widely used parameters for describing parabolic antennas: The first is $p = F/D$, the ratio of the focal distance F and size of aperture D which defines the geometrical configuration of reflector. The second one is the ratio D/λ which defines the wave size of reflector. If an infinite parabola is excited by a plane wave, operating at extremely high frequencies, the reflected radiation is focussed to one single point: *the focal point*. The theory predicting such behaviour of reflected radiation is based on geometrical optics (GO) concepts, where the plane wave may
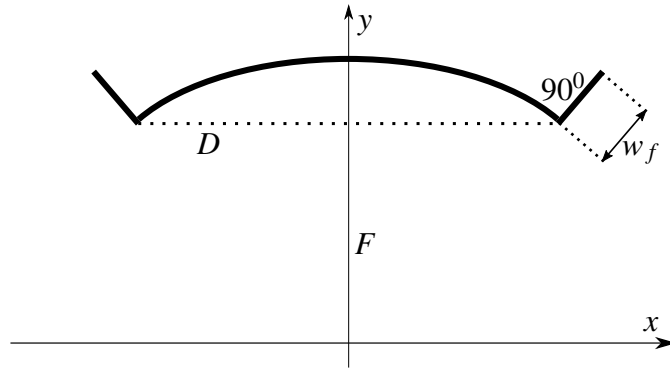
Figure 6.1: Parabolic reflector: classical ($w_f = 0$), with attached flanges ($w_f > 0$).

be presented as a bundle of parallel rays. In practise, antennas have a shape of a finite parabola, operating with finite values of wavelength. Therefore, the reflected wave is not focused in a single point, but in a *focal region*, the characteristic size of which is equal to roughly one wavelength λ. The formation of focal spot or region slightly shifts the location of the intensity maximum from the idealized GO focal line. Let us illustrate this concept by a few examples for parabolic reflectors ($w_f = 0$) with parameters $p = 0.5, 1$ and $D/\lambda = 40, 80$. For visualisation of the focusing effect, it is convenient to use our computation of the spatial distribution of the magnetic field density $\left|H_z^{tot}\right|$, considering the "deep" ($p = 0.5$) and "shallow" ($p = 1$) reflectors with wave sizes $D/\lambda = 40$ and 80. The results for these two reflectors are shown in Figure 6.2.

The formation of the focal region can easily be observed in the distribution of $\left|H_z^{tot}\right|$, presented in these figures. A distinctive feature of the distribution of the electromagnetic field in the focal region is the train of maxima instead of a single focused focal point. Despite that the geometrical size of focal region decreases as wave size of the reflector D/λ increases, the size of this region, measured in wavelengths, remains constant. A rough estimate for the area of the focal region is λ^2. For all values of parameters F/D, the longitudinal size of the focal region exceeds the value of wavelength λ, while the transverse size is smaller than λ. Knowledge of the fine structure of the field distribution in focal region is quite necessary for the design of effective line feeds often used in antenna techniques. A suitably designed line feed provides a source with distributed parameters which (ideally) should match the amplitude-phase distribution of the focused field in the focal region of the receiving reflector antenna. Its use significantly improves the effectiveness of transmission. More detail of the structure of the magnetic field

(a) $D/\lambda = 40$, $F/D = 0.5$

(b) $D/\lambda = 80$, $F/D = 0.5$

(c) $D/\lambda = 40$, $F/D = 1$

(d) $D/\lambda = 80$, $F/D = 1$
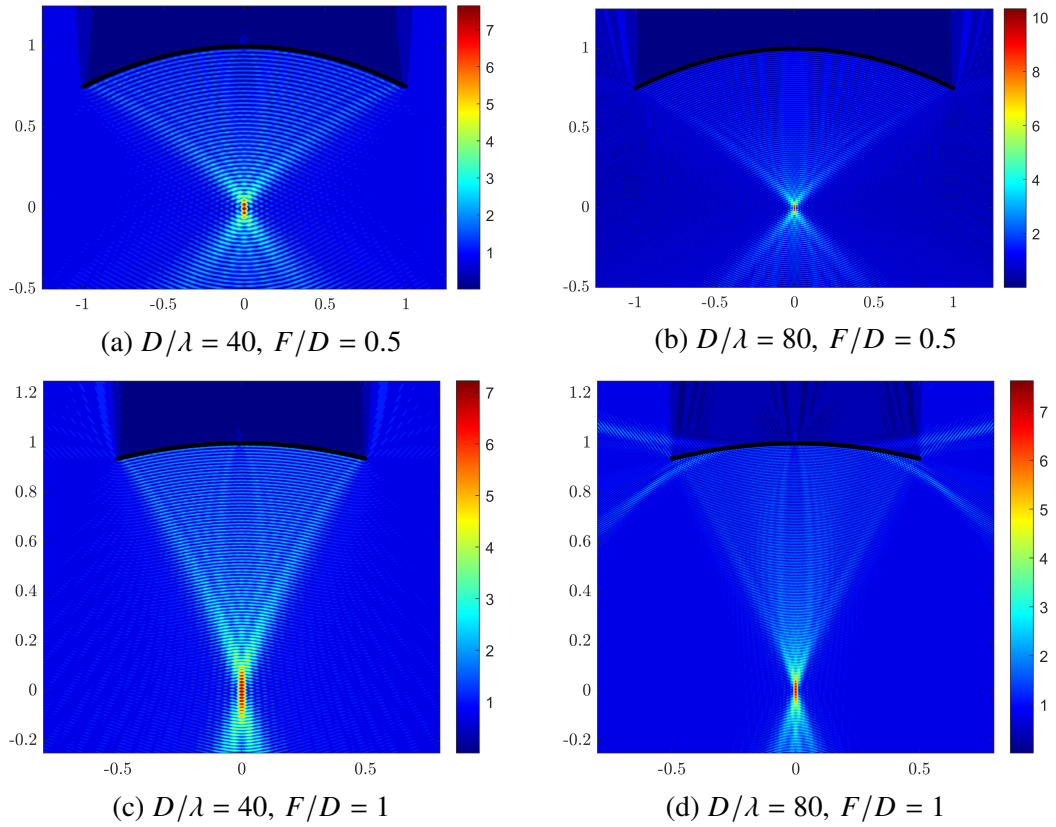
Figure 6.2: Distribution of $\left|H_z^{tot}\right|$ for a parabolic reflector deep ($F/D = 0.5$), and shallow ($F/D = 1$), incident angle $\alpha = 90°$.

$\left|H_z^{tot}\right|$ in the focal region may be seen in the plots of $\left|H_z^{tot}(y_F)\right|$ shown in Figure 6.2. Before turning to parabolic reflector antennas with attached flanges, it is worth noting that effective control of the off-axis and backward radiation of reflector antennas is a relevant problem in many applications in radio astronomy, radars, and telecommunications. Two techniques that are widely used to address this problem are considered: modifying the geometry of the reflector rim, and loading the reflector rim with absorbers. It was shown in [122] and [123] that the best behaviour is obtained by using a right-angled flange (i.e., a flange forming a right angle with the reflector surface), and that a significant field level reduction can be obtained in a wide angular sector at the rear without affecting the field radiated in the forward half-space. For theoretical analysis, the geometrical theory of diffraction (GTD), equivalent edge currents, and physical optics (PO) have been used in proper angular sectors. All of these well-established methods are widely used in modelling practical reflector antennas, but in many cases their accuracy is uncertain, especially when the operating frequency range is far from the high-frequency region. On the other hand, the MAR approach extended for analysis of arbitrary 2D configurations is valid over the full range of angular frequencies and electrical sizes of reflectors, delivering a predefined accuracy

(a) $D/\lambda = 20$, $F/D = 0.5$

(b) $D/\lambda = 40$, $F/D = 0.5$

(c) $D/\lambda = 20$, $F/D = 1$

(d) $D/\lambda = 40$, $F/D = 1$
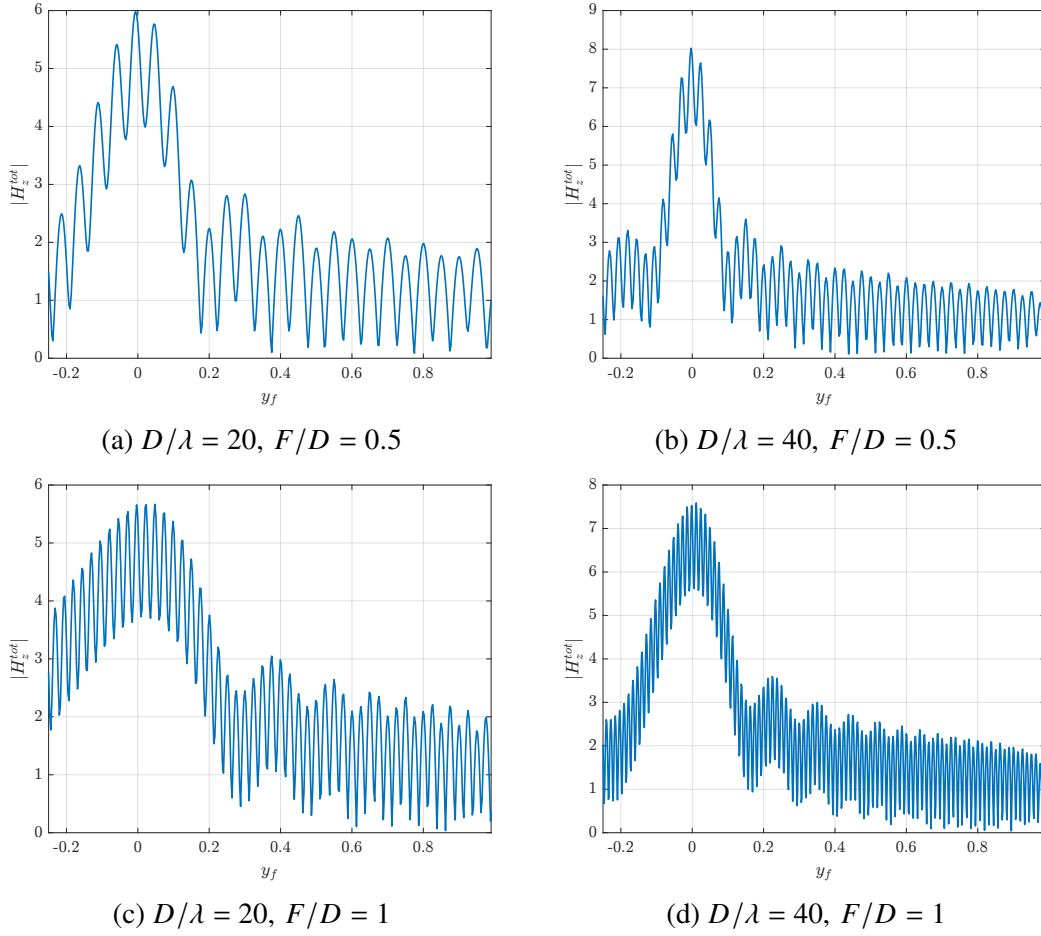
Figure 6.3: Distribution of $\left|H_z^{tot}\right|$ for a parabolic reflectors ($F/D = 0.5$ and 1) as a function of y_f at $x_f = 0$, incident angle $\alpha = 90°$.

of computation. Although we do not conduct an exhaustive investigation for the operation of flanged antennas nor a critical analysis of the results contained in [122], we present illustrative results which clearly demonstrate the applicability of the MAR to the considered problem. One convenient way to analyse the behaviour of reflector antennas with and without flanges is through the distribution of the total field $\left|H_z^{tot}\right|$. An example for a flanged parabolic reflector with parameters $F/D = 1$, $D\lambda = 20$, $w_f/D = 0.1$ is shown in Figure 6.4.

Let us now we focus on the field density behind the reflector (the shadowed region) and compare the density levels for parabolic reflectors with and without flanges attached in Figures 6.5 and 6.6. To emphasise the difference, we use very large flanges ($w_f = 0.2D$). One can observe the weak appearance of the Poisson's spot emerging behind the reflector in Figure 6.6, the difference between the two configuration can be seen clearly in Figures 6.5b and 6.6b by comparing the level of $\left|H_z^{tot}\right|$ in the region $x_f = 0$, $y_f = 1$ to $y_f = 1.05$. This phenomenon, also known as Arago's spot, explains the bright spot at the centre of the parabolic reflector
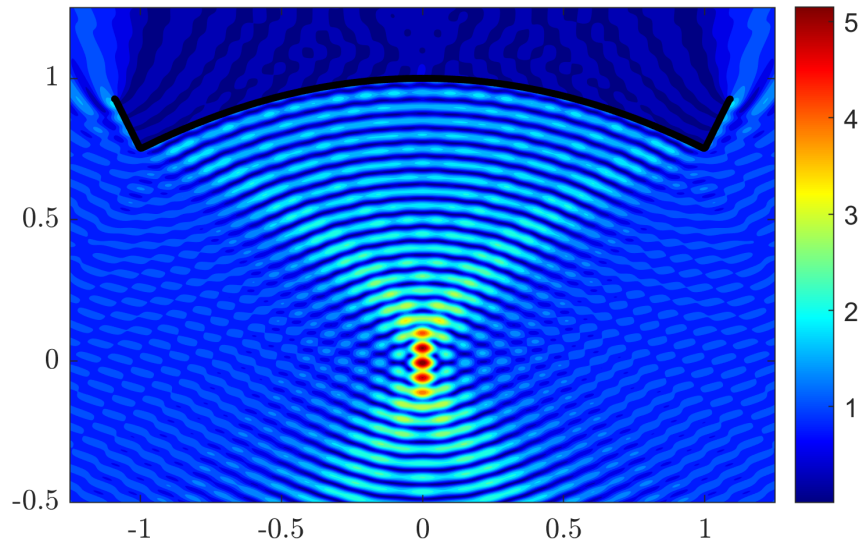
Figure 6.4: Distribution of $\left|H_z^{tot}\right|$ for a parabolic reflector ($F/D = 1, D/\lambda = 20$) with flanges $w_f/D = 0.1$, incident angle $\alpha = 90°$

(a)   (b)

Figure 6.5: a) Distribution of $\left|H_z^{tot}\right|$ for a parabolic reflector ($F/D = 1$, $D/\lambda = 10$, $w_f = 0$) and b) as a function of y_f at $x_f = 0$, incident angle $\alpha = 90°$.

(a)   (b)
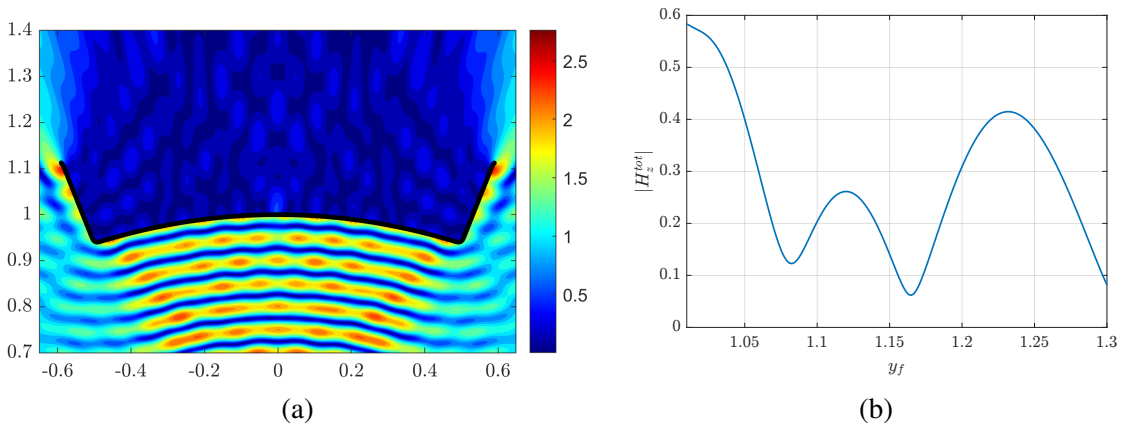
Figure 6.6: a) Distribution of $\left|H_z^{tot}\right|$ for a parabolic reflector ($F/D = 1$, $D/\lambda = 10$, $w_f = 0.2$) and b) as a function of y_f at $x_f = 0$, incident angle $\alpha = 90°$

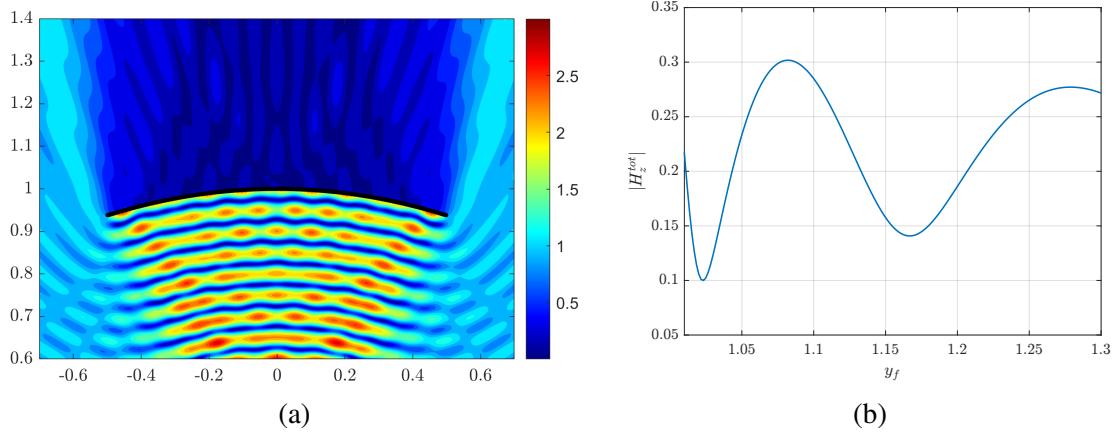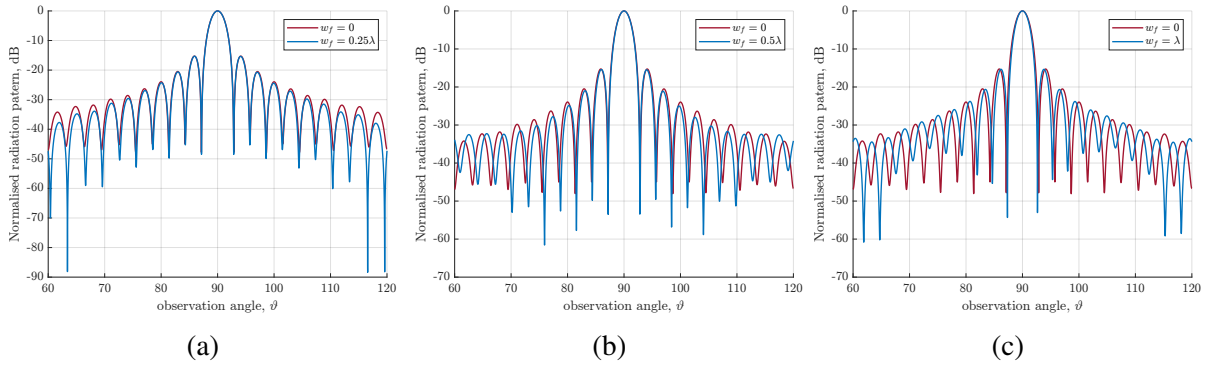Figure 6.7: Radiation pattern for a parabolic reflector antenna ($D/\lambda = 10$, $F/D = 0.5$), incident angle $\alpha = 90°$.
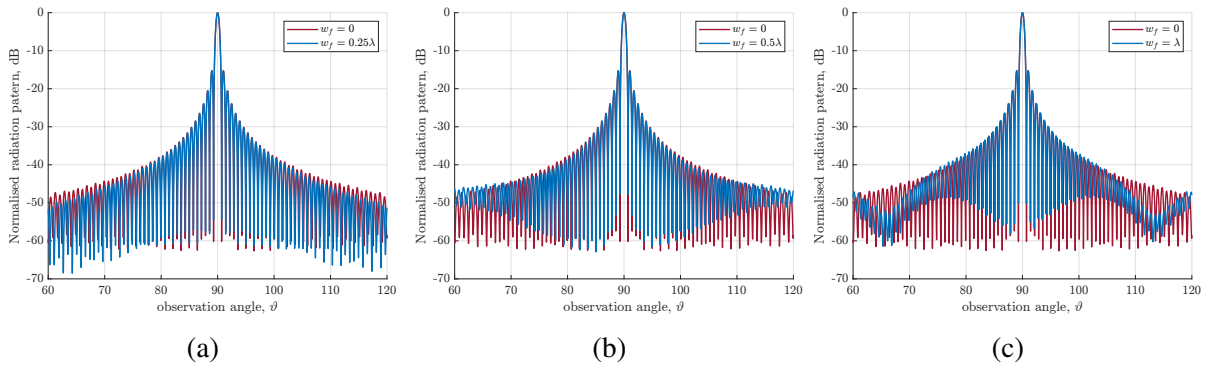
Figure 6.8: Radiation pattern for a parabolic reflector antenna ($D/\lambda = 40$, $F/D = 0.5$), incident angle $\alpha = 90°$.

shadow, which becomes nearly as bright as if the obstacle were absent. Without seeking the truly optimal choice of the wave size of the flanges, let us calculate the radiation patterns of reflector antennas for various sizes of flanges. In these calculations, we use the settings: $D/\lambda = 10, 40$, and $w_f = 0, \lambda/4, \lambda/2, \lambda$. So, from the initial illustrative example involving large flanges ($w_f = 0.2D$), we turn to more realistic values of $D/\lambda = 10$ (with $w_f = 0.025, 0.05, 0.1$), and $D/\lambda = 40$ (with $w_f \simeq 0.0062, 0.0125, 0.025$). The radiation patterns presented in Figures 6.7 and 6.8 reveal notable influence of the flanges on the decrease of the side-lobe level in the far-field. The level of decrease strongly related to size of the flanges. The most pronounced effect in reduction of the side-lobe level is revealed in Figure 6.8c (for $w_f = \lambda$, $D/\lambda = 40$, $F/D = 0.5$). The drops in the pattern are observed in the angular sectors $65° < \theta < 75°$ and $105° < \theta < 115°$, where a drop from $0.5dB$ to $8dB$ across the observation angles can be seen. The parametrisation of the parabolic reflector and flexibility to analyse any desired frequency range makes the MAR a suitable tool to conduct further studies on optimisation of parabolic reflectors and on the effect of flanges, in terms of their size and orientation.

6.2   Right-angled Corner Reflectors

Corner reflectors are standard passive radar targets which offer one of the best solutions for SAR (synthetic aperture radar) calibration. Radar cross section (RCS) of corner reflectors plays a vital role for estimation of the calibration parameters and, hence, of the back-scatter coefficient for airborne and spaceborne SAR images ([124]). Backscattering studies of corner reflectors have been successfully conducted by approximate asymptotic high-frequency techniques and various well-known methods of computational electromagnetics have been intensively used. In many cases, the RCS analysis of corner reflectors is based on physical optics (PO) which produces results sufficient for practical needs. In this section, we illustrate how the MAR approach may contribute to the theory of corner reflectors, focusing on the $90°$-dihedral corner reflector. The geometry of this structure is shown in Figure 6.9.
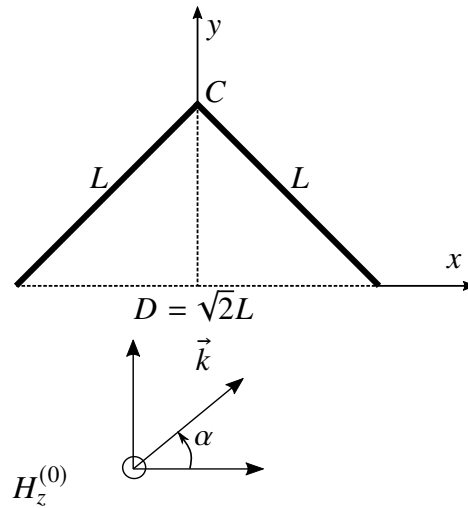
Figure 6.9: $90°-$dihedral (right angle) corner reflector.

The $90°-$dihedral corner reflector is formed by two equilateral PEC strips of length L meeting at the point C at the right angle. The aperture size of the reflector is $D = \sqrt{2}L$. According to basic GO, under a normally incident plane wave ($\alpha = 90°$) the incoming rays (through the aperture), after reflecting from both sides of the corner reflector return to aperture plane as a bundle of parallel rays. As a result, strong backscattering is expected to be generated. With an increase in the electrical size of the aperture ($D/\lambda \gg 1$), this phenomenon should become more pronounced. Plots of the distribution of $\left|H_z^{tot}\right|$ calculated by employing the MAR confirm this obvious assumption. Figure 6.10 contains the distribution for increasing values of D/λ ranging
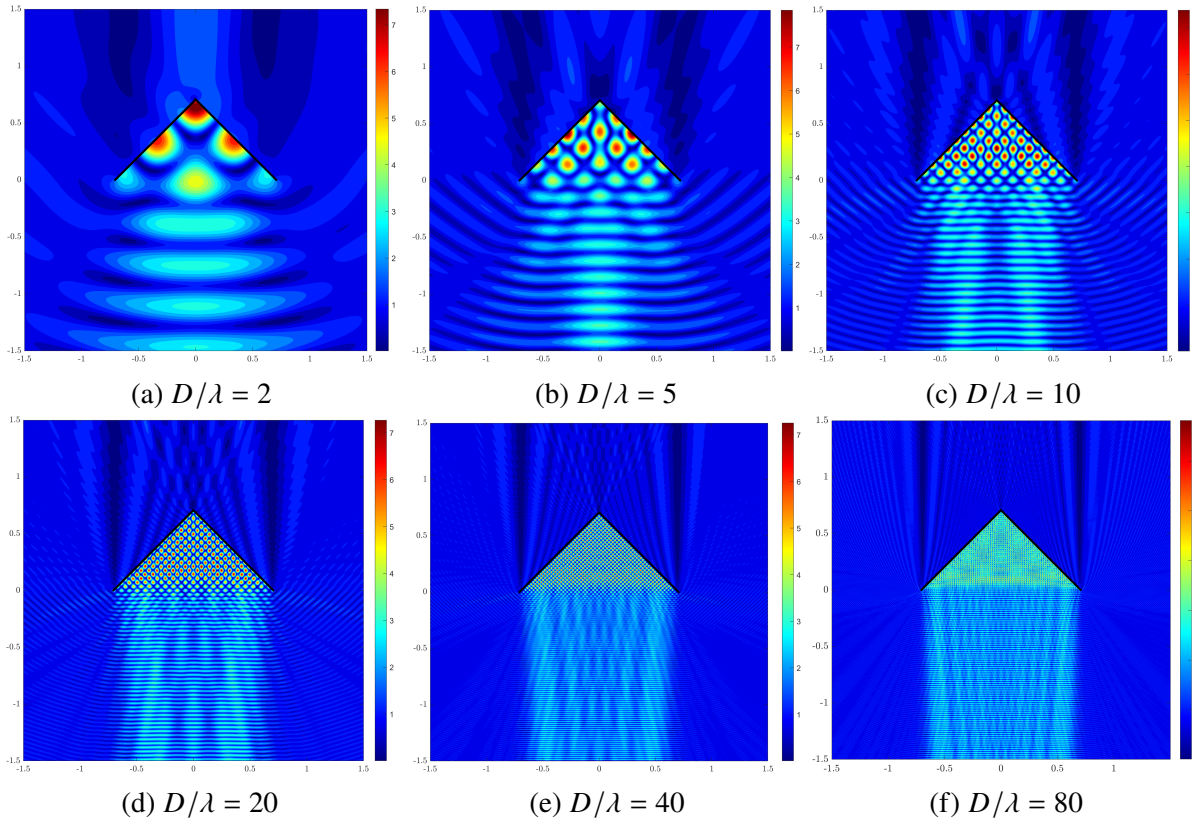
Figure 6.10: Distribution of $\left|H_z^{tot}\right|$ for a $90°-$dihedral corner reflector, incident angle $\alpha = 90°$.

from $D/\lambda = 2$ to $D/\lambda = 80$. In Figure 6.11, magnified view of the near-field distribution for interior region of the corner reflector is provided for $D/\lambda = 80$.

The evolution of the field distribution $\left|H_z^{tot}\right|$ (as the relative wave size of aperture ranges through the values $D/\lambda = 2, 5, 10, 20, 40, 80$) presents an instructive picture describing the wave interference in its classical form. This interference phenomenon is especially pronounced in Figure 6.11, where one can distinguish the nodes and anti-nodes of standing waves separated by a half-wavelength $\lambda/2$, forming a regular grid inside the corner reflector. Except near the narrow "transition" zone in the close vicinity of the aperture, the reflected field outside the reflector transforms into a well-collimated wave beam, propagating back to the source. This leads to the steady increase of RCS with the growth of the aperture wave size (D/λ). As usual, we present RCS plots in the normalised form and use relative wavenumber $kD = 2\pi (D/\lambda)$. The frequency dependence of the normalised RCS, σ_B, is given in Figure 6.12a for the incident angles $\alpha = 90°, 85°$ and in Figure 6.12b for the incident angles $\alpha = 75°, 60°$.
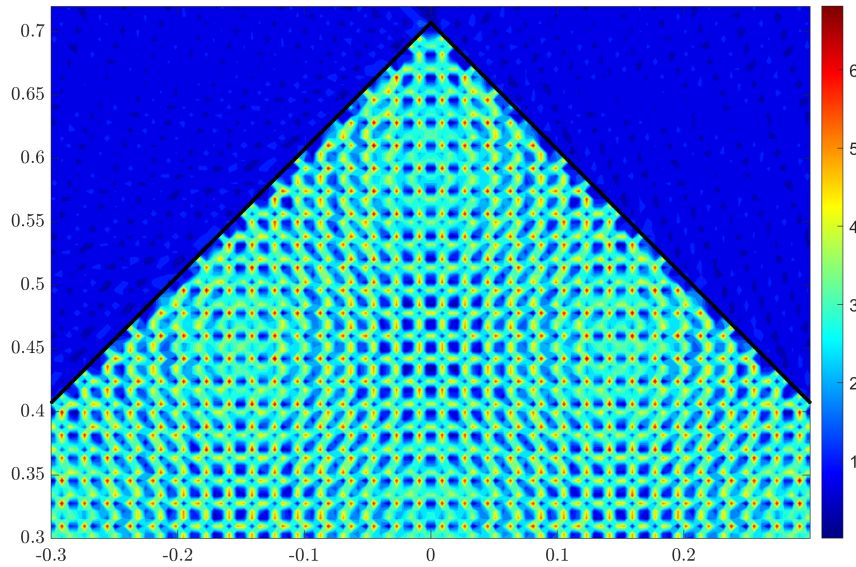
Figure 6.11: Magnified view of the near-field for a corner reflector with the relative wave size of aperture $D/\lambda = 80$.

(a)   (b)
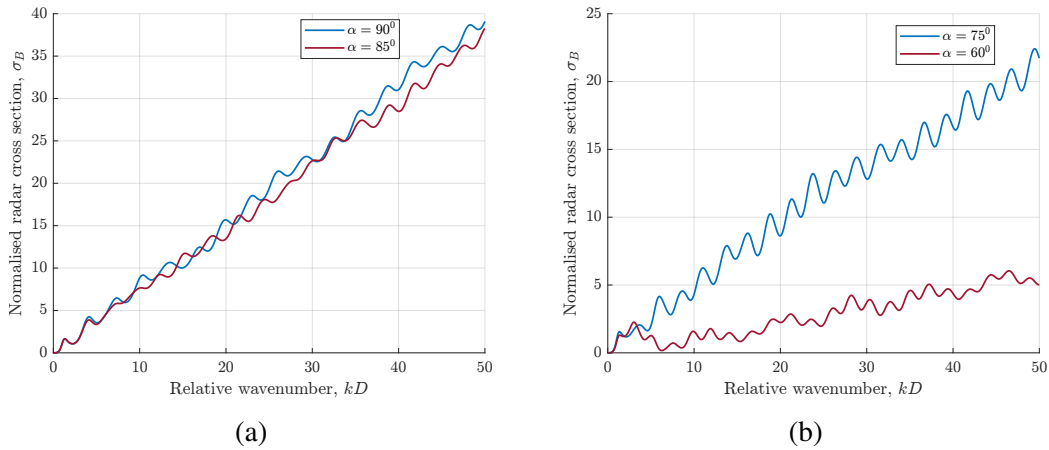
Figure 6.12: Frequency dependence of the normalised radar cross section of a $90°−$dihedral corner reflector, various incident angles.

6.3   Finite Sinusoidal Gratings

There are various analytical and numerical methods devoted to the analysis of diffraction by finite gratings in electromagnetic theory and optics. Gratings play an important role in several applications: for example, they are used as parts of corrugated reflector antennas and in optical instruments such as spectroscopes. Full wave analysis of diffraction by sinusoidal gratings of an obliquely incident $E−$polarised plane wave was conducted using the MAR in [125],[126]. In general, the MAR approach is characterised by its capability to analyse wave scattering problems without any limitations imposed on the parameters of scatterers, and finite sinusoidal gratings are not an exception: the problem may be analysed in a wide frequency band

without limitations on depth of the sinusoidal corrugation and wave size of the gratings. Since our goal is to conduct only a preliminary investigations of sinusoidal gratings illuminated by an $H-$polarised plane wave, we leave aside an extended preliminary discussion about merits and demerits of the various methods applied for analysis of finite gratings. All such methods possess different kind of limitations discussed in numerous surveys on this subject (see, for example, [127] and [128]). A clear picture of the state-of-the-art in this area is given in [125]. We extract two principal points from these investigation. The first and, possibly, the main point is finding the correlation between a realistic finite grating and its mathematical idealisation (the infinite grating); in other words, to what extent are the theoretical results for infinite gratings applicable for their finite counterparts. The second point is emergence of diffraction beams (Floquet modes) in finite gratings and the correspondence of the angular directions of diffraction beams to those given by the well-known grating formula. The most effective way of finding the correlation between properties of finite and infinite gratings is a comparison of the surface current density induced by an incident plane wave under sequential increase of the number of periods. The idea behind such comparison is the tendency of the magnitude of the induced current to stabilise, tending to its limiting value which is characteristic for an infinite grating (see, for example, [129]).
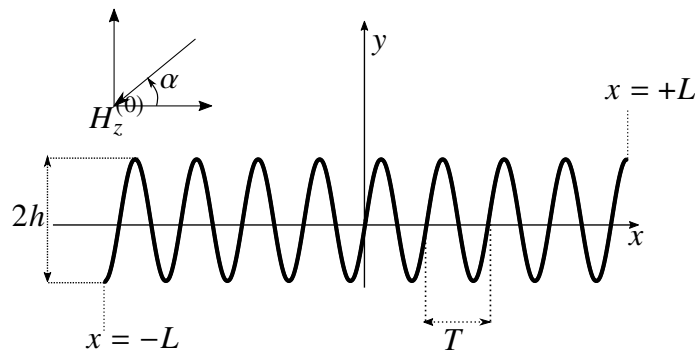
Figure 6.13: Excitation of a finite sinusoidal grating by an obliquely incident $H-$polarised plane wave.

Let us start with a description of geometry of a finite sinusoidal grating shown in Figure 6.13. The grating surface is assumed to be infinitely thin, perfectly conducting, and uniform in the z-direction, and it is defined by $y(x) = h \sin mx$ for $|x| \leq 1$. Thus, the depth of the grating is $2h$ and the period is $T = 2\pi/m$, where m is some positive constant; the number of periods on the grating is chosen as $n_T = n + 1/2$, where $n = 1, 2, \ldots$. The grating width can then be found

Figure 6.14: Surface current density distribution $|J(x)|$ for a finite sinusoidal grating $h = 0.25\lambda$, $T = 0.25\lambda$, $n_T = 6.5, 12.5, 18.5$, incident angle $\alpha = -90°$.

as $w = 2L = n_T T$. Although it contrasts with the rest of this thesis, a non-standard definition (shifted by π) of the incidence angle α is chosen for the ease of comparison with the results obtained in [122].

Not repeating in detail all the arguments presented in [122], when investigating the influence of edge effects on the distribution of surface current density $|J(\phi)|$, we concentrate on the main points only. The surface current does not depend on polarisation of the incident plane wave. First, the distortion of the electromagnetic field over one period in a finite grating (in comparison with an infinite grating) is due to its finiteness. It can be predicted that distortion along the central part of the finite grating should be significantly smaller than the distortion at its peripheral parts, neighbouring the grating edges. The presence of the edges should have a notable impact only on the terminating sections of the finite grating. As the frequency increases the "edge effects" should diminish since at a high frequency the interaction of an electromagnetic wave with the metallic surface has a local character and the scattering from one part of the surface does not strongly affect scattering from more distant parts of that surface. These assumptions are of general character. Roughly, the edge effects, independently of the polarisation of an incident field, substantially influence the distribution of the surface current density at a distance of approximately one wavelength λ from the ends of the finite grating.

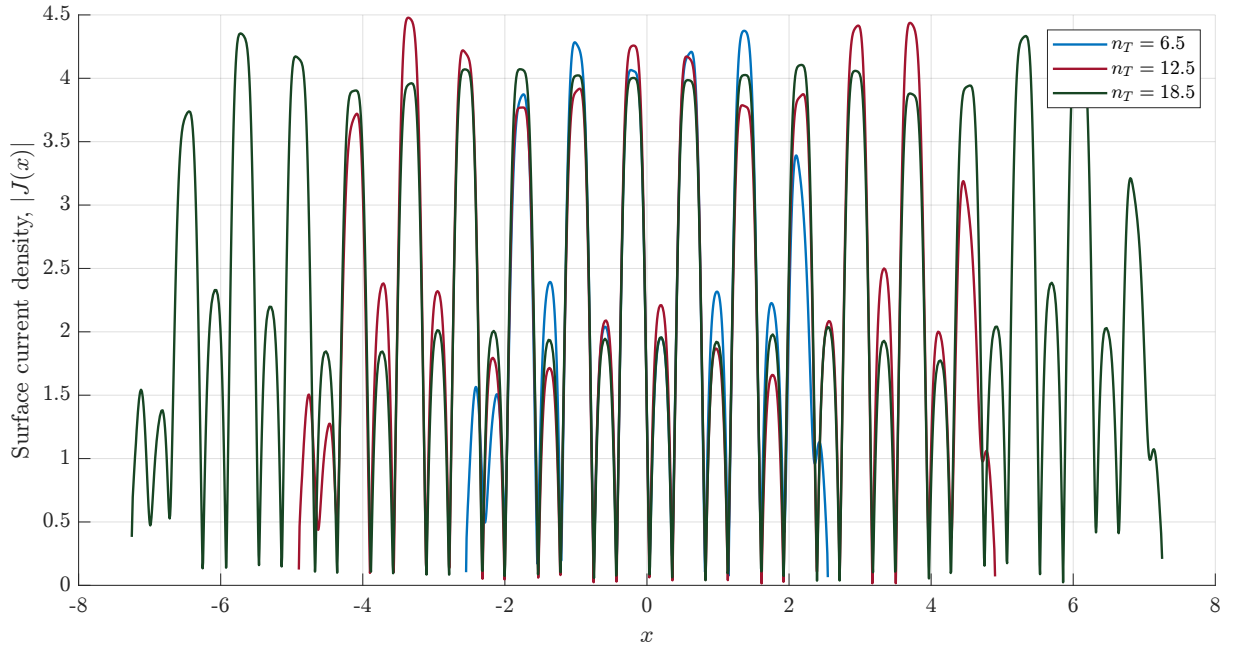The surface current density $|J(x)|$ plots in Figures 6.14 and 6.15 reveal reasonable adherence
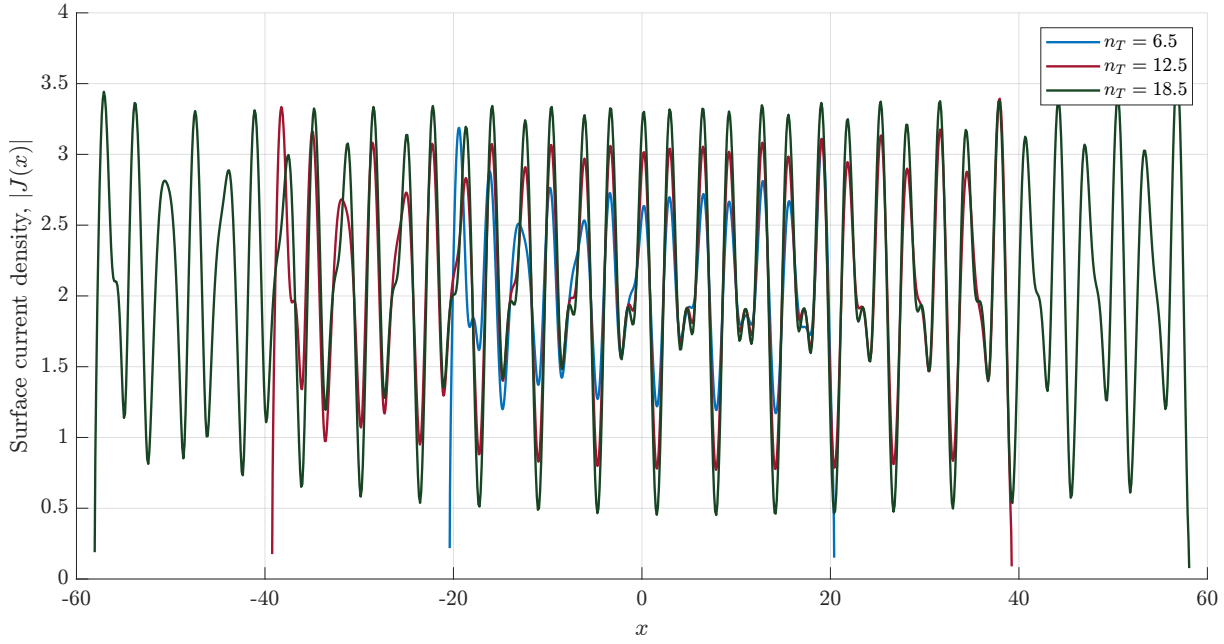
Figure 6.15: Surface current density distribution $|J(x)|$ for a finite sinusoidal grating $h = 0.1\lambda$, $T = 0.25\lambda$, $n_T = 6.5, 12.5, 18.5$, incident angle $\alpha = -90°$.

to periodicity of this function on the finite sinusoidal grating of the fixed depth as the number n_T of periods increases from 6.5 to 18.5. Perceptible distortion of the function is observed only near to edges, though the edge distortion for the deeper grating in Figure 6.15 is more pronounced than for the shallower grating in Figure 6.14. Magnified views of the surface current density $|J(x)|$ examined close to the left edges of the gratings are shown in Figures 6.16a and 6.16b. Comparison of the values of $|J(x)|$ for the larger grating ($n_T = 18.5$) clearly reveals the scale of distortion caused by the sharp edges compared to smaller gratings. Another observation is that the scale of distortion and stabilisation of the currents for gratings excited by $H-$polarised waves differ insignificantly from that of observed in case of $E-$polarisation ([122]).

The normalised radiation patterns presented for finite gratings in Figure 6.17 ($n_T = 8.5$) and Figure 6.18 ($n_T = 100.5$), show the emergence of the diffraction beams even for the grating with small ($n_T = 8.5$) number of periods. While keeping the rest of parameters the same, namely, ($2h = 0.5\lambda, T = 5\lambda,$ and $\alpha = 60°$), the normalised radar cross section for a substantially larger multi-period grating ($n_T = 105.5$) reveals the same diffraction beams but more tightly collimated. In grating theory, the emergence of these well-collimated beams is explained by the grating formula

$$\cos\phi_m = -\left(\cos\alpha + m\frac{\lambda}{T}\right), \quad m = 0, \pm1, \pm2, \dots \tag{6.1}$$

(a) $x = -3.25$ for $n_T = 6.5$

(b) $x = -6.25$ for $n_T = 12.5$
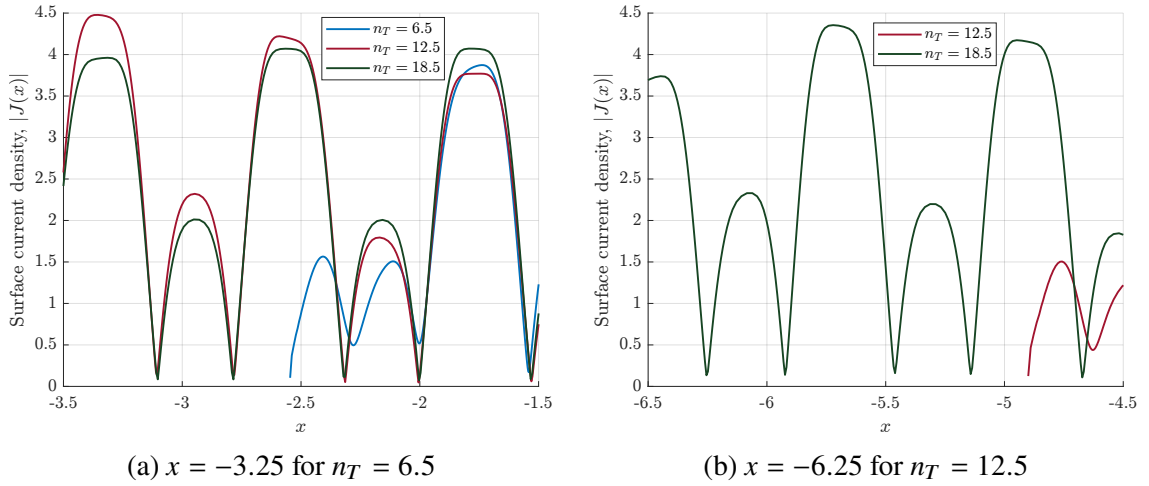
Figure 6.16: The magnified view of the surface current density $|J(x)|$ for $h = 0.25\lambda$, $T = 0.25\lambda$, $n_T = 6.5, 12.5, 18.5$ near the left edge.

Equation (6.1) governs the angular locations ϕ_m of the principal intensity maxima when a plane wave of wavelength λ is diffracted from a grating of spacing T. Here, m is the diffraction order (or spectral order). Equation (6.1) is applicable to the infinite gratings while in this section we examine finite gratings. It can be reasonably anticipated that approximate agreement of the direction in the computed data and those directions ϕ_m of the emerging diffraction beams (or Floquet space harmonics) calculated by the infinite gratings formula be observed for a finite grating with a sufficient number of periods. Ideally, for an infinite grating with $\alpha = 60°$ and $\lambda/T = 0.2$, the grating formula predicts the emergence of diffractions beams with ten values of the diffraction order: $m = -7, -6, -5, -4, -3, -2, -1, 0, 1, 2$. In practice, for a finite grating with the number of periods $n_T = 8.5$, the diffraction beam of order $m = -7$ does not emerge, as shown in Figure 6.17. This result along with the rest of calculations collected in the Table 6.1 are in excellent agreement with those obtained in [122] for case of $E-$polarisation. Moreover, the data in Table 6.1 reveals the excellent agreement between angular locations ϕ_m, defined by the grating formula in equation (6.1) and calculated values for lower Floquet space harmonics ($m = -3, -2, -1, 0, 1, 2$) even for gratings with a small number of periods (e.g. $n_T = 8.5$). For higher Floquet space harmonics ($m = -7, -6, -5, -4$), the agreement may be described as satisfactory.

In conclusion, it is worth noting the very large wave size of the grating of 100.5 periods: $2L = 502.5\lambda$. Also we note that the truncation system size $N = 2048$ used for the normalised scattering pattern calculation of the large grating has a computation time of 90 seconds. This size indicates the advance into the quasi-optical frequency region, demonstrating the usefulness
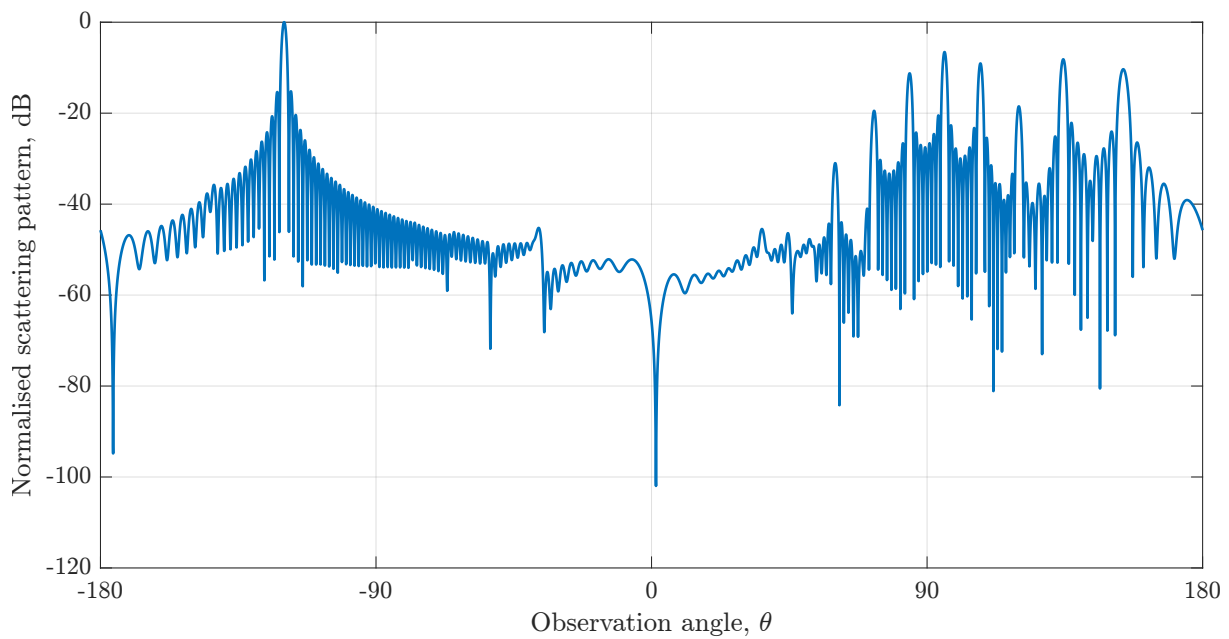
Figure 6.17: Normalised radiation pattern for a sinusoidal grating $h = 0.25\lambda$, $T = 5\lambda$, $n_T = 8.5$, $\alpha = 60°$.
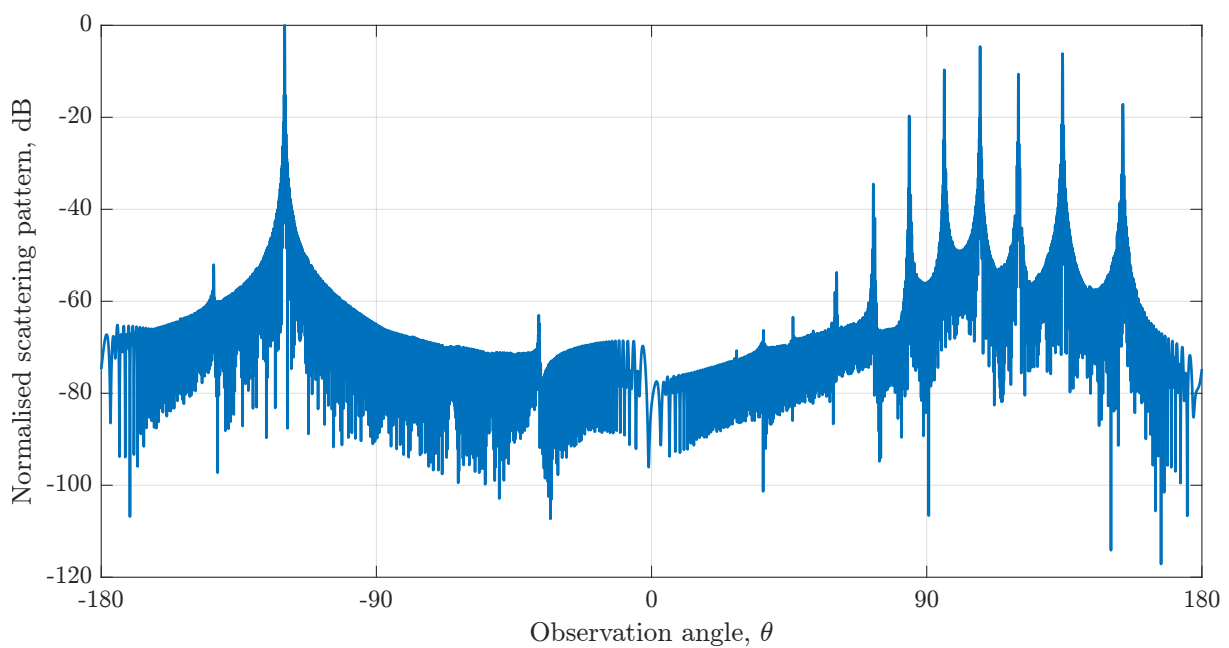
Figure 6.18: Normalised radiation pattern for a sinusoidal grating $h = 0.25\lambda$, $T = 5\lambda$, $n_T = 100.5$, $\alpha = 60°$.

Table 6.1: Angular locations ϕ_m of Floquet space harmonics for finite sinusoidal grating ($2h = 0.5\lambda, T = 5\lambda$).

m	Eq. (6.1)	$n_T = 8.5$	$n_T = 100.5$
-7	25.84°	–	26.63°
-6	45.57°	44.55°	46.28°
-5	60.00°	59.71°	60.54°
-4	72.54°	72.70°	72.56°
-3	84.26°	84.23°	84.26°
-2	95.73°	95.57°	95.75°
-1	107.45°	107.41°	107.45°
0	120.00°	119.98°	120.01°
1	134.42°	134.52°	134.41°
2	154.15°	154.32°	154.16°

of the MAR for modelling optical diffraction gratings.

6.4 A Short Investigation of Backscattering from Targets with Complex Shape

Prediction of the radar cross section of targets with complex shape is a problem that usually requires utilisation of multiple methods of computational electromagnetics (or acoustics). Contributions to the backscattering from different parts of such targets (which, in general possess distinctively different wave sizes) should be carefully modelled by different techniques. Without going deeply into technical detail, it is relevant to note that the main constructive elements of complex targets possess relatively big wave sizes. Thus, asymptotic, high-frequency methods dominate over other techniques in modelling backscattering response of such targets.

Currently, the design of computational software for calculating the radar cross section of complex targets is mostly concentrated in the big companies for which this problem is a part of their general engineering activity. As an example, [130] presents the development and verification of RECOTA (return from complex target), created at Boeing Aerospace for calculating the radar cross section of complex targets. The software utilises a computer-aided

(a) $L/\lambda \simeq 0.016$ (b) $L/\lambda = 1$ (c) $L/\lambda = 25$
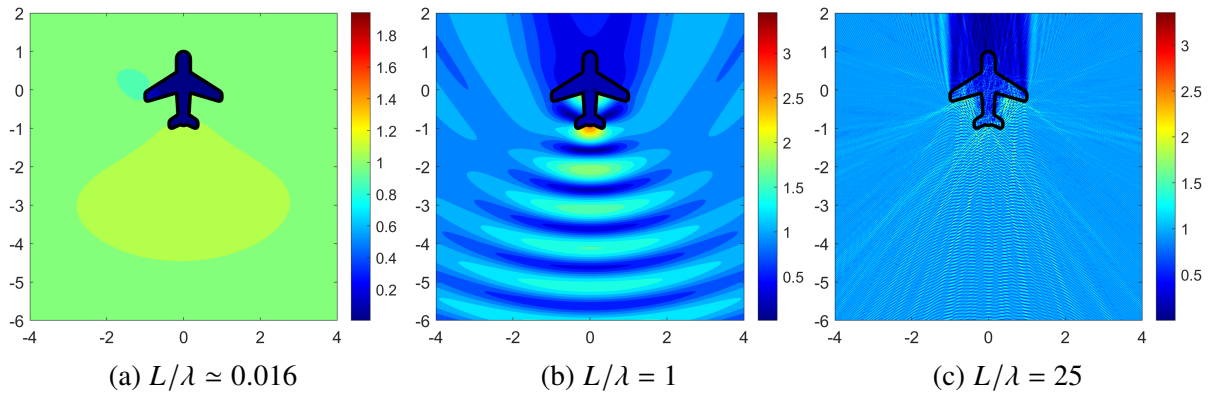
Figure 6.19: Distribution of $\left|H_z^{tot}\right|$ for an airplane, incident angle $\alpha = 90°$.

(a) $\alpha = 0°$ (b) $\alpha = 90°$
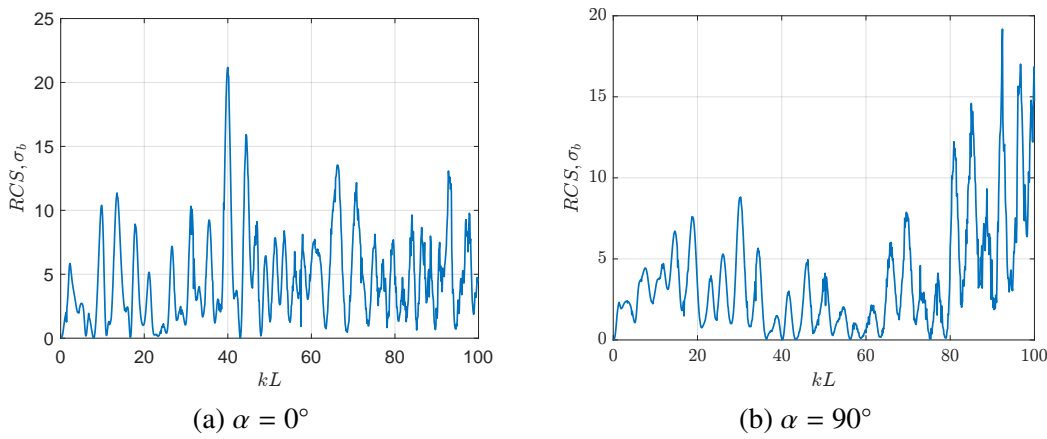
Figure 6.20: Frequency dependence of the normalised radar cross section of an airplane.

design package for modelling target geometry in terms of facets and wedges. It is based on physical optics, physical theory of diffraction, ray tracing, and semi empirical formulations, and it accounts for shadowing, multiple scattering, and discontinuities in the radar cross section calculations. An example of the RCS analysis by extracting a part from a complex target is demonstrated in [131]. In particular, high frequency calculations for a metallic cavity with realistic dimensions where the combination of radar returns from the cavity interior and from the rest of the complex target are considered. The solution for the re-radiation from the cavity interior involves the usage of a normal-mode technique in conjunction with the Stratton-Chu integral.

A study of further relevant publications leads to the following conclusion: there is no unique and universal method capable of tackling the discussed problem by itself, especially, in case of realistic 3D wave scattering. For 2D scattering, the situation is different: the MAR, for example, allows one to predict the RCS of 2D targets without any restrictions on their shape and complexity.

(a) $L/\lambda \simeq 0.016$ (b) $L/\lambda = 1$ (c) $L/\lambda = 25$
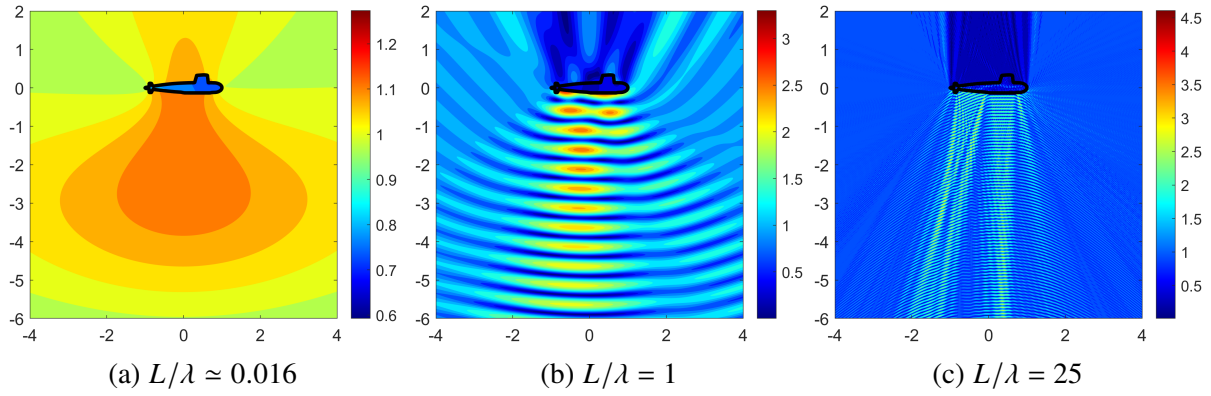
Figure 6.21: Distribution of $\left|H_z^{tot}\right|$ for a submarine, incident angle $\alpha = 90°$.

(a) $\alpha = 0°$ (b) $\alpha = 90°$
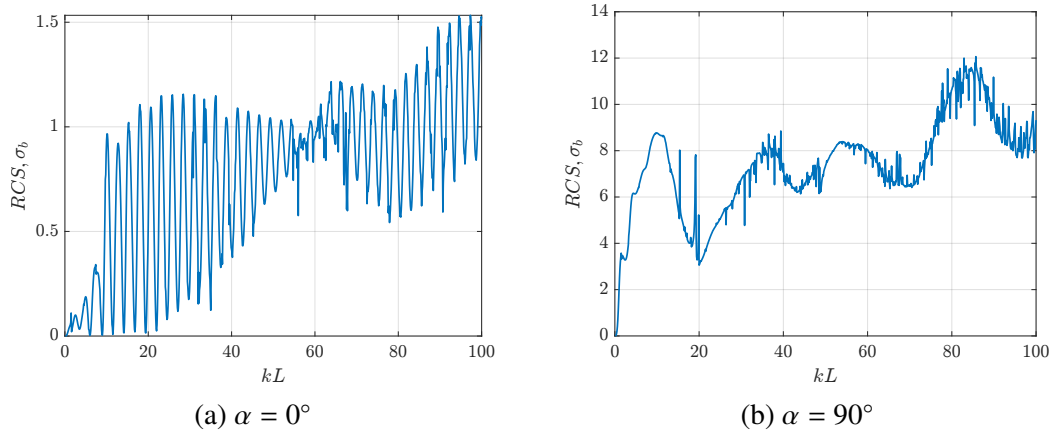
Figure 6.22: Frequency dependence of the normalised radar cross section of a submarine.

To illustrate this assertion, we conduct calculations of the near-field distribution and normalised RCS for an airplane and submarine of simplified shape. For the near-field calculations, the maximum relative wave size L/λ of the targets (L is maximum size) is chosen to characterise wave scattering in Rayleigh scattering region ($L/\lambda \simeq 0.016$), diffraction region ($L/\lambda = 1$) and high-frequency region ($L/\lambda = 25$). We note that the truncation number $N = 512$ is used resulting in an average computation time of 40 seconds for calculation of near-field distribution and an average of 800 seconds for calculation of RCS across the selected frequency range. The results for the "airplane" and "submarine" shapes are presented in figures 6.19-6.20 and 6.21-6.22, respectively.

Though the presented calculations are merely of illustrative character, they are performed with the high accuracy the MAR provides. However, the results for 2D scattering cannot be used directly for prediction of backscattering of realistic 3D targets. 2D modelling may be used in more accurate modelling of the elongated parts of complex targets. Possibly, the main significance of the accurate simulation of the backscattering from complex 2D targets is the establishment of

benchmark results which may be used for further revision of existing numerical codes developed for RCS calculation of 3D targets. Since the currently used numerical methods and software contain not only well-established algorithms, but plenty of empirical formulas, such comparison may lead to their revision and, hence, to improvement in the accuracy of computation for 3D targets.

7

Conclusions

In this thesis a mathematically rigorous, numerically accurate method has been developed for analysis of diverse wave scattering problems for open sound-hard cavities in acoustics, and open slotted arbitrary PEC cylinders excited by $H-$polarised radiation in electromagnetics. From the mathematical point of view, both problems are described by the Neumann boundary value problem for the Helmholtz equation in two-dimensional arbitrarily shaped open domains. Employing the Method of Analytical Regularisation (MAR), the surface integral equation in the form of double-layer potential with a hyper-singular kernel is separated into singular and regular parts, then regularised and transformed into a coupled, well-conditioned infinite system of linear algebraic equations of the second kind. The compactness of the matrix operators allowed us to solve the coupled equations effectively by the truncation method. Numerical experiments confirmed the established theoretical convergence of the solution of the truncated system to the exact solution, as well as the fast convergence rate. Another aspect of the numerical solution effectiveness derives from the ease of matrix filling as the computation of matrix elements is mostly accomplished using Fast Fourier Transforms and recurrence formulas. As a result, solutions with predefined accuracy can be obtained with a proper choice of the truncation number.

One of the key outcomes of the thesis is the generalisation of the solution to arbitrary domains, including those of polygonal nature, such as ridge waveguides, coupled rectangular resonators,

magnetron type cavities, etc. Parametrisation of bounding contours of the scatterers using Piecewise Cubic Interpolation Polynomials is the first step in modelling arbitrary non-canonical cross-sections. This parametrisation is then further treated by employing the Frederich's mollifier in the Sobolev's approximation, resulting in smooth contours with continuous third derivative. Considering the numerous steps in realisation of the computational codes (implemented using MATLAB), it was of paramount significance to validate the obtained numerical results against those available in literature. An exhaustive validation has been done for analytical, polygonal and arbitrary cross sections which revealed an excellent agreement with the available results as well as demonstrating the characteristics of the second kind Fredholm equations and the truncation method, including fast convergence of the system condition number to its limiting value.

The analytical-numerical method based on the MAR was applied to the analysis of various problems of practical interest in acoustics and electromagnetics. Spectral characteristics of slotted cavities were studied in Chapters 3 and 4. Helmholtz resonators with attached necks, and arrays of them (consisting of two identical resonators) widely use in application are analysed in detail. The effects of parameters defining the structures are presented in terms of the unloaded $Q-$factors of respective resonators. Taking advantage of the highly effective computational algorithms, the spectrum of circular, elliptic, and rectangular slotted cavities were comprehensively investigated; the complex eigenvalues are calculated with an accuracy of 5 or 6 significant decimal places.

In Chapter 5, resonance wave scattering and radiation from various structures were analysed using complex oscillations and calculations of radar cross section and scattering patterns. We also discussed distinctive aspects of resonance scattering, in particular, the occurrence of resonance duplets arising when the relative wavenumber approaches the real part of a complex eigenvalue.

The capabilities of the developed method are further demonstrated in Chapter 6, where the MAR was applied to the analysis of the classical parabolic cylindrical reflectors, concentrating on finding the fine details in the distribution of the reflected electromagnetic field in the neighbourhood of the geometric optics focal line. In addition, parabolic reflectors with attached flanges were also considered. For this type of reflector, we performed calculations of illustrative character that clearly demonstrated the method's capability for further accurate analysis. The analysis of these reflectors can easily be extended to more complicated shapes, such as an approximate parabolic shape, or a parabolic reflector with an arbitrary shaped feed.

Analogous results are also presented for corner reflectors. High efficiency of the MAR was beneficial in the investigation of finite sinusoidal gratings: the computations revealed that space harmonics (the Floquet modes) are observed for both small and large size of gratings ranging from a few to a half a thousand wavelengths. Finally, the capability of the MAR for comprehensive analysis of backscattering from complex 2D targets was briefly explained. Because the high-frequency regime is the most challenging for all the methods currently employed in the scientific literature, it is of strong interest to explore these and other applications in that regime.

Although a wide range of applications in acoustics and electromagnetics are investigated in the thesis, the list of other practical problems, acoustic and electromagnetic, to which the MAR can be applied is far from exhausted. Some of the possible research directions include: analysis of finite reflective gratings with arbitrary profile, excited by plane waves and compact sources; narrow band resonant microwave antennas; accurate modelling of corrugated horns; studies of approximate parabolic (and other) reflector antennas; and finding the complex spectrum of Fabry-Perot resonators with arbitrarily corrugated mirrors.

Other directions for future studies concern theoretical aspects of the rigorous solution and its extension to the Neumann problem for 2D open arbitrary cavities with multiple slits, the formulation and solution of the Neumann problem for ensembles of 2D open and closed cavities, and the study of the third kind (impedance) boundary value problems for the Helmholtz equation in 2D open domains.

Bibliography

[1] H. Lin, J. Ge, and J. Wang. *Scaling relationships between acoustic and electromagnetic scattering by an infinite cylinder*. AIP Advances **9**(12), 125315 (2019).

[2] J. Carcione and F. Cavallini. *On the acoustic-electromagnetic analogy*. Wave Motion **21**(2), 149 (1995).

[3] J. M. Carcione. *Chapter 8 - The Acoustic-Electromagnetic Analogy*. In *Wave Fields in Real Media (Third Edition)*, pp. 421–508 (Elsevier, Oxford, 2015), third edition ed.

[4] A. Snakowska. *Acousto-electromagnetic analogies in diffraction phenomena occurring in the semi-infinite cylindrical waveguide*. Acta Physica Polonica-Series A General Physics **116**(3), 410 (2009).

[5] G. Guimarães, R. Pirk, C. Souto, and L. Góes. *Acoustic modification prediction using FRF: application of Helmholtz resonators on a rocket engine combustion chamber*. In *Int. Conf. Noise Vib. Eng.*, vol. 5, pp. 4115–4128 (2012).

[6] A. I. Nosich and V. P. Shestopalov. *Electromagnetic analogue of Helmholtz resonator*. In *Doklady Akademii Nauk*, vol. 234, pp. 53–56 (Russian Academy of Sciences, 1977).

[7] R. R. Gadyl'shin. *On acoustic Helmholtz resonator and on its electromagnetic analog*. Journal of Mathematical Physics **35**(7), 3464 (1994).

[8] I. Y. Popov. *Model of point-like window for electromagnetic Helmholtz resonator*. Zeitschrift für Analysis und ihre Anwendungen **32**(2), 155 (2013).

[9] P. Bouchon, P. Chevalier, and R. Hadar. *Optical Helmholtz resonators*. In *META 2019* (2019).

[10] P. Chevalier, P. Bouchon, J.-J. Greffet, J.-L. Pelouard, R. Haïdar, and F. Pardo. *Giant field enhancement in electromagnetic Helmholtz nanoantenna*. Physical Review B **90**(19), 195412 (2014).

[11] D. Colton and R. Kress. *Integral equation methods in scattering theory* (SIAM, 2013).

[12] S. Zaman. *A comprehensive review of boundary integral formulations of acoustic scattering problems*. Sci. Tech. Special Review pp. 281–310 (2000).

[13] S. Yang. *A boundary integral equation method for two-dimensional acoustic scattering problems*. The Journal of the Acoustical Society of America **105**(1), 93 (1999).

[14] Q. Sun, E. Klaseboer, A. J. Yuffa, and D. Y. Chan. *Field-only surface integral equations: scattering from a perfect electric conductor*. JOSA A **37**(2), 276 (2020).

[15] R. Kress. *On the numerical solution of a hypersingular integral equation in scattering theory*. The Journal of the Acoustical Society of America **61**(3), 345 (1995).

[16] Y. Wu, F. Rizzo, D. Shippy, and J. Wagner. *An advanced boundary integral equation method for two-dimensional electromagnetic field problems*. Electric Machines and Electromechanics **1**(4), 301 (1977).

[17] V. Rokhlin. *Rapid solution of integral equations of scattering theory in two dimensions*. Journal of Computational Physics **86**(2), 414 (1990).

[18] F. P. Andriulli and E. Michielssen. *A regularized combined field integral equation for scattering from 2-d perfect electrically conducting objects*. IEEE Transactions on Antennas and Propagation **55**(9), 2522 (2007).

[19] M. Costabel. *Principles of boundary element methods*. Computer Physics Reports **6**(1), 243 (1987).

[20] A. Y. Poyedinchuk, Y. A. Tuchkin, and V. Shestopalov. *New numerical-analytical methods in diffraction theory*. Mathematical and computer modelling **32**(9), 1029 (2000).

[21] H. A. Schenck. *Improved integral formulation for acoustic radiation problems*. The Journal of the Acoustical Society of America **44**(1), 41 (1968).

[22] A. Burton and G. Miller. *The application of integral equation methods to the numerical solution of some exterior boundary-value problems*. Proceedings of the Royal Society of London. A. Mathematical and Physical Sciences **323**(1553), 201 (1971).

[23] W. Hall and W. Robertson. *Standard Helmholtz integral equation calculations near characteristic frequencies*. Journal of Sound and Vibration **126**(2), 367 (1988).

[24] A. Seybert and Z. Reut. *A note on methods for circumventing non-uniqueness when using integral equations*. Journal of Sound and Vibration **115**(1), 171 (1987).

[25] Z. Reut. *On the boundary integral methods for the exterior acoustic problem*. Journal of Sound and Vibration **103**(2), 297 (1985).

[26] S. Marburg. *The Burton and Miller method: Unlocking another mystery of its coupling parameter*. Journal of Computational Acoustics **24**(01), 1550016 (2016).

[27] C. Langrenne, A. Garcia, and M. Bonnet. *Solving the hypersingular boundary integral equation for the Burton and Miller formulation*. The Journal of the Acoustical Society of America **138**(5), 3332 (2015).

[28] R. J. Adams. *Physical and analytical properties of a stabilized electric field integral equation*. IEEE Transactions on Antennas and Propagation **52**(2), 362 (2004).

[29] A. D. Yaghjian. *Banded-matrix preconditioning for electric-field integral equations*. In *IEEE Antennas and Propagation Society International Symposium 1997. Digest*, vol. 3, pp. 1806–1809 (IEEE, 1997).

[30] D. Yuan and X. Zhang. *An overview of numerical methods for the first kind Fredholm integral equation*. SN Applied Sciences **1**(10), 1 (2019).

[31] M. A. Golberg. *Numerical solution of integral equations*, vol. 42 (Springer Science & Business Media, 2013).

[32] A. Burton. *The solution of Helmholtz'equation in exterior domains using integral equations*. NPL Report NAC 30, Teddington, Middlesex, UK (1973).

[33] S. I. Zaman. *Integral equation formulations of exterior acoustic scattering problems*. Ph.D. thesis, City University, London, UK (1994).

[34] P. Krutitskii. *On a uniquely solvable integral equation in a mixed Dirichlet-Neumann problem of acoustic scattering*. Quarterly of Applied Mathematics **59**(3), 493 (2001).

[35] Q. Sun, E. Klaseboer, B.-C. Khoo, and D. Y. Chan. *Boundary regularized integral equation formulation of the Helmholtz equation in acoustics*. Royal Society Open Science **2**(1), 140520 (2015).

[36] E. Klaseboer, Q. Sun, and D. Y. Chan. *Non-singular boundary integral methods for fluid mechanics applications*. arXiv preprint arXiv:1902.03342 (2019).

[37] S.-A. Yang. *Acoustic scattering by a hard or soft body across a wide frequency range by the Helmholtz integral equation method*. The Journal of the Acoustical Society of America **102**(5), 2511 (1997).

[38] L. Gurel and O. Ergul. *Singularity of the magnetic-field integral equation and its extraction*. IEEE Antennas and Wireless Propagation Letters **4**, 229 (2005).

[39] Y. A. Tuchkin. *On the analytical regularization method in scattering and diffraction*. In K. Kobayashi and P. D. Smith, eds., *Advances in Mathematical Methods for Electromagnetics*, Electromagnetic Waves, chap. 13, pp. 303–328 (Institution of Engineering and Technology, 2020).

[40] R. Mittra and S. Lee. *Analytical Techniques in the Theory of Guided Waves*. Macmillan series in electrical science (Macmillan, 1971).

[41] A. I. Nosich. *The method of analytical regularization in wave-scattering and eigenvalue problems: Foundations and review of solutions*. IEEE Antennas and Propagation Magazine **41**(3), 34 (1999).

[42] S. S. Vinogradov, P. D. Smith, and E. D. Vinogradova. *Canonical problems in scattering and potential theory, Part I: Canonical structures in potential theory* (Boca Raton: Chapman & Hall/CRC, 2001).

[43] S. S. Vinogradov, P. D. Smith, and E. D. Vinogradova. *Canonical problems in scattering and potential theory, Part II: Acoustic and electromagnetic diffraction by canonical structures* (CRC Press, 2002).

[44] A. I. Nosich. *Method of analytical regularization in computational photonics*. Radio Science **51**(8), 1421 (2016).

[45] P. Smith. *Recent advances in regularization techniques for scattering and diffraction*. Radio Science **42**(06), 1 (2007).

[46] Y. A. Tuchkin. *Wave scattering by open cylindrical screens of arbitrary profile with Dirichlet boundary conditions*. In *Soviet Physics Doklady*, vol. 20, p. 1027 (1985).

[47] Y. A. Tuchkin. *Wave scattering by an unclosed cylindrical screen of arbitrary profile with the Neumann boundary condition*. In *Doklady Akademii Nauk*, vol. 293, pp. 343–345 (Russian Academy of Sciences, 1987).

[48] V. Shestopalov, Y. A. Tuchkin, A. Y. Poyedinchuk, and Y. K. Sirenko. *Novel methods for solving direct and inverse problems of diffraction theory, vol. 1*. Kharkov, Ukraine: Publishing House Osnova (in Russian) (1997).

[49] E. Vinogradova. *Reflectivity of two-dimensional airfoils illuminated by H-polarized plane wave: Rigorous approach*. Electromagnetics **37**(6), 377 (2017).

[50] E. Sever, F. Dikmen, and Y. A. Tuchkin. *A rigorous algorithm for the boundary value problem of dielectric bodies based on the analytical regularization method*. In *2021 International Applied Computational Electromagnetics Society Symposium (ACES)*, pp. 1–4 (IEEE, 2021).

[51] S. Vinogradov, E. Vinogradova, C. Wilson, I. Sharp, and Y. A. Tuchkin. *Scattering of an E-polarized plane wave by two-dimensional airfoils*. Electromagnetics **29**(3), 268 (2009).

[52] E. Vinogradova. *Electromagnetic plane wave scattering by arbitrary two-dimensional cavities: Rigorous approach*. Wave Motion **70**, 47 (2017).

[53] E. D. Vinogradova. *Scattering of E-polarized plane wave by rectangular cavity with finite flanges*. Radio Science **52**(11), 1374 (2017).

[54] E. D. Vinogradova. *Complex eigenvalues of slotted arbitrary cylindrical cavities: Sound-soft elliptic cavity with variably placed longitudinal slit*. The Journal of the Acoustical Society of America **144**(3), 1146 (2018).

[55] E. D. Vinogradova. *Resonance scattering of plane waves by a soft elliptic cavity with a variably placed longitudinal slit*. The Journal of the Acoustical Society of America **147**(5), 3294 (2020).

[56] A. Poedinchuk, Y. A. Tuchkin, and V. Shestopalov. *Regularization of spectral problems of wave scattering on open screens*. In *Soviet Physics Doklady*, vol. 32, p. 640 (1987).

[57] V. P. Shestopalov and Y. V. Shestopalov. *Spectral theory and excitation of open structures*. 42 (IET, 1996).

[58] F. Fedorov. *On the theory of infinite systems of linear algebraic equation*. TWMS J. Pure Appl. Math **6**(2), 202 (2015).

[59] J. F. Traub. *Iterative methods for the solution of equations*, vol. 312 (American Mathematical Soc., 1982).

[60] G. Hsiao and R. Kleinman. *Mathematical foundations for error estimation in numerical solutions of integral equations in electromagnetics*. IEEE Transactions on Antennas and Propagation **45**(3), 316 (1997).

[61] E. Sever, F. Dikmen, and Y. A. Tuchkin. *Superalgebraically converging galerkin method for electromagnetic scattering by dielectric cylinders*. Radio Science **52**(10), 1282 (2017).

[62] E. Sever, Y. A. Tuchkin, and F. Dikmen. *On a superalgebraically converging, numerically stable solving strategy for electromagnetic scattering by impedance cylinders*. Journal of Computational Electronics **17**(1), 427 (2018).

[63] J. Gielis. *A generic geometric transformation that unifies a wide range of natural and abstract shapes*. American Journal of Botany **90**(3), 333 (2003).

[64] S. S. Vinogradov, E. D. Vinogradova, C. Wilson, I. Sharp, and Y. A. Tuchkin. *Scattering of an e-polarized plane wave by two-dimensional airfoils*. Electromagnetics **29**(3), 268 (2009).

[65] S. Naser and N. Dib. *Design and analysis of super-formula-based UWB monopole antenna and its MIMO configuration*. Wireless Personal Communications **94**(4), 3389 (2017).

[66] S. Khajevandi, H. Oraizi, and M. Poordaraee. *Design of planar dual-bandstop FSS using square-loop-enclosing superformula curves*. IEEE Antennas and Wireless Propagation Letters **17**(5), 731 (2018).

[67] S. Guler, C. Onol, O. Ergul, E. Sever, F. Dikmen, and Y. A. Tuchkin. *Fastly converging 2d solutions of te-efie on modified superformula contours optimized via genetic algorithms*. In *2017 IEEE International Symposium on Antennas and Propagation USNC/URSI National Radio Science Meeting*, pp. 1461–1462 (2017).

[68] C. De Boor and C. De Boor. *A practical guide to splines*, vol. 27 (Springer-verlag New York, 1978).

[69] T. Topal. *Rigorous analysis of TM modes in arbitrary shaped closed and slotted waveguides*. Macquarie University, Sydney (2017). MRes thesis.

[70] M. Sagradian. *Potential and acoustic diffraction problems for arbitrarily shaped rotationally symmetric doubly-connected screens*. Macquarie University, Sydney (2021). PhD thesis.

[71] F. N. Fritsch and R. E. Carlson. *Monotone piecewise cubic interpolation*. SIAM Journal on Numerical Analysis **17**(2), 238 (1980).

[72] K. O. Friedrichs. *The identity of weak and strong extensions of differential operators*. Transactions of the American Mathematical Society **55**(1), 132 (1944).

[73] K. Ebnabbasi, D. Busuioc, R. Birken, and M. Wang. *Taper design of Vivaldi and coplanar tapered slot antenna (TSA) by Chebyshev transformer*. IEEE Transactions on Antennas and Propagation **60**(5), 2252 (2012).

[74] D. Roberts, M. Rahm, J. Pendry, and D. Smith. *Transformation-optical design of sharp waveguide bends and corners*. Applied Physics Letters **93**(25), 251111 (2008).

[75] S. Manenkov. *Use of a spline approximation to solve the problem of diffraction by an unclosed screen located in a planar waveguide*. Journal of Communications Technology and Electronics **52**(12), 1307 (2007).

[76] F. N. Fritsch and R. E. Carlson. *Monotone piecewise cubic interpolation*. SIAM Journal on Numerical Analysis **17**(2), 238 (1980).

[77] *Pchip*. https://au.mathworks.com/help/matlab/ref/pchip.html. Accessed: 2021-03-08.

[78] C. A. Balanis. *Advanced engineering electromagnetics* (John Wiley & Sons, 2012).

[79] C. Oleson and A. Denning. *Millimeter wave vector analysis calibration and measurement problems caused by common waveguide irregularities*. In *56th ARFTG Conference Digest*, vol. 38, pp. 1–9 (IEEE, 2000).

[80] S. Schelkunoff. *Electromagnetic Waves* (Van Nostrand, Princeton, 1943).

[81] G. PÓLYA. *A note on the principal frequency of a triangular membrane*. Quarterly of Applied Mathematics **8**(4), 386 (1951).

[82] C. Wang. *Exact solution of equilateral triangular waveguide*. Electronics Letters **46**(13), 925 (2010).

[83] P. Overfelt and D. White. *TE and TM modes of some triangular cross-section waveguides using superposition of plane waves (short paper)*. IEEE Transactions on Microwave Theory and Techniques **34**(1), 161 (1986).

[84] M. Lucido, G. Panariello, D. Pinchera, and F. Schettino. *Cut-off wavenumbers of polygonal cross section waveguides*. IEEE Microwave and Wireless Components Letters **24**(10), 656 (2014).

[85] J.-M. Guan and C.-C. Su. *Analysis of metallic waveguides with rectangular boundaries by using the finite-difference method and the simultaneous iteration with the Chebyshev acceleration*. IEEE Transactions on Microwave Theory and Techniques **43**(2), 374 (1995).

[86] J. Gil and J. Zapata. *A new scalar transition finite element for accurate analysis of waveguides with field singularities*. IEEE Transactions on Microwave Theory and Techniques **43**(8), 1978 (1995).

[87] B. Ooi and G. Zhao. *Element-free method for the analysis of arbitrarily-shaped hollow conducting waveguides*. IEE Proceedings-Microwaves, Antennas and Propagation **152**(1), 31 (2005).

[88] A. Selamet, V. Kothamasu, and J. Novak. *Insertion loss of a Helmholtz resonator in the intake system of internal combustion engines: an experimental and computational investigation*. Applied Acoustics **62**(4), 381 (2001).

[89] S. Noh, H. Lee, and B. Choi. *A study on the acoustic energy harvesting with Helmholtz resonator and piezoelectric cantilevers*. International Journal of Precision Engineering and Manufacturing **14**(9), 1629 (2013).

[90] R. Ma, P. E. Slaboch, and S. C. Morris. *Fluid mechanics of the flow-excited Helmholtz resonator*. Journal of Fluid Mechanics **623**, 1 (2009).

[91] R. A. Stoneback. *Applications of the electromagnetic Helmholtz resonator* (The University of Texas at Dallas, 2009).

[92] L. Rayleigh. *The theory of the Helmholtz resonator*. Proceedings of the Royal Society of London. Series A, Containing Papers of a Mathematical and Physical Character **92**(638), 265 (1916).

[93] V. Koshparenok and V. Shestopalov. *Diffraction of a plane electromagnetic wave by a circular cylinder with a longitudinal slot*. USSR Computational Mathematics and Mathematical Physics **11**(3), 222 (1971).

[94] J. Rayleigh. *The theory of sound. 2nd revised and enlarged* (1945).

[95] U. Ingard. *On the theory and design of acoustic resonators*. The Journal of the Acoustical Society of America **25**(6), 1037 (1953).

[96] V. Koshparenok and V. Shestopalov. *Diffraction of a plane electromagnetic wave by a circular cylinder with a longitudinal slot*. USSR Computational Mathematics and Mathematical Physics **11**(3), 222 (1971).

[97] A. I. Nosich and V. P. Shestopalov. *Electromagnetic analogue of Helmholtz resonator*. In *Doklady Akademii Nauk*, vol. 234, pp. 53–56 (Russian Academy of Sciences, 1977).

[98] E. Veliev, A. Nosich, and V. Shestopalov. *Propagation of electromagnetic waves in a cylindrical waveguide with a longitudinal slit*. Radio Engineering and Electronic Physics **22**, 466 (1977).

[99] E. Veliev, A. Nosich, and V. Shestopalov. *Propagation of electromagnetic waves in a cylindrical waveguide with a longitudinal slit*. Radio Engineering and Electronic Physics **22**, 466 (1977).

[100] J. G. Van Bladel. *Electromagnetic fields*, vol. 19 (John Wiley & Sons, 2007).

[101] W. Rostafinski. *Analysis of propagation of waves of acoustic frequencies in curved ducts*. The Journal of the Acoustical Society of America **56**(1), 11 (1974).

[102] R. L. Panton and J. M. Miller. *Resonant frequencies of cylindrical Helmholtz resonators*. The Journal of the Acoustical Society of America **57**(6), 1533 (1975).

[103] Y. Duan, W. Koch, C. M. Linton, and M. McIver. *Complex resonances and trapped modes in ducted domains*. Journal of Fluid Mechanics **571**, 119 (2007).

[104] M. E. Kaliberda, L. M. Lytvynenko, S. A. Pogarsky, and M. P. Roiuk. *Diffraction of the H-polarized plane wave by a finite layered graphene strip grating*. International Journal of Microwave and Wireless Technologies **11**(4), 326–333 (2019).

[105] M. Kaliberda, L. Litvinenko, and S. Pogarskii. *Operator method in the analysis of electromagnetic wave diffraction by planar screens*. Journal of Communications Technology and Electronics **54**(9), 975 (2009).

[106] V. V. Veremey and Y. A. Tuchkin. *Resonance phenomena of π-mode forming in multi-element gratings*. International Journal of Infrared and Millimeter Waves **18**(4), 909 (1997).

[107] Y. V. Svishchov. *The field of a vertical magnetic dipole in the presence of a sphere with a circular aperture*. Radiophysics and Quantum Electronics **43**(9), 693 (2000).

[108] S.-J. Zhang and Y.-C. Shen. *Eigenmode sequence for an elliptical waveguide with arbitrary ellipticity*. IEEE Transactions on Microwave Theory Techniques **43**(1), 227 (1995).

[109] A. Snakowska. *Waves in ducts described by means of potentials*. Archives of Acoustics **32**(4 (S)), 13 (2014).

[110] D. M. Pozar. *Microwave engineering* (John Wiley and Sons Inc., 1998).

[111] V. V. Komarov. *Eigenmodes of regular polygonal waveguides*. Journal of Infrared, Millimeter, and Terahertz Waves **32**(1), 40 (2011).

[112] C. Wang. *Cutoff frequencies of perturbed circular waveguides and polygonal waveguides*. Journal of Electromagnetic Waves and Applications **16**(2), 151 (2002).

[113] P. J. B. Clarricoats and A. D. Olver. *Corrugated horns for microwave antennas*. 18 (IET, 1984).

[114] K. K. Chan and S. K. Rao. *Design of high efficiency circular horn feeds for multibeam reflector applications*. IEEE Transactions on Antennas and Propagation **56**(1), 253 (2008).

[115] M. N. M. Kehn and P.-S. Kildal. *Miniaturized rectangular hard waveguides for use in multifrequency phased arrays*. IEEE Transactions on Antennas and Propagation **53**(1), 100 (2005).

[116] T. Dubroca, A. N. Smith, K. J. Pike, S. Froud, R. Wylde, B. Trociewitz, J. McKay, F. Mentink-Vigier, J. van Tol, S. Wi, *et al. A quasi-optical and corrugated waveguide microwave transmission system for simultaneous dynamic nuclear polarization NMR on two separate 14.1 T spectrometers*. Journal of Magnetic Resonance **289**, 35 (2018).

[117] U. Balaji *et al. Radial mode matching analysis of ridged circular waveguides*. IEEE Transactions on Microwave Theory and Techniques **44**(7), 1183 (1996).

[118] A. Sangster and J. Grant. *Mode degeneracy in circular cylindrical ridge waveguides*. Progress In Electromagnetics Research Letters **9**, 75 (2009).

[119] R. G. Carter. *Microwave and RF vacuum electronic power sources* (Cambridge University Press, 2018).

[120] T. I. Tkachova, V. I. Shcherbinin, and V. I. Tkachenko. *Selectivity properties of cylindrical waveguides with longitudinal wall corrugations for second-harmonic gyrotrons*. Journal of Infrared, Millimeter, and Terahertz Waves **40**(10), 1021 (2019).

[121] K. U. Ingard. *Fundamentals of waves and oscillations* (Cambridge University Press, 1988).

[122] O. Bucci, C. Gennarelli, and L. Palumbo. *Flanged parabolic antennas*. IEEE Transactions on Antennas and Propagation **30**(6), 1081 (1982).

[123] O. Bucci, C. Gennarelli, and L. Palumbo. *Parabolic antennas with a loaded flange*. IEEE Transactions on Antennas and Propagation **33**(7), 755 (1985).

[124] A. Freeman. *SAR calibration: An overview*. IEEE Transactions on Geoscience and Remote Sensing **30**(6), 1107 (1992).

[125] E. D. Vinogradova, K. Kobayashi, and T. Eizawa. *Full wave analysis of plane wave diffraction by a finite sinusoidal grating: E-polarization case*. Wave Motion **86**, 44 (2019).

[126] E. D. Vinogradova and K. Kobayashi. *Complex eigenvalues of natural TM-oscillations in an open resonator formed by two sinusoidally corrugated metallic strips*. IET Microwaves, Antennas & Propagation (2021).

[127] E. K. Miller. *A selective survey of computational electromagnetics*. IEEE Transactions on Antennas and Propagation **36**(9), 1281 (1988).

[128] S. Rao and N. Balakrishnan. *Computational electromagnetics - a review*. Current Science pp. 1343–1347 (1999).

[129] J. L. Volakis, A. Chatterjee, and L. C. Kempel. *Review of the finite-element method for three-dimensional electromagnetic scattering*. JOSA A **11**(4), 1422 (1994).

[130] N. Youssef. *Radar cross section of complex targets*. Proceedings of the IEEE **77**(5), 722 (1989).

[131] Y. Stoyanov, C. Schumacher, M. Sekellick, and A. Stoyanov. *Electromagnetic scattering from a complex target with re-entrant structures*. In *Antennas and Propagation Society Symposium 1991 Digest*, pp. 1070–1073 (IEEE, 1991).